Studie naar solventeffecten in chemische, biochemische en polymerisatiereacties met behulp van statische en dynamische moleculaire modellering

Solvent Effects in Chemical, Biochemical and Polymerization Reactions, Studied with Static and Dynamic Molecular Modeling Techniques

Bart De Sterck

Promotoren: prof. dr. ir. V. Van Speybroeck, prof. dr. M. Waroquier
Proefschrift ingediend tot het behalen van de graad van
Doctor in de Ingenieurswetenschappen

Vakgroep Toegepaste Fysica
Voorzitter: prof. dr. ir. C. Leys
Faculteit Ingenieurswetenschappen
Academiejaar 2010 - 2011

UNIVERSITEIT
GENT

ISBN 978-90-8578-386-2
NUR 914, 928
Wettelijk depot: D/2010/10.500/62

Center for
Molecular Modeling

Dit onderzoekswerk werd uitgevoerd binnen het Centrum voor Moleculaire Modellering

Voorwoord

In 2006, op hetzelfde moment wanneer horden schoolkinderen met weemoed terugkeken op de voorbije twee maanden en tegelijkertijd vol spanning en met een boekentas gevuld met nagelnieuwe kleurtjes, opnieuw aan de schoolpoort stonden, begon ook ik met volle moed en veel verwachtingen aan dit werk. Drie zomers zijn voorbijgegleden, zonnig gekabbeld en voorbijgedreven sindsdien. De vierde zomer duurde opmerkelijk langer, was intenser, turbulenter ook. Één van de redenen daarvoor was zeker en vast het schrijven aan dit proefschrift. Die laatste zomer ging gepaard met wanhoop, vreugde, vertwijfeling en ontdekking. Deze vier woorden vatten volgens mij het proces achter een doctoraat goed samen. Het werkt niet! Het werk wel! Werkt het wel? Ja, het werkt! Het is dan ook niet gespeend van enige trots dat ik deze traditioneel laatste regels typ die een werk van vier jaar afronden.

Dit proefschrift was natuurlijk niet mogelijk geweest zonder de aanwezigheid van de nodige materiële en intellectuële steun. Hiervoor wil in in het bijzonder mijn promotoren, Veronique Van Speybroeck en Michel Waroquier, bedanken om mij de kans te geven dit onderzoek uit te voeren in het Centrum voor Moleculaire Modellering (CMM). De vele discussies over dit onderzoek hebben het naar een hoger niveau getild en waren zeer leerrijk.

Daarnaast wil ik ook alle andere leden van het CMM bedanken voor de zeer aangename werksfeer en de gezellige (middag)pauzebabbels tussendoor. In het bijzonder een grote dank-je-wel aan Karen en Toon, mijn af-en-aan bureaugenoten, met wie ik gedurende de afgelopen 4 jaar lief en leed heb kunnen delen. Ik wens hen allebei het allerbeste, zowel op professioneel als op persoonlijk vlak. Een speciale vermelding voor Wim is ook op zijn plaats hier. Bedankt voor alle hulp met de grafische kanten van dit proefschrift, met name ettelijke figuren en de uitnodiging voor mijn verdediging. Another thank you goes out to Saron to whom I owe the discovery of new parts of this globe but also of the interesting world of biochemical reactions and the computational techniques associated with it.

Ik wil ook graag de mensen van buiten het CMM bedanken met wie ik in de afgelopen jaren heb kunnen samenwerken. In de eerste plaats gaat mijn dank uit naar Norbert De Kimpe en Sven Mangelinckx van de Faculteit Bio-ingenieurswetenschappen. A second partner in science is Viktorya Aviyente from the Boğaziçi University in Istanbul whom I would like to thank for the interesting collaboration in the field of free radical polymerization. Tenslotte wil ik graag mijn waardering uitdrukken voor de gastvrijheid van en de samenwerking met Rosa Bula van de Vrije Universiteit Amsterdam . Tijdens mijn verblijf in Amsterdam had ik de gelegenheid om de stad te ontdekken (Je kan er naar Van Gogh gaan kijken, dat zou je eigenlijk eens moeten doen) en om me verder te verdiepen in de methodologische aspecten van vrije-energieberekeningen.

De laatste vier jaren heb ik langs professionele weg een heel aantal boeiende mensen leren kennen, maar er zijn natuurlijk ook de mensen die ik al vele jaren ken. In de eerste plaats wil ik de vrienden van de chemie bedanken met wie ik vier jaar geleden afstudeerde en waarmee ik hopelijk nog vele jaren intens contact kan hebben. Ik wil hen dan ook graag heel veel geluk, succes, etentjes en weekendjes weg toewensen.

Andere mensen die absoluut een bloemetje verdienen voor het aangenaam doorkomen van de voorbije negen jaar zijn Jon, Tim, Petra en Endre. Een sprookjesachtige ontmoeting in de Efteling, net na het afwerken van mijn thesis, heb ik te danken gehad aan Kristof, Elke, Hannes en Sara. De ontspanning was welgekomen, het gezelschap kon niet beter zijn. Ik wil ook graag van deze gelegenheid gebruik maken om Patrick te bedanken. Ik wens hem veel succes toe in zijn verdere leven.

Tot slot wil ik mijn ouders en broer in de bloemetjes zetten voor de interesse waarmee ze mij de voorbije vier jaar gevolgd hebben, alhoewel het niet altijd evident moet geweest zijn om te snappen waarover ik aan het doordrammen was. Zij hebben me steeds gesteund in mijn keuzes en ik ben hen daar zeer erkentelijk voor.

En uiteraard wil ik ook u, de lezer, bedanken om niet enkel dit voorwoord te lezen maar dapper door te zetten en u in de volgende pagina's te verdiepen in hoe solventeffecten op chemische reacties kunnen gemodelleerd worden. Succes!

'Ik leef,' fluisterde hij, 'ik adem. En ik beweeg.
Ik adem, ik beweeg, dus ik leef. Wat kan er nog gebeuren?
Er kunnen rampen komen, pijnen, verschrikkingen. Maar ik leef.
Ik kan opgesloten zijn, of door gruwelijke ziekten worden bezocht.
Maar steeds adem ik, en beweeg ik. En ik leef.'
Hij liep terug naar de keuken, voltooide het poetsen
en betrad zijn slaapkamer.

De avonden, Gerard Reve

Leden van de examencommissie

Voorzitter

Prof. dr. ir. Rik Van de Walle (Universiteit Gent)

Leescommissie

Prof. dr. Viktorya Aviyente (Boğaziçi University, Istanbul)
Prof. dr. Rob Meier (DSM research Geleen (Nederland), University of York)
Prof. dr. Marie-Françoise Reyniers (Universiteit Gent)
Prof. dr. ir. Veronique Van Speybroeck (Universiteit Gent, promotor)

Overige leden

Dr. Rosa Bulo (Vrije Universiteit Amsterdam)
Dr. Saron Catak (Universiteit Gent)
Prof. dr. ir. Norbert De Kimpe (Universiteit Gent)
Prof. dr. ir. Karen De Clerck (Universiteit Gent)
Prof. dr. Dimitri Van Neck (Universiteit Gent)
Prof. dr. Michel Waroquier (Universiteit Gent, promotor)

Contents

List of Figures

List of Tables

Samenvatting

Chemie is overal om ons heen: in laboratoria waar nieuwe verbindingen en reacties worden onderzocht, bij de industriële productie van zowel bulkchemicaliën als specialiteitsprodukten, in de natuur, in de atmosfeer, in het menselijk lichaam,... De opkomst van de moderne kwantummechanica zorgde ervoor dat chemische reacties niet meer alleen experimenteel in labo's bestudeerd konden worden, maar bood de mogelijkheid om moleculen en reacties op een fundamantele, theoretische manier te onderzoeken. De basisvergelijking van het moleculair systeem is de veeldeeltjes-Schrödingervergelijking die niet exact oplosbaar is, maar waarvoor benaderende oplossingen nodig zijn. Met de opkomst van Hartree-Fock (HF) theorie en in een later stadium dichtheidsfunctionaaltheorie (DFT), werd het mogelijk om chemische reacties te modelleren met behulp van computersoftware. Dit onderzoeksgebied staat bekend als kwantumchemie of computationele chemie. Deze theoretische doorbraak, gecombineerd met de recente toename in processorsnelheid en rekentijd en met de ontwikkeling van geavanceerde modellen, snellere hardware en parallellisatietechnieken, maakt het mogelijk om grote, vrij realistische modellen voor chemische reacties te bestuderen. In het merendeel van de gevallen speelt de moleculaire omgeving een zeer belangrijke rol aangezien een groot aantal chemische reacties wordt beïnvloed door het milieu waarin ze doorgaan. Het doel van dit proefschrift is om te onderzoeken hoe een oplosmiddel het reactiemechanisme en de reactiesnelheidscoëfficiënt kan beïnvloeden en welke theoretische modellen hiervoor het meest geschikt zijn. Daartoe werden een aantal reacties geselecteerd die in oplossing doorgaan.

Aangezien het modelleren van een solventomgeving een grote uitdaging is in de computationele chemie, is het niet verwonderlijk dat er reeds gedurende lange tijd modellen ontwikkeld worden om soluut-solvent interacties te modelleren. In de meestgebruikte techniek worden één of meer solventmoleculen expliciet in rekening gebracht in de *in vacuo* berekeningen; dit is het zogenaamde expliciet solventmodel. Het is een handige manier om solventeffecten in rekening te brengen op voorwaarde dat er een sterke interactie bestaat tussen het solvent en het soluut zoals waterstofbruggen of kation-zuurstof interacties. Wanneer de interactie zwakker is, is het positioneren van het solvent ten opzichte van de bestudeerde molecule een zeer ambiguë opdracht. Als alternatief kan het solvent ook gemodelleerd worden als een continuë omgeving die gekarakteriseerd wordt door zijn diëlektrische constante. Deze methode is algemeen bekend als het impliciet solventmodel. Met deze benadering kan het effect van de bulk van het solvent in rekening gebracht worden, maar ze is niet geschikt om specifieke, gerichte interacties mee te beschrijven. Daarom wordt in de praktijk vaak een gecombineerd model gebruikt waarbij een expliciet gesolvateerd complex wordt ingebed in een continuë, diëlektrische omgeving wanneer reacties in oplossing worden bestudeerd. Een conceptueel eenvoudigere methode waarin alle solventmoleculen die nodig zijn om het soluut in voldoende mate te omringen, aanwezig zijn, is de moleculaire dynamica techniek. Deze houdt in dat een periodieke simulatiecel op een gegeven temperatuur wordt gesimuleerd door de bewegingsvergelijkingen van Newton op te lossen. Het moleculair traject dat op deze manier berekend wordt, kan vervolgens geanalyseerd worden en geeft informatie over de evenwichtstoestand van het bestudeerde systeem op de gekozen temperatuur. Het systeem kan op deze manier de meest gunstige configuratie aannemen zonder dat er *a priori* informatie nodig is over de specifieke solvent-soluut interacties die optreden.

De modellen die in vorige paragraaf kort zijn beschreven, worden in dit proefschrift toegepast op drie verschillende chemische systemen. Het eerste probleem bestaat uit een onderzoek naar de stereochemie en reactiviteit van gemetalleerde, gehalogeneerde organische anionen (3-halo-3-methyl-1azaallylische anionen). Dit onderzoek is geïnspireerd door een samenwerking met de onderzoeksgroep van Prof. De Kimpe van de faculteit Bioingenieurswetenschappen van de universiteit Gent. Vanuit een experimenteel oogpunt is tetrahydrofuraan (THF) een geschikt solvent voor deze structuren. Omdat het aantal solventmoleculen dat nodig is om de verschillende isomeren van deze kation-anion complexen te solvateren afhankelijk is van het type isomeer, is een combinatie van statische en dynamische methoden nodig om een globaal en correct beeld te krijgen. Een gecombineerd experimenteel-theoretisch onderzoek toont aan dat er slechts één isomeer van het bestudeerde 3-chloro-3-methyl-1-azaallylisch anion gecomplexeerd met lithium aanwezig is in de oplossing, het Z/*anti* isomeer. Bovendien tonen de theoretische berekeningen aan dat dit isomeer slechts met één THF molecule coördineert, terwijl het Z/*syn* isomeer met twee solventmoleculen interageert en bovendien minder stabiel is. Dit onderzoek werd uitgebreid met een grote set gelijkaardige 3-halo-3-methyl-1azaallylische anionen waarbij zowel het tegenion als het halogeen gevarieerd werd. In alle gevallen is het Z/*anti* isomeer het meest stabiel. Deze informatie over de stereochemie van deze moleculen is zeer belangrijk aangezien ze een impact zullen hebben op de stereochemie van de producten die gevormd worden in reacties.

Een tweede systeem dat onderzocht wordt, komt uit het domein van de vrije radicalaire polymerisatie. In deze studie wordt het effect van water op de polymerisatiesnelheid van enkele acrylamides onderzocht. Dit onderzoek toont aan dat de berekende reactiesnelheidscoëfficiënt voor de propagatie van acrylamide en N-methylacrylamide significant groter wordt wanneer het solvent in rekening gebracht wordt. Deze conclusie geldt zowel voor expliciete watermoleculen die assisteren in de transitietoestand als voor het impliciet watermodel. Het feit dat deze berekende reactiesnelheidscoëfficiënten in vergelijking met de berekende waarden in de afwezigheid van solvent veel beter overeenstemmen met de experimenteel bepaalde waarden, toont aan dat solventeffecten zeer belangrijk zijn en dat ze in rekening gebracht moeten worden bij het modelleren van de reacties. In een onderzoek in samenwerking met Prof. Aviyente van de Boğaziçi Universiteit in Istanboel, werd de invloed onderzocht van waterstofbrugvormende solventen op de tacticiteit van polymethylmethacrylaat. Dit onderzoek toont dat de syndiotacticiteit toeneemt wanneer perfluoro-*tert*-butyl alcohol als solvent wordt gebruikt in plaats van methanol. De studie toonde ook aan dat dit effect veroorzaakt wordt door de watertsofbruggen die gevormd worden in de transitietoestand.

De laatste toepassing komt uit het domein van de biochemische reacties en heeft als doel om de degradatie van asparagine (Asn) en glutamine (Gln) zijketens in peptides en proteïnen te begrijpen. Hiertoe worden moleculaire dynamica simulaties uitgevoerd voor acetamide en N-methylacetamide in water. Deze moleculen zijn een goed model, zowel voor de zijketens als voor het peptideketen zelf. Vanuit methodologisch standpunt is dit een interessant probleem aangezien water in dit systeem zowel het solvent als een reactieve molecule is in de hydrolysereactie. Deze reactie werd bestudeerd met de metadynamica methode. Deze methode laat toe om zeldzame gebeurtenissen (e.g. conformationele transities, chemische reacties,...) te versnellen en om het vrije-energieoppervlak te reconstrueren waarop deze gebeurtenis plaatsvindt.

De systemen die in dit proefschrift worden onderzocht zijn allemaal tot op zekere hoogte onderworpen aan solventeffecten. Afhankelijk van het systeem, de onderzoeksvraag en de aard van het solvent kan een gepast model geselecteerd worden. Wanneer goedgedefinieerde interacties tussen het soluut en het solvent aanwezig zijn, zoals de waterstofbruggen in de acrylamide polymerisatie, kan een groot deel van het solventeffect gemodelleerd worden met statische berekeningen. Wanneer het effect minder duidelijk gedefinieerd is, wanneer statische berekeningen tonen dat verschillende toestanden van het systeem een andere solvatatie vertonen of wanneer het solvent ook een reactant is, kunnen moleculaire dynamica en meer geavanceerde technieken om zeldzame gebeurtenissen te beschrijven, gebruikt worden. Deze methoden laten toe om chemische reacties in oplossing op een correcte en accurate manier te beschrijven.

Summary

Chemistry is everywhere: in laboratories where new compounds and reactions are investigated, in the industrial production of bulk chemicals and specialized products, in nature, in the atmosphere, in our own bodies,... With the rise of modern quantum mechanics, molecules and chemical reactions could be investigated in a fundamental, theoretical way. This research field is often called quantum chemistry or computational chemistry. The basic equation of the molecular system is the many-particle Schrödinger equation which is not exactly solvable and needs approximative solution methods. With the introduction of Hartree-Fock (HF) theory and later Density Functional Theory (DFT) it has become possible to model chemical reactions with computer software. These theoretical breakthroughs combined with the recent rise in computer speed, advanced models, process parallelization techniques and hardware now make it possible to treat large, quite realistic models for chemical problems. In the majority of cases, the environment plays a very important role as numerous reactions are influenced to a large extent by their surroundings. The reactions studied in this thesis were selected since they all occur in a solution and the focus is set on how a solvent can influence the reaction mechanism and the reaction rate and also on which theoretical model is best suited for describing these effects.

Modeling the solvent environment is a great challenge in computational chemistry and several models have been developed in order to take solvent effects into account. The most used technique is the inclusion of one or more explicit solvent molecules in the gas phase calculations, the so-called explicit solvent model. This is a convenient way to account for solvent effects if the solute and solvent molecule have a strong mutual interaction like hydrogen bonding or cation-oxygen interactions. When this is not the case, defining the position of the solvent relative to the species under investigation is an ambiguous task as the interaction is very ill-defined. Therefore, the solvent can also be modeled as a continuous environment, characterized by its dielectric constant, which surrounds the solute. This approach is generally known as the 'implicit solvent model'. This model allows taking into account the effect of the bulk solvent but it is not suitable for describing specific, directed solute-solvent interactions and therefore, a combined model in which an explicitly solvated cluster is embedded in a continuum model can give good results when studying solutes and reactions in solution. A conceptually even more straightforward method is a molecular dynamics

approach in which all solvent molecules are taken into account explicitly in a periodic box that is large enough to accommodate the solute and a large amount of solvent molecules. This system is then treated at a well-defined temperature by solving Newton's equations of motion and analyzing the molecular trajectory that results from it. In this way, the system can adopt the most feasible configuration without the need for *a priori* information about the specific solvent-solute interactions that take place.

The above sketched solvation models have been applied on three sets of chemically interesting problems. The first set of reactions is the stereochemistry and reactivity of metalated, halogenated organic anions (3-halo-3-methyl-1-azaallyl anions) and was inspired by a collaboration with the research group of Prof. De Kimpe (Faculty of Bioengineering). For these species, tetrahydrofuran (THF) is the solvent of choice from an experimental point of view. As the amount of solvent molecules that is needed to solvate the various isomers is not fixed, a combination of static and dynamic methods was necessary in order to to obtain an overall and correct image of the determining factors. A combined experimental and theoretical dynamic study has shown that only one isomer of lithiated 3-chloro-3-methyl-1-azaallylic anion is present in solution (the Z/*anti* isomer) and that this isomer has a different first solvation shell compared to the E/*anti* isomer. This was investigated further for a large set of similar 3-halo-3-methyl-1-azaallyl anions, bearing different counterions and halogens, confirming the Z/*anti* isomer to be the most stable for all species studied. This delivers important information when studying reactions that involve these species as the stereochemistry of the starting product is often determining for the product distribution.

A second set of reactions were selected from the field of free radical polymerization. For these reactions, water was used as a solvent and the rate enhancement due to this particular liquid was investigated for the polymerization of several acrylamide based monomers. This study showed that the calculated reaction rate coefficient for acrylamide and N-methylacrylamide significantly increased when taking into account the effect of the solvent, either by adding assisting water molecules to the calculated transition states in the gas phase, either by including them in a dielectric continuum. As the resulting rate coefficients were in much better agreement with the experimentally available values compared to the previously performed gas phase calculations, the importance of including solvent effects is illustrated. Also, the effect of solvent on the tacticity of methyl methacrylate was studied in cooperation with Prof. Aviyente from the Boğaziçi University of Istanbul showing that the preference to form syndiotactic polymer is indeed enhanced by using perfluoro-*tert*-butyl alcohol instead of methanol. This effect was shown to be governed by hydrogen-bonding effects in the transition state.

The last application lies in the field of biochemical reactions and is aimed at helping to understand the degradation of asparagine (Asn) and glutamine (Gln) sidechains that are present in peptides and proteins. For this purpose, molecular dynamics simulations were performed on acetamide and N-methylacetamide as model components for both the sidechains and the peptide backbone. The interesting aspect from a methodological point of view in this system is the fact that water is both the solvent and one of the reactants for the hydrolysis reaction that takes place. For this problem, the metadynamics method was used that allows the acceleration of rare events (e.g. conformational transition, chemical reactions,...) the construction of the free energy surface on which several possible reaction pathways can be mapped.

In conclusion, the systems that have been studied in this thesis are all subject to solvent effects to a certain extent. Depending on the system, the problem, and the nature of the solvent, different solvent models have to be considered in order to select the most suited one. When very specific interactions are present, like the water bridges in the acrylamide polymerization, a large effect can be seen from static calculations from which experimental observations can be explained. When the effect is less defined, when static calculations show that different interesting states show a different solvation behavior, or when the solvent can also act as a reactant, molecular dynamics and more advanced rare events techniques have to be used in order to correctly describe the chemical reaction one is interested in.

Part I

Solvent Effects in Chemical, Biochemical and Polymerization Reactions

1

General Introduction

Chemistry is everywhere: in laboratories where new compounds and reactions are investigated, in the industrial production of bulk chemicals and specialized products, in nature, in the atmosphere, in our own bodies,... A lot of these chemical processes and reactions occur in an appropriate solvent. Among all possible solvents, water is very important for many chemical reactions due to several reasons. When looking at the human body for instance, water is abundant and the numerous chemical reactions occurring are influenced by the presence of water. Also from an ecological point of view, industrial processes that can be carried out in water, deliver a lot of benefits as no large amounts of possibly polluting and often expensive solvents have to be used. In laboratory conditions, numerous solvents (like ethanol, tetrahydrofuran,. . .) can be used depending on the specific properties that are required for the reaction under study.

A characterizing property of a liquid is the dielectric constant, ϵ, which quantifies the polarity and polarizability of the solvent molecule. In Table 1.1, a brief set of solvents and their dielectric constant is shown. Based on this property, solvents can be ranked from apolar or polar as their dielectric constant increases. Within the polar category, a distinction can be made between protic (acetic acid, ethanol, water) and aprotic (pyridine, acetonitrile) solvents depending on whether an acidic proton is present or not. Another way of looking at the molecules in Table 1.1 is by making a distinction between solvent molecules that can directly interact with a solute molecule (ethyl ethanoate, tetrahydrofuran) and those who will interact through more disperse interactions (benzene, chloroform). In this thesis, focus is set on systems in solution in which the solute and solvent directly interact with each other, e.g. through hydrogen bonding and metal-oxygen interactions.

With the rise of modern quantum mechanics, chemistry also could be

Table 1.1: An overview of dielectric constants for a range of commonly used solvents.

Solvent	ϵ
Cyclopentane	1.96
Carbon Tetrachloride	2.23
Benzene	2.27
Toluene	2.37
Dibutyl Ether	3.05
Diethyl Amine	3.58
Diethyl Ether	4.24
Chloroform	4.71
Ethyl Ethanoate	5.99
Acetic Acid	6.25
Tetrahydrofuran	7.43
Pyridine	12.98
2-Butanol	15.94
Ethanol	24.85
Methanol	32.61
Acetonitrile	35.69
Water	78.36

looked at from another perspective. This research field is often called quantum chemistry. In the early years, the basic equations of the molecular system were available but were not solvable due to the complexity of the quantum mechanical problem to be treated. With the introduction of Hartree-Fock (HF) theory and later Density Functional Theory (DFT) it has become possible to model chemical reactions with computer software. These theoretical breakthroughs combined with the recent rise in computer speed, advanced models, process parallelization techniques and hardware now make it possible to treat large, quite realistic models for chemical problems that range from biochemistry, DNA studies and protein-pharmaceutics interaction to industrial products, polymers, and heterogeneous catalysis.

In all of these systems, the environment plays a very important role as every reaction that was mentioned is influenced to a large extent by its surroundings. The reactions studied in this thesis were selected since they all occur in a solution and the focus is set on how a solvent can influence the reaction mechanism and the reaction rate and also on which theoretical model is best suited for describing these effects. The applications that were chosen may seems very diverse but they were inspired by various collaborations.

The advantage of such a broad set of reactions is that it shows that every system needs its own methodology.

Although modeling the solvent environment of a chemical reaction seems like a very logical and intuitive step, practice shows that it is far from a trivial expansion of the traditional modeling environment i.e. *in vacuo*, often referred to as the gas phase. Due to the methodological challenges associated with solvent modeling, up to a few years ago most of the theoretical studies have neglected the environment. The most common practice for including the solvent environment is by using relatively simple continuum models that will be sketched later in this thesis. As there are a lot of experimental indications that solvents may have a crucial importance on organic reactions, therefore, a vast amount of research has been conducted over the last 60 years on developing appropriate computational tools for solvent modeling. In general, there are two approximations to the problem of simulating the solvent environment that differ fundamentally in the way the solvent is treated. The solvent can be modeled explicitly, meaning that solvent molecules are included in the model and these can interact directly with the solute under study. This is of course the most straightforward method, but selecting a limited number of solvent molecules and determining the position of these species with respect to the solute is a far from trivial procedure.

Another method that has received a lot of attention throughout the years is a so-called implicit inclusion of the solvent in which no explicit solvent molecules are taken into account, but the solvent is modeled as a continuous environment that is characterized solely by its dielectric constant. These two methods will be further addressed to as the static methods as they only take into account the properties of a few points on the potential energy surface and do not follow the time evolution of the system. In order to simulate the system in a dynamic way, allowing fluctuations in the solvation pattern, a large amount of explicit solvent molecules must be taken into account in such a way that the solute or reaction under study is properly embedded in the solution. This method of course requires more computational resources as the model space of the molecular system gets larger but it avoids a lot of problems that are inherent to the static methods discussed before, like the fact that no interaction positions have to be determined in advance. For this purpose, in principle Molecular Dynamics (MD) or Monte Carlo simulations (MC) can be used. In this thesis, the MD methodology was applied as this is the most efficient way to treat a solvent system. In this way, the time evolution and collective motion of the system can be studied avoiding computationally expensive rejected steps in MC simulations.

The above sketched solvation models have been applied on three sets of chemically interesting problems. The first set of reactions is the stereochemistry and reactivity of metalated, halogenated organic anions (3-halo-3-methyl-1-azaallyl anions) and was inspired by a collaboration with the research group of Prof. De Kimpe (Faculty of Bioengineering). For these species, tetrahydrofuran (THF) is a commonly used solvent in an experimental setup. As the amount of solvent molecules needed to solvate the various isomers is not fixed, a combination of static and dynamic methods was necessary to obtain a correct image of the determining factors. A second set of reactions was selected from the field of free radical polymerization. For these reactions, water was used as a solvent and the rate enhancement due to this particular liquid was investigated for the polymerization of several acrylamide based monomers. Also, the effect of solvent on the tacticity of an acrylate was studied in cooperation with Prof. Aviyente from the Boğaziçi University of Istanbul and other projects are still running. The last application is the hydrolysis reaction of acetamides, a model for peptide sidechain degradation in which water takes the role of both the solvent and the reactant.

In the following chapter, first the theoretical tools that are needed to describe the solvent effects in the aforementioned systems will be explained. This includes the implicit and explicit static methods as well as the dynamic treatment of large solvated systems and the determination of energy differences in this model using a methodology called metadynamics. In the third chapter, a brief overview of the applications from the previous paragraph will be presented and finally, general conclusions regarding these systems and solvent modeling will be drawn.

2

Theoretical Methods

In this chapter, the most important methodologies for modeling solvent effects in quantum chemical simulations are described. There are two categories of models that will be treated: static methods in which the total energy of a given system is minimized and dynamic methods that simulate the time evolution of a chemical system at finite temperature. Both the static and the dynamic simulations are carried out using quantum mechanical based methods. A variety of electronic structure methods was used that are either based on the Hartree-Fock (HF) formalism or Density Functional Theory (DFT). An extensive description of these methods will not be presented here as the focus of this methodological section is the modeling of solvent effects. An overview of these methodologies can be found in several text books.[1,2]

In the static method, two approaches of solvent modeling are common. The solvent can be treated as a continuous environment characterized by its dielectric constant that surrounds the solute. This approach is generally known as the '**implicit solvent model**' or the '**continuum solvent model**'. Another, more straightforward way of treating solvent, is including explicit solvent molecules in the gas phase calculations: the '**explicit solvent model**', '**solvated cluster**' approach, or '**microsolvation**'. In this way, interactions between the solvent and the solute are taken into account explicitly (e.g. hydrogen bonding). Of course, one can combine these two approaches by embedding a solvated complex in a continuum. This is generally known as '**the combined explicit/implicit solvent model**'.

When using dynamic methods, a lot of information can be obtained by molecular dynamics (MD) simulations in a canonical or isothermal-isobaric ensemble about structural parameters of the species in solution. This method performs well for studying equilibrium properties of solvated species. Reaction pathways, however, are inherently non-equilibrium states and therefore require other techniques that enable the system to leave its initial equilibrium state (the reactant state), cross a reaction barrier (and thereby undergo a rare event) and end up in another equilibrium state (a reaction intermediate or the product region). A variety of methods has been developed to this aim, an overview of which can be found in a recent review on Free Energy calculations.[3] In this thesis, the metadynamics (MTD) method was used which introduces an accelerating bias that forces the system to explore non-equilibrium states and provides a mean to estimate the Gibbs free energy profile of the pathway(s) under study.

2.1 Static Solvation Models

2.1.1 Continuum Solvation

In the continuum solvation approach, the solute molecule under study is placed in a molecular-sized (and usually molecular-shaped) cavity that is surrounded by a continuous dielectric medium mimicking the solvent. That medium is characterized by the dielectric constant of the bulk solvent, ϵ, while a vacuum is assumed inside the cavity. Considering the importance of these models, it is not surprising that the literature on continuum solvation models is very elaborate.[4–7]

In a solvation process, the Gibbs free energy of solvation, ΔG_{sol}, is defined as the reversible work that is needed to transfer the solute from the gas phase to the solution under the condition of constant temperature, pressure and solvent composition.[4,8] In this definition, the free energy contains contributions from both solute-solvent interactions and from internal changes in the solute and the solvent that arise from solvation. In practical applications, the free energy of the solute in the dielectric environment can then be determined as the sum of an electrostatic and a non-electrostatic contribution. However, no thermodynamically unique way exists in defining these two parts as only their sum is a state function and not their individual contributions that depend on the specific continuum model that is used (see further). The difference between the various implicit solvent models lies in the way in which the parameters for the electrostatic and non-electrostatic terms are defined. The most general expression for ΔG_{sol} is shown in equation 2.1.[7] This expression consists of the free energy of solvation due to the electrostatic interaction, ΔG_{el}, and non-electrostatic contributions due to repulsion and Van der Waals type dispersion interactions, $G_{rep} + G_{dis}$, and to the formation of the cavity in the continuum, G_{cav}.

$$\Delta G_{sol} = \Delta G_{el} + G_{rep} + G_{dis} + G_{cav} \tag{2.1}$$

In this section, first the basic ideas behind the electrostatic and non-electrostatic contributions will be explained. In the next section, one important class of implicit models will be discussed: the apparent surface charge (ASC) model.

The Electrostatic Contribution to the Free Energy

For the electrostatic contribution, one can see that the charge distribution of the solute molecule, $\rho_M(\vec{r})$ (the quantum mechanical electron density), will induce polarization of the surrounding dielectric medium which in turn will polarize the solute charge density, hence resulting in a self-consistent problem. The total electric potential in the continuum model, $\hat{V}$, can be expressed as the sum of the electrostatic potential of the solute, $\hat{V}_M$, and the electric potential due to the polarization of the dielectric and the solute, the interaction potential or reaction field $\hat{V}_{int}$ (see equation 2.2).

$$\hat{V} = \hat{V}_M + \hat{V}_{int} \tag{2.2}$$

Some implicit solvation models exist that are based on multipole expansions (MPE methods) of the solute charge density and the solvent reaction field potential like the Onsager model.[7,9] In this quite simple model, the solute is described as a dipole in a spherical cavity. Another example of a multipole method (where the multipoles are truncated at the first term, the charges on the nuclei) is the generalized Born approach (GB) that uses a Coulomb-type equation to determine the free energy in the implicit solvent model.[7,10] In this work, however, only the so-called density-based implicit models that take into account the continuous nature of the charge distribution will be considered.

The total potential is the solution of the non-homogeneous Poisson equation (NPE, in Gaussian units) in which $\rho_M(\vec{r})$ is the solute charge density and $\epsilon(\vec{r})$ is the dielectric function of the medium:

$$\nabla \cdot (\epsilon(\vec{r}) \nabla \hat{V}) = -4\pi \rho_M(\vec{r}) \tag{2.3}$$

Within the cavity, vacuum is assumed ($\epsilon(\vec{r}) = 1$) and the dielectric function takes on a constant value outside the cavity that equals the dielectric constant of the medium ($\epsilon(\vec{r}) = \epsilon$), see also Figure 2.1, resulting in the following set of equations in which C is the space occupied by the cavity:

$$\begin{aligned} \nabla^2 V(\vec{r}) &= -4\pi\rho_M(\vec{r}) \quad \textit{within } C && (2.4) \\ \epsilon\nabla^2 V(\vec{r}) &= 0 \quad \textit{outside } C && (2.5) \end{aligned}$$

On the cavity surface, Γ, boundary conditions are required in order to avoid discontinuities. These can be described as the following jump conditions:

$$\begin{aligned} [V] &= V_{in} - V_{out} = 0 \quad \textit{on } \Gamma && (2.6) \\ [\delta V] &= \left(\frac{\delta V}{\delta \vec{n}_{I,II}}\right)_{in} - \epsilon\left(\frac{\delta V}{\delta \vec{n}_{I,II}}\right)_{out} = 0 \quad \textit{on } \Gamma && (2.7) \end{aligned}$$

Condition 2.6 imposes the continuity of the potential across the surface whilst the second condition (equation 2.7) ensures the continuity of the perpendicular component of the field. $\vec{n}_{I,II}$ is the normal vector on the cavity surface pointing outwards (from region I in the cavity to region II outside the cavity), see also Figure 2.2. In this way, equation 2.3 can be solved in a self consistent way when coupled to the quantum mechanical electron density and will result in the total potential from which the self consistent reaction field (SCRF) potential, $\hat{V}_{int}$, in the implicit solvent can be calculated. Once the interaction potential is known, it can be used to calculate the Gibbs free energy in solution, G^S, using the Schrödinger equation with a linearized effective Hamiltonian that consists of the Hamiltonian in vacuo, $\hat{H}^0_M$, and half of the interaction potential, see equation 2.8. The expectation value of the $\hat{H}^0_M + \frac{1}{2}\hat{V}_{int}$ operator gives indeed a Gibbs free energy, as proven by Yomosa et.al.[7,11].

$$G^S = \langle\Psi|\hat{H}^0_M + \frac{1}{2}\hat{V}_{int}|\Psi\rangle \qquad (2.8)$$

The factor $\frac{1}{2}$ actually accounts for the work that is spent in polarizing the continuum as a result of introducing a charge distribution (the solute electron density, $\rho_M(\vec{r})$) in the dielectric. This work cannot be recovered by taking the molecule out of the dielectric. It is therefore irreversible and only half of that work (the part that polarizes the solute) should be considered when calculating the free energy.

The Non-Electrostatic Contribution to the Free Energy

In a solvation process, not only the electrostatics are important, but also non-electrostatic effects, like dispersion, should be taken into consideration. The relative importance of both contributions to the total free energy in solution depends on the nature of the solvent: in more polar solvents, the electrostatics will outweigh the other effects while in apolar liquids, the opposite will occur. In general, there's three important contributions to this part of the free energy originating from cavitation (G_{cav}), repulsion (G_{rep}) and dispersion (G_{dis}).

Cavitation Free Energy In order to determine G_{cav}, first of all the cavity itself has to be defined. The principle of cavity definition is explained in Figure 2.1 for the most simple model: a spherical solute (with radius R_M) in a spherical solvent (with radius R_S). Two surfaces can be defined based on Figure 2.1. The Solvent Excluding Surface (SES) is defined by the solute radius as no solvent molecules are able to cross this surface. When taking the locus defined by the geometric center of the solvent sphere as it rolls on the solute molecule, the Solvent Accessible Surface (SAS) is defined. This is the smallest radius around the solute in which solvent molecules can penetrate.[7] The latter surface has been used very frequently in order to determine the cavity, but more recently the Van der Waals surface was applied e.g. in the latest version of the Gaussian software package.[12] The definition of the cavity surface is a key component in any PCM model as it also defines the $\epsilon(\vec{r})$ function. Within the cavity, vacuum is assumed, so $\epsilon(\vec{r}) = 1$ whereas outside the cavity, this function becomes constant and takes on the value of the dielectric constant of the solvent under study as is illustrated in the graph in Figure 2.1.

The contribution from cavitation is calculated as the work that is needed to create a cavity in the continuum in the absence of solute-solvent interactions. It can therefore be seen as a hypothetical term for which the interactions are switched off whereas the other terms in equation 2.1 can be evaluated once the interactions are switched on again. Since the beginning of this concept,[13–15] several techniques have been developed that are either based on solvent's surface tension,[13,16] on the isothermal compressibility[5,17] or on the effective radii of the solute and solvent, the so-called Pierotti formalism.[18] As this formalism is the most frequently used in modern quantum chemistry packages, a more detailed description of this theory will be given here. Under the assumption that the solute behaves as hard spheres, the cavitation Gibbs free energy, G_{cav}, can be expanded in powers of R_{MS}, the sum of the radii of the solute (R_S) and the solvent (R_M),see equations 2.9 to 2.15.

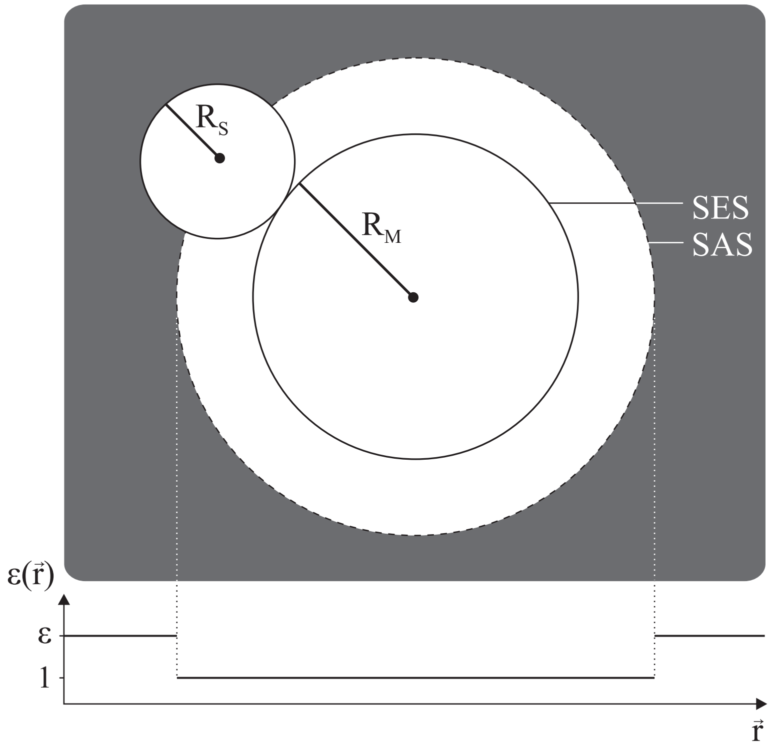

Figure 2.1: Definition of the Solvent Accessible Surface (SAS) and the Solvent Excluding Surface (SES) for a spherical solute surrounded by spherical solvent molecules. The dielectric function on the r-axis through the center of the solute sphere is plotted at the bottom of the figure.

This formalism works well for spherical-shaped solutes and solvents, but it gets more complicated when non-spherical molecules come into play. In that case, an effective radius, $R_{eff,M}$, (like in equation 2.16) will have to be estimated from the molecular volume, V_M. For non-spherical solutes, the contribution of each atom to the cavitation Gibbs free energy can be weighed by the fraction of solvent-exposed surface (S_i) of all the atoms i that are part of the solute, see equation 2.17.[5,19] Even though the dielectric solvation energy (DSE) that is obtained through a PCM calculations is very dependent on the cavity model that is used, the relative values (e.g. the the energy difference between two isomers) is much less sensitive to the choice of the molecular cavity.

$$\begin{aligned}
R_{MS} &= R_M + R_S && (2.9)\\
G_{cav} &= K_0 + K_1 R_{MS} + K_2 R_{MS}^2 + K_3 R_{MS}^3 && (2.10)\\
K_0 &= RT\left[-ln(1-y) + \frac{9}{2}\left(\frac{y}{1-y}\right)^2\right] - \frac{4\pi R_S^3 P}{3} && (2.11)\\
K_1 &= -\frac{3RT}{R_S}\left[\frac{y}{1-y} + 3\frac{9}{2}\left(\frac{y}{1-y}\right)^2\right] + 4\pi R_S^2 P && (2.12)\\
K_2 &= \frac{3RT}{R_S}\left[\frac{y}{1-y} + \frac{3}{2}\frac{9}{2}\left(\frac{y}{1-y}\right)^2\right] - 4\pi R_S P && (2.13)\\
y &= \frac{4\pi R_S^3 n_S}{3} && (2.14)\\
K_3 &= \frac{4\pi P}{3} && (2.15)
\end{aligned}$$

$$\begin{aligned}
R_{eff,M} &= \left(\frac{3V_M}{4\pi}\right)^{\frac{1}{3}} && (2.16)\\
\Delta G_{cav} &= \sum_{i\,\in\,atoms(M)} \frac{S_i}{4\pi R_i^2}\Delta G_{cav}(R_i) && (2.17)
\end{aligned}$$

Dispersion and Repulsion Free Energy The contributions from dispersion and repulsion are often combined into a single Van der Waals contribution to the interaction energy. The physical interpretation of the repulsion interaction is a quantum mechanical repulsion due to the mutual penetration of the solute's and solvent's charge distribution. The dispersion interactions account for the attractive interaction due to induced dipoles or London interactions.[5,20,21]

Apparent Surface Charge methods

Taking into account an infinite continuum explicitly is of course computationally very challenging and therefore, a very convenient approximation for implicit solvent models is the reduction of the entire continuum to a surface charge. This apparent surface charge (ASC) mimics the effect of the dielectric, making the problem computationally and conceptually easier. By the introduction of these charges, the reaction field, $\hat{V}_{int}(\vec{r})$, can be written as a function of the charge density, $\sigma(\vec{s})$, on a surface Γ:

$$\hat{V}_{int}(\vec{r}) = \hat{V}_{\sigma}(\vec{r}) = \int_{\Gamma} \frac{\sigma(\vec{s})}{|\vec{r}-\vec{s}|} ds \qquad (2.18)$$

This potential is exactly $\hat{V}_{int}(\vec{r})$ if the correct apparent surface charges are used. A computationally efficient way of treating this problem is by performing a discretization of the cavity surface in a set of small finite elements that are called tesserae (Latin for 'quadrilateral' and used as a general term for small mosaic tiles). This discretization assumes that $\sigma(\vec{s})$ is constant for a certain tessera and therefore a point charge can be associated with it that equals the local value of the charge density times the tessera surface area, A_k, leading to the following expression:

$$\hat{V}_{\sigma}(\vec{r}) \simeq \sum_k \frac{\sigma(\vec{s_k})A_k}{|\vec{r}-\vec{s_k}|} = \sum_k \frac{q_k}{|\vec{r}-\vec{s_k}|} \qquad (2.19)$$

This expression for the reactive potential has to be solved in an iterative way in order to obtain correct values for the surface charges and the solute charge density. The way in which the apparent surface charges are defined, determines the ASC model. In the following part, the basic idea behind the three most common ASC models will be treated: the original Polarizable Continuum Model (PCM or dielectric PCM (D-PCM)), the conductor-like PCM (C-PCM or COSMO) and the integral equation formulation of the model (IEF-PCM).

The original PCM model, that has been renamed D-PCM in order to distinguish between the other versions of this model,[22] is based on the polarization vector on the surface, $P_i(\vec{r})$, which is defined by the gradient of the total potential:

$$\vec{P_i}(\vec{r}) = -\frac{\epsilon_i - 1}{4\pi} \nabla \hat{V}(\vec{r}) \qquad (2.20)$$

The index i indicates the region with dielectric constant ϵ_i (for example regions I and II in Figure 2.2). The charge distribution on the surface is given by taking the normal component of the difference in polarization vectors on the boundary between regions i and j (see equation 2.21), where $\vec{n_{ij}}$ is the normal vector pointing from medium i to medium j (see Figure 2.2).

$$\sigma_{ij} = -(\vec{P_j} - \vec{P_i}) \cdot \vec{n_{ij}} \qquad (2.21)$$

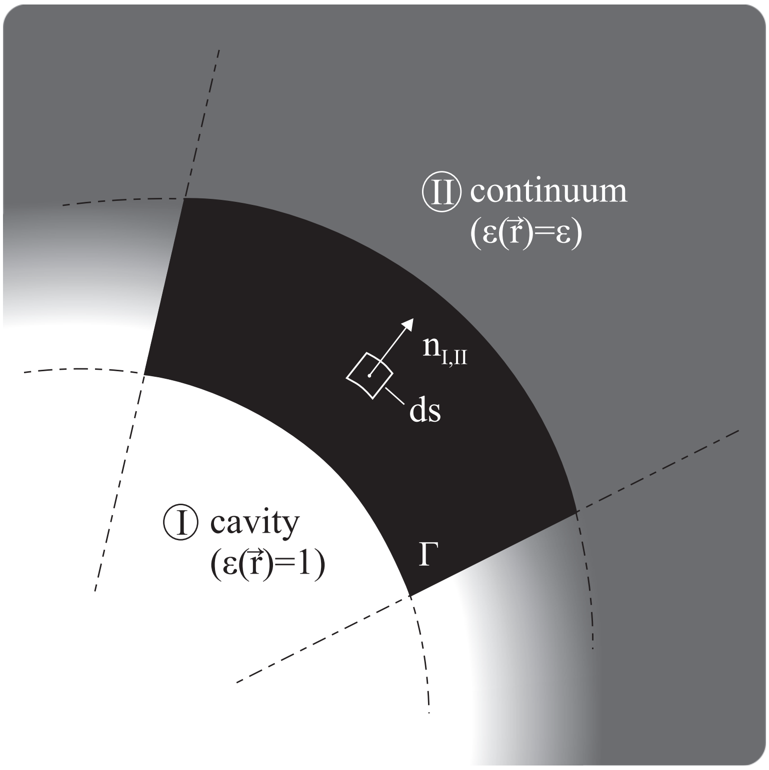

Figure 2.2: Illustration of the cavity surface, Γ, dividing the two regions with different dielectric constant and the normal vector pointing outwards in the direction of the continuum.

When applied to the cavity surface, Γ, the surface charge density can be expressed in terms of the normal gradients of the potential on the internal part of the surface (see Equation 2.22).

$$\sigma(\vec{s}) = \frac{\epsilon - 1}{4\pi\epsilon} \frac{\partial}{\partial \vec{n}} (\hat{V}_M + \hat{V}_\sigma)_{in} \tag{2.22}$$

In the conductor-like polarizable continuum model (C-PCM), the dielectric is treated as a conductor (with infinite ϵ), leading to the boundary condition that the total potential has to disappear on the cavity surface:

$$\hat{V}_M + \sum_k \frac{\sigma(\vec{s_k^*}) A_k}{|\vec{r} - \vec{s_k}|} = 0 \tag{2.23}$$

The ideal screened charge density, $\sigma^*(s)$, that results from this self consistent problem has to be rescaled by a function of the real value of the dielectric constant (Equations 2.24 and 2.25). In the latter function, k is a small number for which different values have been proposed. For solvents with a high dielectric constant, the value of k is irrelevant, but for less polar solvents, the results are dependent on this parameter.[7] For neutral solutes, k=0.5 should give the best solvation free energy results whereas k=0 is preferred for charged solutes.[23] In the Gaussian03 implementation of this model, a value of 0 was adopted for k.[23–25] A comparative study where both 0.5 and 0 were used for this parameter, also favored the latter value.[26]

$$
\begin{aligned}
\sigma(\vec{s_k}) &= f(\epsilon)\sigma^*(\vec{s_k}) && (2.24)\\
f(\epsilon) &= \frac{\epsilon - 1}{\epsilon + k} && (2.25)
\end{aligned}
$$

A third form of the PCM model is a more technical, computational formulation, rather than a conceptually different version, as D-PCM and C-PCM are. In the integral equation formalism for the PCM model (IEF-PCM), the surface charges are derived from a more general expression by expressing the potentials as the Green functions corresponding to the ∇^2 operator:[27–29]

$$\nabla_r^2 G(\vec{r}, \vec{r}\,') = -\delta(\vec{r} - \vec{r}\,') \tag{2.26}$$

The solvent charge density appears as the source function in the inhomogeneous Poisson equation 2.3, hence:

$$V(\vec{r}) = \int G(\vec{r}, \vec{r}\,')\rho_M(\vec{r}\,')d\vec{r}\,' \tag{2.27}$$

Further elaborations[7,27–29] lead to an expression of the surface charges according to:

$$\left[2\pi\left(\frac{\epsilon+1}{\epsilon-1}\right) - \hat{D}_i\right]\hat{S}_i\sigma(\vec{r}) = -(2\pi - D_i)\hat{V}_M(\vec{r}) \tag{2.28}$$

$\hat{S}_i$ and $\hat{D}_i$ refer to linear operators that are formally defined as the surface integrals on the internal part of the cavity (i) in Equations 2.29 and 2.30, respectively.

$$\hat{S}_i\sigma(\vec{r}) = \int\limits_{\Gamma} G_i(\vec{r},\vec{r}\,')\sigma(\vec{r}\,')d\vec{r}\,' \tag{2.29}$$

$$\hat{D}_i\sigma(\vec{r}) = \int\limits_{\Gamma} \left[(\epsilon_i\vec{\nabla}_{\vec{r}\,'}G(\vec{r},\vec{r}\,'))\cdot\vec{n}_{\vec{r}}\right]\sigma(\vec{r}\,')d\vec{r}\,' \tag{2.30}$$

The most important conclusion from this equation and from the C-PCM equation 2.23 however, is that the apparent surface charges, $\sigma(\vec{r})$, are only dependent on the solute potential $\hat{V}_M$ and no longer on the normal component of the electric field. The calculation of the latter is computationally less demanding and numerically more stable. That is probably also the reason why the D-PCM model is not available in Gaussian03 anymore, the standard PCM method being the IEF-PCM formalism. An advantage of the IEF-PCM model over the C-PCM model is that the former one automatically (due to its formulation) includes the outlying charge, i.e. the fraction of $\rho_M(\vec{r})$ that lies outside the cavity whereas the C-PCM determined surface charges must be renormalized. A last important feature of the IEF approach is that both the D-PCM and C-PCM model can be derived as special cases of the general equations.

Even though the PCM suite was originally intended for optimizing molecules under the influence of the dielectric field, experience has shown that it can be very problematic, especially for larger molecules and transition states. In most cases, the optimization in the presence of the reaction field does not converge. Therefore, a very common approach is performing a single point calculation in the dielectric that allows the calculation of the Gibbs free energy change due to the dielectric environment, the dielectric solvation energy (DSE). In this way, no effect of the changing geometry has to be taken into account. In the latest Gaussian software release, Gaussian09,[12] a new SCRF feature in which the surface point charges are expanded in terms of spherical Gaussian functions is implemented, resulting in continuous derivatives with respect to atomic coordinates and the external field.[30] In this way, faster and more reliable optimizations can be performed. This procedure could not be tested in the time frame of this thesis as the latest version of Gaussian, Gaussian09,[12] was released only very recently.

2.1.2 Explicit Solvation in an Implicit Solvent Environment

In a very general way, one can say that a solvent can interact in two ways with a solute molecule: either via bulk electrostatic interactions, or via a more direct, explicit interaction e.g. hydrogen bonding, π-stacking,... It is clear that an implicit solvent model only accounts for the first type of interaction, but the explicit interactions are not described although some models are parameterized to take into account direct interactions. Especially hydrogen bonding is very poorly modeled in an implicit solvent model. For instance, in a study of the polymerization of ethyl-2-(hydroxymethyl)acrylate (EHMA) in water, the gap between experiment and theory increased by three orders of magnitude upon inclusion of a continuum solvation model.[31] Therefore, it is useful and chemically more accurate to incorporate some solvent molecules explicitly in the continuum. This computational model in which a solvated cluster is embedded in a continuous solvent model is widely used and is often referred to as the '**combined implicit/explicit model**', the '**cluster-continuum method**' or the '**supermolecule method**'.[32,32–34]

This is illustrated in Figure 2.3 for the solvation process of a general solute X in water, but analogous schemes can be applied to a more general chemical reaction. The solvation Gibbs free energies of the in vacuo process, ΔG_{sol}^{vacuo}, can be combined with the solvation energies due to the dielectric continuum (DSEs) in a thermodynamic cycle to result the process's Gibbs free energy profile in solution, ΔG_{sol}^{pcm}.[33,35–38] In the case of a solvation process in water, the first contribution accounts for the effect of hydrogen bonding (or other types of explicit interactions) on the solute's structure and electron density while the second contribution essentially takes into account the permanent dipole moment of the surrounding water molecules.

This procedure is analogous to widely used thermodynamic cycles for the determination of pK_a values[39] and has been applied with success to a wide range of chemical reactions. Although the determination of the amount and the location of the explicit solvent molecules is not always trivial (one should only include the relevant solvent molecules that strongly interact with the solute),[40,41] this model has proven to be very useful in reaction and solvation modeling. A comparative study of continuum, explicit and mixed solvation models has been performed for studying phosphate hydrolysis by the group of Warshel.[41] It turned out that the mixed implicit/explicit solvation model gave unreliable results due to a misestimation of the entropic contributions if the number of explicit solvent molecules became too large or if the solvent molecules didn't show the correct orientation. Therefore, it

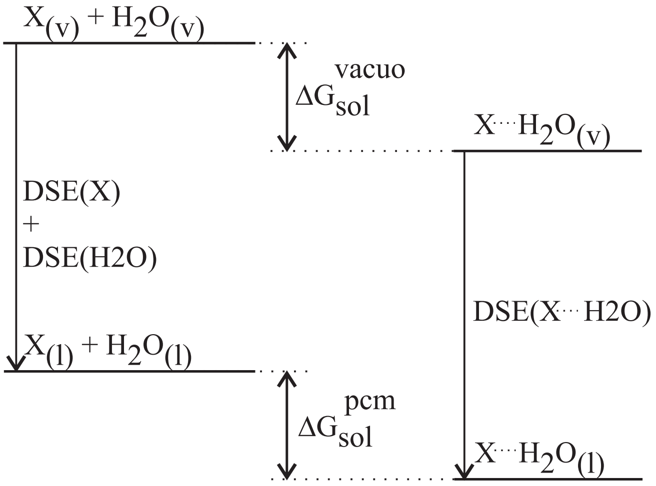

Figure 2.3: Thermodynamic cycle for the determination of the free energy of solvation of a solute, X, in a dielectric, ΔG_{sol}^{pcm}, calculated from the free energy of solvation in vacuo, ΔG_{sol}^{vacuo}, and the dielectric solvation energies (DSEs). The subscripts 'v' and 'l' indicate the *in vacuo* phase and the liquid phase, respectively.

is crucial to compare different possible solvation configurations. This can be done by identifying all possible interaction sites and calculating the interaction energies or coordination solvation energies (CSEs) and free energies for these possible sites. By systematically adding more solvent molecules as long as the free energy of solvation is negative, a proper solvated structure can be obtained. This methodology leads to a systematic approach of the solvation problem, at least for relatively small systems with a limited amount of interaction sites. Another possible methodology is performing molecular dynamics (MD, see Section 2.2) simulations, identifying the direct interactions that occur and using these structures as starting structures for geometry optimizations.[41] A drawback of this method however, is that cutting a cluster from a dynamic simulation at finite temperature (typically 300K) and subsequently optimizing it, might result in some artifacts. These are due to the fact that the bulk solvent that contributed to the structure and position of the explicit solvent molecules is removed. This might still lead to major solvent reorganization upon optimization. There is no such thing as an ideal procedure and both methods have their merits in literature, the former one being more suitable for smaller systems whereas the latter one is more appropriate when a lot of interaction sites are present.

2.2 Dynamic methods

A conceptually more straightforward method for describing solute-solvent interactions and the solvent influence, is a model in which all solvent molecules in the vicinity of the solute are explicitly taken into account, with consideration of temperature effects which can be expected to have a large influence. Such a model can only be obtained with molecular dynamics simulations. These simulations are carried out in a periodic simulation cell that consists typically of 1 solute molecule or 1 set of reactants and a sufficient amount of solvent. The system under study (solute and solvent) easily consists of hundreds of atoms and associated degrees of freedom and cannot be treated in the same way as in the previous section as it consists of a vast amount of local minima due to small solvent reorganizations.

Therefore, dynamic simulations at finite temperature are required in order to sample the system and obtain time averages of various equilibrium properties of interest. In order to study chemical reactions, structural reorganizations or other 'rare events', an additional methodology is required in order to study the non-equilibrium behavior of the system under study. In this work, the metadynamics method was used to study several reaction pathways and structural transformations.

2.2.1 Molecular Dynamics

In molecular dynamics (MD), the basic equation is the Newtonian equation of motion:

$$\vec{F}_j = m_j \cdot \frac{d^2\vec{r}_j}{dt^2} \tag{2.31}$$

The forces on the atoms j, $\vec{F}_j$, are derived from the potential resulting from an electronic structure calculation and can be used to evaluate the position and the velocity of the atoms at a certain time. For practical reasons, this equation can be solved numerically for finite timesteps and allows the simulation of the time-evolution of the system under study. A frequently used algorithm for this purpose is the so-called velocity-Verlet or Leapfrog algorithm (equations 2.32 and 2.33).[42,43]

$$\vec{r}(t+\Delta t) = \vec{r}(t) + \vec{v}(t)\Delta t + \frac{\vec{f}(t)}{2m}\Delta t^2 \tag{2.32}$$

$$\vec{v}(t+\Delta t) = \vec{v}(t) + \frac{\vec{f}(t) + \vec{f}(t+\Delta t)}{2m}\Delta t \tag{2.33}$$

These equations can be solved under various boundary conditions that correspond to thermodynamic ensembles. The best known ensembles are the microcanonical or NVE ensemble (constant amount of particles (N), constant volume (V) and constant energy (E)), the canonical or NVT ensemble (with constant temperature (T)) and the isothermal-isobaric or NPT ensemble (with constant pressure (P)). The aim of molecular dynamics simulations is obtaining equilibrium properties in a certain ensemble (microcanonical, canonical, ...) by time-averaging that particular property. This approach is supported by the ergodic principle that states that the time average of a property equals the ensemble average for infinite times. In practice, this also holds for a sufficiently long time.

In general, every molecular dynamics simulation consists of three parts: the initialization, the equilibration and the production stage. The initialization itself consists of the entire system setup that comprises the selection of a suitable model system, the generation of an initial geometry and velocities and the selection of a suitable method to describe the system. Of course, model system selection is very problem-dependent and requires a balance between the computational cost (making the model as small as possible) and the accuracy (including as many environment effects as possible). When studying molecules in solution, a sufficiently large solvent box is required so that the first solvation shells are well reproduced and that the solute is not interacting with its periodic image. As the initial geometries can be quite large and consist of a numerous amount of atoms, software is available for constructing solvent boxes e.g. Packmol[44] and Zeobuilder.[45]

The equilibration stage is sometimes called the warming up stage, considering the fact that one starts from an optimized geometry and assigns velocities to the atoms that correspond to the desired simulation temperature. Coupling the system to a thermostat will lead to a convergence towards the desired temperature with fluctuations of 5-10% for a system with 100-1000 degrees of freedom.[42] Of course, temperature is not the only criterion for equilibration: all properties should become invariant over time in order to get statistically meaningful results.

In the production stage, the system is sampled and the required data is collected. The desired properties can be calculated and averaged out over the simulation time. An interesting equilibrium property when studying solvent systems and solutes in a liquid, is the radial distribution function (RDF), g(r). This function describes the average number density relative to the ideal gas density as a function of the distance from a central point e.g. an atom or a set of atoms, a center of mass of a molecule... For an ideal gas, g(r) = 1 by construction and any derivation from unity reflects correlations between atoms or molecules and gives insights in the local structure of the liquid under study. A more formal way of defining g(r) is shown in Equation 2.34 in which N is the total amount of particles, V is the total volume and n(r) is the one-dimensional particle density at a given distance from the central atom.

$$g(r) = \frac{n(r)dr}{4\pi r^2 dr \frac{N}{V}} \tag{2.34}$$

In this way, the RDF relates the real amount of particles in a sphere shell with volume rdr to the amount of particles in the same shell when the former are uniformly distributed in the volume V. In practice, the analysis is carried out by constructing a distance dependent histogram. The analysis of MD simulations and the calculation of the desired properties can be easily and conveniently done with the MD-TRACKS software that is developed at the Center for Molecular Modeling.[46]

2.2.2 Metadynamics

In order to investigate non-equilibrium dynamics or transitions between different equilibrium states, several methods have been developed in order to simulate 'rare events' and calculate free energy differences.[3] These events can be any transformation of the system leading it from its initial equilibrium state to another equilibrium state. Examples of such transformations are conformational changes, solvent reorganization, chemical reactions,... A lot of these methods are based on constraining a reaction coordinate and performing a set of molecular dynamics simulations of the constrained system in order to calculate the force along the reaction coordinate. The knowledge of this force allows the determination of the Gibbs free energy profile of the transformation under study. These methods are very useful if the reaction coordinate is well defined and the pathway is more or less known. This is not always the case and if multiple pathways are possible, other methods like metadynamics are more suited.

In this method, the free energy surface (FES) is dynamically explored as a function of a set of well-chosen collective variables (CVs).[47] These variables that are functions of the coordinates of the system must be able to describe possible minima, intermediates and products and also distinguish between the pathways that interconnect these equilibrium states. The dynamics of the system in the space of these CVs is enhanced by a history-dependent potential constructed as a sum of Gaussians centered along the trajectories of the CVs. These Gaussians are characterized by their height, w, and their width, δs. The time interval between the deposition of consecutive Gaussians is denoted as τ_G, the deposition time. For system with a set of d collective variables that are a function of the system's coordinates x, $s(x) = (s_1(x), ..., s_d(x))$, the biasing potential at a time t is given by equation 2.35:

$$V_G(s(x),t) = w \cdot \sum_{\substack{t'=\tau_G,2\tau_G,... \\ t'<t}} exp\left(\sum_{\alpha=1}^{d} \frac{-(s_\alpha(x) - s_\alpha(x(t')))^2}{2\bar{\delta s}_\alpha^2}\right) \tag{2.35}$$

The basis assumption of the metadynamics method is that the biasing potential evolves towards the negative of the free energy Surface for long simulation times:[47]

$$\lim_{t\to\infty} V_G(s(x),t) \sim -F(s) \tag{2.36}$$

In Figure 2.4, a schematic overview is given of the metadynamics methodology. After a short molecular dynamics run of length τ_D (Figure 2.4.a), a Gaussian hill is added to the potential energy at that position in CV space (Figure 2.4.b). After a while, depending on the width and depth of the left well, the latter will be completely filled with Gaussians, allowing the walker (the virtual object of the dynamics that 'walks' over the biased potential energy surface) to escape the left well, and cross the barrier (a rare event) to start exploring other regions of the CV space (Figure 2.4.c). After a while, all the wells in the potential energy surface are filled and the FES can be reconstructed by taking the negative of the sum of the Gaussians added (Figure 2.4.d). In this way, metadynamics does not only allow reconstructing the FES as a function of the CVs, but also accelerates the rare events within the subspace of the chosen CVs.

From this short description of the metadynamics methodology, it is clear that there are several factors that determine the success of a metadynamics simulation: the Gaussian parameters w and δs, the chosen set of CVs and the error resulting from biasing the potential. These will be discussed in the following parts, starting with the error estimate. The error of metadynamics simulations has been derived for various cases using an empirical setup consisting of four known free energy profiles for which the average error as a function of the number of Gaussians was calculated.[47] The error as a function of the set of CVs can be expressed in terms of the average over a set of metadynamics runs, $\langle\cdot\rangle_M$:

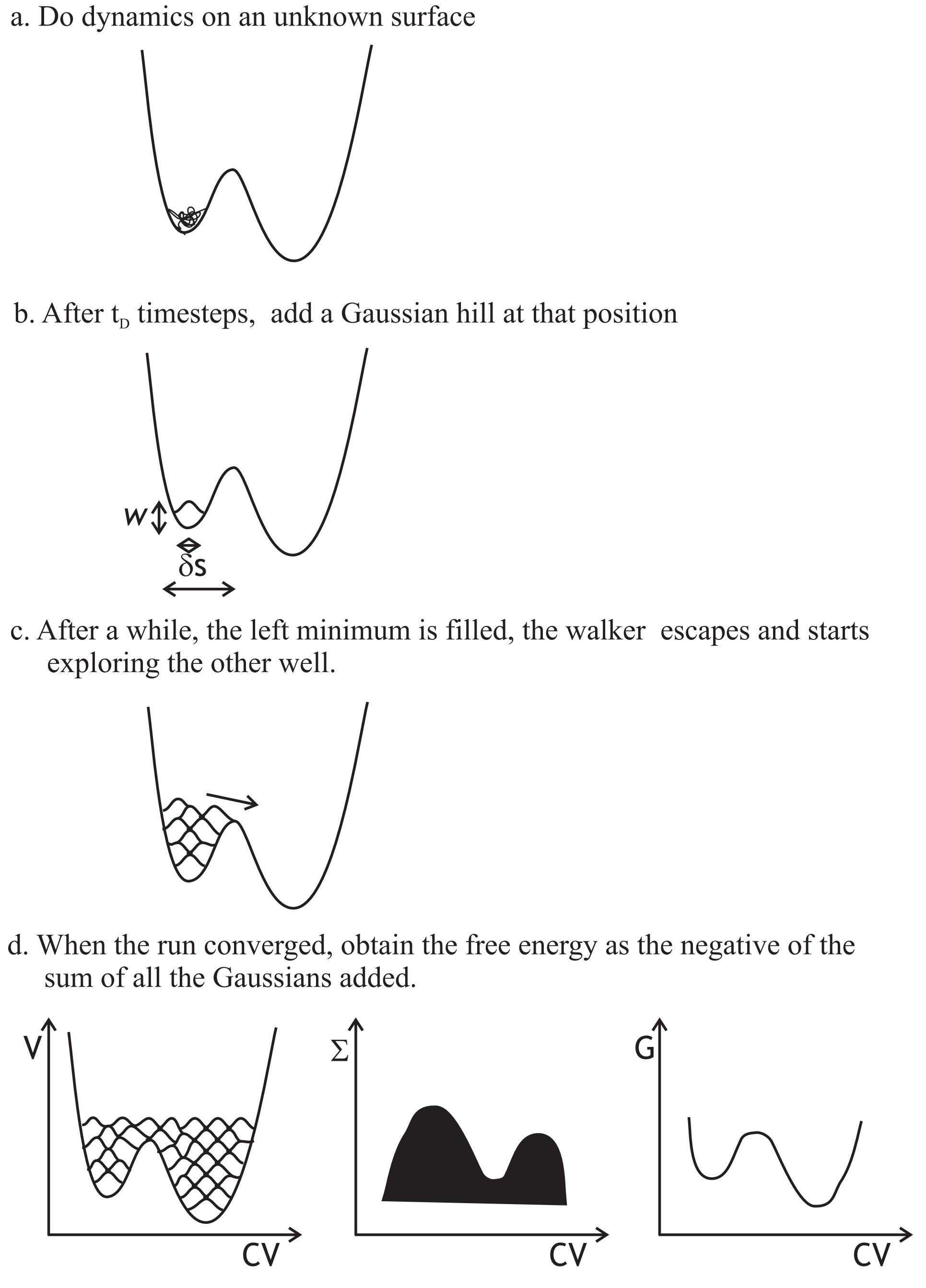

a. Do dynamics on an unknown surface

b. After t_D timesteps, add a Gaussian hill at that position

c. After a while, the left minimum is filled, the walker escapes and starts exploring the other well.

d. When the run converged, obtain the free energy as the negative of the sum of all the Gaussians added.

Figure 2.4: Schematic representation of the metadynamics method for a one dimensional double-well problem.

$$\varepsilon^2(s) = \langle (V_G(s) - \langle V_G(s) \rangle_M)^2 \rangle_M \tag{2.37}$$

An important result of this study is that the average error is indeed independent of the FES, as long as the other metadynamics parameters (w, δs, τ_G) are chosen wisely. After empirically correlating the average error with the simulation parameters, equation 2.38 was derived in which C is a constant that depends on the dimensionality of the CV vector, d, D is the diffusion coefficient, β is temperature inversed and S is the system size in the CV space. The value of C(d) is determined as 0.5 if d=1 and 0.3 if d=2.

$$\varepsilon = C(d) \sqrt{\frac{S^2}{D\tau_G} \frac{w}{\beta} \frac{\delta s}{S}} \tag{2.38}$$

The error on the FES can be expressed in a formal way by modeling the evolution of the CVs as a Langevin-type dynamics.[48] Using this approach, which is representative for a large class of realistic systems when the proper collective variables are chosen, it can be proven that the average of the biasing potential over a set of metadynamics runs is an unbiased estimate of the FES i.e. that the average error equals zero. Moreover, the analysis shows that, in order to optimize the accuracy of a metadynamics simulation, the ratio of the Gaussian width with respect to the system width, $\delta s/S$, has to be chosen as large as possible. An important precondition to this statement concerns the resolution that is needed in order to map the underlying FES accurately. Indeed, small details of the FES will be wiped out by the accumulating tails of too large Gaussian hills. Therefore, the originally suggested value of 0.1 seems like a reasonable choice considering both equation 2.38 and the resolution precondition.[47] This results from the different dependence of the formally derived error on $\delta s/S$ whereas the dependence on the other metadynamics variables (β, D, S, w, τ_G) is the same in both expressions.

Similar considerations can be made for the height of the Gaussian hills, w, which can ideally be very small - the so-called slow deposition limit. In this situation, equation 2.36 holds as $V_G(s,t)$ varies very slowly and the error on the FES will be of the order of the height of one Gaussian.[47] The other side of the story however is that small hills require more simulation time in order to explore the FES and that the error is proportional to $\sqrt{w}$. However, for large enough simulation times and sufficiently small hills, the error depends only very weakly on the hill size.[49]

The deposition time, τ_G, appears in the denominator of the error expression (equation 2.38) indicating that long intervals between adding Gaussians to the potential are beneficial. This can easily be understood from the following point of view: when adding a Gaussian hill to the potential, the probability for the system to adopt that position in CV space decreases. Therefore, the system will evolve to a region away from that point in space towards regions of lower energy. As metadynamics is a dynamic technique, this movement will take a certain time. So, if the deposition time is too small, the system will remain in the close vicinity of the configuration of the previous hill and hills will be placed on top of each other, causing a locally strong elevation of the potential. More precisely, the error in equation 2.38 is dependent on the ratio of the hill height and the deposition time, w/τ_G, showing that larger hills require longer deposition times.[47]

The most important and most challenging task when setting up a metadynamics simulation, is selecting appropriate collective variables. These can be any combination of system coordinates like a bond distance, an angle or a dihedral angle or combinations of such variables e.g. a distance difference. Although these variables are quite robust and indispensable for describing chemical reactions, more complex CVs are required to take into account solvent effects. An example of such a collective variable is the coordination number (see equation 2.39) that describes the amount of atoms of a subset, A, that are within a cutoff distance, r_0, of a central atom, S.

$$CN(S-A) = \sum_{allA_i} \frac{1-\left(\frac{r_{SA_i}}{r_0}\right)^n}{1-\left(\frac{r_{SA_i}}{r_0}\right)^{2n}} \tag{2.39}$$

The parameter n is often chosen to be 6, in order to achieve similarity with a step function but with preservation of smoothness so that the derivative of the coordination number is sufficiently far away from zero in the interesting region. The cutoff distance has to be determined depending on the specific nature of the atoms S and A. These parameters, of course, depend on the system under study and the coordination number function can be tuned accordingly. The features of this function are illustrated in Figure 2.5: n parameter n determines the steepness of the function whilst r_0 defines the point in which the function takes on the value 0.5. A lot of other possible CVs exist, some of which have been tailored for specific problems like the box shape for crystal structure transformations[50] or protein-specific variables that allow studying folding and docking processes.[51,52]

In order to get a good description of the chemical reaction or configurational change one wants to study, some rules of thumb exist for selecting the

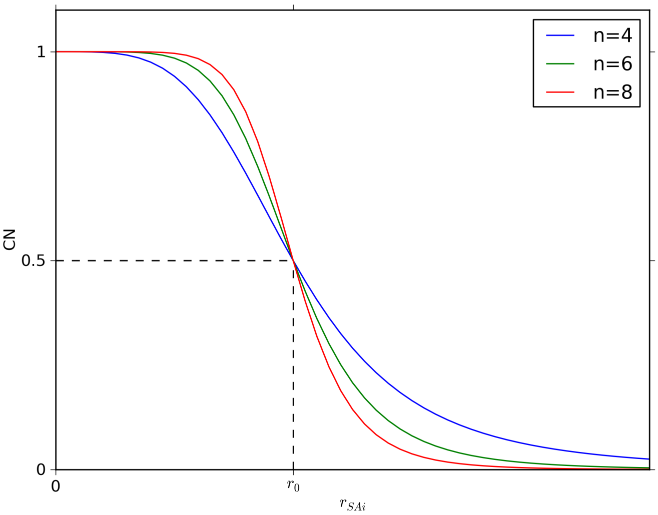

Figure 2.5: Illustration of the coordination number function and the influence of the parameters n and r_0 on the shape and steepness.

appropriate collective variables.[51] A first and very obvious requirement is that the selected CVs have the ability to distinguish between the interesting structures, the possible intermediates during the reaction and the pathways. This means in general that a good assessment of the system and of the possible rare events that can occur is necessary when designing the CVs. As dynamic simulations typically consume a lot of computational resources, it is important to select only a limited number of CVs. In practice, three can be considered as a proper number of CVs that keeps the simulations feasible and still allows a relatively easy interpretation of the results.

However, it is not at all certain that every process can adequately be described with only three CVs or combinations of CVs. Therefore, it is essential that all the slow variables of the process under study are taken into account. Otherwise, hysteresis may occur and the FES will not converge.[51] When more CVs are required to describe the FES of interest, other methods might be more interesting like using a path variable as a CV in metadynamics[53,54] or performing bias-exchange metadynamics (BEM)[55,56] in which several parallel metadynamics simulations or walkers are ran with different variables. After a certain time the coordinates of two walkers may be switched resulting in a linear scaling multidimensional metadynamics formalism.

The last important aspect concerning the choice of CVs is that any reaction or transformation that is studied, has to be reversible. When looking at Figure 2.4.d, this means that once the right well is filled, the system has to be able to go back to the left and diffuse over the almost flat surface. This seems very logical for the FES in Figure 2.4, but when one considers for instance a bond breaking process, the reactant has a well-defined minimum but the product well is in principle infinitely long along the bond distance CV. For this reason, interference with the FES is possible by adding a wall to the FES at a predetermined value of the CV. Readdressing the bond distance example, a quadratic function with a high force constant can be added to the potential at sufficiently large separation distance in order to constrain the system to the region that is of interest.

3

Applications

In this chapter, three chemical systems will be discussed for which the solvent effect on the studied reactions and molecules is different in each system. The applications were selected based on several collaborations with other research groups and by the suitability of these systems to study solvent effects. In the first application (Section 3.1), the E/Z isomerization of metalated 3-halo-3-methyl-1-azaallylic anions, the polar, aprotic tetrahydrofuran (THF) is used that can interact strongly with the metal cation that is present. In the other two applications, water is used as a polar and protic solvent. In the free radical polymerization (Section 3.2), water takes up the role of an assisting (through hydrogen bonding) molecule in the transition states. In the last application (Section 3.3), the hydrolysis of acetamide and N-methylacetamide, water is not only an assisting solvent, but also a reactant. The study of three chemically different systems in which different types of solvents and solvent roles are present will allow to make more general conclusions regarding modeling solvent effects.

3.1 Properties and Reactivity of Metalated 3-halo-3-methyl-1-azaallylic Anions

The applications that are mentioned in this section, were performed in collaboration with the research group of Prof. De Kimpe (Faculty of Bioengineering, Ghent University). Metalated 3-halo-1-azaallylic anions are important building blocks for the preparation of a wide variety of heterocyclic and highly functionalized compounds. They are the imine analogues of α-haloketones **1** (see Figure 3.1). α-Heteroatom substituted carbanions stabilized by an electron-withdrawing group (acyl, alkoxycarbonyl, sulfonyl,

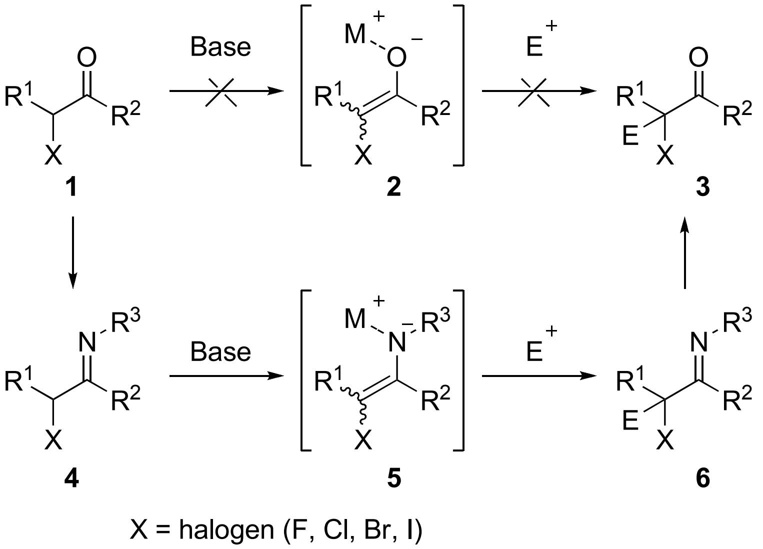

Figure 3.1: Conversion of α-haloketones **1** to α-haloimines **4** and further to functionalized imines **6** and ketones **3**.

sulfinyl, cyano, carbanoyl) have been used intensively as synthetic building blocks for the synthesis of various organic compounds, including a wide variety of azaheterocyclic compounds.[57] However, one combination appears to be unsuccessful, when a halogen and an acyl group are combined (e.g. if R^2 is an alkyl group in Figure 3.1). This is due to the instability and non-selective reactivity of α-haloenolates **2** (see Figure 3.1).[58,59] A convenient way to overcome these problems is the conversion of α-haloketones **1** towards the corresponding less reactive α-haloimines **4**. After deprotonation of the latter, the corresponding 1-azaallylic anions **5** can be easily used in different organic transformations.[58–61] In that respect, mainly α-chlorinated imines have been used as precursors for interesting acyclic, carbocyclic and heterocyclic compounds.[62–72] While the corresponding brominated and iodinated imines are generally more difficult to handle because of their instability,[58,59,65,73] 1-azaallylic anions derived from α-fluorinated imines have been used to study the regioselective deprotonation and stereoselective alkylation,[64,73] and have recently proved to be useful building blocks for interesting fluorinated heterocycles.[74]

The chemistry of 1-azaallylic anions leads to basic heterocyclic systems such as aziridines, azetidines, pyrrolidines, pyrroles, piperidines, oxiranes, oxolanes,. . . and higher functionalized ring systems, currently of interest for the pharmaceutical chemistry and agrochemistry. The application of cer-

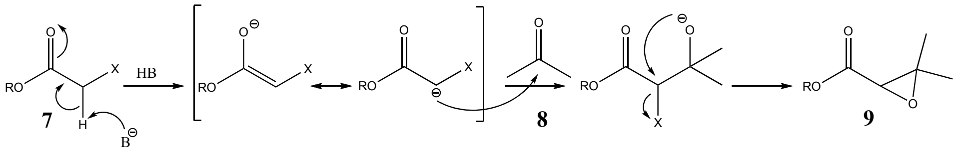

Figure 3.2: Darzens reaction of a α-haloester **7** (bearing an alkoxycarbonyl group as an electron withdrawing group) with a ketone **8** to ultimately form an epoxide **9** after halogen ejection.

tain halogenated counterparts, i.e. the 3-halo-3-methyl-1-azaallylic anions, in sensu stricto by the group of De Kimpe and in sensu largo by the group of Florio, which incorporated the 3-halo-3-methyl-1-azaallylic moiety into heterocyclic structures, has led to the synthesis of various important classes of compounds such as cyclopropanes,[75–78] tetrahydrofurans,[79–81] tetrahydropyrans,[81] chloroimines,[67] oxiranes,[82–86] aziridines,[83,85,87–90] pyrroles and pyridines,[70] steroids,[91] alkenylheterocycles,[77] and oxazetidines.[87] As mentioned, 3-halo-3-methyl-1-azaallylic anions can be used for the synthesis of functionalized oxiranes and aziridines since the former anions behave as nucleophiles in Darzens- (see Figure 3.2) and aza-Darzens-type reactions with carbonyl compounds and imines.[82–90]

One of the determining factors in the stereochemical outcome of these Darzens-type reactions is the E/Z-stereochemistry of the starting 1-azaallylic anion.[92] Therefore, it is important to know and understand the configurational properties of 3-halo-3-methyl-1-azaallylic anions in order to perform aldol- and Mannich-type reactions with these intermediates in a stereocontrolled manner. An important aspect that has to be considered when studying the configuration and configurational stability of these anions, is the presence of tetrahydrofuran (THF) as a solvent. This frequently used solvent is a small cyclic ether which is characterized by its low polarity and aprotic nature. It exhibits a high volatility and a low freezing point and the ability to solvate both polar and nonpolar species. It is used as a solvent in very diverse applications, from polymer production to the manufacturing of pharmaceuticals being a clean solvent that can easily be separated from the product mixture.[93]

In this section, the stereochemistry will first be addressed with static methods, focusing on equilibrium and solvated properties of the azaallylic anions. A more proper treatment of solvent effects can be performed by simulating the dynamic properties of the anions under investigation in a complete THF environment. In order to perform such elaborate study, we

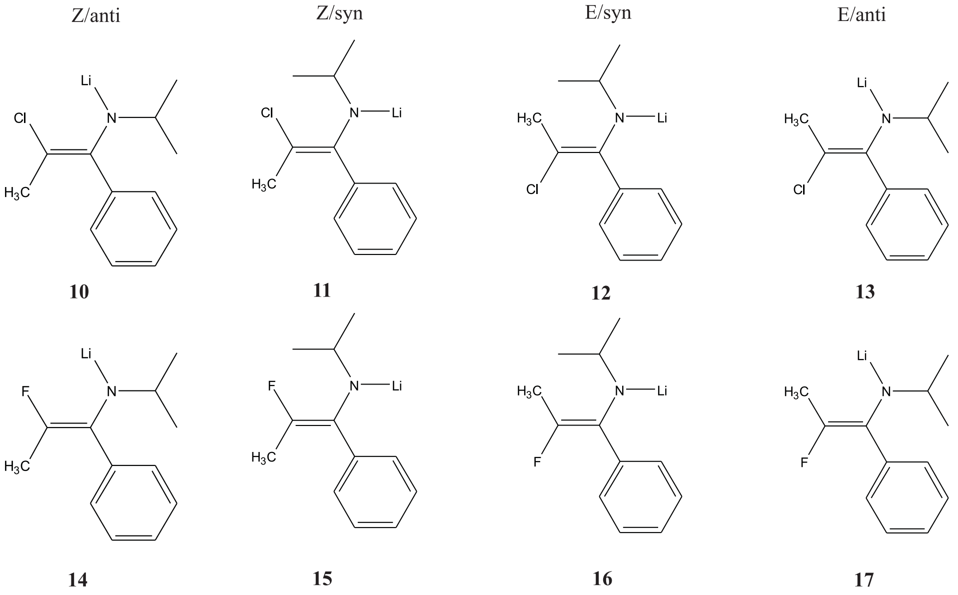

Figure 3.3: Nomenclature and structure of the selected species studied in this section.

first studied the properties of the THF solvent itself and afterwards treated the equilibrium properties of a lithiated 3-chloro-3-methyl-1-azaallylic anion and the E/Z isomerization. Finally, the reaction of this model compound with benzaldehyde will be discussed.

3.1.1 Static and Equilibrium Solvated Properties

In a first step of this research project, the static properties of various isomers of 3-halo-1-azaallylic anions and their solvation energy in THF using the combined cluster-continuum solvation model (see Section 2.1.2) were investigated. The results of this study are described in more detail in ***Paper 1***. All geometry optimizations and energy calculations are carried out using the hybrid mPW1PW91[94,95] hybrid functional as this method proved to be the most accurate in reproducing geometries and energies of chloro- and fluoroalkyllithium compounds.[96] A double-ζ 6-31+G(d) basis set is used comprising both diffuse and polarization functions for a good description of the oxygen atoms and the ionic character of the species.[96] The effect of solvation is modeled as described in Figure 2.3, using single-point calculations at the mPW1PW91/6-31+G(d) level with the C-PCM continuum solvation method as described in Section 2.1.1.

First of all, possible isomers for 3-fluoro- and 3-chloro-1-azaallylic anions coordinated to lithium are considered as lithium (aza)enolates are important building blocks in organic synthesis.[97–100] The structures that are mentioned in this section, are shown in Figure 3.3. The bold numbers indicating the different structures that are used in this text are different from the numbers that are used in ***Paper 1*** as selected results from that paper are mentioned in this part. For each of the monohalogenated species **10-17**, four isomers can be suggested a priori, each of them characterized by the stereochemistry about the C=C bond (E or Z) and the position of the N-isopropyl group (*syn* or *anti*).[101] The energy scheme in Figure 3.4 shows that both fluorinated and chlorinated species exhibit a stable global minimum in which the lithium cation and the halogen atom interact intensely. The isomerization process is characterized by two types of internal rotations: amide rotations for *syn*/*anti* isomerization (TS1 and TS3) and carbon-carbon double bond rotations or E/Z isomerizations (TS2). The stable minima for the fluorinated species **14-17** are shown in Figure 3.5, while the other structures are shown in the Supporting Information of ***Paper 1***.

A remarkable aspect of the energetic minimum is the position of the phenyl group. One would expect this group to be positioned coplanar with the carbon-carbon double bond in order to obtain more electron delocalization. The structure, however, does not allow this kind of conformation due to steric hindrance of the phenyl group with the methyl and isopropyl group on the adjacent carbon and nitrogen atoms, respectively, resulting in an almost perpendicular configuration (for instance, the dihedral angle in structure **14** in Figure 3.5 amounts to 71 degrees). Because of the strong interaction between fluorine or chlorine and lithium, no barrier could be found in vacuo for the rotation from Z/*anti* to E/*anti*. The latter structure exists as two energetically equivalent structures in which the lithium cation is pyramidally η^3 coordinated (species **13** in Figure 3.5). These two structures are connected through a planar transition state (TS4) with an energetic barrier of 17 and 23 kJmol^{-1} for the chlorinated and fluorinated species, respectively. This type of coordination was already reported in previous studies of 1-azaallylic anions[101,102] and is a result of the repulsive interaction between Li and the methyl group directing the metal out of plane towards the π-cloud of the carbon-carbon double bond.

From here on, only the *anti* configurations will be considered because the *Z/anti* conformers are the most stable; the *E/anti* isomer will be considered too as the stereochemistry about the C-C double bond is important for the stereochemical outcome of reactions. The Gibbs free energy of solvation was calculated in vacuo and in the C-PCM model as shown in Figure 2.3. The monosolvated structures of the Z/*anti* and E/*anti* isomer of the lithiated

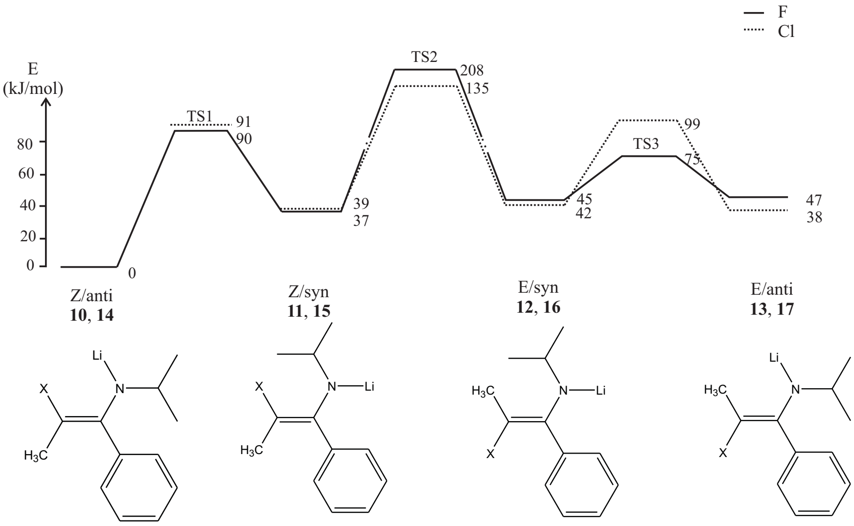

Figure 3.4: Energy profile for the conformational analysis of chlorinated species **10-13** (X=Cl) and fluorinated species **14-17** (X=F).

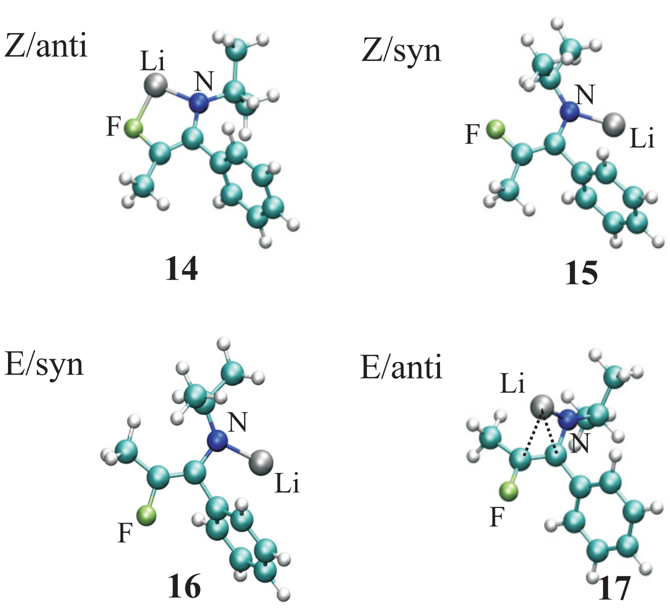

Figure 3.5: Optimized geometries for lithiated 3-fluoro-1-azaallylic species **14-17**.

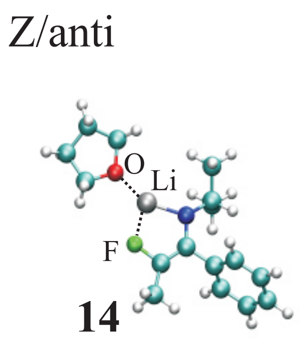

Figure 3.6: Monosolvated structures for lithiated 3-fluoro-1-azaallylic species **14** and **17**.

3-fluoro-1-azaallylic anions are shown in Figure 3.6. The values for the explicit solvation with 1 and 2 THF molecules are shown in Table 3.1 for fluorinated and chlorinated species. The lithiated 3-halo-1-azaallylic anions in Table 3.1 always coordinate with at least one THF molecule because of the favorable lithium-oxygen interaction. Their coordination with a second THF molecule is generally less favored. Intuitively, the solvation of the E isomers **13** and **17** by a second THF molecule should be more favorable compared to the Z isomers **10** and **14** since the former isomers lack a halogen-lithium interaction. A remarkable number in Table 3.1 is the relatively large and positive second solvation free energy of the chlorinated Z/*anti* isomer **10**. This value indicates that the coordination with a second THF molecule is unlikely as the state where the species is solvated by one THF molecule and a separate solvent molecule at infinite distance is the most stable. One must notice however, that some values for the second solvation are very close to zero and are probably smaller than the error for these single-point C-PCM calculations.

In Table 3.2, an overview is given of the relative energy of the E isomer with respect to the Z isomer, $\Delta G - E - Z$, for different solvation states using the explicit, implicit and combined explicit/implicit method. These values show that independent of the amount of solvent molecules used and of the method applied, the Z isomer is always the most stable indicating the importance of the metal-halogen interaction. At this point, drawing conclusions for ΔG_{E-Z} is very difficult as both isomers seem to show a different coordination number (and thereby a different total amount of atoms) which makes their energy difference difficult to calculate as the reference state is not clear. Also, the effects of the C-PCM are quite large and at this point,

Table 3.1: Coordination solvation free energy (ΔG_{sol}^{vacuo}) and solvation free energy (ΔG_{sol}^{cpcm}) for mono- and bisolvated structures using the explicit and implicit/explicit solvation model for the *anti* configuration of lithiated complexes. The subscripts 1 and 2 refer to the first and second THF that is added to the structures. All values are in kJmol^{-1}.

	$\Delta G_{sol,1}^{vacuo}$	$\Delta G_{sol,1}^{cpcm}$	$\Delta G_{sol,2}^{vacuo}$	$\Delta G_{sol,2}^{cpcm}$
Fluorinated				
Z/*anti* (**14**)	-31.1	-3.5	8.2	-0.2
E/*anti* (**17**)	-41.8	-9.2	0.6	-2.3
Chlorinated				
Z/*anti* (**10**)	-33.9	-14.7	9.5	12.7
E/*anti* (**13**)	-38.9	-10.0	4.5	-0.5

it is not completely sure to what extent the solvent effects are correctly described by the simple continuum model. Therefore, a molecular dynamics study on the isomerization of the chlorinated compound was conducted which will be described in the next paragraphs.

Table 3.2: The free energy difference between the E/*anti* and the Z*anti* isomers, ΔG_{E-Z}, for the fluorinated and chlorinated species using the explicit, implicit and combined explicit/implicit method.

	Chlorinated species		Fluorinated species	
	In vacuo	C-PCM	In vacuo	C-PCM
0 THF	38.1	36.4	47.0	35.6
1 THF	33.0	41.2	36.3	29.9
2 THF	28.1	28.9	28.7	27.7

3.1.2 Equilibrium Properties and Structure of Tetrahydrofuran

Prior to the study of the solvation properties of reactive species in THF it is essential to validate in how far the properties of pure THF can be modeled using a periodic approach. Despite its frequent use, there are not many theoretical investigations on the solvation properties and structure of THF. A characteristic property of THF is the presence of a pseudorotation motion, moving the atoms out of plane and making different conformations accessible avoiding the energetically unfavorable planar geometry.[103] In literature, four THF conformers are described: the planar geometry, the oxygen envelope, the carbon envelope and the twisted conformer, they are depicted in Figure 3.7.[103,104] Using the coordinate system from Figure 3.8, conformational assignments can be made by evaluating the Z coordinate of the C_1 and C_4 carbon atoms. The X,Y plane coincides with the plane through the O, C_2 and C_3 atoms, see Figure 3.8. The center of this triangle is the origin of the framework, the X axis going through O as well. Next, the Z axis is chosen perpendicular to the plane in such a way that at least one of the remaining carbon atoms has a positive Z coordinate. The Y axis lies in the O, C_2, C_3 plane in such a way that a positive coordinate system is defined.

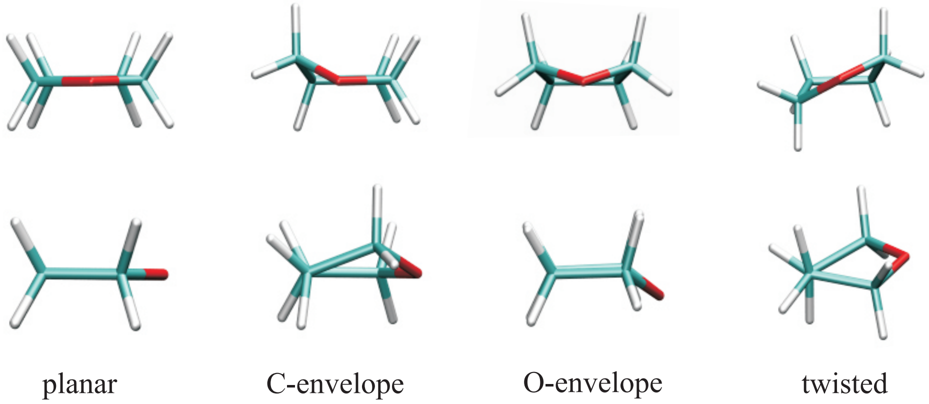

Figure 3.7: Frontal view and projection along the C_2,C_3 axis (bottom part, notation: see Figure 3.8) of the four THF conformers as reported in literature.

An overview of different possible combinations and corresponding conformations is given in Table 3.3. The planar geometry is unambiguously assigned as a high energy transition state which cannot compete with the energetically lower ring puckering motion.[104,105] The nature of the three other species has been the subject of considerable debate, but the latest and most advanced theoretical calculations show that the oxygen envelope and the twisted conformation are minima.[103] In this study, the carbon envelope forms are transition states along the pseudorotation coordinate. These results are in correspondence with recent experimental data and the large majority of theoretical investigations.[103] The relative stability of the oxygen envelope and the twisted conformer however, is highly dependent on the method used. This is the case for both experimental and theoretical methods and therefore, the relative position of these structures on the energy axis stays uncertain.

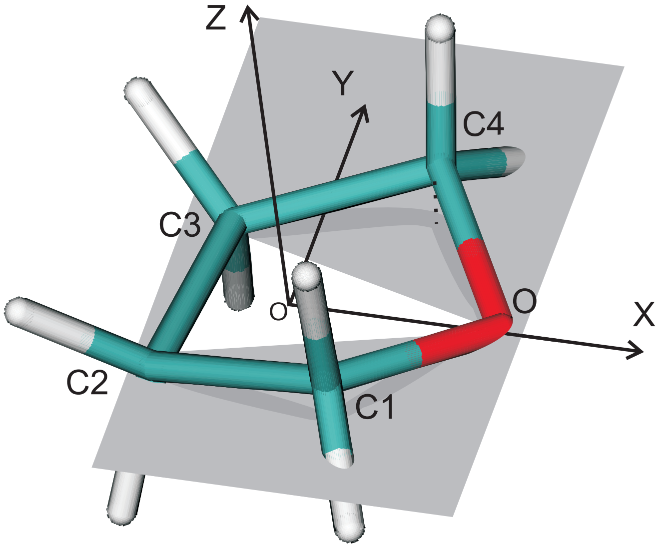

Figure 3.8: Coordinate axes reference frame of the THF molecule.

Table 3.3: Conformational assignment of THF depending on the Z-coordinates of C_1 and C_4

Z(C_1)	Z(C_4)	conformer
> 0	> 0	oxygen envelope
	< 0	twisted
	$=0$	carbon envelope
$= 0$	$\neq 0$	carbon envelope
	$= 0$	planar

Despite this, the pseudorotation motion was rarely implemented in the different molecular mechanics (MM) and Monte Carlo (MC) simulations. An overview of available MM and MC studies of THF is given by Bedard-Hearn et.al.[106] Only once, a MC simulation was carried out using a pseudorotational potential function.[107] The frequently used planar geometry is unstable[103] and the pseudorotation is a nearly unhindered, rapid motion[104] and should therefore be included in temperature dependent dynamics simulations.

In order to assess the solvent structure, we have performed canonical (NVT) quantum mechanical (QM) dynamics on cubic simulation cells con-

Table 3.4: Simulation details for the QM molecular dynamics simulations on pure THF.

# THF	cell parameter	timestep	equilibration time	production time
8	10.287 Å	1.0 fs	2.5 ps	10.0 ps
27	15.430 Å	1.0 fs	2.5 ps	10.0 ps
64	20.574 Å	1.0 fs	0.5 ps	10.0 ps

taining 16, 27, and 64 THF molecules using the CP2K/QUICKSTEP[108] code. The BLYP[109,110] gradient-corrected density functional was used together with a TZVP-PSP[111] basis set and pseudopotentials developed by Goedecker and co-workers.[112,113] This functional was chosen as it was the most tested functional within the CP2K suite. At the time of this research, hybrid functionals were not yet implemented. Also, using a non-hybrid functional offers the possibility to run longer simulations as the computational cost increases strongly when HF exchange needs to be calculated.

Each simulation cell size was chosen to correspond with the experimental density of 0.88 Kg/m^3,[114,115] and each system was equilibrated at room temperature (300 K) using chains of Nosé-Hoover thermostats attached to the nuclear degrees of freedom. The simulation details for each run can be found in Table 3.4 and characteristic snapshots for the three considered box sizes are shown in Figure 3.9. From these simulations, the radial distribution functions (RDF, see also Equation 2.34 in Section 2.2) were calculated and compared to the experimentally derived Empirical Potential Structure Refinement (EPSR) radial distribution functions to assess the quality of this solvent model. Also, the probability distribution of the different structures of THF was studied.

Figure 3.10 shows the RDFs of the THF centers of mass for the above-mentioned simulation cell sizes. These are compared with the RDF calculated recently, which was derived from Empirical Potential Structure Refinement (EPSR) techniques applied on neutron diffraction experimental data.[93] A priori, the 8 THF cell was expected to yield the least reliable results of all cell sizes under consideration, as the periodic boundary conditions (PBCs) by design force a pairwise arrangement in every dimension. Surprisingly, the RDF still reproduces the major characteristics of the benchmark EPSR-derived RDF, with the exception of the unphysical peak found at a distance of 10.28 Å, which equals the norm of the smallest vector connecting the periodic images. Note that any RDF derived from periodic calculations will feature these peaks at distances connecting the periodic images. In the

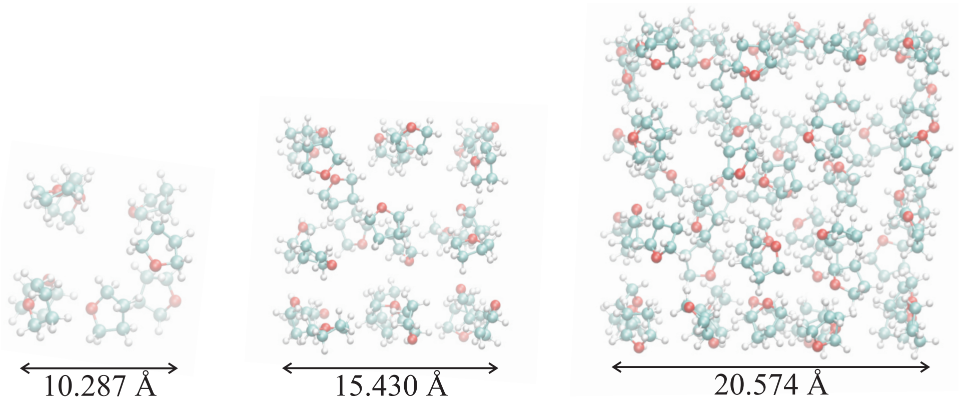

Figure 3.9: Characteristic snapshots for the THF simulation cells containing 8, 27 and 64 molecules.

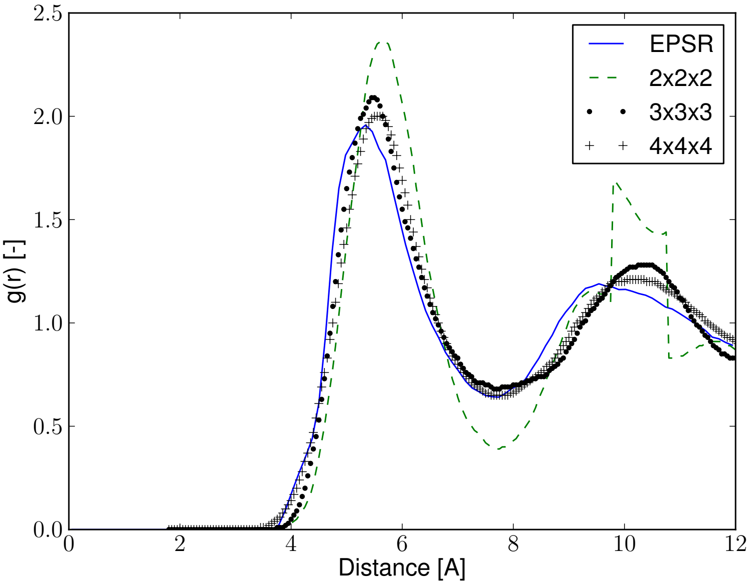

Figure 3.10: Comparison of DFT (using different unit cell sizes) and EPSR-derived molecular centers radial distribution functions. The center of the molecule is defined as the geometric center of the oxygen atom and four carbon atoms that make up the five-membered ring.

27 THF cell, the molecules can now be independently arranged, and this greater freedom results in a substantially better reproduction of the bench-

Table 3.5: Distance towards the first maximum in the RDF (r_{max}), distance towards the first minimum in the RDF (r_{min}), number of THFs in the FSS (# THF), and the mean distance from the THFs in the FSS ($< r >$) for the radial distribution functions shown in Figure 3.10.

	r_{max}	r_{min}	# THF	$< r >$
EPSR	5.34 Å	7.74 Å	13.30	6.05
8 THF	5.65 Å	7.70 Å	13.48	6.03
27 THF	5.50 Å	7.70 Å	13.55	6.09
64 THF	5.55 Å	7.70 Å	13.53	6.08

mark RDF. One exception is the behavior around 10 Å, where the agreement is rather poor. This is likely due to the periodic boundary conditions, which cause each THF to contribute more than once in the shown radial range, and hence disturb the RDF in this range.

In order to eliminate this problem, the cell size should in principle be further enlarged in each dimension to at least twice this range, which would dramatically increase the computational cost. The RDF calculated in a 64 THF cell further decreases the discrepancies with the benchmark RDF. For example, the aforementioned discrepancy at around 10 Å is slightly reduced. But most importantly, the behavior of the nearest neighbors (at 4 Å) is more accurately predicted. To describe the solvation effects of reactive species properly in THF the accurate account of the nearest neighbors is of utmost importance. In view of this, we will from hereon focus exclusively on the 64 THF cell. At this point it is also appropriate to introduce the First Solvation Shell (FSS), which is defined as the region up to the first minimum in the RDF. In Table 3.5 some characteristic properties of the FSS are tabulated, which reconfirm that all three of our simulations perform rather well in reproducing the benchmark RDF.

As it was mentioned in the introduction, the MD simulation allows pseudorotation and therefore, different THF conformations can exist and can be converted into each other. In this paragraph, we will discuss the distribution of these configurations. The geometries in Table 3.3 are quite arbitrary because all kinds of intermediate geometries will be accessible during the dynamic simulation and an exact zero Z coordinate will never occur. Therefore, a Å interval around the Z axis is introduced (dashed lines in Figure 3.11) for the classification of the different conformers. The distribution of Z coordinates of C_1 and C_2 is represented in Figure 3.11 for the 64 THF model. It is clear that the twisted conformer is prominently present in the simulation. The oxygen envelope conformer is less pronounced, but clearly

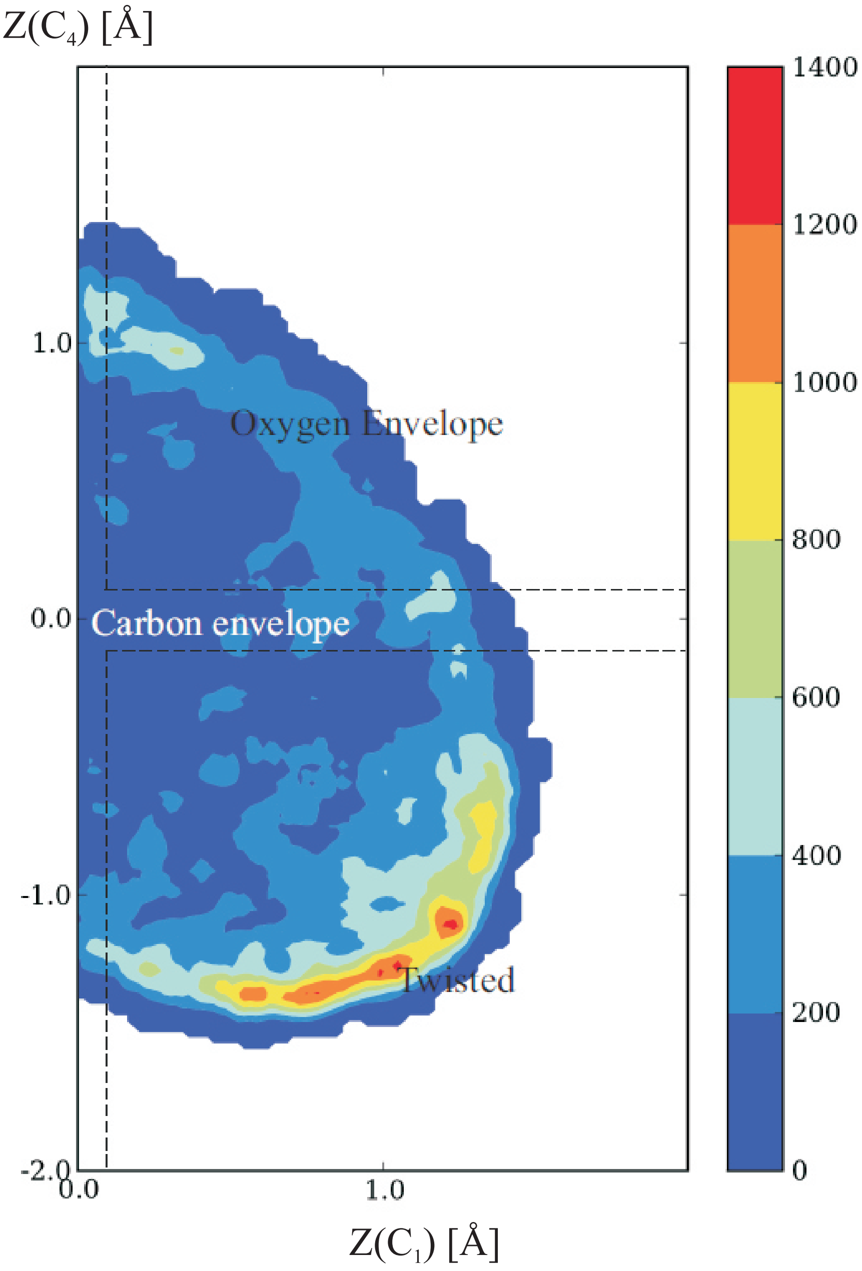

Figure 3.11: Contourplot of the distribution of THF configurations. The color bar shows the amount of times each conformation was visited. No planar geometry at position (0,0) is observed during the simulation.

present. Also, some carbon envelope geometries are observed at coordinates of about (0,1), (0,-1) and (1,0).

In total, the relative occupancy of the twisted, oxygen envelope and carbon envelope are 65%, 23% and 12% respectively. This carbon envelope structure is in fact a transition structure between the two stable geometries. When following a single molecule during the dynamic simulation, various transitions from oxygen envelope tot twisted and vice versa can be observed. This is in correspondence with our own BLYP/TZVP-AE calculations that predict a zero-point energy corrected energy difference between the stable twisted and oxygen envelope conformations of -0.97 kJmol^{-1}, favoring the twisted conformer. A Maxwell-Boltzmann distribution of this energy difference gives a population of 60% twisted and 40% oxygen envelope. The difference in these values is due to the fact that in the dynamic simulation, various minima and transition-like structures appear which gives a better representation of the real solvent structure compared to static calculations. The general behavior of the molecules is reproduced well and is consistent with previous post Hartree-Fock calculations (complete basis set extrapolated CCSD(T)/cc-pVTZ energies) that resulted in a distribution of 57% twisted and 43% oxygen envelope.[103,104] Now that the structure of THF is well studied, we can use this model for the solvation of the 3-halo-3-methyl-1-azaallylic anions.

3.1.3 Dynamic Properties and Isomerization of a Model Compound

Even though the static cluster models from section 3.1.1 are capable of giving good insights in the problem under study concerning the Z isomer stability and the different solvation behavior of the E and Z isomer, several disadvantages are associated with these solvent models. One of them is the fixed amount of explicit solvent molecules while, when considering chemical reactions, the amount of coordinating solvent molecules may alter along the reaction coordinate. Moreover, the exact location of these solvent molecules is not known a priori and might also be changing during the reaction. In addition, the static calculations showed that the results are largely influenced by the continuum model. Therefore, a further validation of the solvation properties by a totally different method is of utmost importance.

Another problem associated with the combined explicit/implicit solvation model is optimizing the solvated cluster in the continuum. For larger clusters, this is a very time consuming calculation that is often unsuccessful, which is reflected in the presence of one or more imaginary frequencies.[116] In this section, the dynamical equilibrium properties of the lithiated 3-chloro-3-methyl-1-azaallyl anions (the *Z/anti* and *E/anti* isomer **10** and **13**, respectively) will be investigated and the effect of the solvent on the E-to-Z isomerization will be studied (see also ***Paper 2***). The studied structures in this section are shown in Figure 3.12. They correspond to species **10** and **13** from Section 3.1.1. We recall the results from Table 3.1 and Table 3.2 in which the solvation with one THF molecule was favored but coordination of the most stable Z isomer with a second THF molecule was not found.

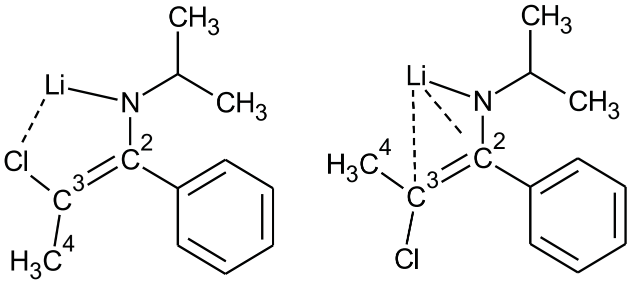

10 (Z) **13** (E)

Figure 3.12: Z isomer **10** and E isomer **13** of the lithiated (2-chloro-1-phenylprop-1-en-1-yl)isopropylamide anion and specific atom nomenclature for this section.

Next to the solvation properties of the E and Z isomer, we also paid attention to the possible C-C bond rotation as this internal motion allows transformation from one isomer to the other and may have important consequences for future studies on their reactivity. The E/Z isomerism for non-halogenated 1-azaallylic anions has been observed and investigated quite frequently. The facile carbon-carbon bond rotation in simple lithiated 1-azaallylic anions was investigated using ^{1}H NMR.[117] In that study, the rotational activation free energy was found to be 74.1 ± 1.3 kJmol^{-1} at 313 K. E/Z isomerization was also observed upon deprotonation of ketimines of 2-butanone at room temperature.[118] For closely related non-chlorinated analogues of the species under study, i.e. the lithiated anion derived from the N-phenylimine of propiophenone, isomerization from the kinetically favored E isomer with the methyl group and the phenyl group at the same side of the C-C double bond to the thermodynamically most stable Z isomer with the methyl group and nitrogen at the same side of the C-C double bond, was observed.[61] Therefore, it was assumed that the lithiated 3-chloro-1-azaallylic anions of the present work could also undergo a similar type of isomerization.

The coordination number for lithium enolates in ethereal solvents is rather difficult to establish but four-coordinate lithium cations have been clearly recognized in NMR studies of solvent separated ion pairs.[96,119–121] For contact ion pairs, coordination is expected to be less important because of the electrostatic effect of the counter ion. Theoretically the structures of a variety of organic lithium compounds were determined in the gas phase and in solution using microsolvation with explicit ethereal ligands and/or continuum models.[36,122] For the 3-halo-3-methyl-1-azaallylic anions as encountered here which are subject to large steric crowding, the degree of coordination is not a priori clear and cannot be deduced straightforwardly from the experimental data.

First, isothermal-isobaric (NPT) molecular dynamics simulations were performed out during a period of 2.5 ps for both isomers after an equilibration time of 2.5 ps to allow the solvent to accommodate to the presence of the solute and vice versa. The simulations were carried out using the BLYP[109,110] gradient-corrected functional, together with a TZVP-PSP[111] basis set and pseudopotentials developed by Goedecker and coworkers.[112,113] Again, the particular choice of functional was inspired by practical reasons. We must keep in mind that the results obtained in Paragraph 3.1.1 were obtained with a different functional. Quantitatively, the results will be difficult to compare but we do expect a good qualitative behavior.

The species were properly embedded in the 64 THF solvent model from Paragraph 3.1.2 by determining, using Pauling atomic radii, the volume associated with their solvent accessible surface.[123] As the volume of THF is 2.96 times smaller compared to the volume of the 3-chloro-1-azaallylic anion, three THF molecules in the simulation cell were replaced by the 3-chloro-1-azaallylic species. These simulations show that the Z isomer is monocoordinated whereas the E isomer features a two-fold coordination with THF (illustrated in Figure 3.13). In the E-isomer the halogen-lithium coordination is not present which allows a second THF molecule to coordinate with the counter ion. The same conclusions can be drawn when looking at the RDF of the lithium to oxygen coordination averaged over the entire simulation in Figure 3.14 in which the FSS is clearly distinguishable at 2 Å. The surface area of the first peaks is indeed 1 for the Z isomer and 2 for the E isomer. This is in agreement with the static calculations in Section 3.1 in which Table 3.1 shows that the E and Z isomer show different solvation behavior.

This difference in solvated structure indicates that studying the configurational differences between the E and Z isomer becomes problematic when using a solvated cluster model. From a computational point of view, com-

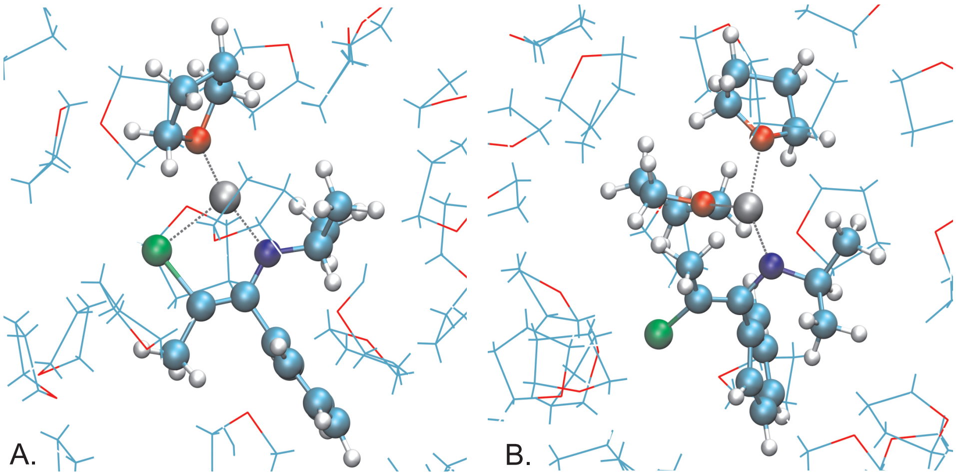

Figure 3.13: Characteristic snapshots from the NVT dynamics of the monocoordinated Z isomer (A) and the bicoordinated E isomer (B) of the lithiated 3-chloro-3-methyl-1-azaallylic anion.

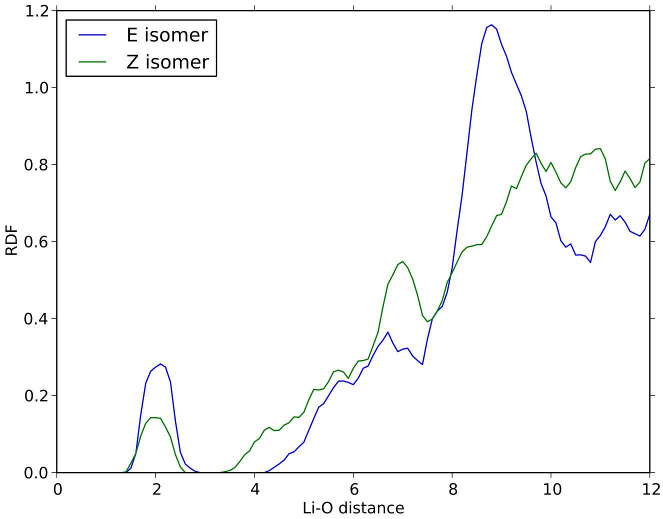

Figure 3.14: Radial distribution functions for the Li$^+$-O(THF) interaction in the E and Z isomer of the lithiated 3-chloro-1-azaallylic anions.

paring structures with different or a different number of atoms (in this case, a different amount of solvent molecules) is quite problematic as there is no well defined reference energy for this problem. Therefore, the free energy difference between both structures should be obtained using this periodic solvent model that allows a change in coordination number. To this end we applied the metadynamics method (see Section 2.2.2) in which the dihedral angles Cl-C3-C2-N and C4-C3-C2-N were chosen as collective variables (see Figure 3.12 for the notation). This choice guarantees the independent movement of the methyl and chlorine substituents. Accurate metadynamics parameter values were determined from Gibbs free energy barrier predictions of the lithiated 3-chloro-1-azaallylic anion in the gas phase (using a supercell approach), including only one THF molecule to impose the limited freedom of the lithium cation (see Figure 3.15). This figure shows the convergence of the activation free energy as the hill height, w, and the hill width, δs, decrease. The set of parameter values $w = 2.0$ kJmol^{-1}, $\delta s = 0.33$ rad and $\tau_G = 50$ fs (for the notation, see section 2.2.2) yielded an energy barrier of 64 kJmol^{-1}, within 1.0 kJmol^{-1} of the convergence limit. The estimated error using these parameters is $\varepsilon = 6.1$ kJmol^{-1}.[124]

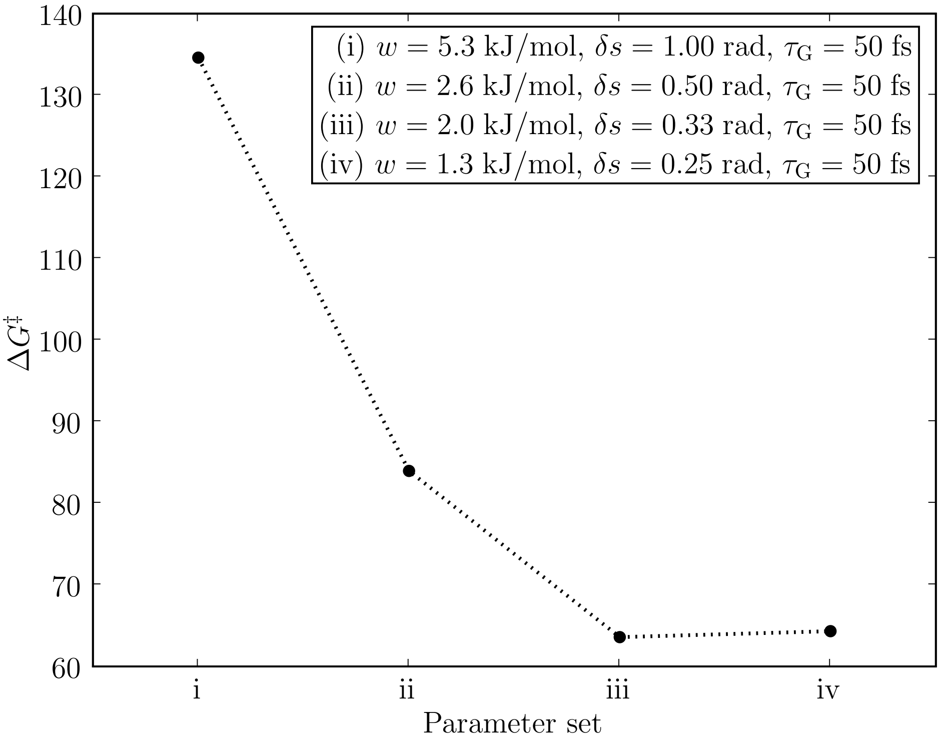

Figure 3.15: Gas phase free energy of activation, $\Delta G^{\ddagger}$, for the Z-to-E isomerization of compound **10** with 1 THF molecule using different values for the Gaussian hill height, w, and width, δs.

After a 40 ps metadynamics simulation on the solvated system, the resulting free energy landscape for the periodic solvent calculations as a function of the two dihedral angles is displayed in Figure 3.16. The Gibbs free energy barriers for E-to-Z and Z-to-E isomerization amount to 107.1 ± 12.1 kJmol^{-1} and 128.6 ± 12.1 kJmol^{-1}, respectively.[47] These barriers are high, preventing isomerization at the experimental temperature. The Z isomer is more stable than the E isomer by $\Delta G_{Z-E} = 21.5 \pm 12.1$ kJmol^{-1}, which indicates that the experimentally observed Z isomer is thermodynamically favored. Within a static cluster approach using a combined explicit/implicit solvent model we were unable to determine the transition state for E/Z isomerization as the coordination number varies during the chemical transformation. By capturing the movement of both dihedral angles, we are able to observe the sp^2-to-sp^3 hybridization transition of the C3 carbon atom upon rotation, a well-known feature of rotations about allylic bonds. This is reflected in the fact that the saddle point, denoted as (E-Z), does not lie on the linear pathway connecting both isomers, which confirms *a posteriori* the importance of capturing the movement of both dihedral angles.

Moreover, the energy difference between both isomers is about 20 kJmol^{-1} lower than the value obtained from the static implicit/explicit solvent calculations in Table 3.2. This value is the result of taking into account a larger explicit solvent environment in which no artifacts from introducing extra solvent molecules are present. The energy difference between both states is not only determined by the intrinsic energy difference, but also by solvent reorganization effects as can be seen from the lower activation barrier that was found in the gas phase metadynamics runs from Figure 3.15. These effects cannot be included based on gas phase (vibrational) free energy calculations.

These theoretical findings are in excellent agreement with the experimental findings resulting from off-resonance ROESY spectroscopy that show ROE effects between the methyl group and the ortho protons of the phenyl ring, indicating a Z configuration. Moreover, the presence of ROE effects between the isopropyl group and the phenyl ring support the *anti* stereochemistry of the anion under study. These strong indications of the presence of only the Z/*anti* are confirmed further by the fact that only a single set of characteristic C^{13} chemical shifts of the lithiated 3-chloro-1-azaallylic anions. The experimental details can be found in ***Paper 2***. This combination of theoretical and experimental results show that the stereochemistry of 3-chloro-3-methyl-1-azaallylic anions is manifestly different compared to their non-chlorinated counterparts and is the result of their configurational stability which should be beneficial during their synthetic use as functionalized intermediates in stereoselective reactions.

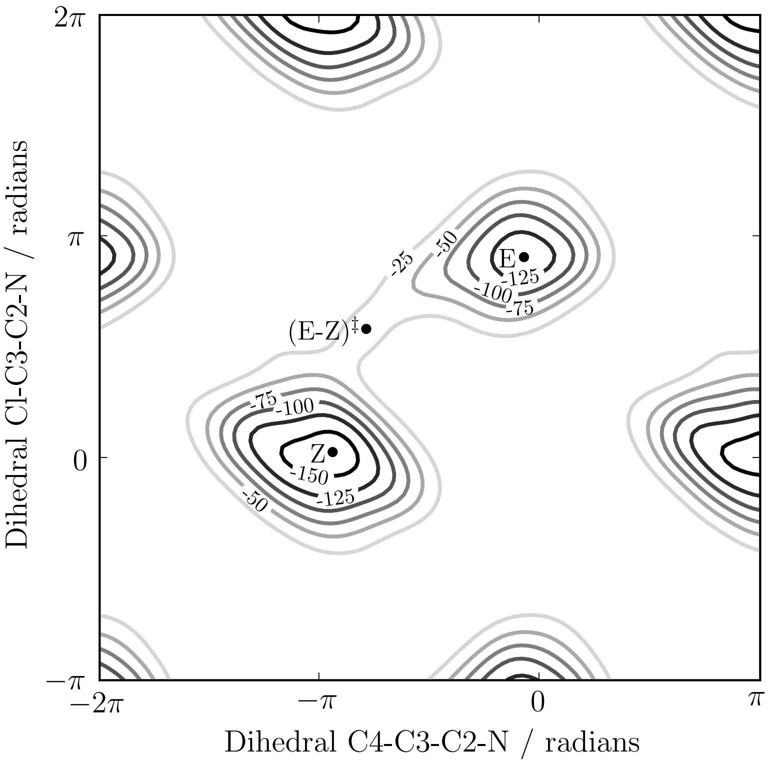

Figure 3.16: Gibbs free energy profile (in kJmol^{-1}) governing the E-Z isomerization of the lithiated 3-chloro-1-azaallylic anion in THF. The positions of both stable isomers E and Z and the saddle point (E-Z) are added. Note that the two collective variables feature a 2π-periodicity.

3.1.4 Aldol-type Coupling of 3-chloro-1-azaallylic Anions with Benzaldehyde

After having established the most stable configuration of the 3-halo-3-methyl-1-azaallylic anions in THF solution, the following step is the investigation of the reactivity of these species. For this aim, the diastereoselective aldol-type coupling with benzaldehyde will be considered as shown in Figure 3.17. This application was inspired by experimental studies performed by our partner of the faculty of Bio-Engineering, Prof. De Kimpe.

Based on the experimental results, it is expected that for lithiated species **10**, the syn/anti ratio is about 58/42 (-78^{o}C, 10 min) whereas for ZnCl^{-} complexed anions, the diastereoselectivity is significantly improved to 89/11 (-78^{o}C, 5 min), strongly favoring the *syn* adducts. As longer reaction times

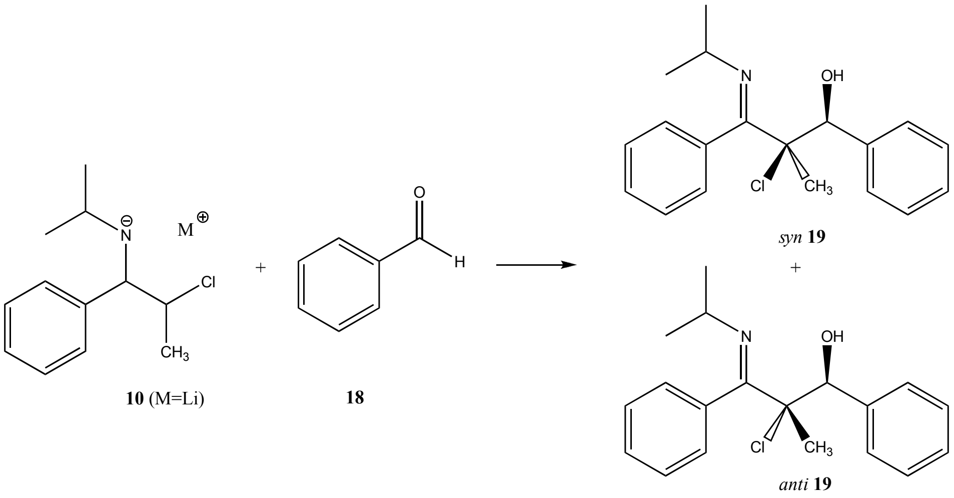

Figure 3.17: Aldol-type addition between the *Z/anti* 3-chloro-1-azaallylic anion **10** and benzaldehyde **18**, resulting in the possible formation of a *syn* and *anti* product **19**.

and higher temperatures result in a less pronounced *syn* selectivity, and therefore it is anticipated that under kinetically controlled conditions the *syn* adduct is preferred whereas under thermodynamically controlled conditions the *anti* product is favored.

For this study, the static methods were used in first place in order to gain insight in the different addition configurations that can occur and to investigate the role and position of counterions and solvent molecules. Initial geometry optimizations were carried out conform to the methodology used in Section 3.1.1, using the mPW1PW91/6-31+G(d) electronic structure method. This method was selected as the study in Section 3.1.1 was performed with this hybrid density functional. After geometry optimizations of the products, a constrained optimization in which the formed bond distance was increased systematically with 0.1 Å steps was performed. The results of this scan along the reaction coordinate is taken up in Figure 3.18.

At the mPW1PW91 level of theory no saddle point could be localized. Therefore the calculations were redone at the B3LYP/6-31+G(d) level of theory using the internal reaction coordinate method (IRC) to localize the reactant complex and product structure, as this method is known to be robust and reliable for geometry optimizations. Using the B3LYP geometries that are shown in Figure 3.19, the transition state and addition product were obtained and subsequently, single point SCF calculations using a range of

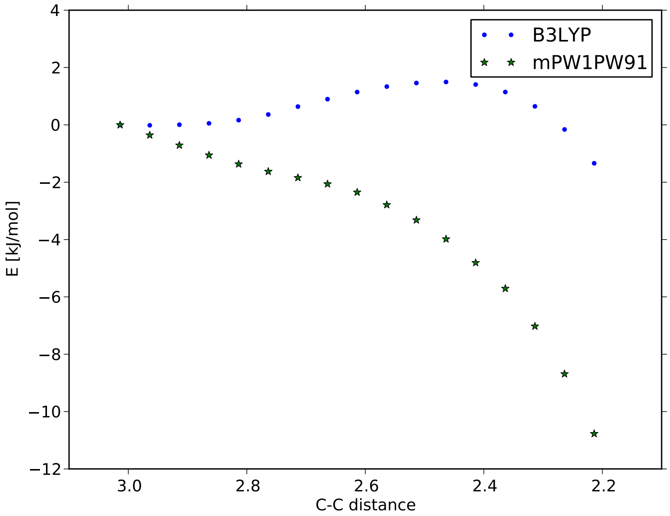

Figure 3.18: Constrained optimization energy profile for the reaction leading to the lithiated *syn* adduct using mPW1PW91 and B3LYP with a 6-31+G(d) basis set. For reference, the energy of the reactant-like structure at 3 Å was set to zero.

density functionals were performed in order to assess the sensitivity of this system to the electronic structure method. These results already show that this system is quite problematic in terms of the electronic level of theory that has to be used.

From Table 3.6, it is clear that this system is very sensitive to the method applied, especially the reaction energies and the forward barriers are mutually very different, the MP2 barrier being strongly negative. This can be rationalized by looking at the structures in Figure 3.19. In contrast to the TS and products, no π-stacking interaction is present in the reactant complex at the B3LYP/6-31+G(d,p) level. The fact that the MP2 method is known to account for dispersive interaction, explains the strong stabilization of the TS with respect to the reactant complex in which no dispersive interactions are present.

In principle, another reactant complex should be found when performing the IRC calculation at the MP2 level. The latter is however not the aim of this study. We will try to explain different stabilities of the *syn* and *anti* transition states instead of focusing on the forward barriers. Because the phenyl rings in the transition states are sufficiently close together, the B3LYP methodology is capable to describe the geometry of the T-stacking, but fails to provide good energies for these kinds of structures. Therefore, only the transition states will be considered in the following part, using a pragmatic approach performing B3LYP/6-31+G(d,p) geometry optimizations for the transition states followed by single point MP2 energy refinements. It is clear that this system is very challenging to describe, not only for the solvation part but also on the level of electronic structure method.

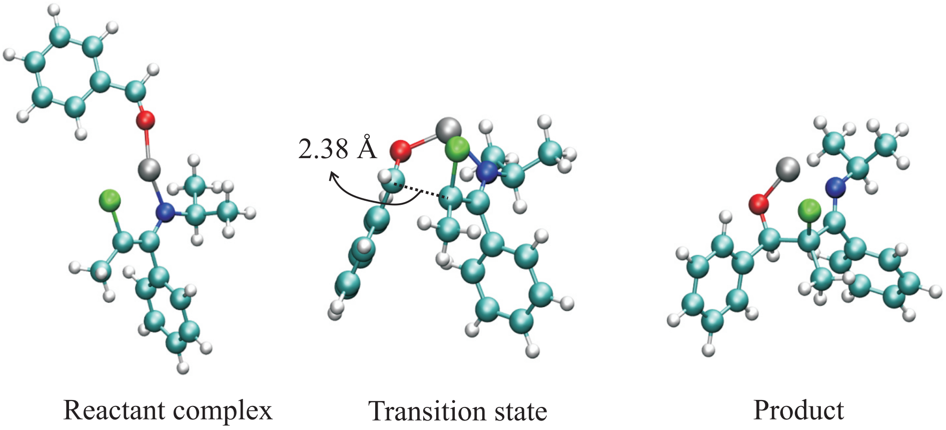

Figure 3.19: Optimized geometries at the B3LYP/6-31+G(d) level for reactant complex, transition state and product for the *syn* addition in the presence of lithium.

Table 3.6: The zero-point energy corrected reaction barrier for the forward and backward reaction, $\Delta E^{\ddagger}_{0,f}$ and $\Delta E^{\ddagger}_{0,b}$, respectively and the reaction energy ($\Delta E_{0,r}$) from single point calculations with various electronic structure methods (mPW1B95, mPWB1K,mPW1PW91, BMK, PBE1PBE, HF, MP2) with a 6-31+G(d,p) basis set on B3LYP/6-31+G(d,p) optimized geometries.

	$\Delta E^{\ddagger}_{0,f}$	ΔE_r	$\Delta E^{\ddagger}_{0,b}$
B3LYP	24.8	-1.4	26.2
BMK	1.6	-54.0	55.6
mPWB1K	10.3	-50.4	60.7
mPW1PW91	11.4	-28.7	40.1
mPW1B95	4.7	-37.9	42.6
PBE1PBE	7.6	-33.9	41.5
HF	65.2	-47.8	70.1
MP2	-24.3	-79.5	55.2

As the exact structure of these species and their transition states in solution is not easy to predict, several possible reaction routes have been investigated. These routes include the addition of benzaldehyde to the azaallyl anions (the anionic transition states) and to the metalated, solvated azaallylic anions and are shown in Figure 3.20.

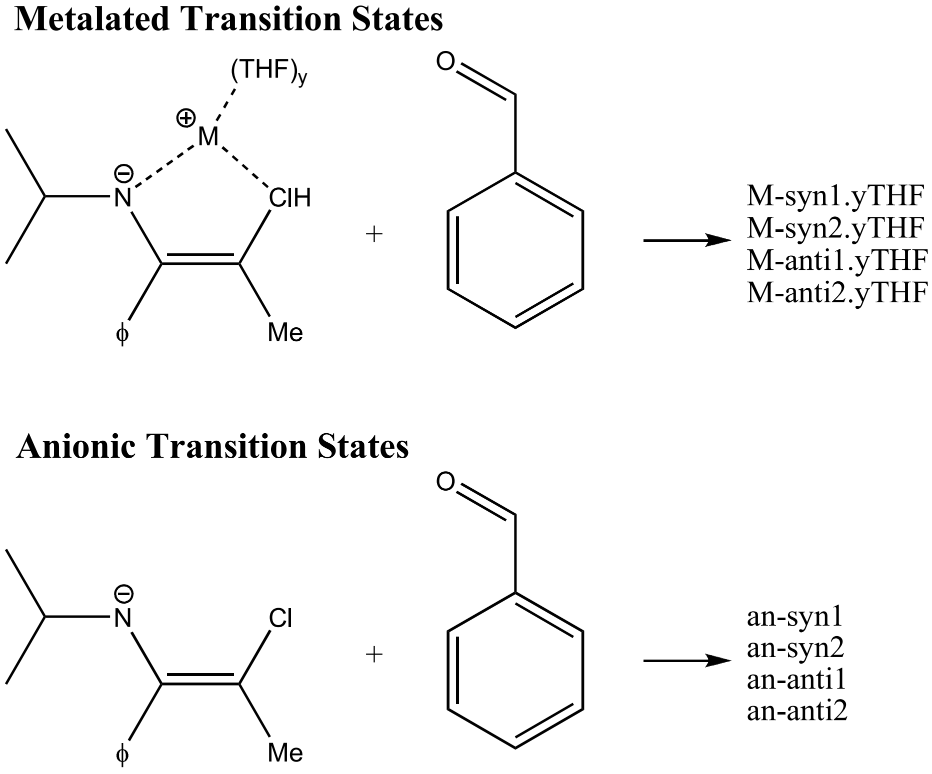
Metalated Transition States

Anionic Transition States

Figure 3.20: Possible reaction routes for the addition of benzaldehyde to azaallyl anions that each result in 4 possible transition states. The transition state nomenclature will be explained further.

As the anionic transition states are the most simple models of the reaction under study, we will start by modeling these. Figure 3.21 shows that two configurations can be found that each lead to the *syn* or *anti* adducts and that can be distinguished between by describing the relative position of the benzaldehyde oxygen with respect to the nitrogen. When the oxygen is pointing towards nitrogen, the number 1 is added to the TS name, otherwise, a number 2 is added. The forming bond distances are also shown in Figure 3.21 and they indicate an important T-stacking effect in the ***an-syn2*** and ***an-anti1*** transitions states, shortening the forming bond because of the beneficial π interaction between the phenyl substituents. When inspecting the MP2 energies in Table 3.7, it is clear that ***an-syn2*** is the most favorable TS in the gas phase in the absence of a counter ion because of the energetically favorable π interaction. The change of the relative energies in comparison with the B3LYP results indicates once again the importance of taking into account the dispersive interactions by means of the MP2 method. When applying a polarizable continuum model (the C-PCM model), energies shift even further, strongly favoring the ***an-syn2*** transition state.

Next, let us consider the lithiated transition states for which the relative Gibbs Free Energies at 298K are shown in Table 3.7 and the optimized structures and Newman projections with forming bond and π-interaction lengths indicated in Figure 3.22. Because of the strong interaction between lithium and the oxygen, nitrogen and chlorine, the ***li-syn1*** and ***li-anti1*** transition states become the most stable. This interaction is so strong that we were unable to optimize the ***li-anti2*** transition state with Li^+ as counterion.

Solvating the structures with a THF molecule in order to fully saturate the lithium cation does not change a lot to the results and neither does the inclusion of a polarizable THF continuum. The latter does stabilize the ***li-syn2***, but it's energy is still 33.4 kJmol^{-1} higher than the lowest energy transition state. From Figure 3.21 and Figure 3.22, it is clear that the presence of the lithium significantly changes the transition state geometries, increasing the forming bond distance whilst the T-stacking distances remain similar.

In the experiments, *syn* selectivity was strongly enhanced by using zincated species. Therfore, similar metalated transition states we localized for these species. Similar conclusions can be drawn from the zincated transition states that are shown in Figure 3.23. In this case, $ZnCl^+$ was used as counter ion and no extra THF was added because the presence of the chloride imposes steric constraints on the accessibility of the zinc atom. The relative Gibbs free energies for the zincated transition states are shown in Table 3.7. As in the lithiated case, the ***zn-syn1*** and ***zn-anti1*** transition states are the most stable because of the strong interaction of zinc with oxygen, nitrogen and chloride. It is also clear that the ***zn-syn2*** and ***zn-anti2*** transition states are much less stable in comparison with the lithiated analogues. The energy difference between ***zn-syn1*** and ***zn-syn2*** does reduce substantially when using the MP2 method and even further when applying the C-PCM model, indicating once again the importance of the disperse interactions and the bulk solvent effect. In a later stadium, also Zn^{2+} was used as a counter ion, but this does not really alter the energetics of the system. In this case however, THF should still be added in order to obtain a good embedding of this bivalent cation.

Table 3.7: Gibbs Free Energies for the coupling transition states using B3LYP/6-31+G(d,p) geometries and energy refinements at the MP2/6-311+G(d,p) level *in vacuo* and in the C-PCM model using Bondi radii at 298K.

		B3LYP	MP2	MP2/C-PCM
Anionic				
	an-syn1	-21.7	-7.7	9.1
	an-syn2	-19.5	-20.8	-14.8
	an-anti1	0.0	0.0	0.0
	an-anti2	-35.5	-11.97	17.8
Li$^+$				
0 THF	li-syn1	0.9	3.8	-1.9
	li-syn2	112.8	86.5	36.3
	li-anti1	0.0	0.0	0.0
	li-anti2[a]	-	-	-
1 THF	li-syn1	0.5	1.0	-2.1
	li-syn2	86.1	65.2	31.3
	li-anti1	0.0	0.0	0.0
	li-anti2[a]	-	-	-
ZnCl$^+$				
	zn-syn1	2.0	4.4	1.5
	zn-syn2	119.4	99.2	70.0
	zn-anti1	0.0	0.0	0.0
	zn-anti2	103.6	105.9	88.1
Zn^{2+}				
	zn^{2+}-syn1	-2.4	-2.4	0.2
	zn^{2+}-anti1	0.0	0.0	0.0

[a] These transition states could not be optimized

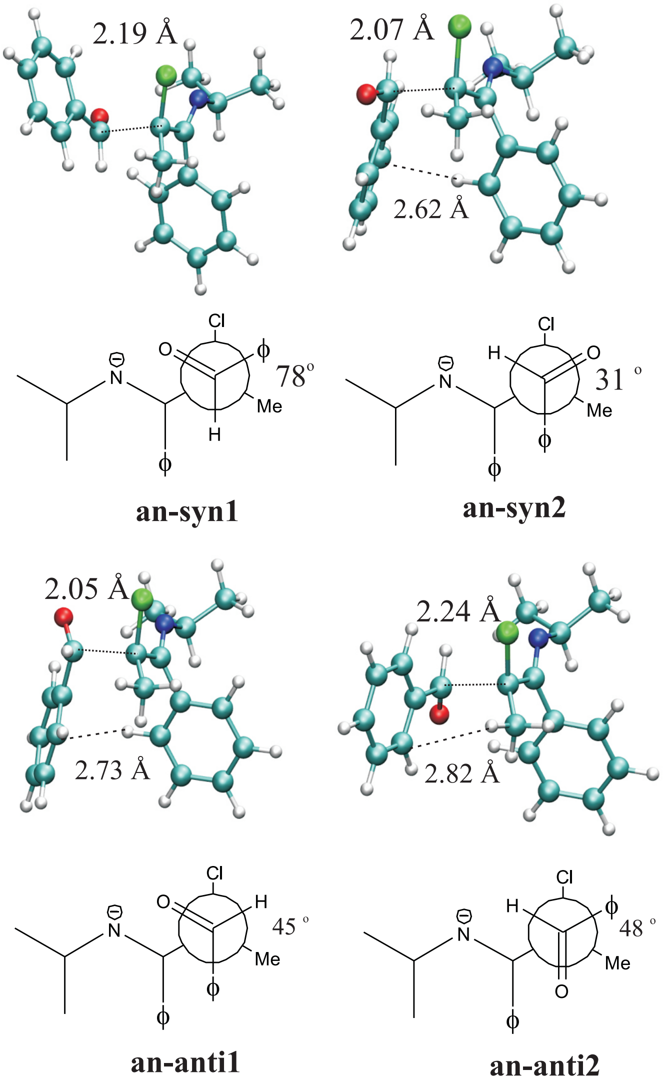

Figure 3.21: Optimized transition state geometries and corresponding Newman projections for *syn* and *anti* product formation using the B3LYP/6-31+G(d,p) electronic structure method. The two configurations for each kind of transition state are indicated with 1 (benzaldehyde O pointing towards N) or 2 (benzaldehyde O pointing away from N).

From these high level results, the experimentally observed *syn*/*anti* ratio in the presence of lithium can not be explained because of the very small energy difference that is found between the *syn* and the *anti* transition states. Given the sensitivity of the energetics and the C-PCM method,

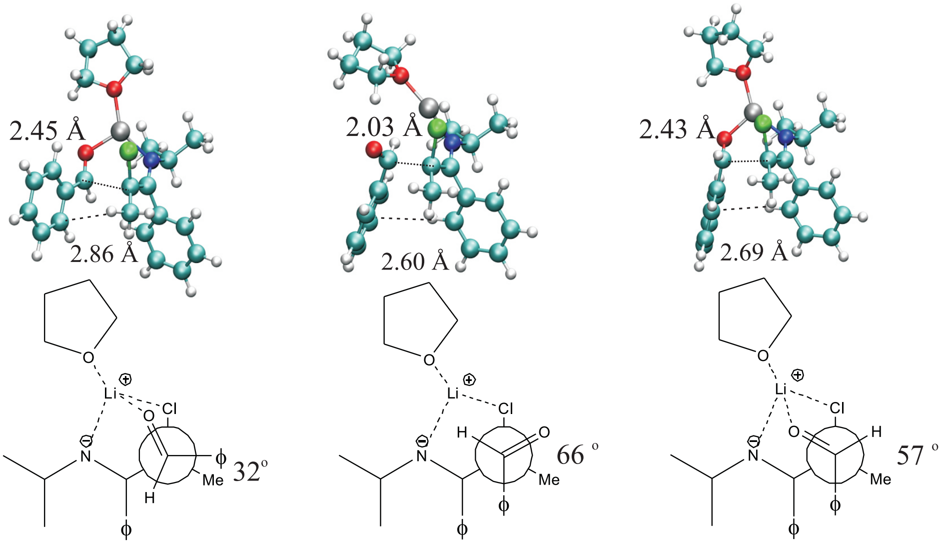

li-syn1.1thf **li-syn2.1thf** **li-anti1.1thf**

Figure 3.22: Optimized transition state geometries and corresponding Newman projections for lithiated *syn* and *anti* transition states using the B3LYP/6-31+G(d,p) electronic structure method. The ***li-anti2*** transition states could not be localized.

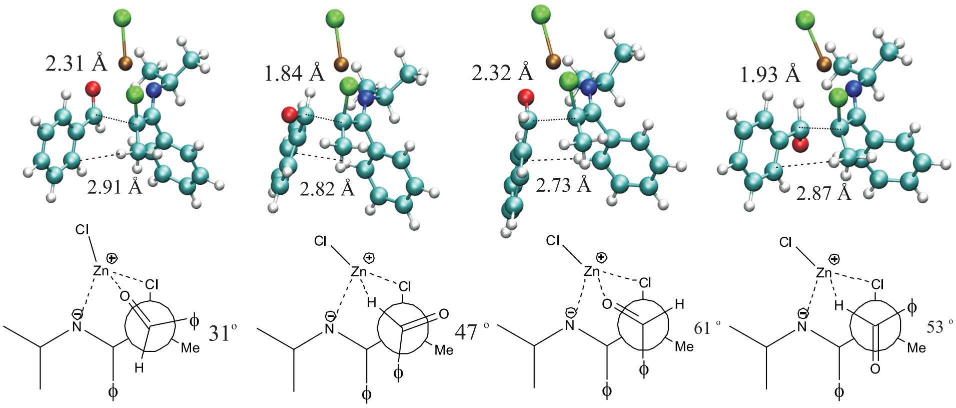

zn-syn1 **zn-syn2** **zn-anti1** **zn-anti2**

Figure 3.23: Optimized transition state geometries and corresponding Newman projections for zincated *syn* and *anti* transition states using the B3LYP/6-31+G(d,p) electronic structure method.

the results are inconclusive at the moment and further research is needed. The assessment of the various electronic structure methods shows that the

Table 3.8: Assessment of different solvent models that were used for studying the E/Z isomerization of lithiated 3-chloro-1-azaallylic anions.

	qualitative	quantitative	structure
In vacuo	✓	✗	✗
Implicit	?	✗	✗
Explicit	✓	✗	✓
Expl/Impl	?	✗	✓
MD/MTD	✓	✓	✓

system is very difficult to describe properly by today's quantum mechanical models. This is probably partly due to the effect of dispersive interactions. Another point which complicates the reproduction of a correct selectivity is that when zinc is used, Li^+ is still present in the solution. This might have a large impact on the optimal transition state structures. Very extensive solvation methods would be needed to study these effects. These are not feasible within the limits of the current methods available.

3.1.5 Conclusions and Model Assessment

As a conclusion to this first chemical system, conclusions can be drawn from the different solvent models that have been used. The models will be judged by their ability to provide good qualitative results, reliable quantitative results and by the quality of the solvated structures that are obtained. An overview of this assessment is presented in Table 3.8.

The results are qualitatively good in the sense that all models used do predict that the Z/*anti* isomer is the most stable one. The different solvation of the E and Z isomer is also consistent when using explicit solvent molecules either by static or dynamic simulations. As the solvation energies for the addition of the second THF molecule is very close to zero for the explicit/implicit model, the question mark is the most appropriate symbol since these results are not conclusive.

A main feature of the isomerization under study is the different solvation pattern for the E and Z isomer of the lithiated 3-chloro-1-azaallylic anion. Only dynamic simulations are capable of consistently including this structural difference in the free energy calculations with the metadynamics method, hence resulting in the most realistic and most accurate free energy difference between both isomers. The rotational barrier obtained with metadynamics could not be studied with the static approach because the very limited amount of solvent molecules highly destabilized the transition state causing the structure to relax in an unphysical way.

Structural analysis of the solvated structures obtained by the static and dynamic methodologies show that the obtained complexes are very similar. In the case of these very well-defined and local interactions between solute and solvent, the solvated cluster approach can indeed give good structural information.

3.2 Free Radical Polymerization

Free radical polymerization is one of the most important reaction mechanisms for the industrial production of a wide variety of polymers. It is a complex multi-step process and the determination of rate coefficients of the various elementary reactions is a challenge both for theoreticians as experimentalists. From the experimental point of view, substantial progress has been made since the establishment of elegant laser-flash photolysis-based techniques, such as pulsed laser polymerization (PLP) and time-resolved PLP. Computational quantum chemistry has the potential to study individual reactions and their rates without kinetic model-based assumptions. However the modeling of radical reactions generally requires high levels of theory which are not feasible for polymeric systems. Nonetheless, due to a continuing increase in computer power and the development of advanced numerical models, computational chemistry has established itself as a useful tool for the radical polymer field. In literature, a rich database exists consisting of both experimental[125–129] and theoretical data for a broad range of radically polymerizing monomers like ethylene,[130,131] (meth)acrylate-type monomers,[31,132,133] styrene,[134] (meth)acrylamide-type monomers, acrylonitrile,[135] and vinyl chloride.[136]

To date there have been relatively few published direct assessments of the influence of solvent on radical reactions. Moreover, experimental solvation energies for radical species are scarce in the literature. However, as some polymerizations are carried out in solution, the knowledge of the effects that are induced by the solvent is crucial for a better understanding of free radical polymerization in solution. Therefore, theoretical modeling of the kinetics of propagation reactions should take solvent effects into account. It has long been recognized that solvents may affect the reaction kinetics but the origin of the solvent effect and the extent of its influence have been the onset of a long debate. Reaction rate coefficients (k_p) for styrene and methyl methacrylate (MMA) polymerizations have been measured in a wide variety of solvents by Olaj et al.[137] and the solvent-induced changes were found to vary around 20 percent. In other experimental work, one notices a significant increase in k_p in some specific polar solvents when the monomer concentration decreases. Recently Beuermann published a very good review on the current status of the solvent influence on the propagation kinetics studied by pulsed laser initiated polymerizations[138]. Various effects may contribute to changes in k_p due to solvent such as hindered rotational modes, hydrogen bonding[139] or electron/pair interactions. These may lead to an enhancement of a factor 10 of the propagation rate. In contrast, non-specific solvent interactions originating from solvent size, local monomer concentration or steric effects lead to less pronounced variations in k_p.[139]

In the framework of this research, four monomers were investigated that show a remarkable solvent effect: acrylamide (AA), methacrylamide (MAA), N-isopropylacrylamide (NIPAM), and methyl methacrylate (MMA). For the first three, a large rate enhancement is observed when their polymerization is carried out in water.[140–143] The work on the MMA monomers was performed in collaboration with the research group of Prof. Aviyente of the Boğaziçi University (Istanbul). For MMA, an increase in the syndiotactic content of the product mixture is observed when using perfluoro-tert-butanol (1,1,1,3,3,3-hexafluoro-2-(trifluoromethyl)propan-2-ol, $(CF_3)_3COH$) instead of methanol (see ***Paper IV***).[144] The research on NIPAM is also performed in collaboration with the Boğaziçi University and is still in progress. The effect of water on the reaction kinetics of AA and MAA will be discussed in the next section, and is also the topic of ***Paper III*** which was published in Macromolecules.[145]

3.2.1 Solvent Effects on AA and MAA Polymerization

In order to investigate the effect of explicitly interacting water molecules and the bulk water environment on the transition state, B3LYP/6-31+G(d,p) geometry optimizations were carried out for the addition of a monomer to a monomeric, dimeric and trimeric radical chain with inclusion of 1 or 2 water molecules. On these optimized structures, energy refinement calculations were carried out with more advanced electronic structure methods of which the MPWB1K[133,146] and BMK[136,147,148] density functional that were parametrized to give good results for reaction kinetics. The functionals are chosen as literature has indicated that they are appropriate for studying free radical polymerization reactions.[133] Apart from the topic of this thesis, it has been recognized that it is very difficult to obtain a good quantitative agreement between experimental and theoretical rate constants. Extensive level of theory studies were conducted by Coote and co-workers[149]. They have shown that very high levels of theory are needed although these are generally not feasible for the systems under study. The methodology used here is a cost efficient method which is expected to give a good qualitative agreement.

The optimized transition state structures for syndiotactic addition of a monomer to a monomeric radical (**aa1**, **maa1**) and for the one water assisted addition to a monomeric radical (**aa1(1H2O)m**, **maa1(1H2O)m**), a dimeric radical (**aa2(1H2O)m**, **maa2(1H2O)m**), and for addition to a trimeric radical (**aa3(1H2O)m**, **maa3(1H2O)m**) in which m represents the fact that the water molecule forms a hydrogen bond with the carbonyl oxygen of the monomer are shown in Figure 3.24. The latter structures were shown to be the most favorable in ***Paper III***.[145]

The Free Energies of solvation in vacuo and in the C-PCM model for these structures are shown in Table 3.9. An interesting feature is that ΔG_{sol}^{vac} for both functionals is within the order of 5 kJmol^{-1}, which is generally considered as 'chemical accuracy'. This indicates that the large negative solvation energy (CSE) is compensated by equally large entropic contributions, yielding overall free energies which are nearly zero. This contribution is relatively large because two separate (at infinite distance) gas phase molecules are brought together resulting in a substantial loss of degrees of freedom. This phenomenon is not really representative for the chemical process in the real molecular environment and therefore, also C-PCM calculations were performed in which the free energy is calculated for bringing the TS and a water molecule together in a dielectric environment. The ΔG_{sol}^{cpcm} are all substantially negative which indicates that the water bridge interaction between the carbonyl oxygen from the monomer and the amide hydrogen from the radical is a likely event for AA and MAA polymerization in water.

A closer look on the monomeric transition states by Newman projections along the forming bond (see Figure 3.25) can give more insight in the origin for this energetically favorable interaction. In the monomeric transition states (**aa1** and **maa1** in Figure 3.25), a very strong interaction between the carbonyl oxygen from the monomer and the amide hydrogen from the radical determines the most stable configuration. This configuration however, is quite hindered about the forming bond, which is reflected in the almost eclipsed configuration of 18 degrees for **aa1** and 5 degrees for **maa1** (see 3.25). The water bridge that replaces the hydrogen bond between the former atoms causes structural relaxation of the TS structure and increases the dihedral angle about the forming bond to 30 and 35 degrees for **aa1(1H2O)m** and **maa1(1H2O)m**, respectively. This is a good example

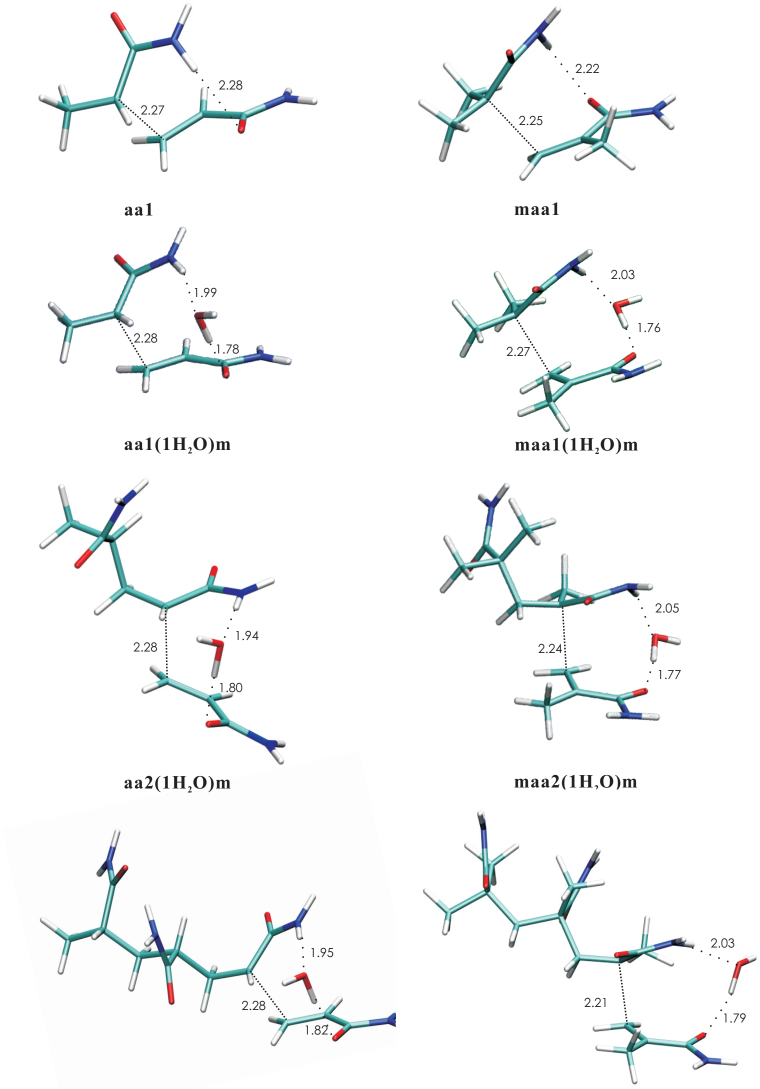

aa1 **maa1**

aa1(1H$_2$O)m **maa1(1H$_2$O)m**

aa2(1H$_2$O)m **maa2(1H$_2$O)m**

aa3(1H$_2$O)m **maa3(1H$_2$O)m**

Figure 3.24: AA and MAA transition state structures *in vacuo* and with 1 explicit water molecule for addition to a monomeric, dimeric, and trimeric radical. The distances on the figure are in Å.

of how a solvent molecule (water in this case) can change the geometry of

Table 3.9: Solvation free energy *in vacuo*, ΔG_{sol}^{vac}, and using the C-PCM method, ΔG_{sol}^{cpcm}, for monosolvation of AA and MAA transition states.

	MPWB1K		BMK	
	ΔG_{sol}^{vacuo}	ΔG_{sol}^{cpcm}	ΔG_{sol}^{vacuo}	ΔG_{sol}^{cpcm}
aa1(1H2O)m	-2.8	-11.9	-0.5	-9.0
aa2(1H2O)m	-4.1	-11.1	-2.3	-7.7
aa3(1H2O)m	0.6	-10.1	3.1	-6.7
maa1(1H2O)m	2.1	-10.3	4.1	-7.3
maa2(1H2O)m	0.9	-7.8	3.1	-4.6
maa3(1H2O)m	3.9	-6.6	5.1	-4.7

species of a reaction under investigation. By lowering the energy of the TS, also the reaction rate will increase, as will be shown in the next part.

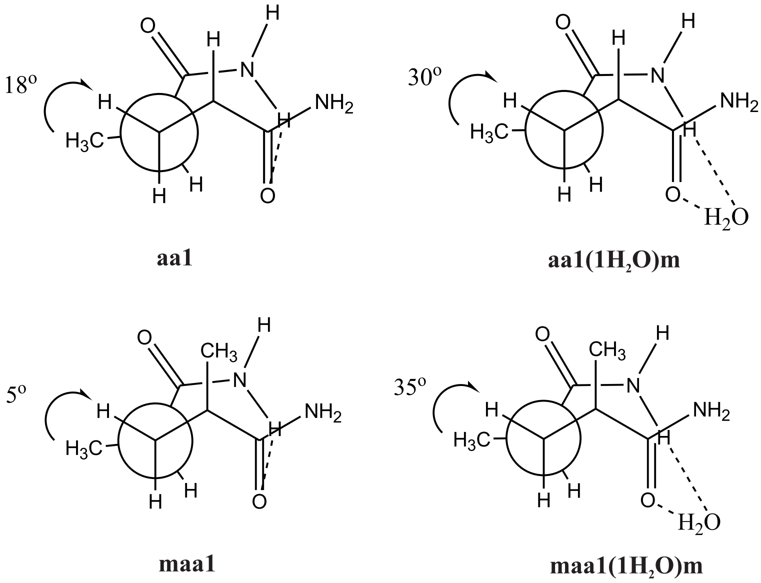

aa1 **aa1(1H$_2$O)m**

maa1 **maa1(1H$_2$O)m**

Figure 3.25: Newman projection along the forming bond for the acrylamide and methacrylamide monomeric transition states with 0 and 1 water molecule assisting.

The reaction rates were calculated using transition state theory (TST) using the partition functions from the B3LYP/6-31+G(d,p) geometry optimizations and subsequent frequency calculations. The energies from the

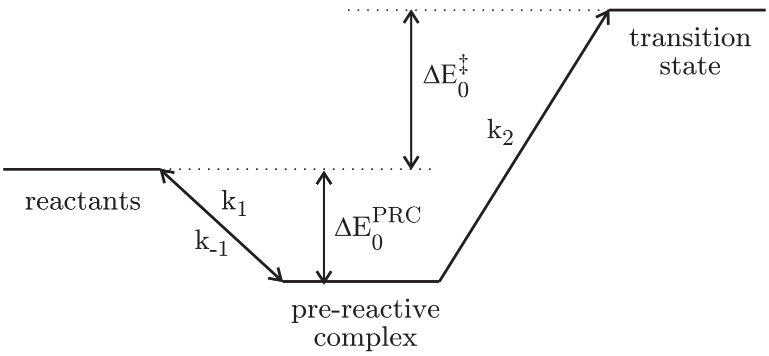

Figure 3.26: Schematic representation of the role of the prereactive complex in the apparent reaction rate coefficient.

Table 3.10: Kinetic parameters for the addition of acrylamide to a monomeric (n=1), dimeric (n=2) and trimeric (n=3) radical chain *in vacuo* and with inclusion of one explicit water molecule with different electronic structure methods. E_A is in kJ.mol^{-1}, A is in m^3.mol^{-1}.s^{-1}, hence k_{298K} is in mol.m^{-3}.s^{-1}.

		MPWB1K		BMK	
	A	E_A	k_{298K}	E_A	k_{298K}
monomer					
aa1	2.08×10^2	17.0	2.2×10^{-1}	19.5	8.0×10^{-2}
aa1(1H$_2$O)m	2.39×10^2	11.2	2.5×10^0	13.1	1.2×10^0
dimer					
aa2	1.42×10^2	13.6	5.9×10^{-1}	17.5	1.2×10^{-1}
aa2(1H$_2$O)m	7.83×10^2	10.3	1.2×10^1	13.0	4.1×10^0
trimer					
aa3	2.30×10^2	15.6	4.3×10^{-1}	18.8	1.2×10^{-1}
aa3(1H$_2$O)m	1.10×10^2	11.1	1.2×10^0	13.6	4.4×10^{-1}
experimental values					
Ref.[141]	1.58×10^4	13.4	7.4×10^1		
Ref.[141]	1.26×10^4	12.9	7.1×10^1		

MPWB1K and BMK density functionals were used. The reference reactant state is either the monomer and radical at infinite separation distance using the ideal gas law (for non-solvated TS's) or the radical and monomer-water complex (for the monosolvated TS's). The difference between both approaches is shown in Figure 3.26.

The Arrhenius parameters (the preexponential factor, A, and the activation energy, E_A) and the rate coefficient at 289K, k_{298K}, are given in Table 3.10 for AA and in Table 3.11 for MAA. An interesting observation from Tables 3.10 and 3.11 is that the preexponential factor hardly changes upon addition of a water molecule. For all the cases studied here and in ***Paper III***, the preexponential factor changes less than one order of magnitude. In the case of AA, the calculated A still underestimates the experimentally obtained one by 2 orders of magnitude. This lies in the line of expectations as only a limited amount of solvent molecules is taken into account and the entropic effects that are captured in this factor are probably wrongly estimated. The effect on the activation energy is more clear, upon addition of a single water molecule, E_A decreases and for MAA, comes very close to the experimentally measured value. This decrease in activation energy is the result of the configurationally more stable transition states that are accessible when mediating the intermolecular hydrogen bond by a water bridge as shown in Figure 3.25. It is interesting to note that the relative shift in activation energy by including a water molecule is approximately the same for both functionals. This confirms earlier findings that absolute rates can be influenced substantially by the functional but that qualitative trends are mostly reproduced independent of the electronic structure method.

In ***Paper III***, tables 4 and 6 show that applying the C-PCM continuum model for these reactions results in a rate increase of at least 2 orders of magnitude, largely overshooting the experimental rate for AA and approaching the experimental value for MAA. An interesting measure for the accuracy of the methods and models that were used here, is the AA/MAA rate ratio. This ratio can be calculated from the experimental values[141,150] and lies within the range between 67 and 75, showing that AA polymerization in water is about 70 times faster than MAA polymerization. In Table 3.12, these ratios for the different models and methods are shown, demonstrating that including an explicit water molecule in the transition state does reproduce the experimental ratio better compared to the ratio in the absence of an explicit water molecule. This table also shows that, even though the continuum model without an explicit water molecule is also performing quite good, the combined implicit/explicit model (column 4) is performing very badly, overestimating the reaction rate for the AA polymerization.

Table 3.11: Kinetic parameters for the addition of methacrylamide to a monomeric (n=1), dimeric (n=2) and trimeric (n=3) radical chain *in vacuo* and with inclusion of one explicit water molecule with different electronic structure methods. E_A is in $kJ.mol^{-1}$, A is in $m^3.mol^{-1}.s^{-1}$, hence k_{298K} is in $mol.m^{-3}.s^{-1}$.

		MPWB1K		BMK	
	A	E_A	k_{298K}	E_A	k_{298K}
monomer					
maa1	7.24×10^1	15.9	1.2×10^{-1}	19.9	2.4×10^{-2}
maa1(1H$_2$O)m	1.78×10^1	11.2	1.9×10^{-1}	14.2	5.7×10^{-2}
dimer					
maa2	3.55×10^1	17.9	2.6×10^{-2}	22.8	3.6×10^{-3}
maa2(1H$_2$O)m	1.04×10^1	12.5	6.7×10^{-2}	16.6	1.3×10^{-2}
trimer					
maa3	5.33×10^1	18.8	2.7×10^{-2}	23.6	3.9×10^{-3}
maa3(1H$_2$O)m	4.08×10^1	18.8	2.1×10^{-2}	21.7	6.5×10^{-3}
experimental values					
Ref.[150]		20.0	1.1×10^0		

Table 3.12: The AA/MAA rate ratio for addition to a trimeric radical in vacuo, with 1 explicit water molecule, in the continuum model and in the combined explicit/implicit solvation model for all studied electronic structure methods. The experimental range for this ratio is 67-75.

	in vacuo		C-PCM	
	without H_2O	with H_2O	without H_2O	with H_2O
MPWB1K	16	57	38	267
BMK	31	68	71	271
experimental		67-75		

These calculations show that an important solvent effect can be attributed to solvent molecules, stabilizing the transition state and thereby lowering the activation energy of the reactions with 4 to 10 kJmol^{-1} depending on the electronic structure method used. As the propagation rates were seriously underestimated when modeled in the gas phase, the inclusion of explicit water molecules brings the propagation rates much closer to the experimental values. The reaction rates also increase significantly by using an implicit solvent model. In general, gas phase calculations can give reliable and quite accurate activation energies when an appropriate description of the system is used in terms of electronic structure method and explicit solvation. A remaining challenge lies in a good description of the pre-exponential factor. Using the ideal gas as a standard state for modeling a reaction in solution will result in an underestimation of the pre-exponential factor.[149] More advanced techniques in which the solvent environment around the reactive center is taken into account entirely, so as to include all possible entropic contributions might contribute to a better description of the pre-exponential factor. This however, is far from trivial and not very much is known about a feasible technique for taking these factors into account. A promising tool for these simulations is the COSMO-RS method[151] that for instance allows for the calculation of activity coefficients and for which it was very recently shown to result in a better correspondence of the rate coefficients with experimental values.[149]

Apart from the absolute comparison of calculated and experimental rate constants it is also very important to validate the relative rates of polymerization of the AA versus the MAA polymerization system. Experimentally, this ratio is estimated at about 70. Simple gas phase calculations underestimate this ratio, but the ratio is well reproduced when using the implicit or the explicit solvation model. The results of the mixed solvation model should be treated with care as the results are very much dependent on the position of the explicit solvent molecules. In general, the BMK and MPWB1K functionals give the best quantitative and qualitative picture for the trimeric model. These results are in agreement with the earlier work of Broadbelt and co-workers.[133]

3.2.2 Conclusions and Model Assessment

For the free radical polymerization, also conclusions can be drawn with respect to the solvent models that were used. In this part of the research, no dynamic simulations were performed, hence the dashes on the MD/MTD row in Table 3.13 in which the results are presented.

Table 3.13: Assessment of different solvent models that were used for studying the free radical polymerization of AA and MAA.

	qualitative	quantitative	structure
In vacuo	✗	✗	✗
Implicit	✓	✓	✗
Explicit	✓	✗	?
Expl/Impl	✗	✓	?
MD/MTD	-	-	-

The measure for a qualitatively good method is the propagation rate ratio for which the results are given in Table 3.12. It seems that, by including an explicit water molecule to the transition state, the rate ratio is very well reproduced. This is also the case when the implicit model is used (without explicit solvent molecules). The reliability of the latter agreement however might be due to some sort of error cancellation.

When looking at the quantitative results for the propagation rate coefficients, the numbers show that an implicit method (with or without explicit water molecules) are needed in order to obtain rate coefficients that lie within an order of magnitude of the experimental values. Even though this is a good agreement, the reliability of these numbers is questionable. The study in ***Paper III*** also includes other functionals (B3LYP, B2-PLYP) and it is seen that the inclusion of a continuum model shifts the rate coefficients by about three orders of magnitude, independent of the electronic structure model that is used.

The main conclusion from this study is that including explicit water molecules in the transition state structure results in structural relaxation and enhances the reaction rate of the free radical polymerization of acrylamide and methacrylamide. The continuum models at this point do not contribute much towards understanding the chemistry occurring as they only result in shifting the rate coefficient upwards. No elaborate findings on the solvated state of these structures can be made at this point as only one or two water molecules were included in the transition state region whereas the remainder of the propagating radical was not solvated for computational efficiency. If one would be interested in a more elaborate solvation study, dynamics methods should be applied.

3.3 Molecular Dynamics Study of Biochemical Systems

The last part of the applications is performed using dynamic methods as the solvent molecules actively participate in the reaction and it is not a priori known which solvent molecule will undergo reaction. The study of biologically relevant reaction mechanisms is a growing research area and it continues to expand because of its importance in understanding chemical processes in the human body. As all of these reactions occur in a complex environment, it is essential to include the latter in the theoretical model. Therefore, molecular dynamics studies are ideally suited in order to give structural information about the molecules under study and the metadynamics method can give insight into the reactions that can occur in the aqueous environment.

In this section, molecular dynamics in a water solution in order to study biochemical reactions will be discussed. The neutral hydrolysis of acetamide (AMD) and N-methylacetamide (MAMD) was studied using both static methods and the metadynamics method for reconstructing the free energy landscape corresponding to this reaction. The results of this research will be discussed in the following sections. First, a short introduction on the hydrolysis of amide bonds will be given, followed by a static and explicitly solvated study on the hydrolysis of AMD. In the last section, the molecular dynamics and metadynamics simulations for AMD and MAMD hydrolysis will be discussed. During this work, I also actively participated in a a project on the determination of both structural and spectroscopic properties of a flavoprotein radical for which the results are discussed in ***Paper VI***.

3.3.1 Introduction on the Hydrolysis of Amide Bonds

The spontaneous - uncatalyzed - hydrolysis of peptide bonds has been subject to extensive debate over the past 40 years. This is not surprising, since both peptide backbones[152,153] and amidic side-chains of asparaginyl (Asn) and glutaminyl (Gln) residues are prone to hydrolysis.[154] Several reaction mechanisms have been previously proposed, and though some experiments suggest a base-catalyzed mechanism in neutral aqueous solution,[155] uncatalyzed hydrolysis of amide bonds has been experimentally observed[153,156] and a stepwise reaction mechanism has been proposed.[157] The most accurate experimental results on the neutral hydrolysis of formamide suggest an activation free energy barrier of 130.7 $\mathrm{kJmol^{-1}}$ which corresponds to a pseudo-first order rate coefficient of 1.1 $10^{-10}\mathrm{s^{-1}}$ or a half life of 199 years.

The knowledge of the reaction mechanism for these reactions is important because it gives insight in the reactivity of amino acids with amide side chain functionalities, as well as amide linkages in the peptide backbone. Moreover, understanding of these uncatalyzed reactions will provide additional insights in enzyme efficiency.

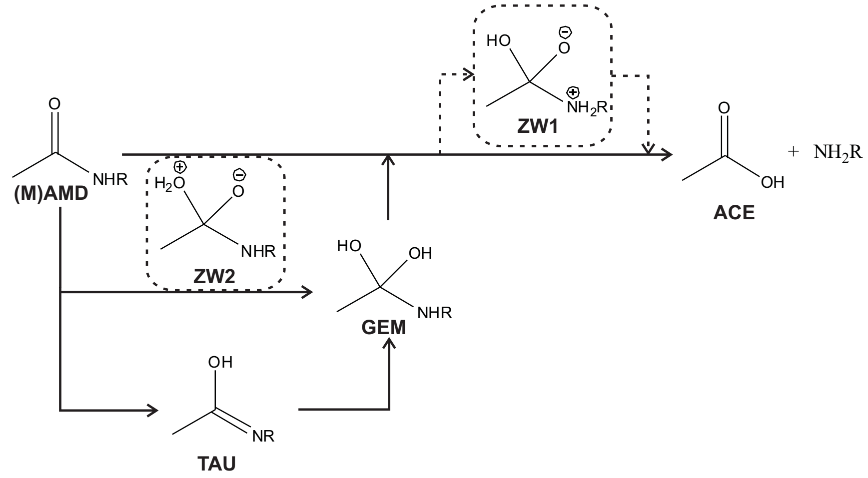

Figure 3.27: Proposed reaction pathways for the neutral hydrolysis of acetamide (AMD, R=H) and N-methylacetamide (MAMD, R=CH_3) to acetic acid (ACE) and NH3 or NH_2CH_3. Concerted and stepwise pathways, two-step via gem-diol (GEM) or three-step through imidic tautomer (TAU), are depicted. Two proposed zwitterionic intermediates are also shown (ZW1 and ZW2).

The model compounds chosen in this study, acetamide (AMD) and N-methylacetamide (MAMD), contain secondary carbonyl moieties, which represent - more realistically - the molecular environment of a peptide carbonyl carbon compared to the primary carbonyl of a formamide. So far, two distinct pathways have been proposed for the neutral hydrolysis reaction: a direct, concerted route and a stepwise pathway going through a *gem*-diol intermediate (GEM, see Figure 3.27). In the concerted mechanism, the nucleophilic attack of water onto the carbonyl is accompanied by a simultaneous proton transfer from the water to the amide nitrogen, leading to the rupture of the amide C-N bond. A zwitterionic intermediate (ZW1) was observed in a computational study employing a combined quantum mechanical and molecular mechanics (QM/MM) methodology[158] and in a gas-phase solvent cluster study, which consisted of ZW1 and explicit solvent molecules embedded in a continuum solvent model.[158,159] In the stepwise mechanism, the water molecule attacking the carbonyl transfers a proton to the carbonyl oxygen, resulting in a tetrahedral intermediate: the gem-diol.

In a constrained Car-Parinello molecular dynamics CPMD dynamics study, the zwitterion ZW2 was identified as an intermediate formed after the addition of water to the carbonyl carbon.[160] The presence of this transient species, however, was later attributed as an artifact of the simulation setup.[161] It is known from computational studies on formamide[162,163] and N-methylacetamide[164] that the tautomerization between the amide and the corresponding imidic acid is possible. Therefore, it has been presented herein as a possible step towards the hydrolysis of AMD and MAMD (bottom arrow in Figure 3.27). Apart from it being a possible pathway facilitating amide hydrolysis, tautomerization of acetamide in itself is an important model reaction for tautomerization in larger nucleic acid bases, which may be responsible for spontaneous point mutations in DNA.[165]

3.3.2 Static Study of the Direct Hydrolysis of Acetamide

In order to gain insight into the system under study and to establish benchmark values for the reaction energies and activation energies, geometry optimizations were performed using the BLYP density functionals with a TZVP basis set and with the MP2/6-31+G(d,p) method. The BLYP functional was chosen here to serve as reference values for the dynamic simulations that were carried out using the same functional for reasons of computational efficiency. Calculations for all reactions in Figure 3.27 were studied with the inclusion of one and two water molecules to assess the influence of these explicit solvent molecules. The transition state nomenclature is shown in Figure 3.28 and the accompanying transition states are depicted in Figure 3.29. The Gibbs free energies of both the minima and transition states are shown in Table 3.14 for the BLYP/TZVP optimizations and in Table 3.15. All calculations were run using the Gaussian03 program,[25] a vibrational analysis of the transition states showed that there was only one imaginary frequency present corresponding to the reaction under study. From these structures, IRC calculations were performed in order to find the reactant and product states.

From the values in Table 3.14 and Table 3.15, it is clear that adding an extra water to the transition states can result in a decrease in activation energy of 50 kJmol^{-1}. Even though these values cannot directly be compared to the values obtained by Gorb et.al.[158] because the model system is different and no PCM calculations were performed here, the values are still quite similar and the conclusions from these calculations remain the same, namely that the 2-step mechanism going through the *gem*-diol intermediate is the most likely pathway and that water molecules decrease the activation

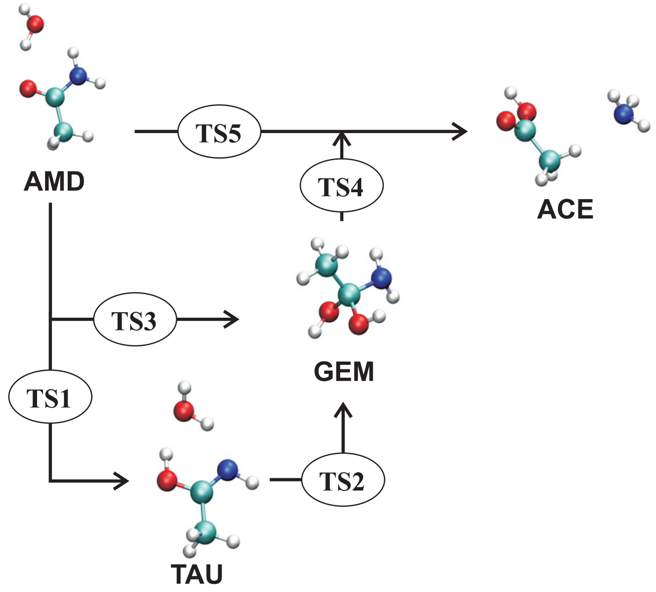

Figure 3.28: Reaction scheme and transition state nomenclature for the static AMD hydrolysis calculations.

Table 3.14: Gibbs free energy scheme for the BLYP/TZVP optimized geometries for the one, two, and three step mechanism in AMD hydrolysis with one or two explicit water molecules. All values are in kJmol^{-1} and are relative to the AMD reactant complex.

	1 H_2O			2H_2O		
	1-step	2-step	3-step	1-step	2-step	3-step
AMD	0.0	0.0	0.0	0.0	0.0	0.0
TS1			71.7			65.2
TAUT			50.1			48.6
TS2			258.0			208.2
TS3		197.2			165.1	
GEM		121.5	121.5		117.8	117.8
TS4		223.0	223.0		170.7	170.7
TS5	197.2			185.8		
ACE	11.0	11.0	11.0	18.6	18.6	18.6

energies by assisting in the proton transfer that occurs in all reaction steps.

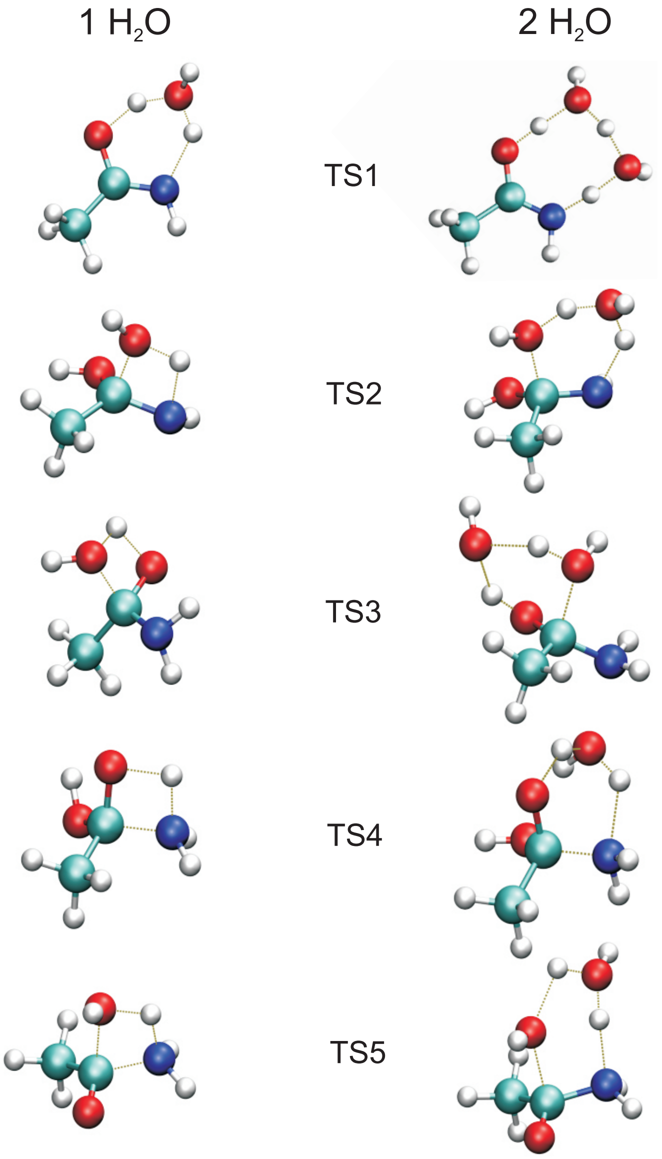

Figure 3.29: BLYP/TZVP optimized structures for the transition states from Figure 3.28 with 1 or 2 explicit water molecules.

3.3.3 Metadynamics Study of Neutral Hydrolysis of Acetamide and N-Methylacetamide

After gaining first insights in the AMD system, MD and MTD simulations can be performed in order to assess the influence of the larger water envi-

Table 3.15: Gibbs free energy scheme for the MP2/6-31+G(d,p) optimized geometries for the one, two, and three step mechanism in AMD hydrolysis with one or two explicit water molecules. All values are in kJmol^{-1}.

	1 H_2O			$2H_2O$		
	1-step	2-step	3-step	1-step	2-step	3-step
AMD	0.0	0.0	0.0	0.0	0.0	0.0
TS1			81.5			68.6
TAUT			44.5			50.8
TS2			276.2			219.3
TS3		192.4			177.4	
GEM		71.3	71.3		84.1	84.1
TS4		208.8	208.8		158.2	158.2
TS5	213.1			205.4		
ACE	13.9	13.9	13.9	27.4	27.4	27.4

ronment on the structure and energetics of the different reaction steps. In order to obtain good starting structures for the metadynamics simulation, 12 Å boxes with AMD and MAMD were packed with 36 water molecules using the PACKMOL program.[44] On these systems, isobaric-isothermal (NPT) dynamics were performed at 300K and atmospheric pressure in order to equilibrate the box size. After an equilibration period, the box size was averaged over by using the MD-TRACKS code[46] resulting in an 11.0877 Å simulation cell for AMD and an 11.0812 Å cell for MAMD. The box size evolution for both systems is shown in Figure 3.30.

The free energy surface (FES) of the system was explored using the collective variables defined in Table 3.16 for AMD and MAMD. The combination of a critical distance (the breaking bond) and two coordination numbers (global variables that take into account all oxygen and hydrogen atoms) ensures a thorough sampling of the system. In order to restrain the system, so that it only samples realistic values for the collective variables, and to steer the dynamics towards the possible reactions, quadratic walls were imposed on the collective variables. The value of the CVs at which these walls are positioned can also be found in Table 3.17. With these collective variables, a 230 ps (for AMD) and 280 ps (for MAMD) metadynamics simulation with a 0.3 fs timestep was carried out for both AMD and MAMD in which Gaussians of height 2.6 kJmol^{-1} and width 0.1 Å were added every 90 steps. This simulation resulted in the FES shown in Figure 3.31.

A Gibbs free energy contour plot for AMD and MAMD hydrolysis, projected on two of the three collective variables from Table 3.16 (the C-H

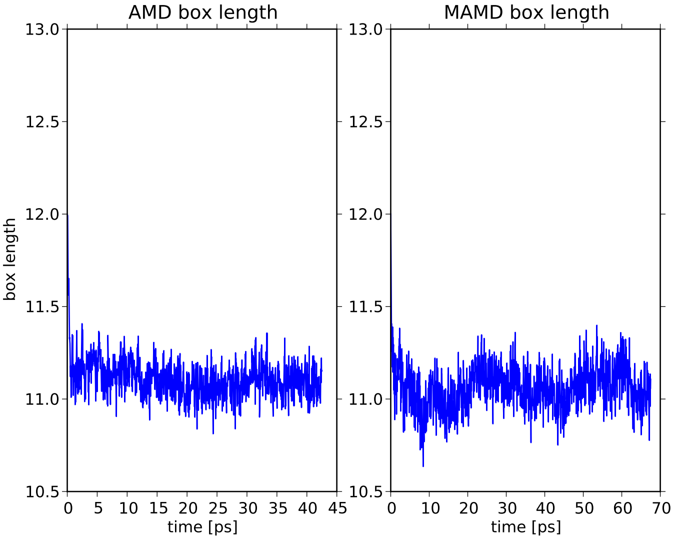

Figure 3.30: Box length evolution as a function of time in the NPT MD simulations for AMD and MAMD.

Table 3.16: Collective variables (CVs) used for the metadynamics simulations of acetamide and N-methyl acetamide hydrolysis in a water box. The subscript 'w' denotes water molecules, CN and D denote coordination number and distance (in Å) respectively, values for MAMD are in brackets when they differ from the AMD values.

	AMD (MAMD)	TAUT	GEM	ACE
	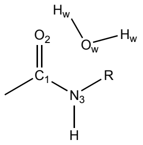	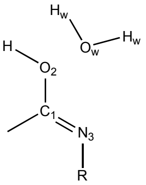	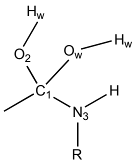	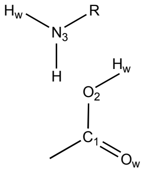
CN(C_1-$O_{w,2}$)	1	1	2	2
CN(N_3-H)	2 (1)	1 (0)	2 (1)	3 (2)
D(C_1-N_3)	≈ 1.4	≈ 1.4	≈ 1.4	> 1.4

coordination number and the C-to-O coordination number) is shown in Figure 3.31 for AMD and in Figure 3.32 for MAMD. The arrows indicate the sampled pathways and the white numbers indicate the order in which the pathways are sampled.

Table 3.17: Position of the quadratic walls for the AMD and MAMD metadynamics simulation for the three CVs.

	AMD		MAMD	
CV	lower limit	upper limit	lower limit	upper limit
CN(C_1-$O_{w,2}$)	0.5	2.5	0.5	2.5
CN(N_3-H)	0.5	3.4	-	2.4
D(C_1-N_3)	-	4.0	-	4.0

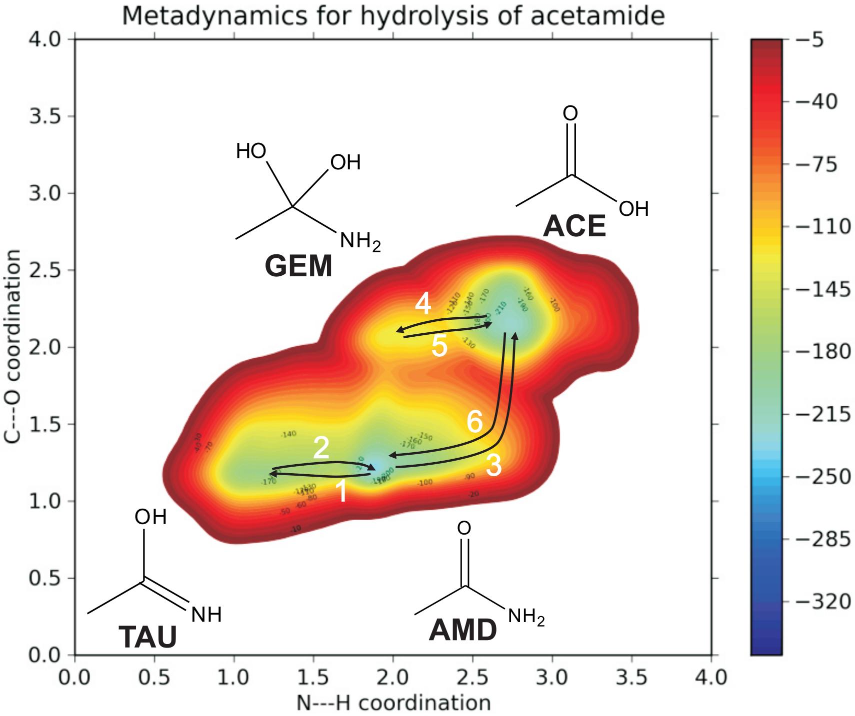

Figure 3.31: Gibbs free energy contour plot for the hydrolysis of acetamide as a function of two collective variables (see also table 3.16). The black arrows indicate the different pathways that were sampled, the white numbers show the order in which the barriers were crossed. The energy scale is in kJmol^{-1}.

The first rare event that occurs in the metadynamics simulation, is the tautomerization of the starting AMD molecule to form the imidic acid form (arrows 1 and 2 in the AMD contour plot in Figure 3.31). Contrary to previous gas-phase cluster calculations with short water-bridges consisting of one or two solvent molecules[162,166], the hydrogen transfer was

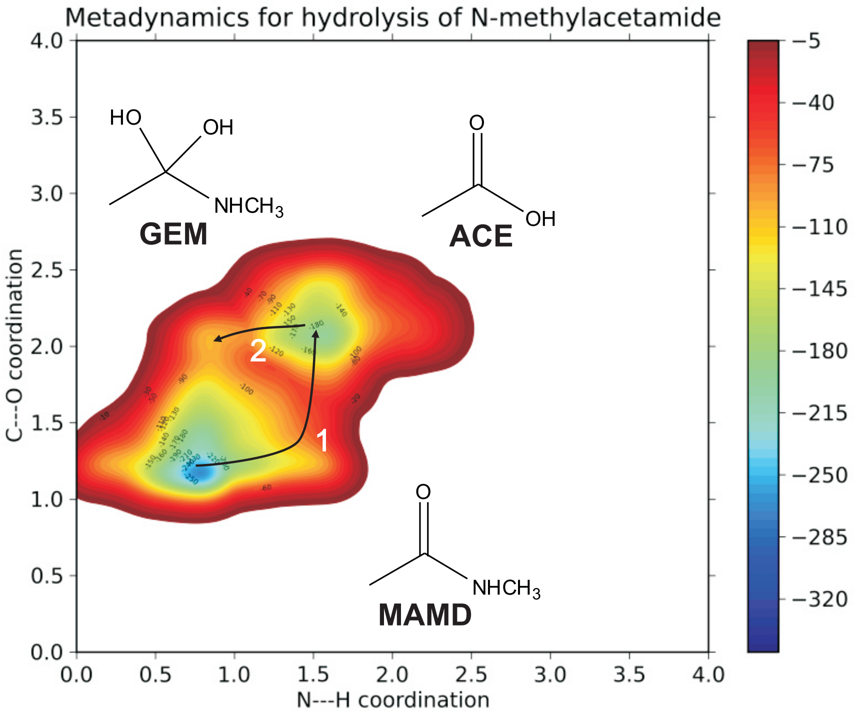

Figure 3.32: Gibbs free energy contour plot for the hydrolysis of N-methylacetamide as a function of two collective variables (see also table 3.16). The black arrows indicate the different pathways that were sampled, the white numbers show the order in which the barriers were crossed. The energy scale is in kJmol^{-1}.

shown to occur through an extended water-bridge that consists of four water molecules for AMD, and crosses the periodic boundaries. This leads to a forward barrier of 65 kJmol^{-1} and a backward barrier of 20 kJmol^{-1}. The trans-tautomer that forms is incidentally the most stable conformation and no further rotation around the C-N bond is necessary.[167] Even though the simulation cell used in this study is not large enough to account for more extended water-bridges, these are known to occur and play a prominent role in hydrogen transfer processes. The numbers obtained here are in correspondence with a previous study where the tautomerization reaction at an Asn sidechain was investigated using B3LYP/6-31+G(d,p) and resulting in a forward barrier of 75.8 kJmol^{-1} and a reverse barrier of 16.8 kJmol^{-1} for the two-water assisted tautomerization reaction.[166] A CCSD(T)/6-311++G(d,p)//B3LYP/6-311++G(d,p) calculation for formamide tautomerization assisted with 2 water molecules resulted in 87.8

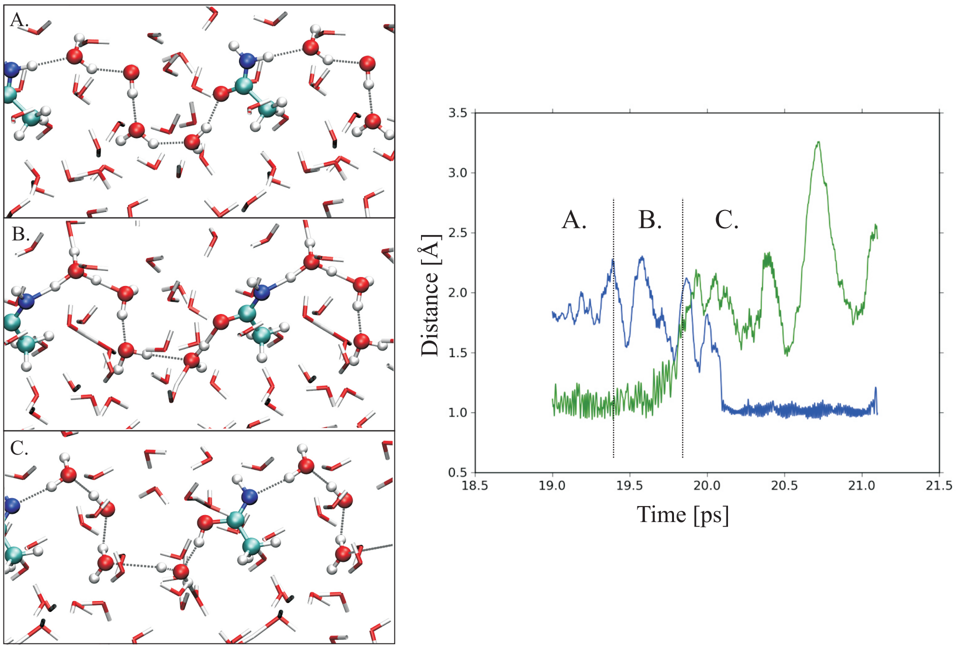

Figure 3.33: Distance profile for forming and breaking bonds and characteristic snapshots for acetamide tautomerization. Three phases can be distinguished: the acetamide phase (A), the transition region (B), and the tautomer phase (C).

kJmol^{-1}, the latter value being within 3 kJmol^{-1} of the result with B3LYP/6-311++G(d,p).[162] For MAMD, no tautomerization was observed in the MTD run indicating that this reaction is higher activated than for the AMD.

After this step, the direct hydrolysis of AMD and MAMD towards ACE, respectively, is observed (arrow 3 for AMD and arrow 1 for MAMD in Figure 3.31 and Figure 3.32, respectively). The free energy of activation for these reactions can be estimated at 230 kJmol^{-1} and 240 kJmol^{-1} for the direct hydrolysis of AMD and MAMD, respectively. These values are higher than the ones from Section 3.3.2 and show the unlikelihood of these reactions. From these products, readdition of the nitrogen results in the formation of the *gem*-diol (GEM, see Figure 3.31, arrow 4 for AMD and Figure 3.32, arrow 2 for MAMD). This appears to be a very unstable compound as the back-reaction (Figure 3.31, arrow 5 for AMD) is very fast as it has an activation free energy of only 30 kJmol^{-1}. Snapshots of both systems during the transition towards the *gem*-diol are shown in Figure 3.34 and show that 5 water molecules transfer the hydrogen from the nitrogen to the carbonyl oxygen through the periodic boundaries. The barriers for this transitions

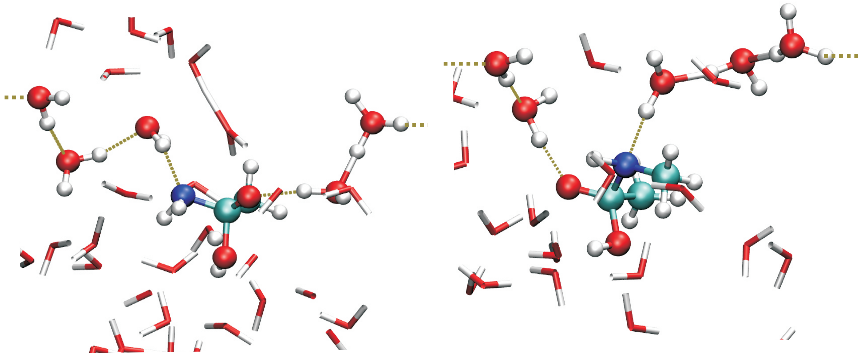

ACE -TO-GEM (AMD) ACE -TO-GEM (MAMD)

Figure 3.34: Characteristic snapshot of the transitions from AMD and MAMD to their *gem*-diol form.

can be estimated from the contour plot to be 90 kJmol^{-1} and 110 kJmol^{-1} for AMD and MAMD, respectively.

At this point, it is an interesting question why the transition from GEM to AMD and vice versa is not sampled in this simulation, considering the fact that the *gem*-diol is generally considered an important intermediate in this reaction and the gas phase calculations indicate that formation of the latter is energetically more feasible than the direct route. Even though there appears to be a saddle point on the FES corresponding to the transition from the starting molecules to their *gem*-diol, an analysis of the trajectories shows that no transition occurs from the (N-methyl)acetamide to the *gem*-diol. Therefore, this point on the FES cannot give a reliable estimate of the Gibbs free energy of activation of this reaction. Consequently, a small test calculation was performed on the dissociation of GEM with only one CV: the distance between one of the oxygen atoms and carbon atom C_1 (see Table 3.16 for the notation). The results from these simulations are one-dimensional free energy profiles as shown in Figure 3.35 that shows the reaction from GEM to AMD and MAMD. From these calculations, it is clear that the *gem*-diol is a very labile intermediate that can readily dissociate into the acetic acid with a free energy of activation of about 30 kJmol^{-1}. Also, the back reaction towards GEM takes place and it has a much lower free energy of activation compared to the direct mechanism that was found in the first simulations in Figure 3.31. This indicates that some artifacts have manifested during the simulations that are probably due to the unequal treatment of the proton-acceptor sites, nitrogen and oxygen. The

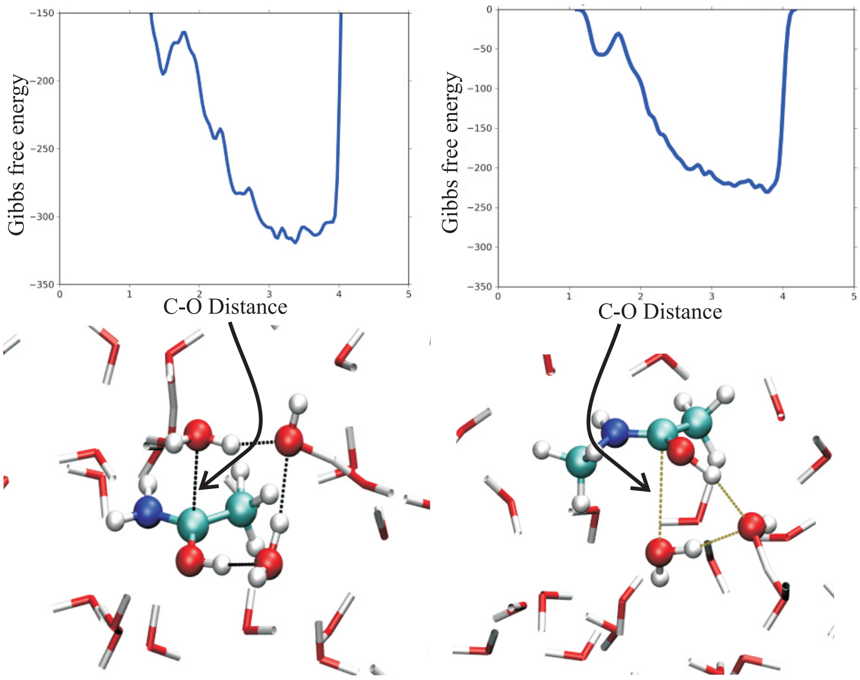

GEM-TO-AMD

GEM-TO-MAMD

Figure 3.35: Preliminary free energy profiles and characteristic snapshots from the transition region for the GEM-to-AMD and GEM-TO-MAMD reactions. The water molecules facilitating the proton shuttle are shown in the ball-and-stick representation. Note that the even though the product well of the GEM-TO-MAMD transition is net completely filled yet. The forward barrier (for GEM dissociation) can be estimated at 60 kJmol^{-1} for both cases.

N-to-H coordination was included in order to enable the sampling of the tautomeric form, but by steering the N-to-H coordination, the probability of a hydrogen transferring to the Nitrogen is biased whilst this is not the case for the oxygens present. The one dimensional simulations show that, without steering the coordination of any atom to N or O, the proton easily transfers to the oxygen atom. In this last simulation, transfer to N would be very unlikely as the C-N distance is not included in the CV set.

When combining both simulations, a free energy profile for both reactions can be constructed, as is shown in Figure 3.36 for AMD hydrolysis and in Figure 3.37 for MAMD hydrolysis. From Figure 3.36, we can conclude that the tautomerization reaction for AMD is a very likely event in a water solution considering the low activation energies. From the combination of

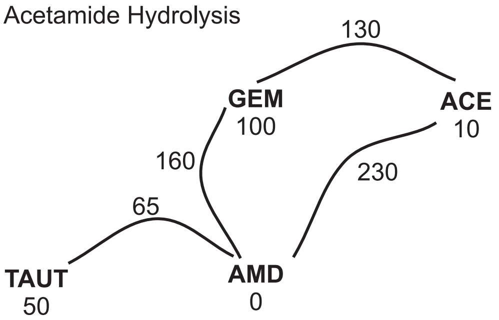

Figure 3.36: Summarizing free energy profile for AMD hydrolysis. All values are in kJmol^{-1}.

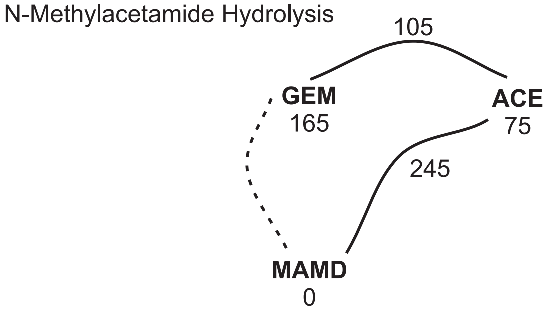

Figure 3.37: Summarizing free energy profile for MAMD hydrolysis. All values are in kJmol^{-1}.

two MTD studies in Figure 3.32 and Figure 3.35, we can see that the stepwise mechanism that goes through the *gem*-diol intermediate is the most favorable pathway. The energies that are obtained for these reactions correlate rather well with the static BLYP results from Table 3.14, the MTD barriers being slightly higher which might be caused by the solvent rearrangements that are needed to reach the transition states. The obtained activation free energy for the formation of the *gem*-diol is about 30 kJmol^{-1} higher compared to the experimental value.

For the hydrolysis of N-metlyacetamide, also no *gem*-diol pathway was found in the MTD run using three collective variables and only the direct route was found for which the activation barrier is comparable to that for AMD hydrolysis. Also, no tautomerization pathway was found here which indicates that the extra methyl group has a large inhibiting effect on this reaction. An important conclusion from the reactive pathways that were observed here, is that these reactions in water occur through extended water bridges that are very difficult to model *in vacuo*. They are quite flexible and need the proximity of other water molecules in order to stabilize the proton shuttle loop. As the transition structures in all simulations are characterized by extended water bridges, their importance in modeling these reactions cannot be underestimated. The extent to which these bridges contribute to the reactions that are observed (different bridges are required for the stepwize and the concerted mechanism) is the topic of current research.

In conclusion, these results show that metadynamics is a viable and promising tool for studying reactions in solution, but also that the collective variables have to be chosen with care so that similar degrees of freedom are treated in a similar way. In this case, for instance, the two proton-accepting sites (N and O) should both be included or both not be included under the assumption that these degrees of freedom evolve much faster compared to the C-N distance and the C-to-O coordination number. The importance of the water bridges is a feature that is difficult to capture in a collective variable, so more research will be needed in order to adequately describe reaction in which they may have a determining role.

The metadynamics method is a very promising method, but it still needs extensive testing and a variety of test systems in order to give fully reliable results. The simulations are also quite expensive indicating that this method cannot be chosen as the standard method for studying solvent effects. The combination of this methodology with an accurate QM/MM scheme would certainly mean an important step in order to practically resolve these problems.

3.3.4 Conclusions and Model Assessment

For the hydrolysis of acetamide and N-methylacetamide, the focus was set on a dynamic treatment of the system since water is both the solvent and the reactant and important effects were expected. For comparison reasons, gas phase explicit solvent calculations were carried out as well. An overviwe of the methodologies used and their assessment is presented in Tabel 3.18.

Both from the static and dynamic free energy calculations, we find qualitative agreement with previous computational studies that the stepwise pathway going through the *gem*-diol is the most favorable reaction path. Also, the relative energetics of the different reaction pathways are comparable for both methods applied and they are in reasonable agreement with

Table 3.18: Assessment of different solvent models that were used for studying the neutral hydrolysis of AMD and MAMD.

	qualitative	quantitative	structure
In vacuo	✗	✗	✗
Implicit	-	-	-
Explicit	✓	✓	✗
Expl/Impl	-	-	-
MD/MTD	✓	✓	✓

the limited experimental data that is available on neutral hydrolysis.

The strength of the MD and MTD simulations lies in the fact that the water bridges that accommodate the proton shuttle, which is very important in these reactions, is adequately modeled through an extended hydrogen bonded network. This structural feature is impossible to model using the static approach in which only short bridges containing no more than two water molecules can be modeled. Longer bridges would have a high flexibility which would make them difficult to converged from a practical point of view. But more important, such a highly structured model in the gas phase would probably give a wrong image of the entropic factors. In the MD simulation however, the abundance of water enables these structures to be stabilized and feasible from a free energetic point of view.

4

Conclusions and Perspective

In this thesis, several solvent models have been used of different complexity in order to describe chemical reactions that are influenced by a solvent environment. Three sets of chemical problems were investigated: organometal compounds, free radical polymerization and peptide sidechain hydrolysis. These applications were inspired by various ongoing collaborations. The chosen solvent model for each problem was chosen depending on the nature of the problem, the solvent itself and the solute-solvent interaction. The three applications can be distinguished by looking at the role of the solvent which is different in all of them. Overall, two types of solvents were encountered in this study: THF and water. For the organometal compounds, the solvent (THF) acts as a stabilizer for the metal cation present, whilst in the polymerization reactions, the water present structurally alters the transition states, making them energetically more feasible. For the amide hydrolysis, the solvent (water) has a dual role being both the solvent and the reactant.

The chemical problems studied in this thesis were very diverse but have the added value that various solvent models could be tested and evaluated. Therefore this thesis should be a good starting point to choose on a rational basis an appropriate solvent model for new chemical problems. In what follows we summarize important steps to take in the evaluation of the molecular environment. In Figure 4.1, a flowchart of different methodologies for studying solvent effects is presented that was assembled by the experiences following this thesis work.

The first step in this strategy is undoubtedly the *in vacuo* modeling of the reaction under study. One side remark that should be made concerns the molecular model that is used during the simulations. For various applications such as the polymerization, the peptide applications, the actual chemical system is too large to be modeled a such in any theoretical model.

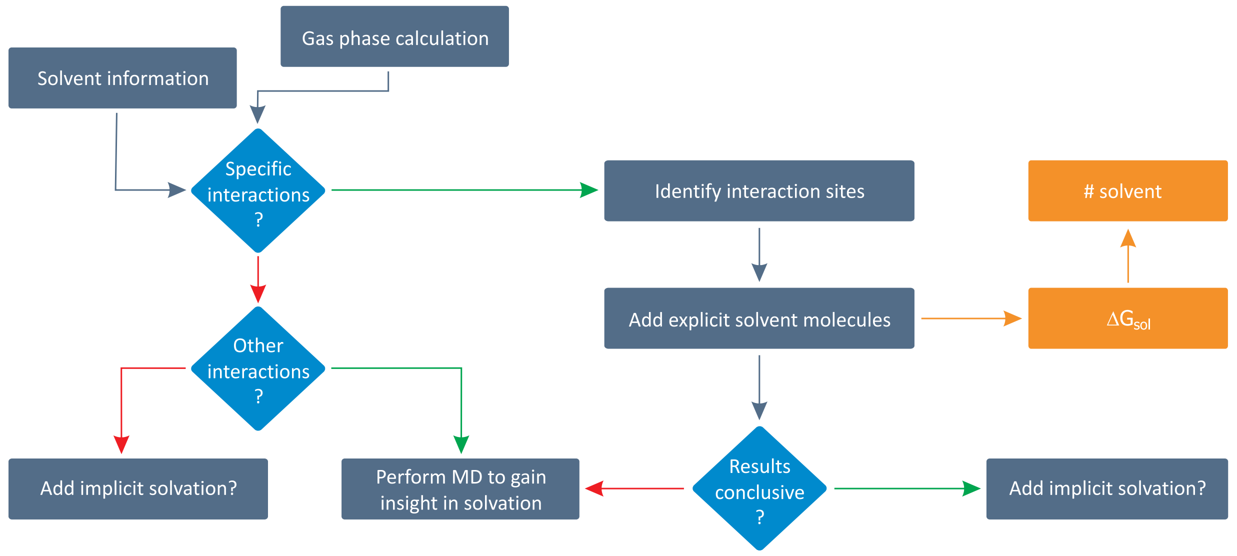

Figure 4.1: Flowchart for determining the most appropriate approach for studying solvent effects on a chemical system.

Therefore one first has to reduce the molecular model to a reasonable size for practical modeling applications. This is what was done both for the polymerization reactions and biochemical reactions.

After this step, an analysis of the gas phase structures together with information about the solvent is needed in order to identify possible specific interactions. When no strong interactions are present (e.g. when the solute or solvent does not contain sites that are prone to hydrogen bonding or a kind of -partial- charge interaction sites) and no other solvent effects are anticipated, a continuum solvent model can be applied. As optimizations in a continuum solvent are often problematic, the main goal of these kind of calculations is energy refinement. If other solvent effects can be expected, like for instance solvent size effects, molecular dynamics will be needed in order to get a realistic model. In the presence of dispersive interactions, the answers to the previous questions are more difficult to find as the interactions are well-defined but not always very strong. Therefore, it would in principle be interesting to study a system that interacts with the solvent through dispersive interactions with molecular dynamics. The main limitation here is the balance between an appropriate method and a reasonable computation time. The description of a system like this still lies beyond the limits of current methodologies. This part of the flowchart lies beyond the scope of this thesis but is added for completeness.

If specific interactions between solute or transition state and solvent can be expected, the interaction sites need to be defined and explicit solvent molecules can be added. This step requires some chemical insight and is the most ambiguous step in modeling solute-solvent interactions. If several interaction sites are possible, they should all be considered in order to select the most likely solute-solvent complex. This study will result in the solvation free energy for all the interactions that were studied and ultimately, for each interaction site, the amount of solvent molecules that is needed to saturate that site. If the results from this study are conclusive with respect to for instance experimental observations, a continuum solvent model can be applied in order to refine energies. The applications studied in this thesis however show that the results of the PCM calculations give very large corrections to the solvation energies which might not be very realistic in the end. It has been recognized that the PCM and C-PCM models are often too limited. Therefore, more advanced methods are implemented in the latest release of the Gaussian software package which are also less sensitive on the cavity model that is used. In very recent literature, other more advanced models are being tested and used such as the COSMO-RS model. Noteworthy is the recent publication by Coote *et.al.*[149] on free radical polymerization which indeed showed that the PCM model overshoots solvent effects.

Finally, a decision can be made on whether or not molecular dynamics simulations (including a large amount of solvent molecules) are necessary for obtaining more insight on the solvated structure of the system under study. It is important to mention that molecular dynamics simulations are computationally very expensive and can not be routinely applied to any chemical problem and therefore, a rational choice should be made. On the other hand it is important to emphasize the possible added value of these high level simulations. The various MD allow a thorough analysis of the equilibrium properties like the first solvation shell by time-averaging the molecular coordinates obtained in the dynamic simulation. Another option at this point, is the determination of the first solvation shell from MD simulations. After the simulation, a cluster consisting of the solute and the first solvation shell is cut out of a representative snapshot from the trajectory and this solvated cluster is then used for the *in vacuo* study. Although this methodology has the benefit that the manual placement of solvent molecules is no longer required, some drawbacks are associated with this method. First of all, the selection of the representative trajectory is not trivial and secondly, some unphysical effects are sometimes noticed due to removing part of the molecular environment. Upon optimization, a large solvent reorganization is anticipated making the cluster less representative for the structure in solution, especially because not all solvent molecules in the first solvation shell will make strong connections to the solute. Once a good equilibrium description of the system is obtained, conformational and chemical changes can be investigated by using a dynamic technique that enables the acceleration of these rare events and allows the construction of the free energy surface. Metadynamics is a valuable method that allows sampling several pathways without determining one path in advance.

The general procedures and methodologies sketched above were applied on a variety of chemical problems. The first set of reactions is the stereochemistry and reactivity of metalated, halogenated organic anions (3-halo-3-methyl-1-azaallyl anions) and was inspired by a collaboration with the research group of Prof. De Kimpe (Faculty of Bioengineering). For these species, tetrahydrofuran (THF) is the solvent of choice from an experimental point of view. As the amount of solvent molecules needed to solvate the various isomers is not fixed, a combination of static and dynamic methods was necessary to obtain a correct image of the determining factors. A combined experimental and theoretical dynamic study has shown that only one isomer of lithiated 3-chloro-3-methyl-1-azaallylic anion is present in solution (the Z/*anti* isomer) and that this isomer has a different first solvation shell compared to the E/*anti* isomer. This was investigated further for a large set of similar 3-halo-3-methyl-1-azaallyl anions, bearing different counterions and halogens, confirming the Z/*anti* isomer to be the most stable for all species studied. Such information is important in order to obtain insight into the stereochemistry of the reactant complexes. We also tested to what extent the current methodologies were applicable for studying the aldol reaction. First of all, it must be mentioned that the reproduction of selectivities is very difficult as the energy differences encountered are very small. For the studied reactions, serious problems were encountered. First of all, the system is very sensitive to the electronic structure method used as also dispersive interactions play an important role. The study of the sensitivity on the level of theory is beyond the scope of this work. Second, the enhanced *syn* selectivity for zincated complexes could not be reproduced.The reason for this might be that solvent effects are not thoroughly enough taken into account or the fact that lithium cations are present in solution. The study of these effects from first principles is beyond the limits of the current methodologies.

A second set of reactions were selected from the field of free radical polymerization. For these reactions, water was used as a solvent and the rate enhancement due to this particular liquid was investigated for the polymerization of several acrylamide based monomers. This study showed that the calculated reaction rate for acrylamide and N-methylacrylamide significantly increased when taking into account the effect of the solvent, either by adding assisting water molecules to the calculated transition states in the gas phase, either by including them in a dielectric continuum. The resulting rate coefficient were in much better agreement with the experimental values after accounting for the appropriate solvent models. This study shows that explicit solvent interactions may substantially stabilize transition states. This is a nice example of the importance of solvent effects on the free radical propagation of vinylic monomers. Also, the effect of solvent on the tacticity of methyl methacrylate was studied in cooperation with Prof. Aviyente from the Boğaziçi University of Istanbul showing that the preference to form syndiotactic polymer is indeed enhanced by using perfluoro-*tert*-butyl alcohol in stead of methanol. This effect was shown to be governed by hydrogen-bonding effects in the transition state.

The last application lies in the field of biochemical reactions and aims at helping to understand the degradation of asparagine (Asn) and glutamine (Gln) sidechains that are present in peptides and proteins. For this purpose, molecular dynamics simulations were performed on acetamide and N-methylacetamide as model components for both the sidechains and the peptide backbone. All theoretical studies up to now in this topic were not conclusive as they either were biased a fixed number of water molecules that were accounted in the static calculations or by constraints that were imposed during the molecular dynamics simulations. The simulations performed in this thesis are performed in such a way that they are completely unbiased an allow all possible coordinations of the surrounding water molecules both as solvent and as reactant molecules. For this problem, the metadynamics method was used that allows the acceleration of rare events (e.g. conformational transition, chemical reactions,. . .) the construction of the free energy surface on which several possible reaction pathways can be mapped. Preliminary results show that the amide hydrolysis occurs via a stepwise mechanism and that larger water bridge systems compared to the gas phase are required to model these reactions adequately.

In conclusion, the systems that have been studied in this thesis are all subject to solvent effects to a certain extent. Depending on the system, the problem, and the nature of the solvent, different solvent models have to be considered in order to select the most suited one. When very specific interactions are present, like the water bridges in the acrylamide polymerization, static calculations already reveal a large effect of taking into account a discrete number of solvent molecules. For more complex molecular environment effects more advanced techniques such as molecular dynamics simulations have te be used. Possible indications to decide on such advanced simulations, are various minima from static calculations that have different solvation effects, or when solvent molecules can either take the role as solvent or reactant. It is however important to mention that such molecular dynamics simulations need to be complemented with advanced techniques to simulate rare events. Any chemical reaction, unless very low activated as a rare event on the potential energy surface and does not occur spontaneously during a MD run. The metadynamics technique is a recent very promising technique to describe such effects.

With the recent expansion of computer speed and CPU time, the focus of molecular modeling research is shifting more and more to larger, more realistic systems. This is a very logical evolution as it is generally acknowledged that environment effects on molecular systems cannot be neglected. Therefore, including solvent environments (or any other possible surroundings) is crucial and a good model for them is absolutely necessary. All the molecular dynamics simulations in this thesis were performed with quantum mechanical methods because the system size was still small enough to do so. When looking at larger systems (like, for instance, peptides or proteins), another approach is indispensable. Therefore, a combination of quantum mechanics and molecular mechanics, QM/MM, offers a good alternative treating the chemically interesting system with high level calculations whilst describing the peripheral area with a classical model. This method has proven its use in a broad range of applications, but is still challenging when working with a liquid. As in principle all solvent molecules are able to coordinate with the species, they can interchange in such a way that a QM solvent molecule can diffuse out of the QM box. This problem requires an adaptive scheme that treats the solvent molecules around the active species QM and allows these molecules to be treated MM as they diffuse away from the reaction area. Several of these methods have been developed but only a few of them are readily available at the moment. Moreover, these classical methods require a large set of parameters that are not always available and that are not easy to determine as these models rely on a certain degree of cancellation of error. Another example of such difficulty is the treatment of a proton that can be shuttled through a large chain of water molecules. The shuttling pathway cannot be determined in advance but it is highly likely that a small QM box is not capable of modeling the optimal path whilst an MM model is generally not able to describe the bond breaking and bond forming processes accompanying this proton transfer.

Modeling solvent effects has given the scientific community a lot of insight in the way chemical reactions and equilibria occur in a solution. Even though molecular modeling is already capable of describing and explaining a lot of observed trends and effects, more detailed models are required in order to model larger, more realistic systems. As this research field is fully developing, a lot of new theoretical models may be expected in the near future which might be useful after intensive testing. In this thesis, all current available models were explored and it gives a insight into the current state-of-the-art. It must also be emphasized that within the time span of this thesis itself a substantial progress has been made to model the molecular environment.This work can be used for future modeling studies as a guide for determining the theoretical solvent model to be used based upon the type of solvent interaction.

Part II

Papers

Paper I

Theoretical Study on the Structural Properties of Various Solvated Metalated 3-Halo-1-azaallylic Anions

De Sterck B., Van Speybroeck V., Mangelinckx S.,
Verniest G., De Kimpe N., and Waroquier M.

J. Phys. Chem. A, **2009**, *113*, 6375-6380

J. Phys. Chem. A **2009,** *113,* 6375–6380 **6375**

Theoretical Study on the Structural Properties of Various Solvated Metalated 3-Halo-1-azaallylic Anions

Bart De Sterck,[†] Veronique Van Speybroeck,*[,†] Sven Mangelinckx,[‡,§] Guido Verniest,[‡] Norbert De Kimpe,[‡] and Michel Waroquier[†]

Center for Molecular Modeling, Ghent University, Proeftuinstraat 86, B-9000 Ghent, Belgium, and Department of Organic Chemistry, Faculty of Bioscience Engineering, Ghent University, Coupure links 653, B-9000 Ghent, Belgium

Received: December 22, 2008; Revised Manuscript Received: March 3, 2009

Metalated 3-halo-1-azaallylic anions are important building blocks for the preparation of a wide variety of heterocyclic and highly functionalized compounds. A theoretical description of the structural properties of halogenated 1-azaallylic anions in vacuo and in tetrahydrofuran (THF) solution is presented to gain insight into their reactivity behavior. The configurational flexibility of fluorinated and chlorinated 1-azaallylic anions is examined, and it is shown that these anions have far less configurational flexibility as compared with nonhalogenated analogues, with a strong preference to occur as *Z*/anti isomers. In addition, the driving force for transmetalation, that is, the replacement of the lithium cations with K$^+$, Cu$^+$, ZnCl$^+$, CuCl$^+$, or MgBr$^+$ is studied. To obtain reliable results, the structures were modeled in THF using the combined implicit/explicit solvent approach resulting in different coordination numbers for lithium in the *Z*/anti and *E*/anti isomers. Calculations on dimerization energies show that coordination with THF is energetically preferred over aggregation.

Introduction

α-Heteroatom-substituted carbanions stabilized by an electron-withdrawing group (acyl, alkoxycarbonyl, sulfonyl, sulfinyl, cyano, carbamoyl) have been used intensively as synthetic building blocks for the synthesis of various organic compounds, including a wide variety of azaheterocyclic compounds.[1] However, one combination appears to be unsuccessful when a halogen and an acyl group are combined. This is due to the instability and nonselective reactivity of β-haloenolates **2**. (See Figure 1.)[2,3] A convenient way to overcome these problems is the conversion of α-haloketones **1** toward the corresponding less-reactive α-haloimines **4**. After deprotonation of the latter, the corresponding 1-azaallylic anions **5** can be easily used in different organic transformations.[2−5] In that respect, mainly α-chlorinated imines have been used as precursors for interesting acyclic, carbocyclic, and heterocyclic compounds.[6−16] Whereas the corresponding brominated and iodinated imines are generally more difficult to handle because of their instability,[2,3,9,17] 1-azaallylic anions derived from α-fluorinated imines have been used to study the regioselective deprotonation and stereoselective alkylation[8,18] and have recently proved to be useful building blocks for interesting fluorinated heterocycles.[19] Unfortunately, very little is known about the stereochemistry of chlorinated and fluorinated 1-azaallylic anions, which makes it difficult to understand their behavior in stereoselective reactions such as aldol condensations. A thorough investigation and comparison of these fluorinated and chlorinated species will lead to new insight into this matter.

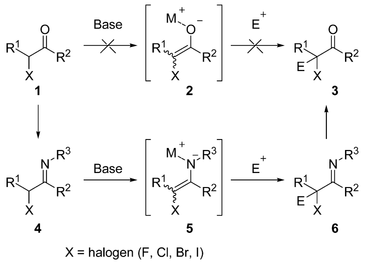

Figure 1. Conversion of α-haloketones **1** to α-haloimines **4** and further to functionalized imines **6** and ketones **3**.

In our previous communication, the *E*-to-*Z* isomerization of lithiated 3-chloro-1-azaallylic anions **7** and **9** (Table 1) in tetrahydrofuran (THF) solution was investigated using quantum mechanical molecular dynamics (QM-MD) and a metadynamics simulation in a periodic box containing 61 THF molecules combined with ROESY-NMR experiments.[20] It was shown that the *Z* isomer **7** is the most stable isomer and that the *Z*-to-*E* isomerization is a highly activated transition that is very unlikely to occur. This was confirmed by NMR experiments demonstrating that only the *Z* isomer **7** is present in solution. Until then, theoretical calculations on chlorinated 1-azaallylic anions had only been performed on heterocyclic lithium azaenolates of chiral oxazolines.[21] The *E* isomer, where the nitrogen, chlorine, and lithium are at the same side of the C=C bond, is therein found to be the most stable isomer. The present study describes an in-depth investigation of the effect of the halogen atom and the metal counterion on the stereochemistry and solvation of a broad range of 1-azaallylic anions. We investigated the influence of the metal counterion by comparing various relevant ions such as Li$^+$, K$^+$, Cu$^+$, CuCl$^+$, ZnCl$^+$, and MgBr$^+$. An overview of all studied structures is given in Table 1.

---

[*] Corresponding author. E-mail: Veronique.Vanspeybroeck@UGent.be.

[†] Center for Molecular Modeling, Ghent University.

[‡] Department of Organic Chemistry, Faculty of Bioscience Engineering, Ghent University.

[§] Postdoctoral Fellow of the Research Foundation-Flanders (FWO).

10.1021/jp811317y CCC: $40.75

TABLE 1: Overview of the Investigated 3-Halo-1-azaallylic Structures and Their Metal Counter Ions

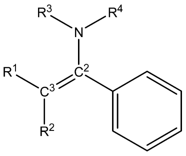

structure	R^1	R^2	R^3	R^4	structure	R^1	R^2	R^3	R^4
7	Cl	Me	Li^+	^iPr	**21**	Me	F	$ZnCl^+$	^iPr
8	Cl	Me	^iPr	Li^+	**22**	Me	F	^iPr	$ZnCl^+$
9	Me	Cl	Li^+	^iPr	**23**	Cl	F	Li^+	^iPr
10	Me	Cl	^iPr	Li^+	**24**	F	Cl	Li^+	^iPr
11	F	Me	Li^+	^iPr	**25**	Cl	F	$ZnCl^+$	^iPr
12	F	Me	^iPr	Li^+	**26**	F	Cl	$ZnCl^+$	^iPr
13	Me	F	Li^+	^iPr	**27**	Cl	F	K^+	^iPr
14	Me	F	^iPr	Li^+	**28**	F	Cl	K^+	^iPr
15	Cl	Me	$ZnCl^+$	^iPr	**29**	Cl	F	Cu^+	^iPr
16	Cl	Me	^iPr	$ZnCl^+$	**30**	F	Cl	Cu^+	^iPr
17	Me	Cl	$ZnCl^+$	^iPr	**31**	Cl	F	$CuCl^+$	^iPr
18	Me	Cl	^iPr	$ZnCl^+$	**32**	F	Cl	$CuCl^+$	^iPr
19	F	Me	$ZnCl^+$	^iPr	**33**	Cl	F	$MgBr^+$	^iPr
20	F	Me	^iPr	$ZnCl^+$	**34**	F	Cl	$MgBr^+$	^iPr

Little is known about the reactive oligomers of 3-halo-1-azaallylic anions and the mechanisms involved in reactions with electrophiles such as aldehydes. Oligomerization of both lithium enolates[22−26] and nonhalogenated lithium azaenolates[27−29] has been the subject of a large amount of experimental and computational research. However, monomers are found to be the most reactive species in a number of experimental studies.[25,30] By analogy to these experimental findings, mainly monomeric halogenated 1-azaallylic anions will be studied. According to a series of NMR spectra and colligative measurements in THF, both monomeric and dimeric species of 1-azaallylic anions will occur at low concentrations.[31−33] Theoretical calculations are able to provide additional insight into dimerization. Therefore, the possible aggregation into dimeric species is investigated for the lithiated 3-chloro-1-azaallylic anion **7**. It should be noted that it is critical to take the solvent into account properly for all calculations. The influence of solvation with THF will be evaluated because this solvent is most frequently used in reactions with 1-azaallylic anions and because it coordinates with the studied species. The solvent will be treated explicitly via DFT calculations on solvated clusters and implicitly by CPCM calculations.[34]

Computational Details. All computations are performed using the Gaussian03[35] package. The hybrid mPW1PW91[36,37] functional is used as an electronic structure method that is suited for the description of fluoro- and chloroalkyllithium compounds in the gas phase and in ethereal solvents.[22] The double-ζ 6-31$^+$G(d) basis set is used comprising both diffuse and polarization functions for a good description of the oxygen atoms and the ionic character of the species.[34,38] We computed and verified stationary points as well as first-order saddle points by calculating the normal modes. The obtained energies are corrected for the zero-point vibrational energies. The effect of solvation is modeled as the sum of two contributions: one resulting from the coordination of one or more solvent molecules to the solute X (coordination solvation free energy, CSE) and one originating from the bulk solvent effect (dielectric solvation free energy, DSE).[34,39−41] Combination of both contributions allows us to calculate the coordination free energy in solution, ΔG_{sol}, as depicted in Figure 2.

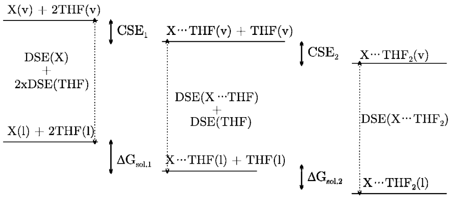

Figure 2. Thermodynamic cycle in two steps for the determination of coordination free energy of species X in solution, ΔG_{sol}, being defined as the driving force for coordination with a THF molecule in solution. The vapor (v) and liquid (l) phase are indicated.

The coordination number of the metal site is determined by requiring a decrease in Gibbs free energy of solvation upon the addition of an explicit solvent molecule.[40] Subsequently, the solvated cluster is embedded in a conductorlike polarizable continuum model (CPCM), and single-point calculations are performed to compute the DSE.[42] The parameter set used for the determination of the cavity in which the system is embedded is crucial for obtaining reliable energies. The standard UA0 method that is implemented in Gaussian03 does not perform properly for ionic species. Therefore, the model based on Pauling radii is used.[43]

Results and Discussion

Configurational Analysis. Because of the importance of lithiated (aza)enolates in organic synthesis,[44−47] 3-fluoro- and 3-chloro-1-azaallylic anions coordinated to lithium are considered at first instance in the present study. For these monohalogenated species **7**−**14**, four isomers can be suggested a priori (Figure 3), each of them characterized by the stereochemistry about the C═C bond (*E* or *Z*) and the position of the *N*-isopropyl group (syn or anti).[27]

The energy scheme in Figure 3 shows that both fluorinated and chlorinated species exhibit a stable global minimum in which the lithium cation and the halogen atom intensely interact. The isomerization process is characterized by two types of internal rotations: amide rotations for syn/anti isomerization (**TS1** and **TS3**) and carbon−carbon double-bond rotations or *E*/*Z* isomerizations (**TS2**). The stable minima for the fluorinated species **11**−**14** are shown in Figure 4, whereas the other structures are shown in the Supporting Information. A remarkable aspect of the energetic minimum is the position of the phenyl group. One would expect this group to be positioned coplanar with the carbon−carbon double bond (the dihedral angle between the C−C double bond and the phenyl ring being equal to zero) to obtain more electron delocalization. The structure, however, does not allow this kind of conformation because of steric hindrance of the phenyl group with the methyl and isopropyl group on the adjacent carbon and nitrogen atoms, respectively, resulting in a dihedral angle of 71° for structure **11.**

Amide C−N bond rotation has been investigated in a number of papers, and a rotational barrier in the range of about 6−100 kJ/mol was found, depending on the nature of the amide.[48−54] The values found here fall within that experimental range. The activation energy for the rotation via **TS1** is quite high, which can be ascribed to the lithium−halogen interaction. The *Z*/syn-to-*E*/syn isomerization in 3-halo-1-azaallylic anions via **TS2** requires a huge amount of energy, whereas in nonhalogenated 1-azaallylic anions, this isomerization is known to occur quite easily.[27,55]

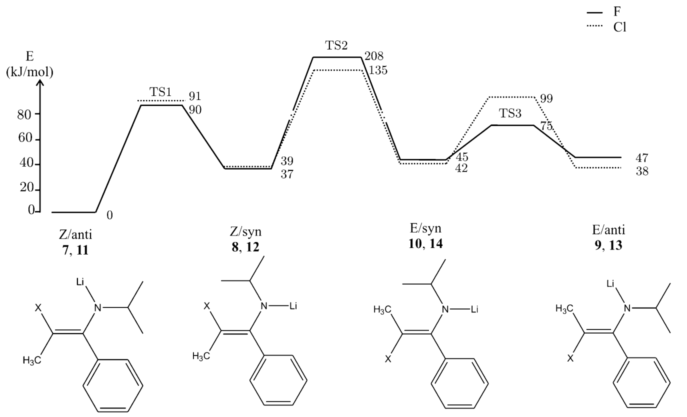

Figure 3. Energy profile for the conformational analysis of chlorinated species **7**−**10** (X = Cl) and fluorinated species **11**−**14** (X = F). The transition-state structures **TS1**−**TS3** for both halogen substituents can be found in the Supporting Information.

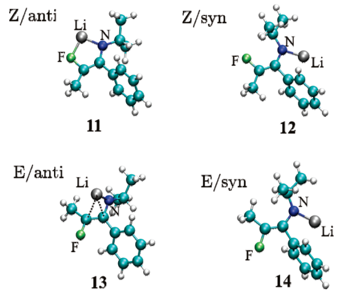

Figure 4. Optimized geometries for lithiated 3-fluoro-1-azaallylic species **11**−**14**.

Because of the strong interaction between fluorine or chlorine and lithium, no barrier could be found in vacuo for the rotation from *Z*/anti to *E*/anti. The latter structure exists as two energetically equivalent enantiomeric structures in which the lithium cation is pyramidally η^3 coordinated (species **13** in Figure 4). This type of coordination was already reported in previous studies of 1-azaallylic anions[21,27] and is a result of the repulsive interaction between Li^+ and the methyl group directing the metal out of plane toward the π cloud of the carbon−carbon double bond.

Solvation in Tetrahydrofuran. The previous results were all obtained in the gas phase, although the investigated species are known to be stabilized by the solvent. We will determine the coordination number of the lithium cation by solvating the 3-halo-1-azaallylic anions using the combined implicit/explicit solvent approach. The free energy decrease in solvation is the result of a coordination free energy (CSE) and a dielectric free energy (DSE). The global free energy of solvation, ΔG_{sol}, can be calculated from the scheme in Figure 2, and the numerical values are shown in Table 2. We will focus on the *Z*/anti isomers in solution because these were found to be the most stable isomers, as shown by the calculations described above, and because the stereochemistry about the C−C double bond is important for the stereochemical outcome of reactions, the *E*/anti isomers will also be considered. Next to lithium, zinc chloride will also be considered because this counterion has a different sterical nature, bearing the chlorine ligand.

The lithiated 3-halo-1-azaallylic anions **7**, **9**, **11**, and **13** always coordinate with at least one THF molecule because of the favorable lithium−oxygen interaction. The coordination with a second THF molecule is generally less favored. Intuitively, the solvation of the *E* isomers **9** and **13** by a second THF molecule should be more favorable compared with the *Z* isomers **7** and **11** because the former isomers lack a halogen−lithium interaction. This is indeed the case. One must notice however, that some values for the second solvation are very close to zero and are probably smaller than the error for these single-point CPCM calculations. The solvated structure of the *E* and *Z* isomers of the 3-chloro-1-azaallylic anions obtained via the explicit/implicit solvent approach is the same as the structure we obtained from ab initio molecular dynamics simulations.[20] For all of the discussed structures, the preferable coordination of the counterion is highlighted in Table 2. For lithium-coordinated species, monosolvated structures are found. The slightly negative $\Delta G_{\mathrm{sol},2}$ for *E*/anti isomers shows a very modest tendency to coordinate with two THF molecules. This finding corresponds with the previously reported molecular dynamics results.[20]

Because $ZnCl^+$ has different characteristics compared with Li^+, the solvation properties of zincated 3-halo-1-azaallylic anions **15**, **17**, **19**, and **21** are also quite different. The chlorine in the $ZnCl^+$ counterion accounts for an important sterical effect. No THF molecule can coordinate with the *Z* isomers **15** and **19**. However, the *E* isomers **17** and **21** do form a solvated complex because of the absence of halogen−zinc interactions. In summary, we find that the zinc counterion in the *Z*/anti isomer does not coordinate with a THF molecule because of steric constraints, whereas the coordination number of zinc in the *E*/anti isomer is one.

The monosolvated structures are shown in Figure 5. The structures differ very little from the ones calculated in vacuo, but the energy difference between the *E* and *Z* isomers is significantly influenced. In Table 3, the energetic preference for the *Z* isomers (ΔG_Z) of the studied species is tabulated as the difference in energy of the *Z* isomer and the *E* isomer. In all cases, the *Z* isomer is the

TABLE 2: Coordination Solvation Energy and Solvation Free Energy for Mono- and Bisolvated Structures Using the Implicit/Explicit Solvation Model for the Anti Configuration of Lithiated and Zincated Complexes[a]

		Lithium					Zinc				
halogen	isomer	nr	CSE_1	$\Delta G_{sol,1}$	CSE_2	$\Delta G_{sol,2}$	nr	CSE_1	$\Delta G_{sol,1}$	CSE_2	$\Delta G_{sol,2}$
F	Z/*anti*	**11**	-75.1	-3.5	-39.7	-0.2	**19**	-49.5	8.1	-13.1	16.4
	E/*anti*	**13**	-83.2	-9.2	-45.7	-2.3	**21**	-56.5	-17.5	-23.8	12.7
Cl	Z/*anti*	**7**	-75.1	-14.7	-37.7	12.7	**15**	-47.8	2.7	9.5	48.8
	E/*anti*	**9**	-83.3	-10.0	-40.8	-0.5	**17**	-58.4	-20.1	-19.9	10.12

[a] All values are in kilojoules per mole. Preferred interactions are highlighted in grey, showing the coordination number of the studied species.

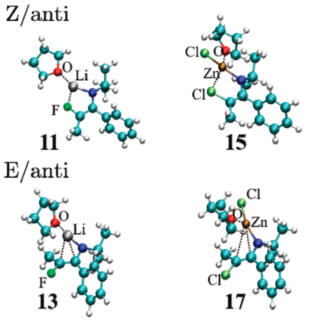

Figure 5. Monosolvated geometries of lithiated 3-fluoro-1-azaallylic anions **11** and **13** and zincated 3-chloro-1-azaallylic anions **15** and **17**.

TABLE 3: Z Preference Energy, ΔG_Z (kJ/mol), for the Anti Isomers of 3-Halo-1-azaallylic Anions in Vacuo and in the Implicit/Explicit Solvent Model for THF

Z vs *E* isomer	halogen	counterion	in vacuo ΔG_Z	in solvent ΔG_Z
7 vs **9**	Cl	Li^+	−38.02	−41.19
15 vs **17**	Cl	$ZnCl^+$	−41.47	−31.99
11 vs **13**	F	Li^+	−46.99	−27.72
19 vs **21**	F	$ZnCl^+$	−27.41	−18.83

most stable one. This is the result of the repulsive interaction between the halogen and the π cloud of the phenyl substituent in the *E* isomers (**9**, **13**, **17**, **21**) and the attractive interaction between the metal cation and the halogen atom in the *Z* isomers (**7**, **11**, **15**, **19**). Table 3 also shows that ΔG_Z is dependent on both the halogen and the counterion.

Transmetalation. In general, 3-halo-1-azaallylic anions **5** are mostly synthesized using lithium diisopropylamide (LDA) as a base for the deprotonation of the starting imines **4**. However, to influence the structural, coordination, and reactivity properties of 1-azaallylic anions[56−58] and to increase the stereoselectivity in organic reactions with these species and related enolates, such as additions across aldehydes[59−64] or imines,[65,66] it can be of considerable benefit to introduce another metal counterion to the anion (as shown above for the zincated 3-chloro-1-azaallylic anion).[58,65,66] The addition of a salt of the desired counterion to the lithiated anions will result in the transmetalation of the starting 3-halo-1-azaallylic anions. In this part, the driving force for the transmetalation reaction will be discussed. A selection of relevant metals was made consisting of K^+, Cu^+, $CuCl^+$, $MgBr^+$, and $ZnCl^+$.

TABLE 4: Metalation Energy ($E_{met} = E_{complex} - E_{metalcation} - E_{anion}$) in the Vapor Phase and the Preference to Interact with Fluorine in Liquid THF for Various Metals[a]

			in vacuo			in solvent
counterion	*Z* isomer	*E* isomer	E^{Cl}_{met}	E^{F}_{met}	ΔE^{vac}_{met}	ΔG^{sol}_{met}
Li^+	**23**	**24**	−649.3	−659.6	−10.3	−13.2
$ZnCl^+$	**25**	**26**	−963.3	−960.7	2.7	2.0
K^+	**27**	**28**	−458.7	−466.1	−7.5	−10.8
Cu^+	**29**	**30**	−780.6	−766.5	14.1	−0.9
$CuCl^+$	**31**	**32**	−1018.5	−1015.3	3.1	1.2
$MgBr^+$	**33**	**34**	−890.9	−900.9	−10.1	−13.0

[a] Preference for the metal to interact with fluorine is given in vacuo (energetic difference, $\Delta E^{vac}_{met} = E^{F}_{met} - E^{Cl}_{met}$) and in the implicit/explicit solvent model (Gibbs free energy difference, ΔG^{sol}_{met}). All values are in kilojoules per mole, and all structures were optimized to obtain the presented energies.

To assess both the chlorine−metal and the fluorine−metal interactions, the 3-chloro-3-fluoro-1-azaallylic anions **23**−**34** are studied. Moreover, these species are synthetically interesting because it has been shown that 3,3-dihalogenated-1-azaallylic anions can be used for the synthesis of a variety of dihalogenated heterocycles such as piperidines[19] and azetidines;[2,67−69] therefore, 3-chloro-3-fluoro-1-azaallylic anions can also be useful as versatile building blocks. For this kind of applications, like in the previous section, the stereoselectivity of the reactions will be determined by the stereochemistry about the C−C double bond. For every metal complex, the metalation energy E_{met} (Table 4) can be determined resulting from metal−chlorine complexation in the *Z*/anti isomers (E^{Cl}_{met}) and metal−fluorine complexation in the *E*/anti isomers (E^{F}_{met}). This number quantifies the difference in the interaction strength of the metal with fluorine and chlorine.

Transmetalation of lithiated 1-azaallylic anions to their zincated analogues by the addition of $ZnCl_2$ is known to occur easily.[44−47] The conversion of lithiated 1-azaallylic anions to their Cu^+(I) analogues using CuI[70] or CuCN[71] is also reported in the literature. The increase in the absolute value of the metalation energy is the driving force for this metal exchange reaction. Indeed, $ZnCl^+$ and Cu^+ interact stronger than Li^+ with the 3-halo-1-azaallylic anion.

The coordination energy difference in vacuo between the *E* and *Z* isomers is expressed as $\Delta E^{vac}_{met} = E^{F}_{met} - E^{Cl}_{met}$ and expresses the relative preference of the metal to interact with fluorine. (See Table 4.) The free energy difference in vacuo in combination with the CPCM energies results in the total free energy difference in solution between the *E* and *Z* isomers, ΔG^{sol}_{met}. If the values of ΔE^{vac}_{met} and ΔG^{sol}_{met} are negative, then the metal will coordinate more strongly with fluorine than with chlorine. Group I and II metals (Li^+, K^+, and $MgBr^+$) tend to interact more strongly with

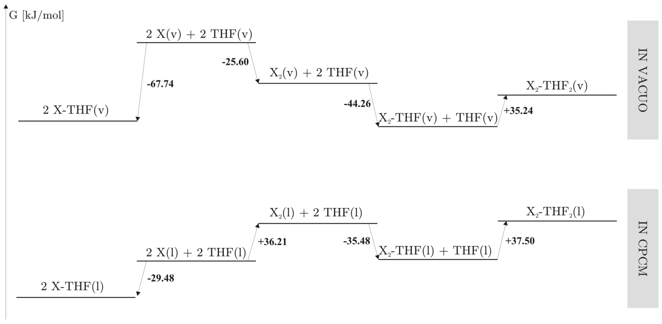

Figure 6. Thermodynamic cycle for the determination of the Gibbs free energy difference between the dimer of the lithiated 3-chloro-3-methyl-1-azaallylic anion **7** (X_2) and the solvated species (X-THF) using the implicit/explicit solvent model. All energy values are in kilojoules per mole.

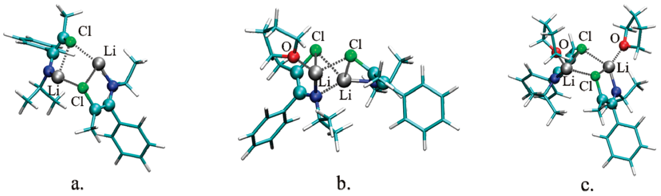

a. b. c.

Figure 7. Optimized structures for (a) the dimer, (b) the monosolvated dimer, and (c) the bisolvated dimer of species **7**.

fluorine, resulting in a modest *E* preference up to 13.2 kJ/mol. The studied transition metals prefer to interact with the chlorine, but there is only a small difference with fluorine. All of the metals studied, except Cu^+(I), need just one THF molecule to be fully solvated. The numerical values for the CSE and DSE can be found in the Supporting Information. In most cases, solvation alters the difference in metalation energy only slightly. In the case of monovalent Cu^+(I) cations, a large solvent effect due to the implicit solvent model is observed.

Aggregation. The aggregation of (lithium) enolates has been the subject of various papers revealing that the formation of oligomers is of considerable importance.[22,24,27] Other studies indicate that, although the formation of di-, tri-, or tetramers occurs, the monomers are the reactive species.[25,30] To assess the importance of aggregation relative to solvation, we performed calculations on the dimer (X_2) of the lithiated 3-chloro-3-methyl-1-azaallylic anion **7**. In Figure 6, the Gibbs free energy profile for solvation and dimerization is shown using an implicit/explicit solvent model analogous to the method described in the previous section. The dimeric structure with and without solvation is shown in Figure 7. In the vapor phase, the solvated monomer (X-THF(v)) and the solvated dimer (X_2-THF(v), Figure 6) are almost isoenergetic, indicating an equilibrium between both structures. When including long-range solvent effects using the CPCM model, the energetic scheme is totally altered, making only the monosolvated monomers (X-THF(l)) feasible in solution. These results might seem to contradict the broad range of published papers in which oligomerization of the analogous enolates readily occurs. However, it can be reasonably understood why the 3-halo-1-azaallylic anions are less prone to aggregation in solution.

In contrast with previously reported studies of nonhalogenated enolates, the presence of the α-halogen substituent in the studied azaenolates enables an intramolecular, stabilizing interaction between the lithium cation and the halogen. This interaction leads to a higher degree of coordinative saturation of the metal[72] and reduces the driving force for aggregation or solvation compared with non-α-halogenated enolates.[25] The results in Figure 6 also show that the interaction energy between lithium and the THF oxygen atom is higher as compared with the dimerization energy, resulting in a preference for solvation rather than dimerization. These calculations indicate that monomeric species will be predominantly present in a THF solution and are therefore worthwhile to investigate.

Conclusions

The theoretical calculations show that the preferred configuration of metalated 3-halo-1-azaallylic anions comprises the anti orientation of the *N*-alkyl substituent with regard to the carbon−carbon double bond and the *Z* configuration, where the nitrogen and halogen are positioned at the same side of the carbon−carbon double bond. These results are valid for both fluorinated and chlorinated 1-azaallylic anions and for a broad range of metal cations. A strong interaction was found between the solvent and the metal center, suggesting a considerable role in the reactivity of 1-azaallylic anions toward electrophiles because the solvent influences the steric environment of the reactive centers. Therefore, the embedding of a solvated cluster in a continuum model is necessary for obtaining a more accurate description of the solvent surroundings and more reliable energies in solution. In addition, it is shown that 3-chloro-3-methyl-1-azaallylic anions interact more strongly with THF than with themselves, indicating that mainly monomeric species are present in solutions. The driving force for transmetalation was assessed for a range of different metal cations. Depending on the application, different metal cations can be selected to perform stereoselective organic reactions with the studied 3-halo-1-azaallylic anions.

Acknowledgment. This work is supported by the Fund for Scientific Research-Flanders (FWO-Vlaanderen) and the Research Board of Ghent University (BOF).

Supporting Information Available: Optimized geometries in *xyz* coordinates and absolute energies of all species. This material is available free of charge via the Internet at http://pubs.acs.org.

References and Notes

(1) Krief, A. *Tetrahedron* **1980**, *36*, 2531–2640.

(2) Giubellina, N.; Aelterman, W.; De Kimpe, N. *Pure Appl. Chem.* **2003**, *75*, 1433–1442.

(3) Mangelinckx, S.; Giubellina, N.; De Kimpe, N. *Chem. Rev.* **2004**, *104*, 2353–2399.

(4) Job, A.; Janeck, C. F.; Bettray, W.; Peters, R.; Enders, D. *Tetrahedron* **2002**, *58*, 2253–2329.

(5) Knorr, R.; Low, P. *J. Am. Chem. Soc.* **1980**, *102*, 3241–3242.

(6) Stork, G.; Dowd, S. R. *J. Am. Chem. Soc.* **1963**, *85*, 2178–2180.

(7) Fraser, R. R.; Banville, J.; Dhawan, K. L. *J. Am. Chem. Soc.* **1978**, *100*, 7999–8001.

(8) Welch, J. T.; Seper, K. W. *J. Org. Chem.* **1988**, *53*, 2991–2999.

(9) De Kimpe, N.; Sulmon, P.; Schamp, N. *Angew. Chem.* **1985**, *97*, 878–879.

(10) De Kimpe, N.; Coppens, W.; Welch, J. T.; De Corte, B. *Synthesis* **1990**, 675–677.

(11) Sulmon, P.; De Kimpe, N.; Schamp, N. *Synthesis* **1989**, 8–12.

(12) Giubellina, N.; De Kimpe, N. *Synlett* **2005**, 976–980.

(13) Giubellina, N.; Mangelinckx, S.; Tornroos, K. W.; De Kimpe, N. *J. Org. Chem.* **2006**, *71*, 5881–5887.

(14) Aelterman, W.; De Kimpe, N.; Tyvorskii, V.; Kulinkovich, O. *J. Org. Chem.* **2001**, *66*, 53–58.

(15) Aelterman, W.; De Kimpe, N.; Declercq, J. P. *J. Org. Chem.* **1998**, *63*, 6–11.

(16) Van Hende, E.; Verniest, G.; Surmont, R.; De Kimpe, N. *Org. Lett.* **2007**, *9*, 2935–2938.

(17) Aelterman, W.; De Kimpe, N.; Kulinkovich, O. *Bull. Soc. Chim. Belg.* **1997**, *106*, 703–708.

(18) Welch, J. T.; Seper, K. W. *J. Org. Chem.* **1986**, *51*, 119–120.

(19) Verniest, G.; Surmont, R.; Van Hende, E.; Deweweire, A.; Deroose, F.; Thuring, J. W.; De Kimpe, N. *J. Org. Chem.* **2008**, *73*, 5458–5461.

(20) Declerck, R.; De Sterck, B.; Verstraelen, T.; Verniest, G.; Mangelinckx, S.; Jacobs, J.; De Kimpe, N.; Waroquier, M.; Van Speybroeck, V. *Chem.—Eur. J.* **2009**, *15*, 580–584.

(21) Florio, S.; Capriati, V.; Luisi, R.; Abbotto, A.; Pippel, D. J. *Tetrahedron* **2001**, *57*, 6775–6786.

(22) Pratt, L. M.; Ramachandran, B.; Xidos, J.; Cramer, C. J.; Truhlar, D. G. *J. Org. Chem.* **2002**, *67*, 7607–7612.

(23) Pratt, L. M.; Truhlar, D. G.; Cramer, C. J.; Kass, S. R.; Thompson, J. D.; Xidos, J. D. *J. Org. Chem.* **2007**, *72*, 2962–2966.

(24) Abbotto, A.; Streitwieser, A.; Schleyer, P. V. *J. Am. Chem. Soc.* **1997**, *119*, 11255–11268.

(25) Streitwieser, A. *J. Mol. Model.* **2006**, *12*, 673–680.

(26) Liou, L. R.; McNeil, A. J.; Ramirez, A.; Toombes, G. E. S.; Gruver, J. M.; Collum, D. B. *J. Am. Chem. Soc.* **2008**, *130*, 4859–4868.

(27) Glaser, R.; Streitwieser, A. *J. Org. Chem.* **1991**, *56*, 6612–6624.

(28) Liao, S. P.; Collum, D. B. *J. Am. Chem. Soc.* **2003**, *125*, 15114–15127.

(29) Zuend, S. J.; Ramirez, A.; Lobkovsky, E.; Collum, D. B. *J. Am. Chem. Soc.* **2006**, *128*, 5939–5948.

(30) Abbotto, A.; Leung, S. S. W.; Streitwieser, A.; Kilway, K. V. *J. Am. Chem. Soc.* **1998**, *120*, 10807–10813.

(31) Wanat, R. A.; Collum, D. B.; Vanduyne, G.; Clardy, J.; Depue, R. T. *J. Am. Chem. Soc.* **1986**, *108*, 3415–3422.

(32) Kallman, N.; Collum, D. B. *J. Am. Chem. Soc.* **1987**, *109*, 7466–7472.

(33) Jackman, L. M.; Scarmoutzos, L. M.; Smith, B. D.; Williard, P. G. *J. Am. Chem. Soc.* **1988**, *110*, 6058–6063.

(34) Van Speybroeck, V.; Moonen, K.; Hemelsoet, K.; Stevens, C. V.; Waroquier, M. *J. Am. Chem. Soc.* **2006**, *128*, 8468–8478.

(35) Frisch, M. J.; Trucks, G. W.; Schlegel, H. B.; Scuseria, G. E.; Robb, M. A.; Cheeseman, J. R.; Montgomery, J. A., Jr.; Vreven, T.; Kudin, K. N.; Burant, J. C.; Millam, J. M.; Iyengar, S. S.; Tomasi, J.; Barone, V.; Mennucci, B.; Cossi, M.; Scalmani, G.; Rega, N.; Petersson, G. A.; Nakatsuji, H.; Hada, M.; Ehara, M.; Toyota, K.; Fukuda, R.; Hasegawa, J.; Ishida, M.; Nakajima, T.; Honda, Y.; Kitao, O.; Nakai, H.; Klene, M.; Li, X.; Knox, J. E.; Hratchian, H. P.; Cross, J. B.; Bakken, V.; Adamo, C.; Jaramillo, J.; Gomperts, R.; Stratmann, R. E.; Yazyev, O.; Austin, A. J.; Cammi, R.; Pomelli, C.; Ochterski, J. W.; Ayala, P. Y.; Morokuma, K.; Voth, G. A.; Salvador, P.; Dannenberg, J. J.; Zakrzewski, V. G.; Dapprich, S.; Daniels, A. D.; Strain, M. C.; Farkas, O.; Malick, D. K.; Rabuck, A. D.; Raghavachari, K.; Foresman, J. B.; Ortiz, J. V.; Cui, Q.; Baboul, A. G.; Clifford, S.; Cioslowski, J.; Stefanov, B. B.; Liu, G.; Liashenko, A.; Piskorz, P.; Komaromi, I.; Martin, R. L.; Fox, D. J.; Keith, T.; Al-Laham, M. A.; Peng, C. Y.; Nanayakkara, A.; Challacombe, M.; Gill, P. M. W.; Johnson, B.; Chen, W.; Wong, M. W.; Gonzalez, C.; Pople, J. A. *Gaussian 03*, revision C.02; Gaussian, Inc.: Wallingford, CT, 2004.

(36) Adamo, C.; Barone, V. *J. Chem. Phys.* **1998**, *108*, 664–675.

(37) Schultz, N. E.; Zhao, Y.; Truhlar, D. G. *J. Phys. Chem. A* **2005**, *109*, 11127–11143.

(38) Lynch, B. J.; Zhao, Y.; Truhlar, D. G. *J. Phys. Chem. A* **2003**, *107*, 1384–1388.

(39) D’hooghe, M.; Van Speybroeck, V.; Waroquier, M.; De Kimpe, N. *Chem. Commun.* **2006**, 1554–1556.

(40) Pliego, J. R.; Riveros, J. M. *J. Phys. Chem. A* **2001**, *105*, 7241–7247.

(41) Pratt, L. M.; Streitwieser, A. *J. Org. Chem.* **2003**, *68*, 2830–2838.

(42) Manukyan, A. K.; Radkiewicz-Poutsma, J. L. *THEOCHEM* **2006**, *766*, 105–112.

(43) Takano, Y.; Houk, K. N. *J. Chem. Theory Comput.* **2005**, *1*, 70–77.

(44) Fujisawa, T.; Hayakawa, R.; Shimizu, M. *Tetrahedron Lett.* **1992**, *33*, 7903–7906.

(45) Barluenga, J.; Pozo Losada, C. d.; Olano, B. *Tetrahedron Lett.* **1993**, *34*, 5497–5498.

(46) Nakamura, M.; Hatakeyama, T.; Hara, K.; Nakamura, E. *J. Am. Chem. Soc.* **2003**, *125*, 6362–6363.

(47) House, H. O.; Crumrine, D. S.; Teranishi, A. Y.; Olmstead, H. D. *J. Am. Chem. Soc.* **1973**, *95*, 3310–3324.

(48) Mo, Y. R.; Schleyer, P. V.; Wu, W.; Lin, M. H.; Zhang, Q.; Gao, J. L. *J. Phys. Chem. A* **2003**, *107*, 10011–10018.

(49) Ataka, S.; Takeuchi, H.; Tasumi, M. *J. Mol. Struct.* **1984**, *113*, 147–160.

(50) Radzicka, A.; Pedersen, L.; Wolfenden, R. *Biochemistry* **1988**, *27*, 4538–4541.

(51) Taha, A. N.; Crawford, S. M. N.; True, N. S. *J. Am. Chem. Soc.* **1998**, *120*, 1934–1935.

(52) Kang, Y. K.; Park, H. S. *THEOCHEM* **2004**, *676*, 171–176.

(53) Wiberg, K. B.; Rablen, P. R.; Rush, D. J.; Keith, T. A. *J. Am. Chem. Soc.* **1995**, *117*, 4261–4270.

(54) Claeys, D. D.; Moonen, K.; Roman, B. I.; Nemykin, V. N.; Zhdankin, V. V.; Waroquier, M.; Van Speybroeck, V.; Stevens, C. V. *J. Org. Chem.* **2008**, *73*, 7921–7927.

(55) Lee, J. Y.; Lynch, T. J.; Mao, D. T.; Bergbreiter, D. E.; Newcomb, M. *J. Am. Chem. Soc.* **1981**, *103*, 6215–6217.

(56) Lalonde, J. J.; Bergbreiter, D. E.; Newcomb, M. *J. Org. Chem.* **1986**, *51*, 1369–1372.

(57) Avent, A. G.; Hitchcock, P. B.; Lappert, M. F.; Sablong, R.; Severn, J. R. *Organometallics* **2004**, *23*, 2591–2600.

(58) Ruano, J. L. G.; Lorente, A.; Ramos, J. H. R. *Tetrahedron: Asymmetry* **1998**, *9*, 2437–2450.

(59) Capriati, V.; Florio, S.; Luisi, R. *Eur. J. Org. Chem.* **2001**, 2035–2039.

(60) Heathcock, C. H.; Buse, C. T.; Kleschick, W. A.; Pirrung, M. C.; Sohn, J. E.; Lampe, J. *J. Org. Chem.* **1980**, *45*, 1066–1081.

(61) Heathcock, C. H.; Davidsen, S. K.; Hug, K. T.; Flippin, L. A. *J. Org. Chem.* **1986**, *51*, 3027–3037.

(62) Evans, D. A.; McGee, L. R. *Tetrahedron Lett.* **1980**, *21*, 3975–3978.

(63) Wei, H. X.; Jasoni, R. L.; Shao, H. W.; Hua, J. L.; Pare, P. W. *Tetrahedron* **2004**, *60*, 11829–11835.

(64) Aoki, Y.; Oshima, K.; Utimoto, K. *Synlett* **1995**, 1071–1072.

(65) Zhao, C. H.; Liu, L.; Wang, D.; Chen, Y. J. *Eur. J. Org. Chem.* **2006**, 2977–2986.

(66) Hou, X. L.; Luo, Y. M.; Yuan, K.; Dai, L. X. *J. Chem. Soc., Perkin Trans. 1* **2002**, 1487–1490.

(67) Aelterman, W.; De Kimpe, N.; Declercq, J. P. *J. Org. Chem.* **1998**, *63*, 6–11.

(68) Dejaegher, Y.; Mangelinckx, S.; De Kimpe, N. *J. Org. Chem.* **2002**, *67*, 2075–2081.

(69) Mangelinckx, S.; Van Speybroeck, V.; Vansteenkiste, P.; Waroquier, M.; De Kimpe, N. *J. Org. Chem.* **2008**, *73*, 5481–5488.

(70) Hitchcock, P. B.; Lappert, M. F.; Layh, M. *J. Chem. Soc., Dalton Trans.* **1998**, 1619–1623.

(71) Hoffmann, R. W.; Holzer, B. *J. Am. Chem. Soc.* **2002**, *124*, 4204–4205.

(72) Caro, C. F.; Lappert, M. F.; Merle, P. G. *Coord. Chem. Rev.* **2001**, *219*, 605–663.

JP811317Y

Paper II

Insight into the Solvation and Isomerization of 3-Halo-1-azaallylic Anions from Ab Initio Metadynamics Calculations and NMR Experiments

Declerck R,. De Sterck B., Verstraelen T.,
Verniest G., Mangelinckx S., Jacobs J.,
De Kimpe N., Waroquier M., and Van Speybroeck V.

Chem.-Eur. J., **2009**, *15*, 580-5840

CHEMISTRY

A EUROPEAN JOURNAL

15/3 2009

Now Weekly!

A Journal of ChemPubSoc Europe

Concept
Artificial Enzyme Catalysis Controlled and Driven by Light
G. Knör

Supported by ACES

WILEY-VCH

CEUJED 15 (3) 553–804 (2009) · ISSN 0947-6539 · Vol. 15 · No. 3 · 2009

www.chemeurj.org

CHEMISTRY
A EUROPEAN JOURNAL

DOI: 10.1002/chem.200800948

Insight into the Solvation and Isomerization of 3-Halo-1-azaallylic Anions from Ab Initio Metadynamics Calculations and NMR Experiments

Reinout Declerck,[a] Bart De Sterck,[a] Toon Verstraelen,[a] Guido Verniest,[b] Sven Mangelinckx,[b] Jan Jacobs,[b] Norbert De Kimpe,*[b] Michel Waroquier,[a] and Veronique Van Speybroeck*[a]

In organic synthesis, it is observed experimentally that the nature of the solvent can influence tremendously the reactivity and overall product selectivity. In this communication, we report on the *E*/*Z* isomerization of a typical solvated species, that is, the stable lithiated 3-chloro-3-methyl-1-azaallylic anion readily accessible from the *N*-isopropylimine of α-chloropropiophenone, from a theoretical and a subsequent NMR study. To date, the configurational properties of these 3-chloro-3-methyl-1-azaallylic anions are poorly understood. Our main emphasis is devoted to the monomeric species as these are believed to be the most important for further reactivity studies (see below). It will be shown that the investigated species is a particular example in which the inclusion of the solvent in the modeling study is of the utmost importance to determine the proper chemical behavior.

The 3-chloro-3-methyl-1-azaallylic anion was chosen as a model compound to obtain a deeper insight into the structural features of 3-halo-1-azaallylic anions and to get a better understanding, and eventually a better control, of the stereochemical outcome of the reactions in which these anions are involved. Since their first use in the early 1960s,[1–3] non-halogenated 1-azaallylic anions have gained a predominant role in organic synthesis due to their ability to form new C−C bonds with a lack of side products.[4] The chemistry of 1-azaallylic anions leads to basic heterocyclic systems such as aziridines, azetidines, pyrrolidines, pyrroles, piperidines, oxiranes, oxolanes, and higher functionalized ring systems, currently of interest for pharmaceutical chemistry and agrochemistry. The application of certain halogenated counterparts, that is, the 3-chloro-3-methyl-1-azaallylic anions, in particular by the group of De Kimpe and more general by the group of Florio, which incorporated the 3-chloro-3-methyl-1-azaallylic moiety into heterocyclic structures, has led to the synthesis of various important classes of compounds such as cyclopropanes,[5] tetrahydrofurans,[6] tetrahydropyrans,[6c] oxiranes,[7] aziridines,[7b,d,8] chloroimines,[9] pyrroles and pyridines,[10] steroids,[11] alkenylheterocycles,[12] and oxazetidines.[13] As mentioned, 3-chloro-3-methyl-1-azaallylic anions can be used for the synthesis of functionalized oxiranes and aziridines since the former anions behave as nucleophiles in Darzens- and aza-Darzens-type reactions with carbonyl compounds and imines.[7,8] One of the determining factors in the stereochemical outcome of these Darzens-type reactions is the *E*/*Z* stereochemistry of the starting 1-azaallylic anion.[14] Therefore, it is important to know and understand the configurational properties of 3-chloro-3-methyl-1-azaallylic anions in order to perform aldol- and Mannich-type reactions with these intermediates in a stereocontrolled manner.

NMR investigation and semiempirical calculations on the stereochemistry of (2-(α-chloroethyl)benzothiazolyl)lithium and (4,4-dimethyl-2-(α-chloroethyl)oxazolinyl)lithium have demonstrated that internal coordination between lithium and chlorine stabilizes the corresponding isomer with nitrogen and chlorine at the same side of the C=C double bond.[15] The lack of such structural investigations on 3-chloro-3-methyl-1-azaallylic anions in sensu stricto urged us to study their stereochemical properties.

The *E*/*Z* isomerism for non-halogenated 1-azaallylic anions has been observed and investigated quite frequently. The facile carbon−carbon bond rotation in simple lithiated 1-azaallylic anions was investigated using ^{1}H NMR spectros-

---

[a] Dr. R. Declerck, B. De Sterck, T. Verstraelen,
Prof. Dr. M. Waroquier, Prof. Dr. V. Van Speybroeck
Center for Molecular Modeling, Ghent University
Proeftuinstraat 86, 9000 Gent (Belgium)
Fax: (+32) 9-264-6697
E-mail: Veronique.VanSpeybroeck@UGent.be

[b] Dr. G. Verniest, Dr. S. Mangelinckx, J. Jacobs, Prof. Dr. N. De Kimpe
Department of Organic Chemistry, Faculty of Bioscience Engineering
Ghent University, Coupure links 653, 9000 Gent (Belgium)
Fax: (+32) 9-264-6243
E-mail: Norbert.DeKimpe@UGent.be

Supporting information for this article is available on the WWW under http://dx.doi.org/10.1002/chem.200800948.

copy.[16] The rotational activation free energy was found to be (74.1 ± 1.3) kJ mol^{-1} at 313 K. E/Z isomerization was also observed upon deprotonation of ketimines of 2-butanone at room temperature.[17] For closely related non-chlorinated analogues of the species **1**–**2** in Figure 1, that is, the lithiated anion derived from the *N*-phenylimine of propiophenone, isomerization from the kinetically favored *E* isomer with the methyl group and the phenyl group at the same side of the C2=C3 double bond (like in *Z*-isomer **1**) to the thermodynamically most stable *Z* isomer with the methyl group and nitrogen at the same side of the C2=C3 double bond (like in *E*-isomer **2**), was observed.[18] Therefore, it was assumed that the lithiated 3-chloro-1-azaallylic anions of the present work could also undergo a similar type of isomerization.

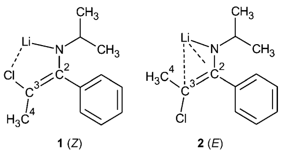

Figure 1. *Z*-isomer **1** and *E*-isomer **2** of the lithiated (2-chloro-1-phenylprop-1-en-1-yl)isopropylamide anion.

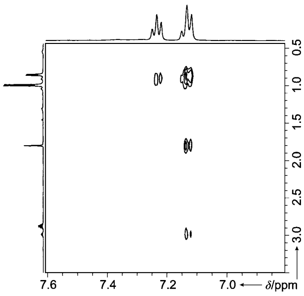

Figure 2. Details of the off-resonance ROESY spectrum of the *Z*-isomer **1** of the lithiated 3-chloro-1-azaallylic anion ([D$_8$]THF). The resonance signals at 0.96 ppm (doublet) and 2.84 ppm (septet) are from diisopropylamine formed upon protonation of LDA.

At first instance, the lithiated 3-chloro-3-methyl-1-azaallylic anion was generated by deprotonation of *N*-(2-chloro-1-phenylpropylidene)isopropylamine with lithium diisopropylamide (LDA) in [D$_8$]THF at 273 K and analyzed by ^{1}H and ^{13}C NMR spectroscopy. The α-chloropropiophenone imine was deprotonated under these conditions to a single stereoisomer as demonstrated by the presence of a single set of characteristic ^{1}H NMR chemical shifts of the methyl group on the double bond (s, $\delta = 1.77$ ppm), methine function (septet, 2.96 ppm) and isopropyl methyl groups (d, 0.83 ppm). Also a single set of characteristic ^{13}C NMR chemical shifts of the lithiated 3-chloro-1-azaallylic anion were observed (see Supporting Information). The stereochemistry of the *Z* anion **1** was determined by off-resonance ROESY spectroscopy showing ROE effects between the methyl group and the *ortho*-protons of the phenyl ring positioned at the same side of the carbon–carbon double bond (Figure 2). Furthermore, the observed ROE effects between the *N*-isopropyl substituent and the phenyl group support the *anti* stereochemistry of the 3-chloro-1-azaallylic anion, that is, the *N*-isopropyl group is oriented anti with respect to the C2=C3 double bond. In contrast to the non-chlorinated species,[19] the aforementioned NMR experiments indicate that in THF only the *Z*/*anti* isomer **1** occurs and that both amide and C=C double bond rotations are inhibited. This particular behavior of chlorinated 1-azaallylic anions demanded a theoretical interpretation. Before elaborating on the theoretical results, it is important to focus on the tendency of 1-azaallylic anions to form higher aggregates in solution. From the extensive work that has been performed on lithium 1-azaallylic anions, higher aggregates are also expected here.[19] It must, however, be stressed that the experimental NMR spectroscopy data gives by no means any information on the solution aggregation number of the title compounds. According to a series of NMR spectroscopic studies and colligative measurements in THF, both monomeric and dimeric species will occur at low concentration of the lithium 1-azaallyl anions.[20] On the other hand, the monomeric lithium 1-azaallylic anions retain in most cases their structural properties in the dimer form;[21] the stereochemical preferences in reactions can readily be explained with the properties of the monomeric form.[22] There are also several indications that the monomeric forms are the most likely reactive forms of these molecules. Studies by Streitwieser and co-workers have shown that the reactive form of lithiated compounds, present in solution for the larger extent as higher aggregates, can be the monomeric form due to a kinetic advantage because of lower-energy transition states as compared to the less reactive higher aggregates.[23] Based on these arguments and the expensive computational resources needed for treating higher arguments, the theoretical part of this communication will focus only on the configuration of the monomeric species, being aware that these might be part of higher aggregates under experimental conditions.

Despite the huge amount of theoretical studies that appeared the last years, modeling of complex phenomena such as chemistry in liquids remains a challenge as standard optimization techniques and ab initio molecular dynamics methods are often not suitable.[24,25] The first set of methods is routinely performed nowadays, but for our systems in which the solvent participates actively, a single optimized structure does not resemble the configurational distribution at finite temperature. First-principle molecular dynamics simulations are often restricted by short simulation times. As such, interesting regions of phase space are often so high in free energy that their sampling during a standard MD simulation is a rare event. Enhanced sampling techniques have become an active research domain.[25] The relatively new metadynamics method has particularly attracted our attention. It was first proposed by Laio and Parrinello and enables an enhanced sampling of separated regions in phase space, simultaneously mapping the underlying free-energy landscape as a function of a limited number of collective variables.[26] The particular implementation is based on the work of Iannuzi et al.[27]

Prior to the modeling of the 1-azaallylic anions, we modeled the liquid structure of pure THF by using first-principle molecular dynamics calculations. The liquid structure of THF was recently assessed via hydrogen/deuterium isotopic substitution neutron-diffraction techniques by Bowron, Finney, and Soper.[28] A periodic cubic simulation cell was filled with 64 THF molecules. This choice represents an optimal compromise between computational cost and a proper embedding of the solute in the solvent. The simulation cell size was chosen to correspond with the experimental density of 0.88 $\mathrm{kg\,dm^{-3}}$.[29] The performance of the THF model was validated by calculating the radial distribution function (RDF) of the molecular centers, which was found to be in excellent agreement with the benchmark RDF reported in reference [28] (see Supporting Information). Moreover, the MD simulations yielded a conformational distribution of 59 % twisted and 41 % oxygen envelope, indicating a thorough sampling of the system.[28]

After the THF model had been successfully assessed, it was applied to study the degree of coordination of the 3-chloro-1-azaallylic anions in solution. The coordination number for lithium enolates in ethereal solvents is rather difficult to establish but four-coordinate lithium cations have been clearly recognized in NMR studies of solvent separated ion pairs.[30] For contact ion pairs, coordination is expected less important because of the electrostatic effect of the counter ion. Theoretically the structures of a variety of organic lithium compounds were determined in the gas phase and in solvation using microsolvation with explicit ethereal ligands and/or continuum models.[31] For the 1-azaallylic anions as encountered here which are subject to large steric crowding, the degree of coordination is not a priori clear and can not be deduced straightforwardly from the experimental data. Isothermal–isobaric (NPT) molecular dynamics simulations during a period of 2.5 ps show that the *Z*-isomer **1** is monocoordinated whereas the *E*-isomer **2** features a two-fold coordination with THF (illustrated in Figure 3). In the *E*-isomer **2** the halogen–lithium coordination is not present which allows a second THF molecule to coordinate with the counter ion.

In order to obtain insight into the occurrence of only one stereoisomer in case of 3-chloro-3-methyl-1-azaallylic anions **1** and **2**, we decided to construct the free-energy landscape connecting the basins of the two isomers. To this end we applied the metadynamics method in which the dihedral angles Cl-C3-C2-N and C4-C3-C2-N were chosen as collective variables. This choice guarantees the independent movement of the methyl and chlorine substituents. The resulting free-energy landscape as a function of the two dihedral angles is displayed in Figure 4. The Gibbs free energy barriers for *E*-to-*Z* and *Z*-to-*E* isomerization amount to $(107.1\pm12.1)\ \mathrm{kJ\,mol^{-1}}$ and $(128.6\pm12.1)\ \mathrm{kJ\,mol^{-1}}$, respectively.[32] These barriers are high, preventing isomerization at the experimental temperature. The *Z*-isomer **1** is more stable than the *E*-isomer **2** by $\Delta G_{Z\text{-}E} = (21.5\pm12.1)\ \mathrm{kJ\,mol^{-1}}$, which indicates that the experimentally observed *Z*-isomer **1** is thermodynamically favored. Within a static cluster approach using a combined explicit/implicit solvent model we were unable to determine the transition state for *E*/*Z* isomerization as the coordination number varies during the chemical transformation. Moreover, the stability of the *Z*-isomer **1** with respect to the *E*-isomer **2** was 20 $\mathrm{kJ\,mol^{-1}}$ too high compared to the metadynamics calculations. By capturing the movement of both dihedral angles, we were able to observe the sp^2 to sp^3 hybridization transition of the C3 carbon atom upon rotation, a well-known feature of rotations about allylic bonds. This is reflected in the fact that the saddle point, denoted as $(E\text{–}Z)^{+}$, does not lie on the linear pathway connecting both isomers, which confirms a posteriori the importance of capturing the movement of both dihedral angles.

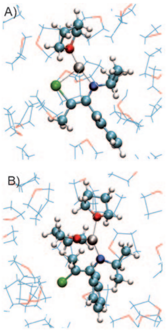

Figure 3. Characteristic snapshot of the MD simulation of the *Z*-isomer **1** (A) and the *E*-isomer **2** (B) solvated in THF.

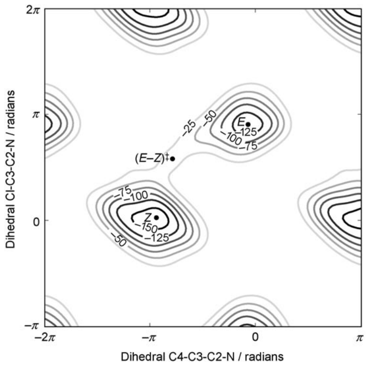

Figure 4. Gibbs free energy profile (in $\mathrm{kJ\,mol^{-1}}$) governing the *E*–*Z* isomerization of the lithiated 3-chloro-1-azaallylic anion in THF. The positions of both stable isomers *E* (**2**) and *Z* (**1**) and the saddle point $(E\text{–}Z)^{+}$ are added. Note that the two collective variables feature a 2π periodicity.

Finally, we infer from both first principle metadynamics and NMR experiments that the *Z* isomer is the only configuration formed upon the deprotonation of the starting imine to the lithium 3-chloro-1-azaallylic anion. The interaction between the counter ion and the halogen, an effect that is not present in the non-halogenated 1-azaenolates, stabilizes the *Z* isomer by 21 kJ mol^{-1}. Moreover, the transition from the *Z* to the *E* isomer is very highly activated and features a change in coordination for the lithium cation as the broken lithium-chlorine interaction is replaced by a lithium–THF interaction. These effects can only be seen because of the explicit inclusion of the large THF model in the QM simulations. These results show that the stereochemistry of 3-chloro-3-methyl-1-azaallylic anions is manifestly different compared to their non-chlorinated counterparts and is the result of their configurational stability which should be beneficial during their synthetic use as functionalized intermediates in stereoselective reactions.

Experimental Section

All molecular dynamics calculations were performed within the cp2k/quickstep code,[33] employing the Gaussian and plane-wave (GPW) density functional method and periodic boundary conditions. A BLYP[34] gradient-corrected functional was used throughout, together with a TZVP-PSP[35] basis set, a 400 Ry cutoff for the auxiliary plane wave grid, and pseudopotentials developed by Goedecker and co-workers.[36] Isothermal-isobaric (NPT) MD simulations of both isomers were conducted. The species were properly embedded in the THF solvent model by determining, using atomic Pauling radii, the volume associated with their solvent accessible surface.[37] As the volume of THF is 2.96 times smaller compared to the volume of the 3-chloro-1-azaallylic anion, three THF molecules in the simulation cell were replaced by the 3-chloro-1-azaallylic species. An equilibration time of 2.5 ps has been respected to allow the solvent to accommodate to the presence of the solute and vice versa, followed by a 40 ps metadynamics run. Accurate metadynamics parameter values were determined from Gibbs free energy barrier predictions of the lithiated 3-chloro-1-azaallylic anion in the gas phase (using a supercell approach), including only one THF molecule to impose the limited freedom of the lithium cation. The set of parameter values $w = 2.0$ kJ mol^{-1}, $s = 0.33$ rad and $G = 50$ fs (notation: see ref. [26]) yielded an energy barrier within 1.0 kJ mol^{-1} of the convergence limit. According to ref. [32] the estimated error using these parameters is $\varepsilon = 6.1$ kJ mol^{-1}.

Lithiated 3-chloro-1-azaallylic anion 1: To a stirred solution of diisopropylamine (0.056 g, 0.55 mmol) in [D_8]THF (1 mL), *n*BuLi (0.22 mL, 0.55 mmol, 2.5 N in hexanes) was added slowly at 273 K. After 30 min of stirring at 273 K, the solution was evaporated in vacuo to dryness, after which, [D_8]THF (0.5 mL) was added and a solution of *N*-(2-chloro-1-phenylpropylidene)isopropylamine (0.11 g, 0.5 mmol) in [D_8]THF (0.5 mL) was dropped to the LDA solution at 273 K and stirring was continued for 1 h. Subsequently, the reaction mixture was allowed to reach room temperature during 15 min. ^{1}H NMR (300 MHz) and ^{13}C NMR (75 MHz) spectra were taken from the prepared 3-chloro-1-azaallylic anion **1** at room temperature. ^{1}H NMR (300 MHz, [D_8]THF): $\delta = 0.83$ (d, $J = 6.33$ Hz, 6H; $(CH_3)_2CH$), 1.77 (s, 3H; CH_3), 2.96 (septet, $J = 6.1$ Hz, 1H; $(CH_3)_2CH$), 7.08–7.14 (m, 3H; *o*-CH_{ar} and *p*-CH_{ar}), 7.18–7.24 ppm (m, 2H; *m*-CH_{ar}); ^{13}C NMR (75 MHz, [D_8]THF): $\delta = 22.3$, 28.1, 48.6, 83.6, 125.9, 127.6, 130.0, 144.0, 155.0 ppm.

Acknowledgements

The authors thank Professor J. Martins (Department of Organic Chemistry, NMR and Structure Analysis, Ghent University) for recording the ROESY spectra, and Dr. D. T. Bowron (STFC Rutherford Appleton Laboratory) for providing the EPSR-derived RDF data. This work was supported by the Fund for Scientific Research-Flanders and the Research Board of Ghent University.

Keywords: azaallylic anions · isomerization · metadynamics · NMR spectroscopy · solvent effects

---

[1] G. Stork, S. R. Dowd, *J. Am. Chem. Soc.* **1963**, *85*, 2178–2180.
[2] G. Wittig, H. D. Fommeld, P. Suchanek, *Angew. Chem.* **1963**, *75*, 978–979.
[3] G. Wittig, H. Reiff, *Angew. Chem.* **1968**, *80*, 8–15.
[4] S. Mangelinckx, N. Giubellina, N. De Kimpe, *Chem. Rev.* **2004**, *104*, 2353–2400 and references therein.
[5] a) N. De Kimpe, P. Brunet, R. Verhé, N. Schamp, *J. Chem. Soc. Chem. Commun.* **1988**, 825–827; b) W. Aelterman, K. Abbaspour Tehrani, W. Coppens, T. Huybrechts, N. De Kimpe, D. Tourwé, J.-P. Declercq, *Eur. J. Org. Chem.* **1999**, 239–250; c) V. Capriati, S. Florio, R. Luisi, M. T. Rocchetti, *J. Org. Chem.* **2002**, *67*, 759–763; d) S. Florio, F. M. Perna, R. Luisi, J. Barluenga, F. Rodríguez, F. J. Fañanás, *J. Org. Chem.* **2004**, *69*, 5480–5482.
[6] a) N. De Kimpe, E. Stanoeva, N. Schamp, *Tetrahedron Lett.* **1988**, *29*, 589–592; b) N. De Kimpe, W. Aelterman, K. De Geyter, J.-P. Declercq, *J. Org. Chem.* **1997**, *62*, 5138–5143; c) W. Aelterman, N. Giubellina, E. Stanoeva, K. De Geyter, N. De Kimpe, *Tetrahedron Lett.* **2004**, *45*, 441–444.
[7] a) P. Sulmon, N. De Kimpe, N. Schamp, J.-P. Declercq, B. Tinant, *J. Org. Chem.* **1988**, *53*, 4457–4462; b) V. Capriati, L. Degennaro, S. Florio, R. Luisi, C. Tralli, L. Troisi, *Synthesis* **2001**, 2299–2306; c) F. M. Perna, V. Capriati, S. Florio, R. Luisi, *J. Org. Chem.* **2002**, *67*, 8351–8359; d) F. Bona, L. De Vitis, S. Florio, L. Ronzini, L. Troisi, *Tetrahedron* **2003**, *59*, 1381–1387; e) L. Troisi, L. De Vitis, C. Granito, P. Metrangolo, T. Pilati, L. Ronzini, *ARKIVOC* **2004**, *xiv*, 61–73.
[8] a) R. Luisi, V. Capriati, S. Florio, R. Ranaldo, *Tetrahedron Lett.* **2003**, *44*, 2677–2681; b) L. De Vitis, S. Florio, C. Granito, L. Ronzini, L. Troisi, V. Capriati, R. Luisi, T. Pilati, *Tetrahedron* **2004**, *60*, 1175–1182; c) R. Luisi, V. Capriati, S. Florio, P. Di Cunto, B. Musio, *Tetrahedron* **2005**, *61*, 3251–3260; d) L. Troisi, C. Granito, C. Carlucci, F. Bona, S. Florio, *Eur. J. Org. Chem.* **2006**, 775–781.
[9] P. Sulmon, N. De Kimpe, N. Schamp, *Synthesis* **1989**, 8–12.
[10] W. Aelterman, N. De Kimpe, V. Tyvorskii, O. Kulinkovich, *J. Org. Chem.* **2001**, *66*, 53–58.
[11] L. Troisi, S. Florio, C. Granito, *Steroids* **2002**, *67*, 687–693.
[12] V. Capriati, L. Degennaro, S. Florio, R. Luisi, *Eur. J. Org. Chem.* **2002**, 2961–2969.
[13] R. Luisi, V. Capriati, S. Florio, E. Piccolo, *J. Org. Chem.* **2003**, *68*, 10187–10190.
[14] V. K. Aggarwal, D. M. Badine, V. A. Moorthie in *Aziridines and Epoxides in Organic Synthesis* (Ed.: A. K. Yudin), Wiley-VCH, Weinheim, **2006**, pp. 1–35.
[15] A. Abbotto, S. Bradamante, S. Florio, V. Capriati, *J. Org. Chem.* **1997**, *62*, 8937–8940.
[16] J. Y. Lee, T. J. Lynch, D. T. Mao, D. E. Bergbreiter, M. Newcomb, *J. Am. Chem. Soc.* **1981**, *103*, 6215–6217.
[17] J. K. Smith, D. E. Bergbreiter, M. Newcomb, *J. Org. Chem.* **1981**, *46*, 3157–3158.
[18] R. Knorr, P. Low, *J. Am. Chem. Soc.* **1980**, *102*, 3241–3242.
[19] a) H. Ahlbrecht, E. O. Düber, D. Enders, H. Eichenauer, P. Weuster, *Tetrahedron Lett.* **1978**, *19*, 3691–3694; b) P. von Ragué Schleyer, R. Hacker, H. Dietrich, W. Mahdi, *J. Chem. Soc. Chem. Commun.* **1985**, 622–624; c) R. Glaser, C. M. Hadad, K. B. Wiberg, A. Streit-

wieser, *J. Org. Chem.* **1991**, *56*, 6625–6637; d) R. Knorr, H. Dietrich, W. Mahdi, *Chem. Ber.* **1991**, *124*, 2057–2063; e) P. B. Hitchcock, M. F. Lappert, D.-S. Liu, *J. Chem. Soc. Chem. Commun.* **1994**, 2637–2638; f) A. Abbotto, A. Streitwieser, P. von Ragué Schleyer, *J. Am. Chem. Soc.* **1997**, *119*, 11255–11268; Schleyer, *J. Am. Chem. Soc.* **1997**, *119*, 11255–11268; Schleyer, *J. Am. Chem. Soc.* **1997**, *119*, 11255–11268; g) L. M. Pratt, T. E. Hogen-Esch, I. M. Khan, *Tetrahedron* **1995**, *51*, 5955–5970; h) L. R. Liou, A. J. McNeil, A. Ramirez, G. E. S. Toombes, J. M. Gruver, D. B. Collum, *J. Am. Chem. Soc.* **2008**, *130*, 4859–4868.

[20] a) R. A. Wanat, D. B. Collum, G. Van Duyne, J. Clardy, R. T. DePue, *J. Am. Chem. Soc.* **1986**, *108*, 3415–3422; b) N. Kallman, D. B. Collum, *J. Am. Chem. Soc.* **1987**, *109*, 7466–7472; c) L. M. Jackman, L. M. Scarmoutzos, B. D. Smith, P. G. Williard, *J. Am. Chem. Soc.* **1988**, *110*, 6058–6063.

[21] a) R. R. Fraser, N. Chuaqui-Offermanns, K. N. Houk, N. G. Rondan, *J. Organomet. Chem.* **1981**, *206*, 131–138; b) R. Glaser, A. Streitwieser, *J. Org. Chem.* **1991**, *56*, 6612–6624; c) R. Glaser, C. M. Hadad, K. B. Wiberg, A. Streitwieser, *J. Org. Chem.* **1991**, *56*, 6625–6637.

[22] a) R. Glaser, A. Streitwieser, *J. Am. Chem. Soc.* **1987**, *109*, 1258–1260; b) R. Glaser, A. Streitwieser, *Pure Appl. Chem.* **1988**, *60*, 195–204; c) R. Glaser, A. Streitwieser, *J. Am. Chem. Soc.* **1989**, *111*, 7340–7348; d) R. Glaser, A. Streitwieser, *J. Am. Chem. Soc.* **1989**, *111*, 8799–8809; e) R. Glaser, A. Streitwieser, *J. Org. Chem.* **1989**, *54*, 5491–5502; f) R. Glaser, A. Streitwieser, *J. Mol. Struct.* **1988**, *163*, 19–50.

[23] A. Streitwieser, *J. Mol. Model.* **2006**, *12*, 673–680.

[24] a) A. V. Marenich, R. M. Olson, A. C. Chamberlin, C. J. Cramer, D. G. Truhlar, *J. Chem. Theory Comput.* **2007**, *3*, 2055–2067; b) C. P. Kelly, C. J. Cramer, D. G. Truhlar, *J. Chem. Theory Comput.* **2005**, *1*, 1133–1152; c) J. Tomasi, M. Persico, *Chem. Rev.* **1994**, *94*, 2027–2094.

[25] B. Ensing, M. De Vivo, Z. Liu, P. Moore, M. L. Klein, *Acc. Chem. Res.* **2006**, *39*, 73–81.

[26] A. Laio, M. Parrinello, *Proc. Natl. Acad. Sci. USA* **2002**, *99*, 12562–12566.

[27] M. Iannuzzi, A. Laio, M. Parrinello, *Phys. Rev. Lett.* **2003**, *90*, 238302.

[28] a) D. T. Bowron, J. L. Finney, A. K. Soper, *J. Am. Chem. Soc.* **2006**, *128*, 5119–5126; b) M. Štrajbl, J. Florián, *Theor. Chem. Acc.* **1998**, *99*, 166–170; c) V. M. Rayón, J. A. Sordo, *J. Chem. Phys.* **2005**, *122*, 204303.

[29] a) D. R. Lide in *CRC Handbook of Chemistry and Physics*, 84th ed., CRC Press, Wiley, New York, **2003**; b) C. Carvajal, K. J. Tölle, J. Smid, M. Szwarc, *J. Am. Chem. Soc.* **1965**, *87*, 5548–5553.

[30] a) L. M. Pratt, N. Văn Nguyên, B. Ramachandran, *J. Org. Chem.* **2005**, *70*, 4279–4283; b) L. M. Pratt, B. Ramachandran, J. D. Xidos, C. J. Cramer, D. G. Truhlar, *J. Org. Chem.* **2002**, *67*, 7607–7612; c) P. L. Fast, M. L. Sanchez, D. G. Truhlar, *Chem. Phys. Lett.* **1999**, *306*, 407–410; d) J. A. Pople, M. Head-Gordon, K. Raghavachari, *J. Chem. Phys.* **1987**, *87*, 5968–5975.

[31] a) L. M. Pratt, A. Streitwieser, *J. Org. Chem.* **2003**, *68*, 2830–2838; b) V. Van Speybroeck, K. Moonen, K. Hemelsoet, C. V. Stevens, M. Waroquier, *J. Am. Chem. Soc.* **2006**, *128*, 8468–8478.

[32] A. Laio, A. Rodriguez-Fortea, F. L. Gervasio, M. Ceccarelli, M. Parrinello, *J. Phys. Chem. B* **2005**, *109*, 6714–6721.

[33] http://cp2k.berlios.de.

[34] a) A. D. Becke, *Phys. Rev. A* **1988**, *38*, 3098–3100; b) C. Lee, W. Yang, R. G. Parr, *Phys. Rev. B* **1988**, *37*, 785–789.

[35] G. Lippert, J. Hutter, P. Ballone, M. Parrinello, *J. Phys. Chem.* **1996**, *100*, 6231–6235.

[36] a) S. Goedecker, M. Teter, J. Hutter, *Phys. Rev. B* **1996**, *54*, 1703–1710; b) C. Hartwigsen, S. Goedecker, J. Hutter, *Phys. Rev. B* **1998**, *58*, 3641–3662.

[37] a) J. Tomasi, B. Mennucci, R. Cammi, *Chem. Rev.* **2005**, *105*, 2999–3093; b) Y. Takano, K. N. Houk, *J. Chem. Theory Comput.* **2005**, *1*, 70–77.

Received: May 18, 2008
Revised: August 29, 2008

Paper III

Solvent Effects on Free Radical Polymerization Reactions: The Influence of Water on the Propagation rate of Acrylamide and Methacrylamide

De Sterck B., Vaneerdeweg R., Du Prez F.,
Waroquier M., and Van Speybroeck V.

Macromolecules, **2010**, *43*, 827-836

Macromolecules
ARTICLE

Macromolecules **2010**, *43*, 827–836 **827**
DOI: 10.1021/ma9018747

Solvent Effects on Free Radical Polymerization Reactions: The Influence of Water on the Propagation Rate of Acrylamide and Methacrylamide

Bart De Sterck,[†] Roel Vaneerdeweg,[†,§] Filip Du Prez,[‡] Michel Waroquier,[†] and Veronique Van Speybroeck*[,†]

[†]Center for Molecular Modeling, Ghent University, Technologiepark 903, B-9052 Zwijnaarde, Belgium, QCMM-alliance, Ghent-Brussels, Belgium and [‡]Department of Organic Chemistry, Polymer Chemistry Research Group (PCR), Ghent University, Krijgslaan 281 S4-bis, B-9000 Ghent, Belgium. [§]Current address: Departement LNE, Afdeling Milieu-inspectie (hoofdbestuur), Koning Albert II-laan 20 bus 8, 1000 Brussels, Belgium

Received August 23, 2009; Revised Manuscript Received October 30, 2009

ABSTRACT: The polymerization of acrylamide (AA) and methacrylamide (MAA) was studied by an extensive set of computational methods with a particular focus on the possible influence of water molecules on the propagation reaction. An extensive set of electronic structure methods was tested, consisting of B3LYP, BMK, MPWB1K, MP2, and B2-PLYP of which some include dispersion effects. The effect of water on the transition state is modeled in two different ways. Explicit water molecules are added to the system, showing that replacing the hydrogen bond that dominates the transition state structure by a water-mediated hydrogen bond, results in more stable, more feasible transition states. This effect is the largest for AA polymerization, a monomer that is known to experience a larger solvent effect than MAA. Additionally, a conductor-like polarizable continuum model (C-PCM) is applied on both the transition states in gas phase and the ones bearing explicit water molecules. This model has a dramatic effect on all the propagation rates, raising them by about 3 orders of magnitude. The inclusion of explicit water molecules gives insight into the role of water molecules and the formation of prereactive complexes. The relative rate of polymerization of AA with regard to MAA is well reproduced for a trimeric propagating radical with inclusion of explicit water molecules or by using an implicit solvation model at the BMK and MPWB1K level of theory.

Introduction

Free radical polymerization is one of the most important reaction mechanisms for the industrial production of a wide variety of polymers. It is a complex multistep process and the determination of rate coefficients of the various elementary reactions is a challenge both for theoreticians and experimentalists. From the experimental point of view, substantial progress has been made since the establishment of elegant laser-flash photolysis-based techniques, such as pulsed laser polymerization (PLP) and time-resolved PLP. Computational quantum chemistry has the potential to study individual reactions and their rates without kinetic model-based assumptions. However the modeling of radical reactions generally requires high levels of theory which are not feasible for polymeric systems. Nonetheless, due to a continuing increase in computer power and the development of advanced numerical models, computational chemistry has established itself as a useful tool for the radical polymer field. In the literature, a rich database exists consisting of both experimental[1−5] and theoretical data for a broad range of radically polymerizing monomers like ethylene,[6,7] (meth)acrylate-type monomers,[8−10] styrene,[11] (meth)acrylamide-type monomers, acrylonitrile,[12] and vinyl chloride.[13]

To date, there have been relatively few published direct assessments of the influence of solvent on radical reactions. Moreover, experimental solvation energies for radical species are scarce in the literature. However, as some polymerizations are carried out in solution, the knowledge of the effects that are induced by the solvent is crucial for a better understanding of free radical polymerization in solution. Therefore, theoretical modeling of the kinetics of propagation reactions should take solvent effects into account. It has long been recognized that solvents may affect the reaction kinetics but the origin of the solvent effect and the extent of its influence have been the onset of a long debate. Reaction rate coefficients (k_p) for styrene and methyl methacrylate (MMA) polymerizations have been measured in a wide variety of solvents by Olaj et al.[14] and the solvent-induced changes were found to vary around 20%. In other experimental work, one notices a significant increase in k_p in some specific polar solvents when the monomer concentration decreases. Recently Beuermann published a very good review on the current status of the solvent influence on the propagation kinetics studied by pulsed laser initiated polymerizations.[15] Various effects may contribute to changes in k_p due to solvent such as hindered rotational modes, hydrogen bonding[16] or electron/pair interactions. These may lead to an enhancement of a factor 10 of the propagation rate. In contrast, nonspecific solvent interactions originating from solvent size, local monomer concentration or steric effects lead to less pronounced variations in k_p.[16]

In this article, attention is focused on two polar monomers, i.e., acrylamide (AA) and methacrylamide (MAA), for which specific interactions between solvent and monomer occur through hydrogen bonding. In aqueous solution, the concentration of a monomer that is prone to hydrogen bonding will influence the reaction rate and the Arrhenius parameters compared to bulk polymerization.[17−19] This was observed for a variety of polar monomers like acrylamide (AA),[20,21] methacrylamide (MAA),[22] *N*-isopropylacrylamide (NIPAM),[23] acrylic acid,[24,25] and methacrylic acid.[26] These effects are often ascribed to the reversible formation of prereactive complexes. In the literature, complexation between radical and monomer[23,27−29] as well as radical-solvent interaction[17] is

---

*To whom correspondence should be addressed. E-mail: veronique.vanspeybroeck@ugent.be.

Scheme 1. Schematic Representation of Different Chain Lengths for Syndiotactic Propagation of Acrylamide (R = H) and Methacrylamide (R = Me)

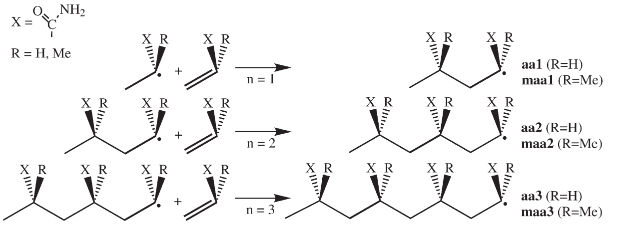

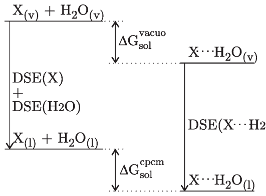

Figure 1. Thermodynamic cycle for the determination of the free energy of solvation of a solute, X, in a dielectricum (ΔG_{sol}^{cpcm}), calculated from the free energy of solvation in vacuo (ΔG_{sol}^{vacuo}) and the dielectric solvation energies (DSEs).

proposed. For the studied system, the polymerization of acrylamide, similar experimental findings and hypotheses are well documented. Several pulsed laser polymerization studies (PLP) clearly show that AA polymerization exhibits a strong solvent effect in aqueous solution.[21,28−30] The class of acrylamides, methacrylamides, and derived monomers have always been interesting monomers for a wide range of applications, for instance for the ability of the corresponding polymer hydrogels to absorb huge amounts of water.[31] These gels have applications ranging from analysis (gel electrophoresis)[32] to nanotechnology.[33] An acrylamide-derived monomer such as NIPAM is one of the most studied monomers as a result of its peculiar lower critical solution behavior. Several studies on the solvation of acrylamide have shown that acrylamide exists as a hydrogen-bonded complex with one or more water molecules.[34,35] This interaction will certainly play a role in the behavior of the reacting monomers and should be incorporated in the molecular model in order to completely account for them in the evaluation of the propagation reaction rate coefficients. An other aspect of acrylamide solvation is the result of the presence of the hydrophobic vinyl bond. Although this entity will not interact directly with the water molecules, an electrostatic effect of the surrounding dipolar water molecules can not be neglected.[36] This is certainly the case for methacrylamide which has a second hydrophobic group.

Until now, the majority of quantum chemical studies on radical polymerizations have been carried out in the gas phase. Gas phase predictions for polymerization in a solvent environment where explicit solvent interactions occur systematically underestimate the propagation reaction rate constants k_p in density functional theory (DFT) methods even if the most advanced functionals are used. More recently, some studies appeared in which the solvent was treated implicitly by a polarizable continuum model. These studies showed that the continuum solvation model is capable of capturing a substantial amount of the solvation effects.[21,29] These models show a minor effect on the polymerization of acrylonitrile and vinyl chloride in toluene, tetrahydrofuran and dimethylformamide[37] and a large (10.5 $\text{kJ}\cdot\text{mol}^{-1}$) decrease in activation energy for acrylic acid in water.[38] However, in the case where the solvent effect is mainly due to hydrogen bonding, these models fail as it was shown for the ethyl α-hydroxymethacrylate (EHMA) system for which the gap between experiment and theory increased by 3 orders of magnitude upon inclusion of a continuum solvation model.[8]

In this article, we will evaluate the influence of solvent effects on the propagation rate of acrylamide and methacrylamide. Therefore, we will not only assess the influence of a dielectric continuum on the reaction rate, but we will also take into account explicit water molecules assisting the transition state. Embedding these molecular clusters in the continuum model is often referred to as the supermolecule method, the cluster-continuum method or the mixed implicit/explicit solvent model.[39,40] Although the determination of the amount and the location of the explicit solvent molecules is not always trivial (one should only include the relevant solvent molecules that strongly interact with the solute),[41,42] this model has proven to be very useful in reaction and solvation modeling. A comparative study of continuum, explicit and mixed solvation models has been performed for studying phosphate hydrolysis by the group of Warshel.[42] It turned out that the mixed implicit/explicit solvation model gave unreliable results if the number of explicit solvent molecules became too large or if the solvent molecules do not show the correct orientation. In this work we tested the adequacy of the three solvation models on the radical polymerization systems. In particular the effect of explicit water molecules on the structures, energies and kinetic parameters for the polymerization of AA and MAA will be investigated combined with a continuum model or not.

Computational Methods

Rate coefficients, Arrhenius parameters, solvation energies and Gibbs free energies were calculated for the propagation reaction of two monomers, namely acrylamide (AA) and methacrylamide (MAA). In each case, transition states for reaction with a monomeric (**aa1**, **maa1**), dimeric (**aa2**, **maa2**), and trimeric (**aa3**, **maa3**) radical were used as a model for growing polymer so as to investigate the chain length effect on the propagation rate. These models are shown in Scheme 1. Notice that only syndiotactic propagation will be considered in this paper as the main scope is to understand how water molecules can interact with the transition state and influence the reaction kinetics.

Several studies have shown a rapid rate of convergence of the kinetic coefficients with respect to the chain length.[10,37,43−45] Notice that it is very important to start with an analogous series of reactants and transition states. Considering the higher flexibility of the longer radicals, it is important to use configurationally similar structures for all the reactions considered. This can be seen in Scheme 1 for the reactions in gas phase.

The effect of the solvent, water, is modeled as the sum of two contributions (see Figure 1): one resulting from the coordination of one or more water molecules to the transition state (X) and one originating from the bulk solvent effect.[39,46−49] The first contribution is the free energy of solvation in vacuo (ΔG_{sol}^{vacuo}) and accounts for the effect of hydrogen bonds that can assist the radical addition reaction while the second contribution essentially takes into account the permanent dipole moment of the surrounding water molecules by placing the transition state in a dielectric continuum, resulting in a dielectric solvation energy (DSE). For the latter effect, single point energy calculations using the C-PCM model as implemented in Gaussian03 is used with Pauling radii for the solute.[50,51] Combination of both contributions allows us to calculate the coordination free energy in solution, ΔG_{sol}^{cpcm}, from the thermodynamic cycle that is depicted in Figure 1.

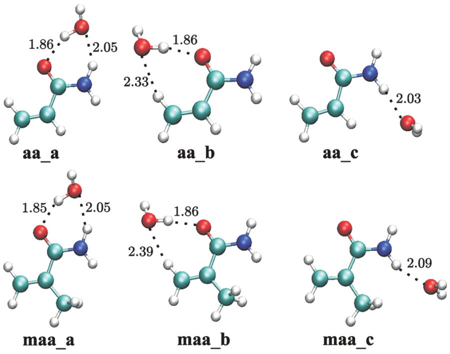

Figure 2. B3LYP/6-31+G(d,p) optimized structures for monosolvated AA and MAA monomers. Distances are in Å.

Table 1. Energies of Solvation for the AA and MAA Monomers Using the B3LYP/6-31+G(d,p) Geometries and Single Point Energy Calculations for a Variety of Electronic Structure Methods[a]

	AA				
	B3LYP	BMK	MPWB1K	MP2	B2PLYP
aa_a	−31.60	−31.30	−34.36	−34.07	−35.41
aa_b	−22.39	−21.59	−23.84	−24.58	−25.71
aa_c	−17.45	−16.70	−19.88	−22.97	−21.40
	MAA				
	B3LYP	BMK	MPWB1K	MP2	B2PLYP
maa_a	−32.03	−31.83	−34.83	−34.65	−36.03
maa_b	−21.39	−20.89	−23.54	−24.26	−24.96
maa_c	−14.35	−13.99	−17.02	−20.46	−18.39

[a] All values are in kJ·mol^{-1}.

Full geometry optimizations for transition states and stable minima are performed with DFT using the B3LYP[52,53] density functional. This method is known for it is ability to produce good geometries and it has been used intensively for the modeling of radical reactions. Test calculations with both the 6-31+G(d,p) and the 6-311++G(d,p) basis set show that the geometries undergo very little influence from the basis set.

The results are corrected for the zero-point energy and a normal-mode analysis is performed to ensure that the calculated structures are either a local minimum (no imaginary frequencies) or a transition state (saddle point, 1 imaginary frequency). All DFT optimizations were carried out using the Gaussian03 software package.[51] For the calculation of the kinetic parameters, no scaling factors were used for the frequencies nor for the zero-point energy correction. The kinetic parameters for the reactions in vacuo were calculated by fitting an Arrhenius equation to the calculated values for the reaction rate coefficient between 200 and 400 K. The C-PCM kinetics was calculated using Gibbs free energy of activation.

Additionally, single point energy calculations were carried out for the optimized structures using more advanced electronic structure methods. The following electronic structure methods are used: MPWB1K, BMK, UMP2, and B2-PLYP with the 6-31+G(d,p) basis set using Gaussian03. The MPWB1K method is selected because of its good description of hydrogen bonding, weak van der Waals interaction, partial bonding, and the more accurate thermochemistry results.[10,54] The BMK functional is chosen because of its good performance for describing the kinetics of radical reactions in general.[13,55,56] The effect of higher order corrections is investigated with the UMP2 second order perturbation method, from here referred to as MP2. The B2-PLYP method, which combines the BLYP[53,57] functional with Hartree−Fock exchange and a perturbative second-order correlation part, is used since it is a promising functional with a high accuracy, taking into account dispersion interactions.[58,59]

Results and Discussion

Solvation. To understand the influence of water molecules on the reaction kinetics, possible solvated structures of the monomers are investigated first. Both monomers feature several sites that are prone to hydrogen bonding, namely the acrylic oxygen atom and the amide hydrogens. Putting a water molecule in the vicinity of these hydrogen bond donors and acceptors, results in 3 conformations for each monomer:

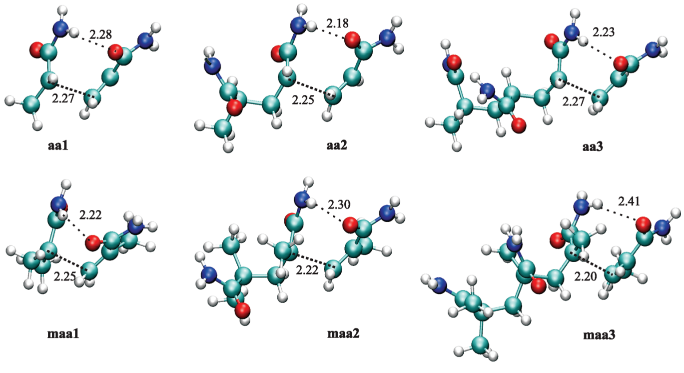

Figure 3. Gas phase transition states for the addition of AA and MAA to a monomeric, dimeric, and trimeric propagating radical.

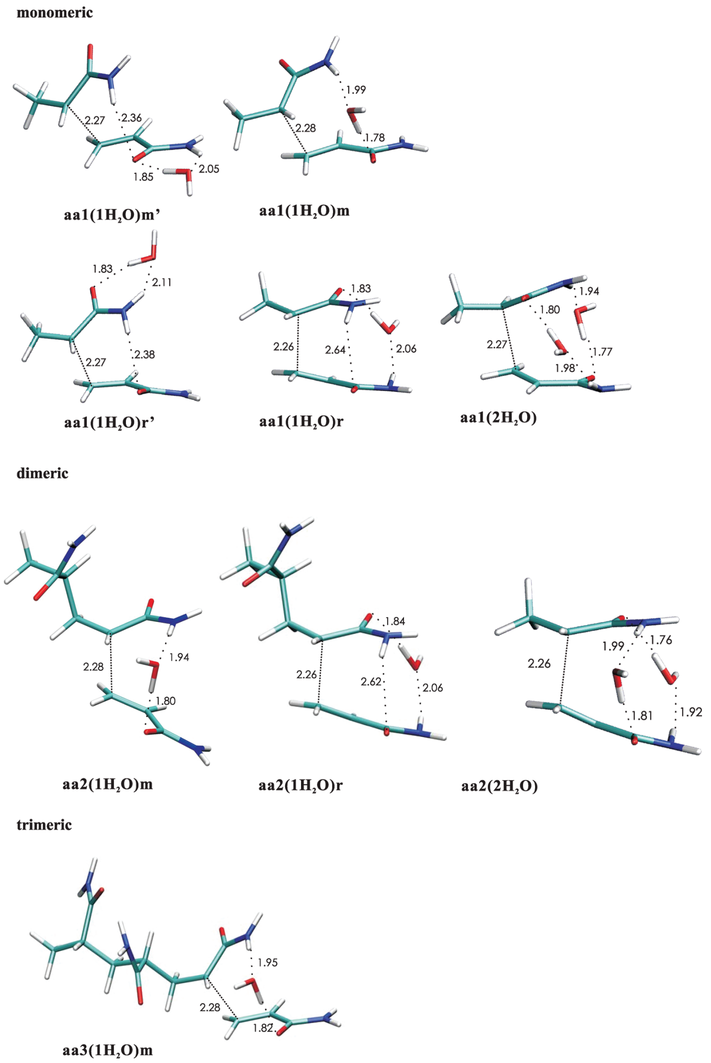

aa1(1H$_2$O)m' **aa1(1H$_2$O)m**

aa1(1H$_2$O)r' **aa1(1H$_2$O)r** **aa1(2H$_2$O)**

aa2(1H$_2$O)m **aa2(1H$_2$O)r** **aa2(2H$_2$O)**

aa3(1H$_2$O)m

Figure 4. Solvated structures of the AA transition states.

aa_a, **aa_b**, **aa_c** and **maa_a**, **maa_b**, **maa_c**, see Figure 2 and Table 1. Both static and dynamic studies on the solvation of acrylamide in water, performed by Balbuena et.al.,[34,35] show that the acrylamide carbonyl oxygen coordinates with water hydrogen and that the bridge-type interactions **aa_a** and **maa_a** are the most stable. These findings are confirmed here for various electronic structure methods. In the rest of this paper, the water bridge solvated monomers **aa_a** and **maa_a** will be taken as a reference reactant for calculating the energetics of the reactions considered.

Next, the transition state for the addition of the acrylamide (AA) and methacrylamide (MAA) monomer to their respective radicals is investigated. In a first step, geometry optimizations for transition states are performed in the gas phase using the B3LYP/6-31+G(d,p) electronic structure method. Moreover, due to the orientation of both molecules in the most stable transition state *in vacuo* for the syndiotactic attack, intermolecular hydrogen bonding takes place between the acrylic oxygen from the monomer and an amide hydrogen from the radical, as shown in Figure 3. On the same figure, the

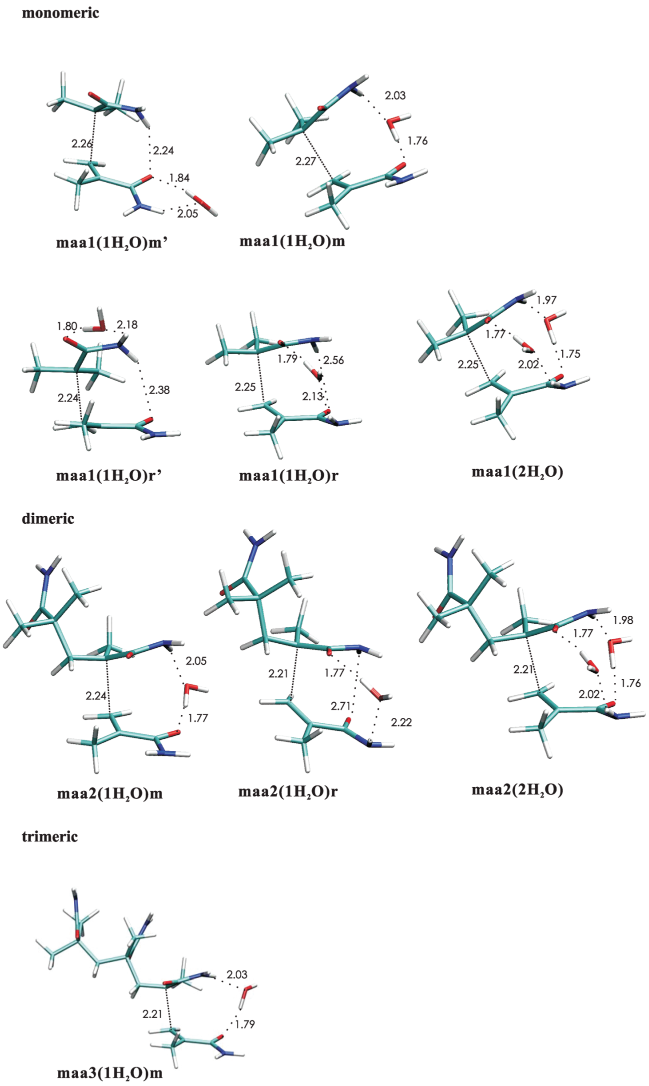

Figure 5. Solvated structures of the MAA transition states.

dimeric and trimeric transition states are also shown for both AA and MAA, and they all show similar characteristics. Rotation of the monomeric transition state about the forming bond does not result in more stable structures, because it would involve breaking of the intermolecular hydrogen bond.

In a next step, solvation of the transition states is studied by explicitly including one or two water molecules to the optimized gas phase geometry and a subsequent reoptimization at the same level of theory. The water molecules were placed around the studied transition states by first identifying the hydrogen bond donors and acceptors in the system. The carbonyl oxygen and the amide hydrogens are the most important sites for interactions with water. Starting with the monomeric transition state, a water molecule was positioned in the vicinity of a hydrogen bond donor or acceptor and the structure was reoptimized to obtain a transition state

Table 2. Gibbs Free Energy (298 K) of Solvation in Vacuo and in the C-PCM Model for the Studied Transition States in the Formation of PAA Using the B3LYP/6-31+G(d,p) Geometries and Single Point Energy Calculations at a Variety of Electronic Structure Methods[a]

	B3LYP		MPWB1K		BMK		MP2		B2PLYP	
	ΔG_{sol}^{vacuo}	ΔG_{sol}^{cpcm}	ΔG_{sol}^{vacuo}	ΔG_{sol}^{cpcm}	ΔG_{sol}^{vacuo}	ΔG_{sol}^{cpcm}	ΔG_{sol}^{vacuo}	ΔG_{sol}^{cpcm}	ΔG_{sol}^{vacuo}	ΔG_{sol}^{cpcm}
aa1(1H$_2$O)m′	5.6	−3.9	2.4	−5.2	6.0	−1.6	1.8	−7.5	1.3	−7.0
aa1(1H$_2$O)r′	2.5	−4.3	−1.4	−6.4	2.4	−2.2	−2.4	−8.7	−1.9	−7.5
aa1(1H$_2$O)m	−2.0	−13.0	−2.8	−11.9	−0.5	−9.0	−7.2	−17.5	−7.3	−16.4
aa1(1H$_2$O)r	4.3	3.9	−1.7	0.5	2.4	4.6	−6.8	−7.4	−4.2	−2.9
aa1(2H$_2$O)	−1.7	−9.4	−9.7	−13.5	−3.1	−6.0	−18.2	−25.4	−15.5	−19.6
aa2(1H$_2$O)m	−3.8	−11.3	−4.1	−11.1	−2.3	−7.7	−10.6	−17.6	−9.6	−15.9
aa2(1H$_2$O)r	3.7	3.9	−1.9	0.4	1.8	4.5	−7.5	−7.5	−4.9	−3.0
aa2(2H$_2$O)	−0.9	−9.1	−8.0	−14.0	−2.5	−6.1	−18.9	−26.5	−15.4	−20.5
aa3(1H$_2$O)m	1.3	−10.3	0.6	−10.1	3.1	−6.7	−6.5	−17.7	−5.1	−15.5

[a] All values are in kJ·mol^{-1}.

Table 3. Gibbs Free Energy (298 K) of Solvation in Vacuo and in the C-PCM Model for the Studied Transition States in the Formation of PAA Using the B3LYP/6-31+G(d,p) Geometries and Single Point Energy Calculations at a Variety of Electronic Structure Methods[a]

	B3LYP		MPWB1K		BMK		MP2		B2PLYP	
	ΔG_{sol}^{vacuo}	ΔG_{sol}^{cpcm}	ΔG_{sol}^{vacuo}	ΔG_{sol}^{cpcm}	ΔG_{sol}^{vacuo}	ΔG_{sol}^{cpcm}	ΔG_{sol}^{vacuo}	ΔG_{sol}^{cpcm}	ΔG_{sol}^{vacuo}	ΔG_{sol}^{cpcm}
maa1(1H$_2$O)m′	6.3	−4.2	4.4	−4.9	7.1	−1.5	2.4	−7.9	2.0	−7.4
maa1(1H$_2$O)r′	4.2	−0.7	−1.2	−4.7	3.4	0.3	−3.7	−8.5	−1.3	−5.1
maa1(1H$_2$O)m	5.6	−7.3	2.1	−10.3	4.1	−7.3	−2.7	−16.0	−1.2	−13.1
maa1(1H$_2$O)r	9.0	25.9	5.5	5.9	7.7	8.8	−1.7	−2.9	0.8	1.4
maa1(2H$_2$O)	4.4	−3.0	−2.4	−8.1	2 2	−1.8	−13.6	−21.3	−10.0	−15.0
maa2(1H$_2$O)m	4.9	−4.2	0.9	−7.8	3.1	−4.6	−5.1	−14.6	−2.8	−11.0
maa2(1H$_2$O)r	9.1	9.5	4.8	6.8	6.8	9.4	−2.7	−2.2	0.4	2.6
maa2(2H$_2$O)	5.9	−3.3	0.0	−7.5	3.9	−1.7	−12.7	−22.0	−8.9	−15.8
maa3(1H$_2$O)m	4.8	−6.4	3.9	−6.6	5.1	−4.7	−0.9	−12.4	−1.2	−11.5

[a] All values are in kJ·mol^{-1}.

with one imaginary frequency. With this procedure, one or two water molecules were added to the system. The resulting structures are compared to each other and the Gibbs free energy of solvation is evaluated with respect to the transition state in vacuo since this number will determine the rate enhancement resulting from the water molecule. The different water positions that are considered at this stage are shown in Figure 4 for acrylamide and in Figure 5 for methacrylamide.

The possible locations of the water molecules are first explained for the monomeric transition state of acrylamide **aa1**. Two different water orientations can be distinguished: nonbridging and bridging solvation. In the former kind, a water molecule coordinates with the propagating monomer (**aa1(1H$_2$O)m′** and **maa1(1H$_2$O)m′**) or radical (**aa1(1H$_2$O)r′** and **maa1(1H$_2$O)r′**). When a water molecule makes a connection between both reactants, it can either replace the existing hydrogen bond by a water bridge (**aa1(1H$_2$O)m** and **maa1(1H$_2$O)m**, the water molecule interacts with the oxygen atom of the monomer) or create a new water bridge at the other side of the structure (**aa1(1H$_2$O)r** and **maa1(1H$_2$O)r**, the water molecule interacts with the oxygen atom of the radical). Analogous sampling for the possible locations of the water molecule were performed for methacrylamide and are shown in Figure 5. For the dimeric and trimeric transition states, the sampling was restricted to bridging structures as they were found to be more stable than the nonbridging geometries. In a further step, single-point C-PCM free energy calculations are performed. This is repeated for a variety of electronic structure methods as outlined in the Computational Details. The Gibbs free energies of solvation for the acrylamide transition states are given in Table 2 for the explicit solvent model (ΔG_{sol}^{vacuo}) and the explicit/implicit solvent model using the C-PCM scheme (ΔG_{sol}^{cpcm}). Table 3 reports the results for methacrylamide.

It is clear that not all the considered positions for water molecules are equally favored. The nonbridging interactions are in general less favorable and therefore, only bridging interactions were considered for the larger chains. The bridging interactions (**aa1(1H$_2$O)m**, **aa2(1H$_2$O)m**, **aa3(1H$_2$O)m** and **maa1(1H$_2$O)m**, **maa2(1H$_2$O)m**, **maa3(1H$_2$O)m**) give rise to the largest negative free energies of solvation, ΔG_{sol}^{cpcm}. This feature is a combined effect from hydrogen bonding and the interaction with the bulk solvent that can be observed over all electronic structure methods studied. Relaxing the intramolecular hydrogen bond also seems to be an incentive for a second water bridge at the other side of the transition state, resulting in negative free energies of solvation for transition states with a double water bridge (**aa1(2H$_2$O)**, **aa2(2H$_2$O)** and **maa1(2H$_2$O)**, **maa2(2H$_2$O)**). For electronic structure methods including dispersion interactions, the total free energy of solvation becomes more negative than with one water molecule. In that case, two water bridges are formed between the monomer and the propagating radical.

The preference to form bridging interactions with water molecules rather than direct hydrogen bonds was calculated before and is important in understanding water-mediated interactions.[60] The free energy decrease means that the presence of the water molecule will increase the reaction rate since the water-assisted transition state is more favorable compared to the gas phase transition state. For the monomeric transition states, the water bridge loosening the intramolecular hydrogen bond is the most favored one and will be considered in the next section. In that section, also dimeric and trimeric structures, with bridging solvation will be considered because that type of interaction will have the most prominent effect on reaction kinetics, as will be shown in the next section.

Reaction Kinetics. In order to determine the reaction rates and kinetic parameters, internal reaction coordinate (IRC) calculations were performed in order to find the reactant and product structures that correspond to each transition state that was selected in the previous section. The gas phase results will be used as a reference point. The IRC calculations

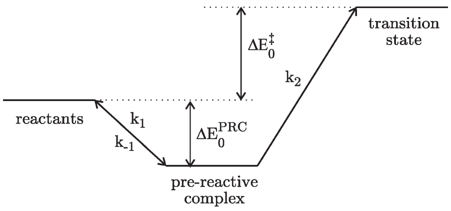

Figure 6. Schematic representation of the role of the prereactive complex in the apparent reaction rate coefficient.

show the existence of prereactive complexes (PRCs) (see Figure 7) and a dimeric, trimeric or tetrameric radical as products. The PRCs are characterized by water molecules forming hydrogen bridges between monomer and radical, but the reactants are not properly aligned to form the carbon−carbon bond.

By considering the PRCs, the apparent kinetic parameters can be split up in two contributions: the unimolecular rate coefficient (k_2) and the equilibrium constant for the formation of the PRC (K_1) as is shown in Figure 6.[61]

$$\mathrm{M} + \mathrm{R}_m^{\bullet} \underset{k_{-1}}{\overset{k_1}{\rightleftharpoons}} \mathrm{PRC} \tag{1}$$

$$\mathrm{PRC} \xrightarrow{k_2} \mathrm{R}_{m+1}^{\bullet} \tag{2}$$

$$r = k_2[\mathrm{PRC}] \tag{3}$$

$$\frac{\mathrm{d}[\mathrm{PRC}]}{\mathrm{d}t} = 0 = -k_2[\mathrm{PRC}] + k_1[\mathrm{M}][\mathrm{R}_m^{\bullet}] - k_{-1}[\mathrm{PRC}] \tag{4}$$

$$r = k_{app}[\mathrm{M}][\mathrm{R}_m^{\bullet}] = \frac{k_1 \times k_2}{k_{-1} + k_2}[\mathrm{M}][\mathrm{R}_m^{\bullet}] = K_1 k_2[\mathrm{M}][\mathrm{R}_m^{\bullet}] \tag{5}$$

$$k_{app} = K_1 k_2 \tag{6}$$

When assuming that the reaction is not diffusion-controlled, the reaction rate can be written as eq 3. The unknown PRC concentration in this equation follows from a pseudo-stationary state hypothesis on these species (eq 4). In eq 5, the factor k_2 in the denominator is smaller than k_{-1} because the reaction is assumed to be kinetically controlled, resulting in the apparent reaction rate coefficient that is shown in eq 6. This also means that calculating the reaction rate from separated reactants will result in exactly the same rate coefficients as compared to calculating the product of the equilibrium constant and the unimolecular reaction rate. Although one could start from the separated reactants, the PRC concept is very valuable to get more insight into the role of the solvent molecules and their ability to stabilize the transition state. In the following the apparent reaction rate coefficient, k_{app}, will be systematically used for the reaction rate constant.

The kinetic parameters for the selected reactions from Table 2 are shown in Table 4 for the polymerization of acrylamide and in Table 6 for the analogous reactions of methacrylamide. The predicted kinetic parameters when

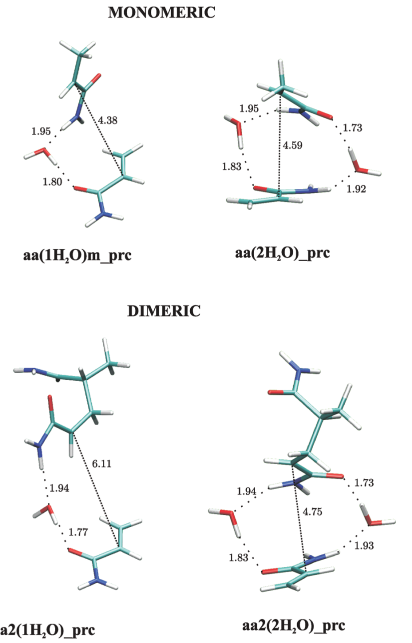

$aa(1H_2O)m\_prc$ $aa(2H_2O)\_prc$ $aa2(1H_2O)\_prc$ $aa2(2H_2O)\_prc$

Figure 7. Prereactive complexes for the polymerization of AA.

applying a C-PCM model to the optimized transition states in vacuo are taken up in Table 5 for AA and in Table 7 for MAA.

It a well-known feature and it is confirmed by these calculations that gas phase predictions (**aa1**, **aa2**, **aa3** in Table 4 and **maa1**, **maa2**, **maa3** in Table 6) with standard DFT functionals like B3LYP systematically underestimate the propagation rate constants.[7,62] Choosing other electronic structure methods like BMK, MPWB1K, or B2PLYP can drastically increase the rate constants (k_p), but the propagation rate remains underestimated by at least 2 orders of magnitude, when not accounting for the molecular environment. For the B3LYP functional it is a common feature that reaction barriers are overestimated, yielding unrealistically low absolute values for the reaction rate constants.[37] With BMK—a functional better suited for reproducing kinetics—the k_p values increase with 2 or 3 orders of magnitude, getting closer to the experimental values. Taking dispersion interactions into account with B2PLYP, only small changes are noticed with respect to the BMK predictions: the similarity of the gas phase k_p predictions in both DzaFT methods is striking. The implicit solvation model preferentially stabilizes the transition state, giving rise to a significant increase of 4 orders of magnitude for the reaction rate coefficient in case of AA (Table 5). This drastic enhancement brings some k_p's closer to experiment but for the more advanced electronic methods (MPWB1K, BMK, ...) one gets an overshoot of 2 orders of magnitude. The situation is somewhat different for MAA where the increase is less drastic (Table 7) resulting in a better overall agreement with experiment. It should be noticed, however, that the k_p ratio for AA and MAA polymerization (which is about 75

Table 4. Kinetic parameters for the addition of acrylamide to a monomeric (*n* = 1), dimeric (*n* = 2) and trimeric (*n* = 3) radical chain for different levels of solvation and different electronic structure methods[a]

	B3LYP			MPWB1K		BMK		MP2		B2PLYP	
	A	E_A	k_{298K}	E_A	k_{298K}	E_A	k_{298K}	E_A	k_{298K}	E_A	k_{298K}
					Monomer						
aa1	2.08×10^{2}	26.3	5.2×10^{-3}	17.0	2.2×10^{-1}	19.5	8.0×10^{-2}	31.8	5.8×10^{-4}	19.7	7.4×10^{-2}
aa1(1H$_2$O)m	2.39×10^{2}	18.6	1.3×10^{-1}	11.2	2.5×10^{0}	13.1	1.2×10^{0}	21.4	4.4×10^{-2}	10.5	3.3×10^{0}
aa1(2H$_2$O)	1.59×10^{1}	7.3	8.3×10^{-1}	−5.0	1.1×10^{2}	−1.5	2.8×10^{1}	3.4	4.0×10^{0}	−5.7	1.5×10^{2}
					Dimer						
aa2	1.42×10^{2}	24.8	6.6×10^{-3}	13.6	5.9×10^{-1}	17.5	1.2×10^{-1}	26.5	3.3×10^{-3}	16.3	1.9×10^{-1}
aa2(1H$_2$O)m	7.83×10^{2}	19.0	3.6×10^{-1}	10.3	1.2×10^{1}	13.0	4.1×10^{0}	16.5	1.0×10^{0}	8.7	2.3×10^{1}
aa2(2H$_2$O)	1.08×10^{1}	6.8	6.7×10^{-1}	−6.4	1.3×10^{2}	−2.7	3.1×10^{1}	−2.4	2.6×10^{1}	−8.6	3.3×10^{2}
					Trimer						
aa3	2.30×10^{2}	26.7	5.0×10^{-3}	15.6	4.3×10^{-1}	18.8	1.2×10^{-1}	25.4	8.3×10^{-3}	17.0	2.4×10^{-1}
aa3(1H$_2$O)m	1.10×10^{2}	20.1	3.3×10^{-2}	11.1	1.2×10^{0}	13.6	4.4×10^{-1}	13.6	4.6×10^{-1}	7.8	4.5×10^{0}
					Experimental Values						
ref 21	1.58×10^{4}	13.4	7.4×10^{1}								
ref 21	1.26×10^{4}	12.9	7.1×10^{1}								

[a] E_A is in kJ·mol^{-1}, A is in m^3.mol^{-1}.s^{-1}, hence k_{298K} is in mol.m^{-3}.s^{-1}.

Table 5. Kinetic Parameters for the Addition of Acrylamide to a Monomeric (*n* = 1), Dimeric (*n* = 2), or Trimeric (*n* = 3) Radical Chain for Different Levels of Solvation and Different Electronic Structure Methods Using the Implicit/Explicit Solvent Model[a]

	k_{298K}				
	B3LYP	MPWB1K	BMK	MP2	B2PLYP
			Monomer		
aa1	6.6×10^{1}	2.6×10^{3}	6.7×10^{2}	7.7×10^{0}	1.0×10^{3}
aa1(1H$_2$O)m	1.7×10^{3}	2.5×10^{4}	8.3×10^{3}	3.7×10^{2}	3.5×10^{4}
aa1(2H$_2$O)	3.9×10^{1}	2.8×10^{3}	5.9×10^{2}	3.7×10^{2}	4.4×10^{3}
			Dimer		
aa2	2.7×10^{1}	1.4×10^{3}	3.4×10^{2}	1.7×10^{1}	7.5×10^{2}
aa2(1H$_2$O)m	3.4×10^{2}	9.8×10^{3}	2.4×10^{3}	8.4×10^{2}	1.7×10^{4}
aa2(2H$_2$O)	1.8×10^{1}	2.5×10^{3}	3.7×10^{2}	1.4×10^{3}	4.8×10^{3}
			Trimer		
aa1	1.4×10^{1}	8.7×10^{2}	2.0×10^{2}	2.6×10^{1}	6.4×10^{2}
aa3(1H$_2$O)m	1.2×10^{2}	4.0×10^{3}	9.5×10^{2}	1.4×10^{3}	1.4×10^{4}
			Experimental Values		
ref 21	7.4×10^{1}				
ref 21	7.1×10^{1}				

[a] k_{298K} is in mol·m^{-3}·s^{-1}.

experimentally) is well reproduced by the MPWB1K, BMK, and B2PLYP methods in the continuum solvent model approach, yielding a ratio of 38, 71, and 94 respectively using the trimer radical (Table 8). None of the gas phase methods succeeds in reproducing this ratio properly. With B3LYP, the ratio is exhaustively too large giving values between 500 and 5000 both with and without implicit solvent model, indicating that this functional does not reproduce the qualitative features of the polymerization, as was earlier reported by Coote et al.[37]

From Table 4 and Table 6, the influence of adding explicit water molecules on the activation energy becomes very clear. Upon the addition of one or two water molecules, a significant decrease in activation energy is observed. Depending on the electronic level of theory the shift varies between 4 and 10 kJ/mol in case of one explicit water molecule. The main effect of the explicit water molecule is loosening the original intermolecular hydrogen bond between the amide hydrogen and the acrylic oxygen. This strong interaction forces the substituents about the forming bond to take an almost eclipsed configuration of 18° for AA and 5° for MAA (see Figure 8) in vacuo. In the presence of a water molecule, the angle between the substituents rises to 30° and 35°, respectively, causing structural relaxation. This results in an increase of the reaction rate coefficient, regardless of the electronic structure method or polymer model that is used.

Some activation energies turn out to become negative upon the addition of two water molecules and require some special attention. Because of the very high negative solvation energy, this transition state can become more stable than its reactants and the reaction can therefore exhibit a negative activation energy. This shows that the modeled reaction is not elementary, but a combination of two events: the formation of the prereactive complex (for which pseudo stationarity is assumed) and the unimolecular reaction transforming this complex into the products. This negative activation energy is a result of linearly fitting the natural logarithm of the obtained numbers for k_p against temperature inversed. At low temperatures, the relative importance of the PRC is higher and it can therefore have an influence on the reaction rate while at higher temperature, it is easily formed and the reaction itself is the only determining factor. For acrylamide, the trimeric model with 1 explicit water molecule (**aa3(1h2o)m**) gives results that lie very close to the experimental ones with the BMK, MPWB1K and B2-PLYP functional and the MP2 method. Especially the activation energy is in good agreement with the experimental value whereas the frequency factor is underestimated for the B3LYP geometries. The same is the case for MAA: although the better electronic structure methods yield activation energies that lie in the near vicinity of the experimental value, the reaction rate is underestimated. For the MAA monomer, the discrepancy is bigger than for AA. Rather than focusing solely on the quantitative agreement between calculated and experimental rate constants, it is more important to validate whether qualitative trends are reproduced. The AA/MAA rate ratios are shown in Table 8. The explicitly solvated trimeric model gives a AA/MAA ratio of 57 and 68 at the MPWB1K and BMK level of theory, which is in very good agreement with the experimental value of 67. B3LYP again significantly overestimates the ratio.

Table 6. Kinetic Parameters for the Addition of Methacrylamide to a Monomeric (*n* = 1), Dimeric (*n* = 2), or Trimeric (*n* = 3) Radical Chain for Different Levels of Solvation and Different Electronic Structure Methods[a]

	B3LYP			MPWB1K		BMK		MP2		B2PLYP	
	A	E_A	k_{298K}	E_A	k_{298K}	E_A	k_{298K}	E_A	k_{298K}	E_A	k_{298K}
					Monomer						
maa1	7.24×10^1	31.6	2.2×10^{-4}	15.9	1.2×10^{-1}	19.9	2.4×10^{-2}	19.6	2.6×10^{-2}	17.5	6.1×10^{-2}
maa1(1H$_2$O)m	1.78×10^1	27.7	2.6×10^{-4}	11.2	1.9×10^{-1}	14.2	5.7×10^{-2}	10.0	3.1×10^{-1}	10.8	2.3×10^{-1}
maa1(2H$_2$O)	1.65×10^0	17.8	1.3×10^{-3}	0.5	1.3×10^0	3.2	4.4×10^{-1}	−4.4	9.4×10^0	−3.0	5.2×10^0
					Dimer						
maa2	3.55×10^1	40.1	3.5×10^{-6}	17.9	2.6×10^{-2}	22.8	3.6×10^{-3}	18.9	1.7×10^{-2}	22.0	5.0×10^{-3}
maa2(1H$_2$O)m	1.04×10^1	36.0	5.4×10^{-6}	12.5	6.7×10^{-2}	16.6	1.3×10^{-2}	7.3	5.3×10^{-1}	14.1	3.5×10^{-2}
maa2(2H$_2$O)	1.29×10^0	28.1	1.6×10^{-5}	4.9	1.7×10^{-1}	8.1	4.8×10^{-2}	−3.9	5.9×10^0	3.0	3.7×10^{-1}
					Trimer						
maa3	5.33×10^1	42.1	2.4×10^{-6}	18.8	2.7×10^{-2}	23.6	3.9×10^{-3}	18.2	3.5×10^{-2}	22.6	5.9×10^{-3}
maa3(1H$_2$O)m	4.08×10^1	40.2	3.9×10^{-6}	18.8	2.1×10^{-2}	21.7	6.5×10^{-3}	13.2	2.0×10^{-1}	18.6	2.2×10^{-2}
					Experimental Values						
ref 29		20.0	1.1×10^0								

[a] E_A is in kJ·mol^{-1}, and A is in m^3·mol^{-1}·s^{-1}; hence, k_{298K} is in mol·m^{-3}·s^{-1}.

Table 7. Kinetic Parameters for the Addition of Methacrylamide to a Monomeric (*n* = 1), Dimeric (*n* = 2), or Trimeric (*n* = 3) Radical Chain for Different Levels of Solvation and Different Electronic Structure Methods Using the Implicit/Explicit Solvent Model[a]

	k_{300K}				
	B3LYP	MPWB1K	BMK	MP2	B2PLYP
			Monomer		
maa1	1.3×10^{-1}	7.0×10^1	9.2×10^0	1.5×10^1	3.9×10^1
maa1(1H$_2$O)m	2.2×10^{-1}	1.9×10^2	3.3×10^1	2.0×10^2	1.7×10^2
maa1(2H$_2$O)	2.7×10^{-3}	2.7×10^0	5.4×10^{-1}	4.4×10^1	8.0×10^0
			Dimer		
maa2	1.1×10^{-2}	5.8×10^1	6.7×10^0	6.0×10^1	1.5×10^1
maa2(1H$_2$O)m	5.2×10^{-3}	6.0×10^1	8.2×10^0	4.6×10^2	2.9×10^1
maa2(2H$_2$O)	8.0×10^{-7}	6.5×10^{-3}	1.1×10^{-3}	3.9×10^{-1}	1.2×10^{-2}
			Trimer		
maa3	2.6×10^{-3}	2.3×10^1	2.8×10^0	5.3×10^1	6.8×10^0
maa3(1H$_2$O)m	3.1×10^{-3}	1.5×10^1	3.5×10^0	1.7×10^2	1.5×10^1
			Experimental Values		
ref 29	1.1×10^0				

[a] k_{298K} is in mol·m^{-3}·s^{-1}.

Table 8. AA/MAA Rate Ratio for Addition to a Trimeric Radical in Vacuo, with 1 Explicit Water Molecule, in the Continuum Model and in the Combined Explicit/Implicit Solvation Model for All Studied Electronic Structure Methods[a]

	in vacuo		C-PCM	
	without H$_2$O	with 1 H$_2$O	without H$_2$O	with 1 H$_2$O
B3LYP	2083	8462	5385	38 710
MPWB1K	16	57	38	267
BMK	31	68	71	271
MP2	0	2	0	8
B2PLYP	41	205	94	933
experimental		67−75		

[a] The experimental range for this ratio is about 67−75.

The mixed implicit/explicit solvent model results, based on the free energy differences in solution, account for a major increase in the reaction rates of about 3 orders of magnitude. They largely overshoot the experimental values for acrylamide polymerization, while reproducing the MAA polymerization rate quite well. As a result the AA/MAA rate ratio is too large, giving values of around 270 at the best levels of theory. At first sight, the mixed solvation models give better results for the MAA polymerization system but these are probably due to a fortuitous cancellation of effects. An interesting study concerning the mixed solvation models was recently published by Warshel et al.[42] The reliability of the mixed solvation models is largely dependent on the conformations of the water molecules. There is no guarantee that the explicit water molecules have the correct orientation as they would have in an explicit infinite system, for instance reulting from QM/MM molecular dynamics runs. For the MAA polymerization system, the combination of a too low k_p prediction with explicit solvent molecules with an excessive effect of the C-PCM model on a system with explicit water molecules leads to a fairly good agreement with the experiment but this is due to a cancellation of errors.

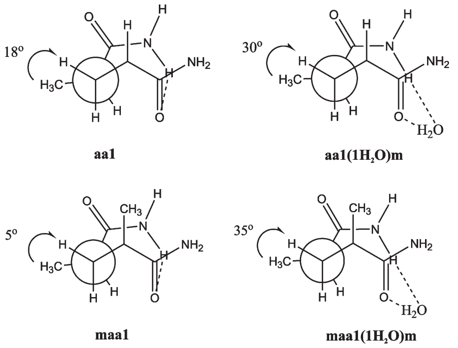

Figure 8. Newman projection along the forming bond for the acrylamide and methacrylamide monomeric transition states with 0 and 1 water molecule assisting.

Conclusion

The radical polymerization reaction for both acrylamide and methacrylamide was studied in the presence and absence of explicit water molecules. The calculations reveal that an important solvent effect can be attributed to these solvent molecules, stabilizing the transition state and thereby lowering the activation energy of the reactions by 4−10 kJ/mol depending on the electronic structure method used. As the propagation rates were seriously underestimated when modeled in the gas phase, the inclusion of explicit water molecules brings the propagation rates much closer to the experimental values. The reaction rates also increase significantly by using an implicit solvent model. In general, gas phase calculations can give reliable and quite accurate activation energies when an appropriate description of the system is used in terms of electronic structure method and explicit solvation. A remaining challenge lies in a good description of the pre-exponential factor. More advanced techniques in which the solvent environment around the reactive center is taken into account entirely, so as to include all possible entropic contributions might contribute to a better description of the pre-exponential factor. Apart from the absolute comparison of calculated and experimental rate constants it is also very important to validate the relative rates of polymerization of the AA versus the MAA polymerization system. Experimentally, this ratio is estimated at 67. Simple gas phase calculations underestimate this ratio apart from B3LYP which gives unrealistically high results. The ratio is well reproduced when using the implicit or the explicit solvation model. The results of the mixed solvation model should be treated with care as the results are very much dependent on the position of the explicit solvent molecules. In general, the BMK and MPWB1K functionals give the best quantitative and qualitative picture for the trimeric model. These results are in agreement with the earlier work of Broadbelt and co-workers.[10]

Acknowledgment. The authors thank the FWO (Fonds voor Wetenschappelijk Onderzoek−Vlaanderen, Fund for Scientific Research−Flanders), the research board of Ghent University and the IAP-BELSPO project in the frame of IAP 6/27 for financial support of this research. Computational resources and services used in this work were provided by Ghent University.

Supporting Information Available: Tables of the *xyz* coordinates and energies of all structures. This material is available free of charge via the Internet at http://pubs.acs.org.

References and Notes

(1) Olaj, O. F.; Bitai, I.; Hinkelmann, F. *Makromol. Chem.* **1987**, *188*, 1689–1702.
(2) Olaj, O. F.; Schnollbitai, I. *Eur. Polym. J.* **1989**, *25*, 635–641.
(3) Van Herk, A. M. *Macromol. Theor. Simul.* **2000**, *9*, 433–441.
(4) Beuermann, S.; Buback, M. *Prog. Polym. Sci.* **2002**, *27*, 191–254.
(5) Barner-Kowollik, C.; Buback, M.; Egorov, M.; Fukuda, T.; Goto, A.; Olaj, O. F.; Russell, G. T.; Vana, P.; Yamada, B.; Zetterlund, P. B. *Prog. Polym. Sci.* **2005**, *30*, 605–643.
(6) Van Cauter, K.; Van Speybroeck, V.; Vansteenkiste, P.; Reyniers, M. F.; Waroquier, M. *ChemPhysChem* **2006**, *7*, 131–140.
(7) Van Cauter, K.; Hemelsoet, K.; Van Speybroeck, V.; Reyniers, M. F.; Waroquier, M. *Int. J. Quantum Chem.* **2005**, *102*, 454–460.
(8) Degirmenci, I.; Avci, D.; Aviyente, V.; Van Cauter, K.; Van Speybroeck, V.; Waroquier, M. *Macromolecules* **2007**, *40*, 9590–9602.
(9) Degirmenci, I.; Aviyente, V.; Van Speybroeck, V.; Waroquier, M. *Macromolecules* **2009**, *42*, 3033–3041.
(10) Yu, X. R.; Pfaendtner, J.; Broadbelt, L. J. *J. Phys. Chem. A* **2008**, *112*, 6772–6782.
(11) Thickett, S. C.; Gilbert, R. G. *Macromolecules* **2008**, *41*, 4528–4530.
(12) Huang, D. M.; Monteiro, M. J.; Gilbert, R. G. *Macromolecules* **1998**, *31*, 5175–5187.
(13) Van Cauter, K.; Van Speybroeck, V.; Waroquier, M. *ChemPhysChem* **2007**, *8*, 541–552.
(14) Olaj, O. F.; Schnoll-Bitai, I. *Monatsh. Chem.* **1999**, *130*, 731–740.
(15) Beuermann, S. *Macromol. Rapid Commun.* **2009**, *30*, 1066–1088.
(16) Beuermann, S.; Garcia, N. *Macromolecules* **2004**, *37*, 3018–3025.
(17) O'driscoll, K. F.; Monteiro, M. L.; Klumperman, B. *J. Polym. Sci. A* **1997**, *35*, 515–520.
(18) Zammit, M. D.; Davis, T. P.; Willett, G. D.; Odriscoll, K. F. *J. Polym. Sci. A* **1997**, *35*, 2311–2321.
(19) Beuermann, S. *Macromolecules* **2004**, *37*, 1037–1041.
(20) Lin, H. R. *Eur. Polym. J.* **2001**, *37*, 1507–1510.
(21) Seabrook, S. A.; Tonge, M. P.; Gilbert, R. G. J. *Polym. Sci. A* **2005**, *43*, 1357–1368.
(22) Jiang, Y.; Garland, M.; Carpenter, K. J.; Suresh, P. S.; Widjaja, E. *J. Polym. Sci. A* **2007**, *45*, 5697–5704.
(23) Ganachaud, F.; Balic, R.; Monteiro, M. J.; Gilbert, R. G. *Macromolecules* **2000**, *33*, 8589–8596.
(24) Kuchta, F. D.; van Herk, A. M.; German, A. L. *Macromolecules* **2000**, *33*, 3641–3649.
(25) Lacik, I.; Beuermann, S.; Buback, M. *Macromolecules* **2003**, *36*, 9355–9363.
(26) Beuermann, S.; Paquet, D. A.; McMinn, J. H.; Hutchinson, R. A. *Macromolecules* **1997**, *30*, 194–197.
(27) Kamachi, M. *Adv. Polym. Sci.* **1987**, *82*, 207–275.
(28) Pascal, P.; Winnik, M. A.; Napper, D. H.; Gilbert, R. G. *Macromolecules* **1993**, *26*, 4572–4576.
(29) Pascal, P.; Napper, D. H.; Gilbert, R. G.; Piton, M. C.; Winnik, M. A. *Macromolecules* **1990**, *23*, 5161–5163.
(30) Seabrook, S. A.; Gilbert, R. G. *Polymer* **2007**, *48*, 4733–4741.
(31) Thiel, J.; Maurer, G.; Prausnitz, J. M. *Chem.-Ing.-Tech.* **1995**, *67*, 1567–1583.
(32) Fernandez-Barbero, A.; Suarez, I. J.; Sierra-Martin, B.; Fernandez-Nieves, A.; de las Nieves, F. J.; Marquez, M.; Rubio-Retama, J.; Lopez-Cabarcos, E. *Adv. Colloid Interface Sci.* **2009**, *147−48*, 88–108.
(33) Seelert, H.; Krause, F. *Electrophoresis* **2008**, *29*, 2617–2636.
(34) Aparicio-Martinez, A.; Hall, K. R.; Balbuena, P. B. *J. Phys. Chem. A* **2006**, *110*, 9183–9193.
(35) Aparicio-Martinez, S.; Balbuena, P. B. *Mol. Simulat.* **2007**, *33*, 925–938.
(36) Barabanova, A. I.; Bune, E. V.; Gromov, A. V.; Gromov, V. F. *Eur. Polym. J.* **2000**, *36*, 479–483.
(37) Izgorodina, E. I.; Coote, M. L. *Chem. Phys.* **2006**, *324*, 96–110.
(38) Thickett, S. C.; Gilbert, R. G. *Polymer* **2004**, *45*, 6993–6999.
(39) Pliego, J. R.; Riveros, J. M. *J. Phys. Chem. A* **2001**, *105*, 7241–7247.
(40) Kelly, C. P.; Cramer, C. J.; Truhlar, D. G. *J. Phys. Chem. A* **2006**, *110*, 2493–2499.
(41) da Silva, E. F.; Svendsen, H. F.; Merz, K. M. *J. Phys. Chem. A* **2009**, *113*, 6404–6409.
(42) Kamerlin, S. C. L.; Haranczyk, M.; Warshel, A. *ChemPhysChem* **2009**, *10*, 1125–1134.
(43) Heuts, J. P. A.; Gilbert, R. G.; Radom, L. *Macromolecules* **1995**, *28*, 8771–8781.
(44) Heuts, J. P. A.; Gilbert, R. G.; Radom, L. *J. Phys. Chem.* **1996**, *100*, 18997–19006.
(45) Zetterlund, P. B.; Busfield, W. K.; Jenkins, I. D. *Macromolecules* **1999**, *32*, 8041–8045.
(46) De Sterck, B.; Van Speybroeck, V.; Mangelinckx, S.; Verniest, G.; De Kimpe, N.; Waroquier, M. *J. Phys. Chem. A* **2009**, *113*, 6375–6380.
(47) Van Speybroeck, V.; Moonen, K.; Hemelsoet, K.; Stevens, C.; Waroquier, M. *J. Am. Chem. Soc.* **2006**, *128*, 8468–8478.
(48) Manukyan, A. K.; Radkiewicz-Poutsma, J. L. *J. Mol. Struct.—THEOCHEM* **2006**, *766*, 105–112.
(49) Kelly, C. P.; Cramer, C. J.; Truhlar, D. G. *J. Chem. Theory Comput.* **2005**, *1*, 1133–1152.
(50) Takano, Y.; Houk, K. N. *J. Chem. Theory Comput.* **2005**, *1*, 70–77.
(51) Frisch, M. J. et al.et al. *Gaussian 03, Revision C.02*; Gaussian, Inc.: Wallingford, CT, 2004.
(52) Becke, A. D. *J. Chem. Phys.* **1993**, *98*, 5648–5652.
(53) Lee, C. T.; Yang, W. T.; Parr, R. G. *Phys. Rev. B* **1988**, *37*, 785–789.
(54) Zhao, Y.; Truhlar, D. G. *J. Phys. Chem. A* **2004**, *108*, 6908–6918.
(55) Boese, A. D.; Martin, J. M. L. *Abstracts of Papers, 229th National Meeting of the American Chemical Society, San Diego, CA*; American Chemical Society: Washington, DC, 2005; p 274-COMP.
(56) Hemelsoet, K.; Van Speybroeck, V.; Waroquier, M. *J. Phys. Chem. A* **2008**, *112*, 13566–13573.
(57) Becke, A. D. *Phys. Rev. A* **1988**, *38*, 3098–3100.
(58) Grimme, S. *J. Chem. Phys.* **2006**, *124*, 034108.
(59) Korth, M.; Grimme, S. *J. Chem. Theory Comput.* **2009**, *5*, 993–1003.
(60) Bennaim, A. *J. Chem. Phys.* **1990**, *93*, 8196–8210.
(61) Singleton, D. L.; Cvetanovic, R. J. *J. Am. Chem. Soc.* **1976**, *98*, 6812–6819.
(62) Van Cauter, K.; Van den Bossche, B. J.; Van Speybroeck, V.; Waroquier, M. *Macromolecules* **2007**, *40*, 1321–1331.

Paper IV

Modeling the Solvent Effect on the Tacticity in the Free Radical Polymerization of Methyl Methacrylate

Değirmençi İ., Eren Ş., Aviyente V.,
De Sterck B., Hemelsoet K.,
Van Speybroeck V., and Waroquier M.

Macromolecules, **2010**, *43*, 5602-5610

5602 *Macromolecules* **2010**, *43*, 5602–5610
DOI: 10.1021/ma100608g

Macromolecules
ARTICLE

Modeling the Solvent Effect on the Tacticity in the Free Radical Polymerization of Methyl Methacrylate

İsa Değirmenci, Şükrü Eren, and Viktorya Aviyente*

Chemistry Department, Boğazici University, 34342, Bebek, Istanbul, Turkey

Bart De Sterck, Karen Hemelsoet, Veronique Van Speybroeck, and Michel Waroquier

Center for Molecular Modeling, Ghent University, Technologiepark 903, 9052 Zwijnaarde, Belgium, and QCMM-Alliance Ghent-Brussels, Belgium

Received March 21, 2010; Revised Manuscript Received May 15, 2010

ABSTRACT: The control of stereochemistry in the free radical polymerization of methyl methacrylate (MMA) is important because the physical properties of PMMA are often significantly affected by the main-chain tacticity. In this study, the role of the solvent on the tacticity of MMA polymerization has been investigated by considering the propagation rate constants for the syndiotactic and isotactic free radical polymerization of MMA in vacuum, in methanol (CH_3OH), and in 1,1,1,3,3,3-hexafluoro-2-(trifluoromethyl)propan-2-ol ($(CF_3)_3COH$). All geometry optimizations have been carried out with the B3LYP/6-31+G(d) methodology. The kinetics of the propagating dimer have been evaluated with the B3LYP/6-31+G(d), B3LYP/6-311+G(3df,2p), MPWB1K/6-311+G(3df,2p), and B2PLYP/6-31+G(d) methodologies. The role of the solvent has been investigated by using explicit solvent molecules and also by introducing a polarizable continuum model (IEF-PCM) with a dielectric constant specific to the solvent. Experimentally, the free radical polymerization of MMA in $(CF_3)_3COH$ is found to be highly syndiotactic (*rr* = 75% at 20 °C): the stereoeffects of fluoroalcohols are claimed to be due to the hydrogen-bonding interaction of the alcohols with the monomers and growing species. This modeling study has revealed the fact that the solvents CH_3OH and $(CF_3)_3COH$, which are H-bonded with the carbonyl oxygens located on the same side of the backbone hinder the formation of the isotactic PMMA to some extent. Methanol is less effective in reducing the isotacticity because of its small size and also because of the relatively loose hydrogen bonds ($\sim$1.9 Å) with the carbonyl oxygens. The methodologies used in this study reproduce the solvent effect on the free radical polymerization kinetics of MMA in a satisfactory way.

Introduction

The mechanical, thermal, and chemical properties of polymers substantially depend on their primary structures as represented by tacticities, molecular weights, and their distributions.[1] The control of tacticity and molecular weight for synthetic polymers contributes to the development of new materials.[2] The precise control of the molecular weight and/or the chain microstructure during radical polymerization is one of the important issues in the field of polymer synthesis because the polymer properties, such as toughness, solvent resistance, surface properties, and thermal resistance, are significantly influenced by their stereoregularity.[3] The stereoregularity of a polymer main chain is referred to as tacticity. Tacticity deals with the relationship between two adjacent monomer units consisting of meso (*m*) and racemo (*r*) diads. In general, stereocontrol based on radical polymerization is difficult to attain because of the planar characteristics of the propagating radical at the chain-end carbon.[4] Although most of the stereospecific polymerizations were reported for the coordination polymerizations of olefins such as propylene, the stereocontrol during free radical polymerization reactions has recently become possible.[5] Many attempts to produce stereospecific or stereoregular polymers have been made in confined media, such as the solid state, inclusion compounds, porous materials, and templates.[6,7] In solution polymerization, it is more difficult to provide a stereospecific environment around the growing radical center because the monomer and growing radical species move freely and diffuse in the reaction media. Therefore, vinyl monomers ordinarily produce polymers with an inherent tacticity specific to their chemical structures. From the viewpoint of production cost, solvent or additive-mediated systems might be the most promising solutions to obtain stereospecific polymers.

Okamoto and co-workers have reported the synthesis of highly stereocontrolled polymethacrylates,[8] polyacrylamides,[9−11] and polymethacrylamides[10−12] through radical polymerization using Lewis acids such as rare earth metal trifluoromethanesulfonates. Furthermore, fluorinated alcohols play an efficient role in controlling the stereospecificity of radical polymerizations of vinyl monomers.[13−15] A relevant study on how tacticity can arise by chain-end control in free radical polymerization of acrylates is given by Tanaka and Niwa.[16] The study suggested that the growing polymer radical end could control the stereochemistry of free radical polymerization depending on the *s-trans* and *s-cis* conformations of the monomer. Many industrially important vinyl polymers including PMMA are produced by free radical polymerization, which is generally poor in stereocontrol. Hence, the development of stereoregulation methods for radical polymerization can contribute to the industrial production of polymers with improved properties.[17] The control of the stereochemistry in MMA polymerization is important because the physical properties of PMMA are often significantly affected by the main-chain tacticity. In the free radical polymerization of MMA three different products are to be expected: syndiotactic (*rr*), isotactic (*mm*), and heterotactic (*mr*). Isobe et al.

---

*To whom correspondence should be addressed.

Table 1. Tacticity in the Free Radical Polymerization of MMA in Various Solvents at 20 °C[13c]

	solvent	tacticity *mm*/*mr*/*rr*
1	bulk	3/31/66
2	CH_3OH	3/32/66
3	$(CF_3)_3COH$	1/24/75

have enhanced the syndiotactic specificity of PMMA by using fluoroalcohols: the polymerization of MMA in perfluoro-*tert*-butyl alcohol (PFTB) $(CF_3)_3COH$ at −98 °C was achieved with the highest syndiotacticity (rr = 93%), whereas the syndiotacticity of PMMA is only 85% in methanol at −78 °C. Table 1 displays the tacticity ratios in the free radical polymerization of MMA at 20 °C.

Another issue concerns the solvent influence on the propagation kinetics in free radical polymerization. For a long time it was assumed that the solvent effects on the rate coefficients were rather small.[18] Propagation rate coefficients for styrene and methyl methacrylate (MMA) polymerizations in a wide variety of solvents (acetonitrile, dimethylformamide, anisole, methyl isobutyrate, bromobenzene, benzene, and 1,2-dichloroethane) only change mostly by around 10% (see review of S. Beuermann and references cited therein[18]). On the other hand, certain solvents, such as benzyl alcohol,[19,20] dimethylsulfoxide,[20] *N*-methylpyrrolidinone,[20] 2,6-dithiaheptane,[21] and 1,5-dithiacyclooctane,[21] turn out to induce a significant increase of k_p. In many cases hydrogen bonding is responsible for this observed increase. Experiments provided by data for acrylamide and *N*-isopropylacrylamide (NIPAM) suggest a strong increase of k_p upon addition of water to the system.[22]

In this study, the role of methanol (CH_3OH) and 1,1,1,3,3,3-hexafluoro-2-(trifluoromethyl)propan-2-ol ($(CF_3)_3COH$) on the tacticity of MMA polymerization will be considered by examining the propagation rate constants for the syndiotactic and isotactic free radical polymerization of MMA.

Computational Procedure

The B3LYP method combined with 6-31+G(d) basis set within the Gaussian 03 program package[23] was chosen as a cost-effective and accurate method for geometry optimizations.[24] To verify that the transition states indeed connect the products and prereactive complexes, intrinsic reaction coordinate (IRC)[25] calculations were performed. All transition states are characterized by only one imaginary frequency and are true first-order saddle points on the potential energy surface.

The energetics and kinetics have been evaluated with the MPWB1K/6-311+G(3df,2p)//B3LYP/6-31+G(d), B3LYP/6-311+G(3df,2p)//B3LYP/6-31+G(d), B3LYP/6-31+G(d)//B3LYP/6-31+G(d), and B2-PLYP/6-31+G(d)//B3LYP/6-31+G(d) methodologies.

The MPWB1K method has proven to be very successful for describing thermochemistry, reaction kinetics, hydrogen bonding, and weak interactions.[26−29] The B2-PLYP method, which combines the BLYP[30] functional with Hartree−Fock exchange and a perturbative second-order correlation part, is also used since it is a promising functional with a high accuracy, taking into account dispersion interactions.[31]

To study the solvent effect, we first apply an explicit solvent model. Isobe et al. have shown experimentally that the concentration of the MMA−$(CF_3)_3COH$ complex was highest when the molar ratio of the two components was approximately 1/1, indicating that the stoichiometry of the reaction was 1/1.[13c] The interaction of the MMA monomer (M) and the radical ($R^\bullet$) with the solvent (S) has been considered as a two-step mechanism that involves a fast preequilibrium between the reactants and the solvent (M···S and S···$R^\bullet$) followed by the formation of a prereactive complex $(S-R-M-S)^\bullet$; this procedure was performed earlier in ref 32.

Scheme 1. Representation of the Role of the Prereactive Complex in the Apparent Rate Coefficient

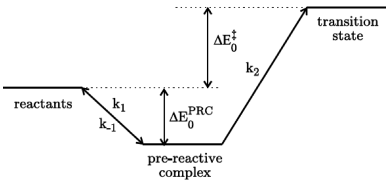

Step 1:

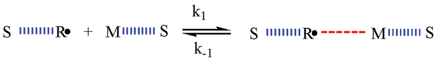

Step 2:

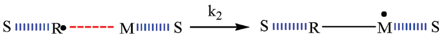

If k_1 and k_{-1} are the rate constants for the forward and reverse reactions in the first step and k_2 corresponds to the second step, the apparent kinetic parameters can be split up in two contributions: the rate coefficient (k_2) and the equilibrium constant K_1 for the formation of the prereactive complex (PRC).[33] A schematic representation of the role of the prereactive complex in the apparent reaction rate coefficient is given in Scheme 1.

$$k_{app} = K_1 k_2 = \frac{k_2 k_2}{k_{-1} + k_2} \approx \frac{k_1 k_2}{k_{-1}} \tag{1}$$

with the equilibrium constant of the fast equilibrium between the reactants and the prereactive complex obeying the basic statistical thermodynamic principles

$$K_1 = \frac{Q_{PRC}}{Q_R} \exp[\Delta E_0^{PRC}/RT] \tag{2}$$

ΔE_0^{PRC} represents the molar energy difference at 0 K between the reactants and the PRC including zero-point vibration energies (ZPVE) .

Q_{PRC} and Q_R are the prereactive complex and the reactants partition functions, respectively.

Similarly, the classical TST formula can be used to calculate k_2[34]

$$k_2 = \sigma \frac{k_B T}{h} \frac{Q_{TS}}{Q_{PRC}} \exp[-(\Delta E_0^\ddagger + \Delta E_0^{PRC})/RT] \tag{3}$$

with $\Delta E_0^\ddagger$ the reaction barrier for the transition state including ZPVE. σ is the reaction path degeneracy that accounts for the number of equivalent reaction paths. k_B represents Boltzmann's constant, T is the temperature, and h is Planck's constant. Finally, the apparent reaction rate coefficient k_{app} becomes

$$k_{app} = \sigma \frac{k_B T}{h} \frac{Q_{TS}}{Q_R} \exp[-\Delta E_0^\ddagger/RT] \tag{4}$$

This also means that calculating the reaction rate from separated reactants will result in exactly the same rate coefficients as compared to calculating the product of the equilibrium constant K_1 and the unimolecular reaction rate k_2. Although one could start from the separated reactants, the PRC concept is very valuable to get more insight into the role of the solvent molecules and their ability to stabilize the transition state.[32]

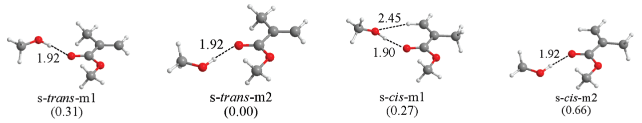

Figure 1. Relative energies (kcal/mol) of the *s-cis* and *s-trans* conformers of MMA with CH_3OH (MPWB1K/6-311+G(3df,2p)//B3LYP/6-31+G(d)).

Scheme 2. Representation of Isotactic and Syndiotactic Radical Polymerization of MMA

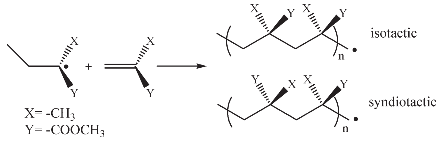

Equation 4 can be rewritten in terms of the molecular Gibbs free energy difference $\Delta G^{\ddagger}$ between the activated complex and the reactants (with inclusion of zero point vibration energies):

$$k_{\mathrm{app}} = \kappa \frac{k_{\mathrm{B}}T}{h} \frac{RT}{p^{\theta}} \exp[-\Delta G^{\ddagger}/RT] \tag{5}$$

where R represents the universal gas constant and κ the transmission coefficient which is assumed to be about 1 and p^{θ} is the standard pressure 10^5 Pa (1 bar).[35]

In the case where the solvent effect is considered implicitly as a polarized continuum medium, the effect of the environment was taken into account by use of the self-consistent reaction field (SCRF) theory, utilizing the integral equation formalism−polarizable continuum (IEF-PCM) model.[36] In the case where the solvent effect has been modeled explicitly and implicitly the effect of the solvent is modeled as the sum of two contributions: one resulting from the explicit coordination with the individual solvent molecules in the reactants and transition states and one originating from the bulk solvent effect as in earlier publications.[37]

Results

The free radical polymerization of MMA is known to start by the generation of free radicals from the nonradical species (initiator).

$$\mathrm{I} \xrightarrow{k_{\mathrm{d}}} \mathrm{R}^{\bullet} \quad \text{(initiation)}$$

The radical $R^{\bullet}$, taken in this study as the methyl ($CH_3^{\bullet}$) radical, adds to the acrylate monomer and forms a backbone with three C atoms. This radical species then adds to the monomer to generate the propagating polymer chain (propagation reaction). $CH_3^{\bullet}$ addition to the carbon−carbon double bond (C=C) was investigated elaborately by Radom et al.[38] Radical addition reaction kinetics of some vinyl monomers was modeled by Coote et al.[39−41] Head-to-tail propagation was assumed to be the most favorable mode of attack.[34,42] Several groups have modeled the structure−reactivity relationship of various acrylates and methacrylates by using quantum chemical tools.[27−29,41,43]

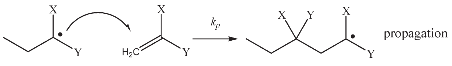

This study aims in elucidating the origins of the syndiotactic/isotactic stereospecificity in the free radical polymerization of MMA, as depicted in Scheme 2.

Scheme 3. Most Stable Conformations of MMA[a]

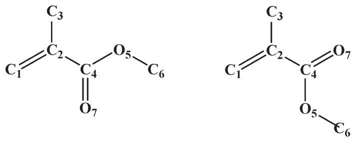

s-*cis* $C_1C_2C_4O_7 = 0°$ (0.39) s-*trans* $C_1C_2C_4O_7 = 180°$ (0.00)

[a] Relative energies in (kcal/mol) are given in parentheses (MPWB1K/6-311+G(3df,2p)//B3LYP/6-31+G(d)).

Scheme 4. Most Stable Conformations of MMAR[a]

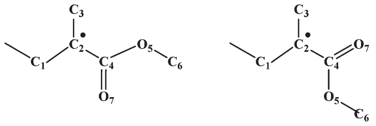

syn-r $C_1C_2C_4O_7 = 0°$ (0.00) *anti*-r $C_1C_2C_4O_7 = 180°$ (0.01)

[a] Relative energies in (kcal/mol) are given in parentheses (MPWB1K/6-311+G(3df,2p)//B3LYP/6-31+G(d)).

A. Free Radical Polymerization of MMA in CH_3OH as Solvent. *MMA−CH_3OH Complex.* In vacuum, the most stable conformation of MMA is found to be *s-trans* ($C_1C_2C_4O_7 = 180°$) as shown in Scheme 3. A conformational search for the MMA−CH_3OH complex was carried out in order to find out the most stable solvated structures of the monomer−solvent entity. For both *s-cis* and *s-trans* conformations the carbonyl oxygen is the only site to be prone to hydrogen bonding. Among the conformations shown in Figure 1, complexation to the *s-trans* conformation of MMA from its methoxy side renders this complex (*s-trans*-m2) slightly more stable than the others. The relative energies of the *s-cis*/*s-trans* monomer−CH_3OH complexes range from 0.3 to 0.7 kcal/mol (Figure 1).

MMAR−CH_3OH Complex. In the gas phase the *syn* and *anti* conformation of the radical are almost isoenergetic, and both have been considered for the formation of possible MMAR−CH_3OH complexes (Scheme 4). Complexation of the radical with the methanol solvent does not alter significantly the energetics: the difference in binding energy between the *syn*-r and *anti*-r remains negligible (Figure 2). CH_3OH preferentially binds to the carbonyl oxygen (*syn*-r1 and *syn*-r2) of the radical. The global minimum for the *syn* conformer of the radical is found to be the structure where methanol forms a hydrogen bond with the carbonyl oxygen with the methyl group away from the propagating chain; the *anti* conformation is slightly more stable than *syn* conformation. The relative energies of the radicals range from 0.1 to 0.5 kcal/mol (Figure 2).

Transition Structures and Prereactive Complexes. The radical can attack the double bond of the monomer to yield

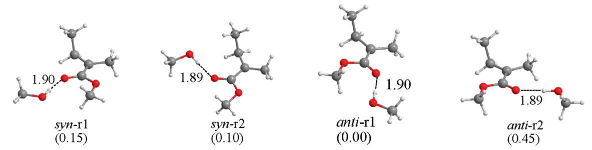

Figure 2. Relative energies (kcal/mol) of the various conformations of the MMAR$-$CH$_3$OH complexes (MPWB1K/6-311+G(3df,2p)//B3LYP/6-31+G(d).

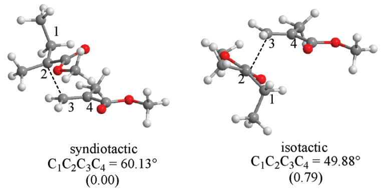

Figure 3. Dimeric transition structures for the free radical polymerization of MMA in vacuo (MPWB1K/6-311+G(3df,2p)//B3LYP/6-31+G(d)).

Scheme 5. Stereoselective Radical (*syn*) Addition to MMA (*s-cis* and s-*trans*)

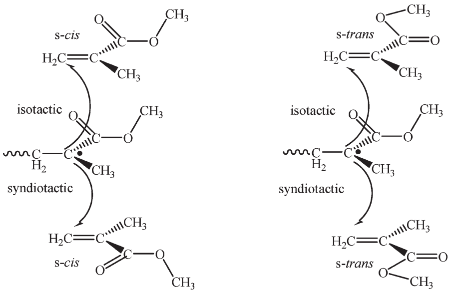

either the isotactic or syndiotactic dimer based on the relative orientation of the two species (Scheme 5). As already discussed in a previous study of the authors, the attack of the radical to the monomer is gauche in the syndiotactic and isotactic polymer chains.[43a]

Solvation of the transition state is studied by including only one methanol solvent molecule per unit. In this picture the propagating radical attacks the monomer while a solvent molecule $-$CH$_3$OH$-$ can form a hydrogen bond with the monomer (MMA) and the propagating radical (MMAR) as depicted in Scheme 6. Our previous study[43a] has shown that the most stable transition structures correspond to the attack of the monomeric radical of MMA in a *syn* conformation to the *s-cis* isomer of the monomer. The solvent can approach the monomer and the radical either from the direction in between the propagating species (inner approach -i) or from outside (outer approach -o). As displayed in Scheme 6, alternative approaches of the solvent molecule to the propagating syndiotactic and isotactic polymer chains have been modeled; the most stable ones in each case have been reported. The nomenclature *syn*-oo, *syn*-oi, *syn*-io, *syn*-ii has been used to identify the approach of the solvent to the syndiotactic chain; similar notation *iso*-oo, *iso*-oi, *iso*-io, *iso*-ii has been employed for the isotactic chain.

In the transition structures for the syndiotactic and isotactic propagating chains the carbonyl oxygen coordinates with methanol with distances varying from 1.86 to 1.91 Å, while the oxygen atom of the methanol is also involved in secondary long-range stabilizing interactions with the methyl hydrogens in close proximity (2.43$-$2.52 Å). The presence of these bridge-type hydrogen bonds are decisive for determining the most stable transition structures. They elucidate mainly why syndiotactic structures are slightly better stabilized by the solvent by 1$-$3 kcal/mol (MPWB1K/6-311+G(3df,2p)//B3LYP/6-31+G-(d), Figure 4). In all transition structures the forming C---C bond distances between the monomer and the radical vary between 2.24 and 2.26 Å. Also note that even though the nomenclature i(inner)/o(outer) is adopted for the approach of methanol to the dimeric chain, optimizations have led to structures where the methanol molecules H-bonded to the carbonyl oxygens lie more or less between the monomer and radical moieties in the dimeric structures.

IRC calculations have yielded the prereactive complexes corresponding to the transition structures. The prereactive complexes correspond to stationary points along the potential energy surface of the propagation reaction where the two CH$_3$OH solvent molecules keep the monomer and the propagating radical in close proximity to each other before these two species have the proper orientation to react. The most favorable reaction paths for both syndiotactic and isotactic dimerizations are shown in Figures 5 and 6. The syndiotactic polymer chain is better stabilized and reacts faster than the isotactic polymer chain ($\Delta E_0^{\ddagger}$ amounts to 3.95 and 5.40 kcal/mol, respectively).

The kinetics of all the paths corresponding to the transition structures depicted in Figure 4 have been considered; the contribution of the *syn*-ii and *iso*-oo structures is found to be higher than the others. As shown in Figure 5, Figure 6, and Table 2 the energy barrier for the syndiotactic reaction (*syn*-ii) is smaller than the one for the isotactic reaction (*iso*-oo) about 1.45 kcal/mol by using explicit solvent. This difference is mainly due to the presence of steric effects in the isotactic transition structure. However, as displayed in Table 3, the ratio k_{syn}/k_{iso} is smaller than the one that would be expected based on energy barriers; this is due to entropic contributions to the rate constants. The vibrational partition function of the isotactic dimeric transition structure (0.74×10^{31}) is greater than the one of the syndiotactic structure (0.17×10^{30}) as a result of greater disorder in the former. The isotactic structure is more disordered due to the presence of the pendant groups on the same side of the backbone. Overall, the isotactic structure is favored entropically ($\Delta G^{\ddagger}$), whereas the syndiotactic structure is favored energetically ($\Delta E_0^{\ddagger}$), as shown in Table 2. The reaction is exothermic slightly in favor of the syndiotactic path. In Table 3 the reaction channels have been considered as concurrent reactions where the sum of the reaction rate constants for the syndiotactic (k_{syn}) and isotactic (k_{iso}) paths have been evaluated. The k_{syn}/k_{iso} ratio is reproduced qualitatively with all the methodologies with implicit and explicit solvent.

Scheme 6. Representation of Solvent Attack to the Syndiotactic and Isotactic Propagating Chains

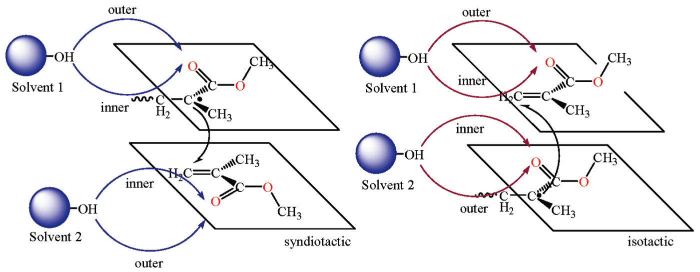

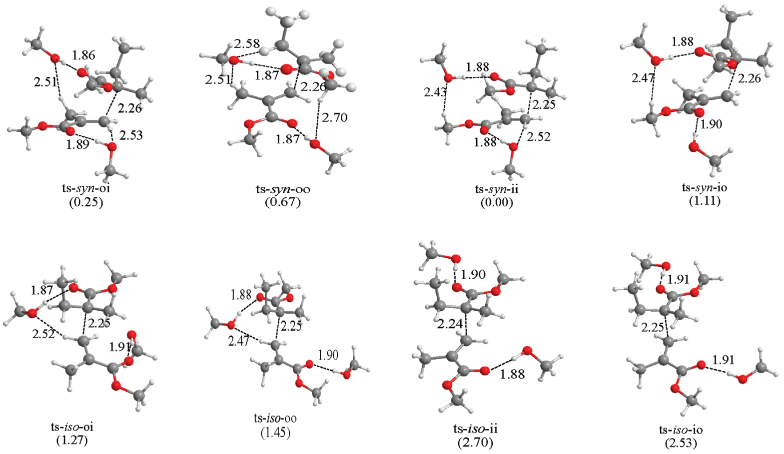

ts-*syn*-oi (0.25) ts-*syn*-oo (0.67) ts-*syn*-ii (0.00) ts-*syn*-io (1.11)

ts-*iso*-oi (1.27) ts-*iso*-oo (1.45) ts-*iso*-ii (2.70) ts-*iso*-io (2.53)

Figure 4. Relative energies (kcal/mol) of the most stable transition structures with CH_3OH (MPWB1K/6-311+G(3df,2p)//B3LYP/6-31+G(d)).

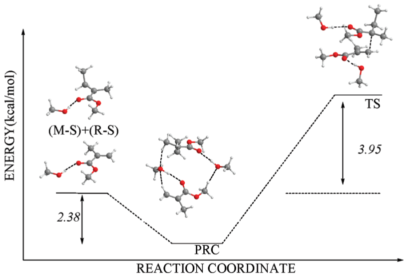

Figure 5. Energetics for syndiotactic dimeric-MMA formation (*syn*-ii) with CH_3OH (MPWB1K/6-311+G(3df,2p)//B3LYP/6-31+G(d)).

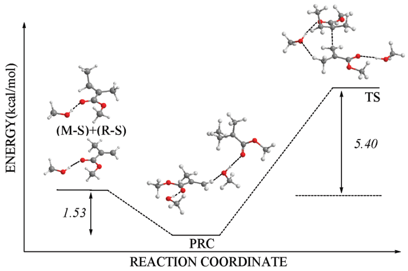

Figure 6. Energetics for isotactic dimeric-MMA formation (*iso*-oo) with CH_3OH (MPWB1K/6-311+G(3df,2p)//B3LYP/6-31+G(d)).

The incorporation of explicit solvent molecules is expected to lead to a decrease in activation energy, resulting in an increase of the reaction rate coefficient as found in a recent work of part of the authors on the effect of explicit water molecules on the propagation rate in acrylamide and methacrylamide.[32] Here the major increase in k_p values results from usage of the explicit/implicit solvation model. As mentioned earlier by Warshell et al., care needs to be taken in absolute evaluation of these values, as this model can also overshoot the solvent effects.[44]

In this study, the presence of explicit and implicit solvent has reproduced qualitatively the experimental expectation in favor of the syndiotactic PMMA.

B. Free Radical Polymerization of MMA in Perfluoro-*tert*-butyl Alcohol ($(CF_3)_3COH$). We now investigate the influence of the solvent type on the stereochemistry in MMA polymerization. We have chosen $(CF_3)_3COH$ as the *rr*-tacticity is the largest in this solvent. Four solvated complexes for the monomer MMA−$(CF_3)_3COH$ and radical MMAR−$(CF_3)_3COH$ are found and displayed in Figure 7. They all show a hydrogen bond between the alcoholic H and the carbonyl oxygen, but due to the larger polarizability of $(CF_3)_3COH$ the coordination distance is found slightly smaller (1.75 Å) than the one for methanol (1.90 Å).

Table 2. Energetics (kcal/mol) for Syndiotactic and Isotactic Paths with Explicit CH_3OH at 293.15 K ((MPWB1K/6-311+G(3df,2p)//B3LYP/6-31+G(d))

	$\Delta E_0^{\ddagger}$	$\Delta G^{\ddagger}$	ΔH
syn-oi	4.20	19.73	−17.00
syn-oo	4.62	19.57	−16.50
syn-ii	3.95	19.24	−17.07
syn-io	5.06	19.98	−17.29
iso-oi	5.22	19.40	−16.85
iso-oo	5.40	18.73	−16.94
iso-ii	6.66	19.88	−15.14
iso-io	6.48	19.69	−15.35

Table 3. Kinetics (k_{app}) for the Syndiotactic and Isotactic Polymerization of MMA in Vacuum and CH_3OH at 293.15 K (B3LYP/6-31+G(d) Geometries Have Been Considered)

	B3LYP/6-31 +G(d)	B3LYP/6-311 +G(3df,2p)	MPWB1K/ 6-311+G(3df,2p)	B2PLYP/ 6-31+G(d)
		Explicit Solvent		
$k_{syn\text{-oi}}$	4.82×10^{-7}	6.87×10^{-8}	2.91×10^{-4}	3.71×10^{-3}
$k_{syn\text{-oo}}$	1.68×10^{-6}	2.36×10^{-7}	3.86×10^{-4}	5.87×10^{-3}
$k_{syn\text{-ii}}$	2.09×10^{-6}	2.12×10^{-7}	6.76×10^{-4}	2.06×10^{-2}
$k_{syn\text{-io}}$	1.29×10^{-6}	1.56×10^{-7}	1.89×10^{-4}	4.96×10^{-3}
$k_{iso\text{-oi}}$	2.51×10^{-6}	3.65×10^{-7}	5.12×10^{-4}	5.88×10^{-3}
$k_{iso\text{-oo}}$	6.71×10^{-6}	1.18×10^{-6}	1.64×10^{-3}	3.97×10^{-3}
$k_{iso\text{-ii}}$	1.54×10^{-6}	2.89×10^{-7}	2.26×10^{-4}	7.53×10^{-4}
$k_{iso\text{-io}}$	2.08×10^{-6}	4.08×10^{-7}	3.12×10^{-4}	5.11×10^{-4}
$k_{syn(\text{tot})}$	5.54×10^{-6}	6.73×10^{-7}	1.54×10^{-3}	3.51×10^{-2}
$k_{iso(tot)}$	1.28×10^{-5}	2.24×10^{-6}	2.69×10^{-3}	1.11×10^{-2}
$k_{syn}/k_{iso}{}^{a}$	0.43	0.30	0.57	3.16
		Implicit + Explicit Solvent		
$k_{syn}/k_{iso}{}^{a,b}$		3.85	9.38	40.57
vacuum				
k_{syn}/k_{iso}	0.74	0.68	1.75	
		Implicit Solvent		
$k_{syn}/k_{iso}{}^{a,c}$		1.04	2.90	

[a] $[k_{syn}/k_{iso}]_{\text{exp}} = 22$ in methanol ($[k_{syn}/k_{iso}]_{\text{exp}} = 22$ in bulk).[13c] [b] Reaction path within a mixed implicit/explicit solvent model (a solvated monomer and solvated radical embedded in a continuum of dielectric constant $\varepsilon = 32.63$). [c] Reaction path within implicit solvent model embedded in a continuum of dielectric constant $\varepsilon = 32.63$.

In the transition structures along the formation of the syndiotactic and isotactic products notice that the F atoms of the $(CF_3)_3COH$ solvent are in close proximity in the isotactic chains rather than in the syndiotactic chains. The steric repulsion between the bulky solvent molecules is much more pronounced in $(CF_3)_3COH$ rather than in CH_3OH.

In PFTB the reaction barrier for the syndiotactic path (*syn*-ii) is smaller than the one for the isotactic path (*iso*-oi) by about 2.57 kcal/mol due to the presence of steric effects in the isotactic transition structure (Table 4). As displayed in Table 5, the k_{syn}/k_{iso} ratio illustrates the same behavior as the activation barriers in contrast to the FRP of MMA in CH_3OH. The FRP of MMA in PFTB favors the syndiotactic path both energetically and entropically; this is probably due to the nature of the H-bonds which are shorter and stronger in PFTB and stabilize better the pendant groups which are more ordered as compared to the ones in CH_3OH. Also note that the free radical polymerization of MMA in PFTB is exothermic ($\Delta H < 0$) in favor of the syndiotactic path.

The dielectric constant of perfluoro-*tert*-butyl alcohol $(CF_3)_3COH$ has been calculated in order to treat it as a polarizable continuum. The Debye equation has been used to evaluate the dielectric constant of $(CF_3)_3COH$ as shown in eq 6

$$\frac{\varepsilon_r - 1}{\varepsilon_r + 2} = \frac{\rho P_m}{M} \tag{6}$$

ρ is the density of $(CF_3)_3COH$, M is its molecular weight, and P_m is the molar polarization. The formalism displayed in eq 6 has been used to find $\varepsilon = 4.49$ for $(CF_3)_3COH$, and calculations in a continuum with $\varepsilon = 4.49$ have been carried out (Table 5). The experimentally observed enhancement of the stereoselectivity in $(CF_3)_3COH$ is pretty well reproduced qualitatively both with the MPWB1K/6-311+G(3df,2p)//B3LYP/6-31+G(d) and the B2PLYP/6-31+G(d)//B3LYP/6-31+G(d) methodologies.

C. Comparison of the Free Radical Polymerization of MMA in CH_3OH and in $(CF_3)_3COH$. The comparison of activation barriers for the propagation reaction in vacuum, in methanol, and in fluorinated alcohol emphasizes the fact that the solvent stabilizes transition states more than the reactants (Table 6). The reaction barriers $\Delta E_0^{\ddagger}$ for the most favorable reaction paths leading to syndiotactic and isotactic dimeric growing polymer chains are in agreement with the experimental findings at 20 °C where PMMA is 66% syndiotactic in methanol and 75.3% in PFTB, whereas it is 1.2% isotactic in PFTB and 2.5% in methanol respectively (Table 6).[13c] On the energetic and kinetic basis the syndiotactic propagation is accelerated as the interaction with the surrounding medium

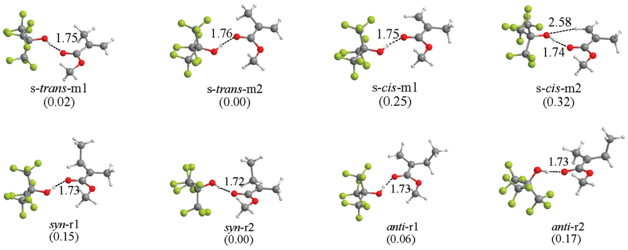

s-*trans*-m1 (0.02) s-*trans*-m2 (0.00) s-*cis*-m1 (0.25) s-*cis*-m2 (0.32)

syn-r1 (0.15) *syn*-r2 (0.00) *anti*-r1 (0.06) *anti*-r2 (0.17)

Figure 7. Relative energies (kcal/mol) of MMA−$(CF_3)_3COH$ and MMAR−$(CF_3)_3COH$ complexes (MPWB1K/6-311+G(3df,2p)//B3LYP/6-31+G(d)).

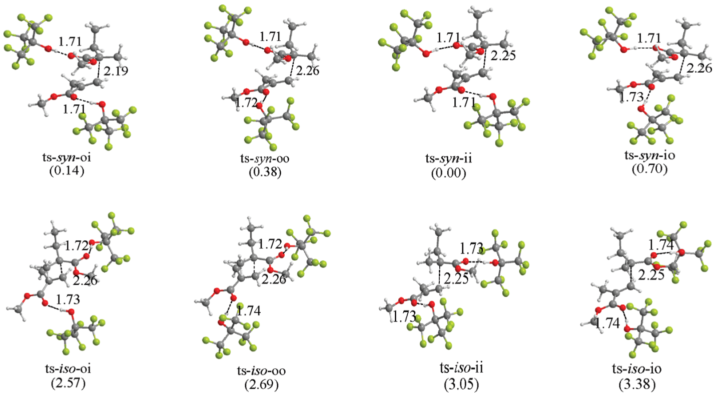

ts-*syn*-oi (0.14) ts-*syn*-oo (0.38) ts-*syn*-ii (0.00) ts-*syn*-io (0.70)

ts-*iso*-oi (2.57) ts-*iso*-oo (2.69) ts-*iso*-ii (3.05) ts-*iso*-io (3.38)

Figure 8. Relative energies (kcal/mol) of the most stable transition structures with $(CF_3)_3COH$ (MPWB1K/6-311+G(3df,2p)//B3LYP/6-31+G(d)).

Table 4. Energetics for Syndiotactic and Isotactic Paths with Explicit $(CF_3)_3COH$ (MPWB1K/6-311+G(3df,2p)//B3LYP/6-31+G(d)) at 293.15 K

	$\Delta E_0^\ddagger$	$\Delta G^\ddagger$	ΔH
syn-oi	2.97	17.44	−20.23
syn-oo	3.22	18.31	−20.12
syn-ii	2.84	17.10	−19.58
syn-io	3.54	18.47	−19.77
iso-oi	5.41	20.93	−18.06
iso-oo	5.52	20.51	−17.57
iso-ii	5.89	19.86	−16.94
iso-io	6.21	19.10	−16.52

Table 5. Kinetics (k_{app}) for Syndiotactic and Isotactic Polymerization of MMA in Vacuum and $(CF_3)_3COH$ at 293.15 K (B3LYP/6-31+G(d) Geometries Have Been Considered)

	B3LYP/6-31 +G(d)	B3LYP/6-311 +G(3df,2p)	MPWB1K/ 6-311+G(3df,2p)	B2PLYP/ 6-31+G(d)
Explicit Solvent				
$k_{syn\text{-oi}}$	7.82×10^{-7}	2.13×10^{-6}	1.47×10^{-2}	1.82×10^{0}
$k_{syn\text{-oo}}$	1.80×10^{-7}	4.83×10^{-7}	3.29×10^{-3}	2.55×10^{-1}
$k_{syn\text{-ii}}$	1.38×10^{-6}	3.49×10^{-6}	2.65×10^{-2}	3.25×10^{0}
$k_{syn\text{-io}}$	2.03×10^{-7}	5.21×10^{-7}	2.53×10^{-3}	2.80×10^{-1}
$k_{iso\text{-oi}}$	8.74×10^{-9}	3.14×10^{-8}	3.68×10^{-5}	1.08×10^{-3}
$k_{iso\text{-oo}}$	2.14×10^{-8}	6.38×10^{-8}	7.65×10^{-5}	8.75×10^{-4}
$k_{iso\text{-ii}}$	5.45×10^{-8}	1.73×10^{-7}	2.31×10^{-4}	3.32×10^{-3}
$k_{iso\text{-io}}$	3.09×10^{-7}	9.38×10^{-7}	8.58×10^{-4}	6.26×10^{-3}
$k_{syn(tot)}$	2.55×10^{-6}	6.63×10^{-6}	4.70×10^{-2}	5.61×10^{0}
$k_{iso(tot)}$	3.94×10^{-7}	1.21×10^{-6}	1.20×10^{-3}	1.15×10^{-2}
k_{syn}/k_{iso} [a]	6.47	5.50	39.07	486.06
Implicit + Explicit Solvent				
k_{syn}/k_{iso} [a,b]		13.19	79.79	477.03
Vacuum				
k_{syn}/k_{iso} [a]	0.74	0.68	1.75	
Implicit Solvent				
k_{syn}/k_{iso} [a,c]		1.06	2.85	

[a] $[k_{syn}/k_{iso}]_{exp} = 75$ in $(CF_3)_3COH$.[13c] [b] Reaction path within a mixed implicit/explict solvent model (a solvated monomer and solvated radical embedded in a continuum of dielectric constant $\varepsilon = 4.49$. [c] Reaction path within implicit solvent model embedded in a continuum of dielectric constant $\varepsilon = 4.49$.

Table 6. Reaction Barriers $\Delta E_0^\ddagger$ (kcal/mol) and Rate Constants for the Most Favorable Reactions (MPWB1K/6-311+G(3df,2p)//B3LYP/6-31+G(d))

	vacuum	CH_3OH	$(CF_3)_3COH$
$\Delta E_{0(syn)}^\ddagger$	5.33	3.95	2.84
$\Delta E_{0(iso)}^\ddagger$	6.12	5.40	6.21
k_{syn} [a]		2.17×10^{9}	4.31×10^{10}
k_{iso} [a]		3.03×10^{8}	2.64×10^{8}

[a] Rate constants have been calculated with IEF-PCM in a polar environment.

Table 7. Gas Phase Activation Barriers ($\Delta E_0^\ddagger$), Interaction Energies ($\Delta E_{int}^\ddagger$), and Distortion Energies ($\Delta E_{dist}^\ddagger$) with Explicit Solvent (MPWB1K/6-311+G(3df,2p)//B3LYP/6-31+G(d), kcal/mol)

	CH_3OH			$(CF_3)_3COH$		
	$\Delta E_0^\ddagger$	$\Delta E_{int}^\ddagger$	$\Delta E_{dist}^\ddagger$	$\Delta E_0^\ddagger$	$\Delta E_{int}^\ddagger$	$\Delta E_{dist}^\ddagger$
syn-oi	4.20	−6.64	10.84	2.97	−6.75	9.72
syn-oo	4.62	−6.33	10.95	5.52	−6.59	9.81
syn-ii	3.95	−7.09	11.04	2.84	−6.84	9.67
syn-io	5.06	−5.74	10.79	3.54	−6.33	9.87
iso-oi	5.22	−6.66	11.88	5.41	−4.83	10.24
iso-oo	5.40	−5.71	11.11	5.52	−4.69	10.21
iso-ii	6.66	−4.40	11.05	5.89	−4.61	10.50
iso-io	6.48	−3.27	9.75	6.21	−3.81	10.02

increases. Notice also that the solvent stabilizes less the isotactic transition structures as compared to the syndiotactic ones: for isotactic PMMA even though interactions with the solvent molecules are favorable, their close proximity inhibits this rearrangement. The size of PFTB molecules being larger than the one of CH_3OH molecules there is greater repulsion between PFTB molecules; this behavior is perfectly well reflected in k_{iso} in methanol (3.03×10^8) being larger than k_{iso} in PFTB (2.64×10^8).

The experimentally observed reaction outcomes have also been rationalized by a comparative analysis of the transition state structures via the distortion/interaction model.[45] The activation strain model of chemical reactivity by Bickelhaupt[45b] was employed.

$$\Delta E_0^\ddagger = \Delta E_{int}^\ddagger + \Delta E_{dist}^\ddagger \tag{7}$$

The distortion/interaction model separates the activation energy ($\Delta E_0^\ddagger$) into distortion energy ($\Delta E^\ddagger_{dist}$) and interaction energy ($\Delta E^{\ddagger}_{\mathrm{int}}$) between distorted fragments, where the former is associated with the strain caused by deforming the individual reactants and the latter is the favorable interaction between the deformed reactants.

When CH_3OH is the solvent, the contribution of the distortion energy is more or less similar for both sydiotactic and isotactic channels. On the other hand, when $(CF_3)_3COH$ is used, the distortion energy is higher in the isotactic channel as expected based on the proximity of the pendant groups. Also in $(CF_3)_3COH$, the interaction energies stabilize the syndiotactic structures more than the isotactic ones; this is confirmed by the stronger H-bonds (1.71 Å) in these structures as compared to the ones in the syndiotactic structures (1.72−1.74 Å). Overall, the distortion/interaction model explains the experimentally determined syndiotactic preference of the free radical polymerization of MMA in the presence of $(CF_3)_3COH$.

Conclusion

In this study, the control of the stereochemistry in methyl methacrylate (MMA) has been modeled with the B3LYP/6-31+G(d)//B3LYP/6-31+G(d), B3LYP/6-311+G(3df,2p)//B3LYP/6-31+G(d), MPWB1K/6-311+G(3df,2p)//B3LYP/6-31+G(d), and B2PLYP/6-31+G(d)//B3LYP/6-31+G(d) methodologies. The role of the solvent on the tacticity of MMA polymerization has been investigated by considering the propagation rate constants for the syndiotactic and isotactic free radical polymerization of MMA in vacuum, in methanol (CH_3OH), and in 1,1,1,3,3,3-hexafluoro-2-(trifluoromethyl)propan-2-ol ($(CF_3)_3COH$). The role of $(CF_3)_3$-COH in inhibiting the isotacticity of PMMA has been explained by the steric hindrance of the pendant solvent molecules strongly hydrogen bonded to the carbonyl oxygens (∼1.7 Å) located on the same side of the backbone. CH_3OH is less effective in reducing the isotacticity because of its small size and because of the relatively loose hydrogen bonds (∼1.9 Å) with the carbonyl oxygen. The methodologies used in this study within the scope of the terminal unit model have effectively reproduced the solvent effect on the FRP kinetics of MMA. The quantitative reproduction of absolute rates of polymerization in solvent remains a challenge for theoretical methods; however, this study proves that qualitative trends on effect of solvent on tacticity can be reproduced by the used theoretical models. Overall, this study has demonstrated the fact that computational chemistry offers a viable alternative to experiment: the effect of solvent on tacticity can be predicted prior to the experiment.

Acknowledgment. The computational resources used in this work were provided by the TUBITAK ULAKBIM High Performance Computing Center, the Bogazici University Research Foundation (Project 08M101), and the National Center for High Performance Computing of Turkey (UYBHM) under Grant 20502009. The authors acknowledge for funding the travel and lodging expenses of I.D., V.A., and V.V.S. in UG and BU and the sixth framework project COSBIOM (FP6-2004-ACC-SSA-2.517991). The UGent authors thank the FWO (Fonds voor Wetenschappelijk Onderzoek - Vlaanderen, Fund for Scientific Research - Flanders), the research board of Ghent University for the bilateral project Ghent - Istanbul, and the IAP-BELSPO project in the frame of IAP 6/27 for financial support of this research. Part of this work has also made use of the computational resources and services provided by Ghent University.

Supporting Information Available: Tables of optimized geometries, total energies, enthalpies, Gibbs free energies, and solvation energies for all structures discussed in this study. This material is available free of charge via the Internet at http://pubs.acs.org.

References and Notes

(1) Gladysz, J. A. *Chem. Rev.* **2000**, *100*, 1167–1168.
(2) Sugiyama, Y.; Satoh, K.; Kamigaito, M.; Okamoto, Y. *J. Polym. Sci., Part A: Polym. Chem.* **2006**, *44*, 2086–2098.
(3) (a) Pino, P.; Suter, U. W. *Polymer* **1976**, *17*, 977–995. (b) Hatada, K.; Kitayama, T.; Ute, K. *Prog. Polym. Sci.* **1988**, *13*, 189–276. (c) Yuki, H.; Hatada, K. *Adv. Polym. Sci.* **1979**, *31*, 1–45.
(4) Matsumoto, A. In *Handbook of Radical Polymerization*; Matyjaszewski, K., Davis, T. P., Eds.; Wiley-Interscience: Hoboken, NJ, 2002; pp 691−773.
(5) (a) Habaue, S.; Okamoto, Y. *Chem. Rec.* **2001**, *1*, 46–52. (b) Miura, Y.; Shibata, T.; Satoh, K.; Kamigaito, M.; Okamoto, Y. *J. Am. Chem. Soc.* **2006**, *128*, 16026–16027.
(6) Tanaka, H. *Prog. Polym. Sci.* **1992**, *17*, 1107–1152.
(7) Satoh, K.; Kamigaito, M. *Chem. Rev.* **2009**, *109*, 5120–5156.
(8) Isobe, Y.; Nakano, T.; Okamoto, Y. *J. Polym. Sci., Part A: Polym. Chem.* **2001**, *39*, 1463–1471.
(9) Isobe, Y.; Fujioka, D.; Habaue, S.; Okamoto, Y. *J. Am. Chem. Soc.* **2001**, *123*, 7180–7181.
(10) Habaue, S.; Isobe, Y.; Okamoto, Y. *Tetrahedron* **2002**, *58*, 8205–8209.
(11) Okamoto, Y.; Habaue, S.; Isobe, Y.; Suito, Y. *Macromol. Symp.* **2003**, *195*, 75–80.
(12) Suito, Y.; Isobe, Y.; Habaue, S.; Okamoto, Y. *J. Polym. Sci., Part A: Polym. Chem.* **2002**, *40*, 2496–2500.
(13) (a) Yamada, K.; Nakano, T.; Okamoto, Y. *Macromolecules* **1998**, *31*, 7598–7605. (b) Isobe, Y.; Yamada, K.; Nakano, T.; Okamoto, Y. *Macromolecules* **1999**, *32*, 5979–5981. (c) Isobe, Y.; Yamada, K.; Nakano, T.; Okamoto, Y. *J. Polym. Sci., Part A: Polym. Chem.* **2000**, *38*, 4693–4703.
(14) Miura, Y.; Satoh, T.; Narumi, A.; Nishizawa, O.; Okamoto, Y.; Kakuchi, T. *J. Polym. Sci., Part A: Polym. Chem.* **2006**, *44*, 1436–1446.
(15) (a) Miura, Y.; Satoh, T.; Narumi, A.; Nishizawa, O.; Okamoto, Y.; Kakuchi, T. *Macromolecules* **2005**, *38*, 1041–1043. (b) Miura, Y.; Satoh, T.; Narumi, A.; Nishizawa, O.; Okamoto, Y.; Kakuchi, T. *J. Polym. Sci., Part A: Polym. Chem.* **2006**, *44*, 1436–1446.
(16) Tanaka, H.; Niwa, M. *Polymer* **2008**, *49*, 3693–3701.
(17) Nakano, T.; Okamoto, Y. In *Controlled Radical Polymerization*; Matyjazsewski, K., Ed.; ACS Symposium Series 685; American Chemical Society: Washington, DC, 1998; pp 451−462.
(18) Beuermann, S. *Macromol. Rapid Commun.* **2009**, *30*, 1066–1088.
(19) O'Driscoli, K. F.; Monteiro, M. J.; Klumperman, B. *J. Polym. Sci., Part A: Polym. Chem.* **1997**, *35*, 515–520.
(20) Zammit, M. D.; Davis, T. P.; Willett, G. D.; O'Driscoli, K. F. *J. Polym. Sci., Part A: Polym. Chem.* **1997**, *35*, 2311–2321.
(21) Harrisson, S.; Barner-Kowollik, C.; Davis, T. P.; Evans, K.; Rizzardo, R.; Stenzel, M.; Yin, M. *Z. Phys. Chem.* **2005**, *219*, 267–281.
(22) Ganachaud, F.; Balic, R.; Monteiro, M. J.; Gilbert, R. G. *Macromolecules* **2000**, *33*, 8589–8596. Seabrook, S. A.; Tonge, M. P.; Gilbert, R. G. *J. Polym. Sci., Part A: Polym. Chem.* **2005**, *43*, 1357–1368.
(23) Frisch, M. J.; Trucks, G. W.; Schlegel, H. B.; Scuseria, G. E.; Robb, M. A.; Cheeseman, J. R.; Montgomery, Jr., J. A.; Vreven, T.; Kudin, K. N.; Burant, J. C.; Millam, J. M.; Iyengar, S. S.; Tomasi, J.; Barone, V.; Mennucci, B.; Cossi, M.; Scalmani, G.; Rega, N.; Petersson, G. A.; Nakatsuji, H.; Hada, M.; Ehara, M.; Toyota, K.; Fukuda, R.; Hasegawa, J.; Ishida, M.; Nakajima, T.; Honda, Y.; Kitao, O.; Nakai, H.; Klene, M.; Li, X.; Knox, J. E.; Hratchian, H. P.; Cross, J. B.; Bakken, V.; Adamo, C.; Jaramillo, J.; Gomperts, R.; Stratmann, R. E.; Yazyev, O.; Austin, A. J.; Cammi, R.; Pomelli, C.; Ochterski, J. W.; Ayala, P. Y.; Morokuma, K.; Voth, G. A.; Salvador, P.; Dannenberg, J. J.; Zakrzewski, V. G.; Dapprich, S.; Daniels, A. D.; Strain, M. C.; Farkas, O.; Malick, D. K.; Rabuck, A. D.; Raghavachari, K.; Foresman, J. B.; Ortiz, J. V.; Cui, Q.; Baboul, A. G.; Clifford, S.; Cioslowski, J.; Stefanov, B. B.; Liu, G.; Liashenko, A.; Piskorz, P.; Komaromi, I.; Martin, R. L.; Fox, D. J.; Keith, T.; Al-Laham, M. A.; Peng, C. Y.; Nanayakkara, A.; Challacombe, M.; Gill, P. M. W.; Johnson, B.; Chen, W.; Wong, M. W.; Gonzalez, C.; Pople, J. A. *Gaussian 03, Revision D.01*; Gaussian Inc.: Wallingford, CT, 2004.
(24) Smith, D. M.; Nicolaides, A.; Golding, B. T.; Radom, L. *J. Am. Chem. Soc.* **1998**, *120*, 10223–10233.
(25) Gonzáles, C.; Schlegel, H. B. *J. Phys. Chem.* **1990**, *94*, 5523–5527.
(26) Zhao, Y.; Truhlar, D. G. *J. Phys. Chem. A* **2004**, *108*, 6908–6918.
(27) Furuncuoğlu, T.; Uğur, İ.; Değirmenci, İ.; Aviyente, V. *Macromolecules* **2010**, *43*, 1823–1835.

(28) Liang, K.; Dossi, M.; Moscatelli, D.; Hutchinson, R. A. *Macromolecules* **2009**, *42*, 7736–7744.

(29) Yu, X.; Pfaendtner, J.; Broadbelt, L. J. *J. Phys. Chem. A* **2008**, *112*, 6772–6782.

(30) (a) Lee, C. T.; Yang, W. T.; Parr, R. G. *Phys. Rev. B* **1988**, *37*, 785–789. (b) Becke, A. D. *Phys. Rev. A* **1988**, *38*, 3098–3100.

(31) (a) Grimme, S.; Steinmetz, M.; Korth, M. *J. Chem. Theory Comput.* **2007**, *3*, 42–45. (b) Grimme, S. *J. Chem. Phys.* **2006**, *124*, 174301–12.

(32) De Sterck, B.; Roel Vaneerdeweg, R.; Du Prez, F.; Waroquier, M; Van Speybroeck, V. *Macromolecules* **2010**, *43*, 827–836.

(33) Singleton, D. L.; Cvetanovic, R. J. *J. Am. Chem. Soc.* **1976**, *98*, 6812–6819.

(34) Pilling, M. J.; Seakins, P. W. *Reaction Kinetics*; Oxford University Press: New York, 1996.

(35) *Atkins' Physical Chemistry*, 8th ed.; Atkins, P., De Paula, J., Eds.; Oxford University Press: New York, 2006.

(36) (a) Tomasi, J.; Mennucci, B.; Cancès, E. *J. Mol. Struct.: THEOCHEM* **1999**, *464*, 211–226. (b) Cancès, M. T.; Mennucci, B.; Tomasi, J. *J. Chem. Phys.* **1997**, *107*, 3032–3041. (c) Mennucci, B.; Tomasi, J. *J. Chem. Phys.* **1997**, *106*, 5151–5158. (d) Mennucci, B.; Cancès, E.; Tomasi, J. *J. Phys. Chem. B* **1997**, *101*, 10506–10517.

(37) (a) Kelly, C. P.; Cramer, C. J.; Truhlar, D. G. *J. Phys. Chem. A* **2006**, *110*, 2493–2499. (b) Kamerlin, S. C. L.; Haranczyk, M.; Warshel, A. *ChemPhysChem* **2009**, *10*, 1125–1134. (c) De Sterck, B.; Van Speybroeck, V.; Mangelinckx, S.; Verniest, G.; De Kimpe, N.; Waroquier, M. *J. Phys. Chem. A* **2009**, *113*, 6375–6380. (d) Van Speybroeck, V.; Moonen, K.; Hemelsoet, K.; Stevens, C.; Waroquier, M. *J. Am. Chem. Soc.* **2006**, *128*, 8468–8478. (e) Kelly, C. P.; Cramer, C. J.; Truhlar, D. G. *J. Chem. Theory Comput.* **2005**, *1*, 1133–1152.

(38) (a) Heuts, J. P. A.; Gilbert, R. G.; Radom, L. *Macromolecules* **1995**, *28*, 8771–8781. (b) Wong, M. W.; Radom, L. *J. Phys. Chem.* **1995**, *99*, 8582–8588. (c) Heuts, J. P. A.; Gilbert, R. G.; Radom, L. *J. Phys. Chem.* **1996**, *100*, 18997–19006. (d) Wong, M. W.; Radom, L. *J. Phys. Chem. A* **1998**, *102*, 2237–2245. (e) Fischer, H.; Radom, L. *Angew. Chem., Int. Ed.* **2001**, *40*, 1340–1371. (f) Gómez-Balderas, R.; Coote, M. L.; Henry, D. J.; Fischer, H.; Radom, L. *J. Phys. Chem. A* **2003**, *107*, 6082–6090. (g) Gómez-Balderas, R.; Coote, M. L.; Henry, D. J.; Radom, L. *J. Phys. Chem. A* **2004**, *108*, 2874–2883. (h) Henry, D. J.; Coote, M. L.; Gómez-Balderas, R.; Radom, L. *J. Am. Chem. Soc.* **2004**, *126*, 1732–1740.

(39) Izgorodina, E. I.; Coote, M. L. *Chem. Phys.* **2006**, *324*, 96–110.

(40) Coote, M. L. *Macromol. Theory Simul.* **2009**, *18*, 388–400.

(41) Lin, C. Y.; Izgorodina, E. I.; Coote, M. L. *Macromolecules* **2010**, *43*, 553–560.

(42) Van Cauter, K.; Van Speybroeck, V.; Waroquier, M. *ChemPhysChem* **2007**, *8*, 541–552.

(43) (a) Değirmenci, İ.; Aviyente, V.; Van Speybroeck, V.; Waroquier, M. *Macromolecules* **2009**, *42*, 3033–3041. (b) Değirmenci, İ.; Avcı, D.; Aviyente, V.; Van Cauter, K.; Van Speybroeck, V.; Waroquier, M. *Macromolecules* **2007**, *40*, 9590–9602. (c) Günaydın, H.; Seyhan, S.; Tüzün, N. Ş.; Avcı, D.; Aviyente, V. *Int. J. Quantum Chem.* **2005**, *103*, 176–189. (d) Salman, S.; Ziylan Albayrak, A.; Avcı, D.; Aviyente, V. *J. Polym. Sci., Part A: Polym. Chem.* **2005**, *43*, 2574–2583.

(44) Kamerlin, S. C. L.; Haranczyk, M.; Warshel, A. *ChemPhysChem* **2009**, *10*, 1125–1134.

(45) (a) Ess, D. H.; Houk, K. N. *J. Am. Chem. Soc.* **2007**, *129*, 10646. (b) Bento, A. P.; Bickelhaupt, F. M. *J. Org. Chem.* **2008**, *73*, 7290–7299. (c) Catak, S.; Matthias D'hooghe, M.; De Kimpe, N.; Waroquier, M.; Van Speybroeck, V. *J. Org. Chem.* **2010**, *75*, 885–896.

Paper V

Zeolite Shape-Selectivity in the gem-Methylation of Aromatic Hydrocarbons

Lesthaeghe D., De Sterck, B., Van Speybroeck V.,
Marin G.B., and Waroquier M.

Angew. Chem. Int. Ed., **2007**, *46*, 1311-1314

Angewandte Chemie

Arene Methylation

DOI: 10.1002/anie.200604309

Zeolite Shape-Selectivity in the *gem*-Methylation of Aromatic Hydrocarbons**

David Lesthaeghe, Bart De Sterck, Veronique Van Speybroeck, Guy B. Marin, and Michel Waroquier**

Herein, we explicitly demonstrate the importance of transition-state-shape selectivity for the conversion of methanol to light olefins (methanol-to-olefins or MTO). The MTO process in acidic zeolites is a prominent research topic, driven both by the possibility of monetizing stranded natural gas reserves, coal, or even biomass and by the ever-increasing demands for ethene derivatives.[1] For the last 30 years, the actual reaction mechanism of this process has been a topic of considerable debate, fueled by countless and often conflicting propositions.[1,2] Most efforts centered on mechanisms proposing "direct" formation of ethene from only methanol and C_1 derivates. Recently, however, experimental studies by Haw and co-workers[3,4] as well as our own theoretical results[5] provided strong evidence for the complete failure of the direct routes.

The most likely alternative, which is more in accordance with experimental observations,[6] is given by the "hydrocarbon-pool" (HP) proposal,[7,8] in which organic species trapped in the zeolite pores undergo repeated methylation followed by olefin elimination. To date, the elementary steps governing this process are not well understood. Ideally, experimental and theoretical efforts should complement each other in unraveling this complex network of reactions. A hydrocarbon pool consisting mainly of polymethylbenzenes has been shown to be active for olefin formation,[9,10] independent of the zeotype catalyst chosen.[11] Additionally, there is strong experimental evidence for cyclic resonance-stabilized cations as persistent species in the pores, such as cyclopentenyl and pentamethylbenzenium cations in HZSM-5[12,13] and hexamethylbenzenium and heptamethylbenzenium ($7MB^+$) cations in HBEA.[14,15] Geminal methylbenzenium ions form the main starting point from which commonly proposed HP routes (such as the "paring" and "side-chain" mechanisms) originate.[16] The heptamethylbenzenium cation, for example, is formed from hexamethylbenzene (HMB) through one-step geminal methylation by methanol as shown in Scheme 1.

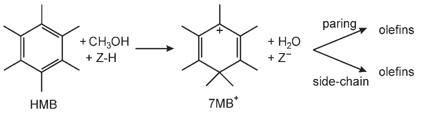

Scheme 1. Initiating step for the formation of olefins from hexamethylbenzene (HMB). Z = zeolite.

The product distribution is defined by the number of methyl groups on the active hydrocarbon-pool species: propene is favored by methylbenzenes with four to six methyl groups, while ethene is predominantly formed from the lower methylbenzenes.[17] As the hydrocarbon-pool mechanism involves bulky cyclic intermediates, it is also a space-demanding process. Therefore, zeolite topology is crucial in defining the hydrocarbon pool, resulting in a strong topological dependence of product distribution as well. The active catalyst is a combined organic–inorganic supramolecular complex of the zeolite framework and the hydrocarbon pool.[2]

Just recently, Cui et al. have reported experimental evidence for transition-state-shape selectivity in studies of methanol-to-olefin conversion on zeolites with varying pore size.[18] Experimental claims to transition-state-shape selectivity are, ideally, verified by theoretical methods,[19–21] since these are more suited for elucidating the extent to which the local shape of the pore influences local reaction rates. To the best of our knowledge, ours is the first theoretical study on the hydrocarbon-pool proposal to take topological concepts explicitly into account, by focusing on both the electrostatic stabilization and geometrical constraints of typical zeolite frameworks on key carbenium ions and transition states.

To separate the effects of hydrocarbon-pool species and zeolite topology, the geminal methylation of several methylbenzenes, ranging from toluene, over *p*-xylene, 1,2,4-trimethylbenzene (pseudocumene), 1,2,4,5-tetramethylbenzene (durene), and pentamethylbenzene (PMB) to hexamethylbenzene (HMB), was first modeled on 5T clusters. These small clusters represent any aluminosilicate and neglect all framework steric and electrostatic effects. Figure 1 a shows the energy barriers and reaction energies for the methylation

---

[*] Ir. D. Lesthaeghe, Ir. B. De Sterck, Dr. Ir. V. Van Speybroeck,
Prof. Dr. M. Waroquier
Center for Molecular Modeling
Ghent University
Proeftuinstraat 86, 9000 Gent (Belgium)
Fax: (+32) 9-264-6697
E-mail: david.lesthaeghe@ugent.be
michel.waroquier@ugent.be
Homepage: http://molmod.ugent.be
Prof. Dr. Ir. G. B. Marin
Laboratorium voor Petrochemische Techniek
Ghent University
Krijgslaan 281-S5, 9000 Gent (Belgium)

[**] This work is supported by the Fund for Scientific Research—Flanders (FWO) and the Research Board of Ghent University.

Supporting information for this article is available on the WWW under http://www.angewandte.org or from the author.

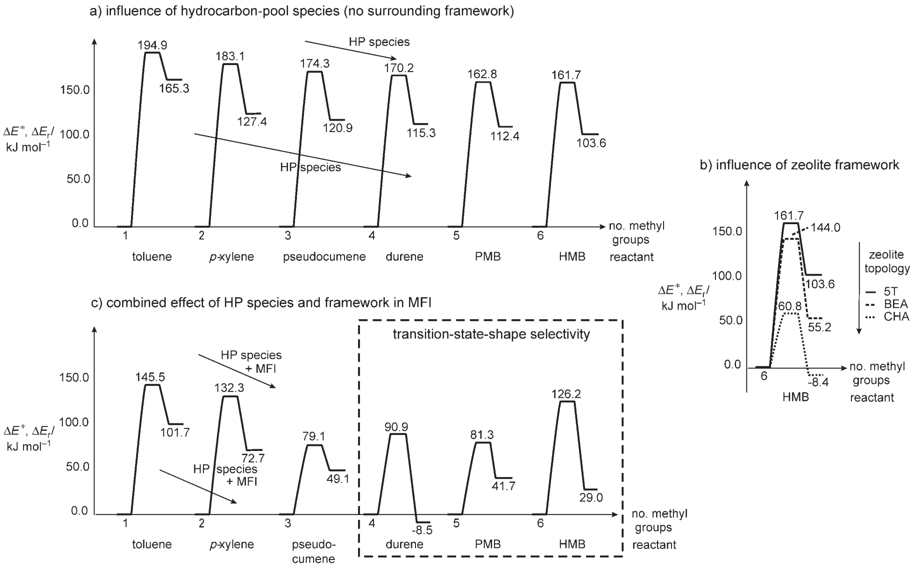

Figure 1. Barrier heights $\Delta E^{\neq}$ and reaction energies ΔE_r in kJ mol^{-1} for a) geminal methylation of different polymethylbenzenes in the 5T cluster, b) geminal methylation of hexamethylbenzene in the zeolite topologies BEA and CHA, and c) geminal methylation of different polymethylbenzenes in the space-limiting MFI structure.

of a series of polymethylbenzenes in the 5T cluster. A steady decrease in both the reaction barrier $\Delta E^{\neq}$ (from 194.9 to 161.7 kJ mol^{-1}) and the reaction energy ΔE_r (from 165.3 to 103.6 kJ mol^{-1}) is observed with the increasing number of methyl groups. Our results for HMB in 5T are similar to the values calculated earlier for HMB in 4T (169 kJ mol^{-1} and 108 kJ mol^{-1}).[22] While these results clearly illustrate the increase of reactivity for higher polymethylbenzenes, the barriers remain relatively high in absolute value. It is expected that the zeolite framework lends additional electrostatic stabilization to the ion pair formed by the cation and the negative aluminum defect.[23] Therefore, the calculations were extended to more advanced 44T and 46T clusters, which represent both the active site and the surrounding zeolite cage[23,24] for various industrially and academically important topologies, such as BEA, CHA, and MFI (shown in Figure 2).

The beta zeolite (BEA topology) has a large pore structure that allows direct introduction of large molecules such as hexamethylbenzene. It is an interesting topology for mechanistic studies, although it is not used as a commercial catalyst because of rapid coke formation and deactivation. Calculations with the BEA topology (Figure 1 b) shows an only slightly reduced reaction barrier of 144.0 kJ mol^{-1} and a reaction energy of 55.2 kJ mol^{-1}. As shown in Figure 2, the large cages in BEA provide limited electrostatic interaction with the organic species that are located centrally in the pores.

Modeling the aluminosilicate chabazite (CHA topology) is a first step towards the commercially important aluminophosphate HSAPO-34, which has the same topology as CHA but an entirely different composition. Composition effects should, however, be treated separately from pure topology effects, and these will be part of a future study. The CHA topology is a structure with spacious cages interconnected by small windows. Methylbenzenes are formed through a "ship-in-a-bottle" synthesis and remain trapped in the catalyst.[9] The calculations with the CHA topology (Figure 1 b) shows a spectacular reduction in energetics. The reaction barrier of merely 60.8 kJ mol^{-1} is easily surmountable, and the reaction energy of −8.4 kJ mol^{-1} even hints at an exothermic initiation of the hydrocarbon-pool cycle in chabazite. Apparently, the enclosing chabazite topology provides an ideal setting for this key reaction step. The term "inverse shape selectivity" immediately springs to mind, although this terminology is usually reserved for the preferential adsorption of neutral branched paraffins rather than for charged species.[25,26] Direct comparison between BEA and CHA clearly shows the strong difference between open and dense framework topologies in solvating this crucial intermediate.

Even though they differ greatly in cage dimensions, both beta and chabazite zeolites contain sufficiently large cages not to impose any geometric constraints on the transition state. This is not the case for HZSM-5, an industrially important zeolite exhibiting the medium-pore MFI topology containing two sets of intersecting channels. Durene is the largest polymethylbenzene that can be introduced directly along the narrow channels.[27] Although MFI does not boast spacious cages, HMB could be formed in the extended space available at the channel intersections. However, its diffusion and reactivity will be sterically restricted. This limited space imposes severe problems for the geminal methylation of methylbenzenes. The spatial demand of the transition state in particular is shown in Figure 2: the two-dimensional methylbenzene is extended perpendicularly into a third dimension in a typical S_N2-type methyl-exchange configuration, while the entire complex remains connected to the active site by hydrogen bonds and the aluminum negative charge, allowing little to no room for flexibility. Deformation of an optimal S_N2-type geometry will invariably lead to an increased reaction barrier.[28]

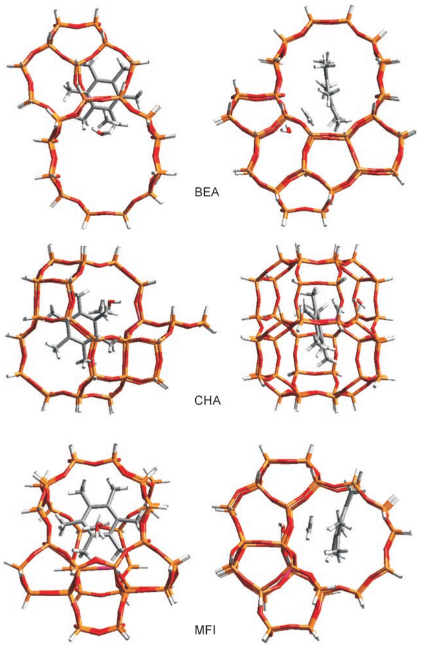

Figure 2. Transition-state geometries for the formation of heptamethylbenzenium in the BEA, CHA, and MFI zeolite topologies.

Not surprisingly, the reaction barrier in the MFI topology (Figure 1 c) is strongly dependent on the number of methyl substituents. For small polymethylbenzenes a steady decrease in both reaction barrier (from 145.5 to 79.1 kJ mol^{-1}) and reaction energy (from 101.7 to 49.1 kJ mol^{-1}) is observed. From durene on, however, the transition state lacks sufficiently ample space to take on the optimal geometry, and the reaction barrier increases significantly to 90.9 kJ mol^{-1}. However, the pentamethylbenzenium ion, which is not as bulky as the transition state, is more stable than the neutral species by 8.5 kJ mol^{-1}. The geminal methylation of pseudocumene and pentamethylbenzene also has a low activation energy (79.1 and 81.3 kJ mol^{-1}) and provides more reactive species for subsequent steps. Each additional methyl group imposes a constant conflict between two opposing effects: on the one hand it leads to a more reactive hydrocarbon-pool species as well as stronger electrostatic interaction with the framework, and on the other hand it is subject to the geometric constraints imposed by the zeolite topology. For HMB this combination of contradictory contributions leads to a reaction barrier of 126.2 kJ mol^{-1} and reaction energy of 29.0 kJ mol^{-1}, which is located between the values obtained for BEA and CHA. In a small-pore catalyst like HZSM-5, the formation of large cations is severely restricted, and the hydrocarbon pool will most likely consist of less sterically demanding methylated benzenes or might even be based on the methylation of smaller branched olefins rather than bulkier methylbenzenes.[29,30]

We conclude that specific combinations of organic reaction centers and the inorganic framework cooperate effectively in stabilizing intermediates and transition states that would, if considered separately, be of excessively high energy. These results offer additional support for the hydrocarbon-pool model by providing a first step towards alternative low-energy pathways for reactions that would otherwise have very high-energy intermediates, as, for example, in the direct oxonium ylide or carbene proposals.[5] Without the solvating effect of the zeolite framework, the number of methyl substitutions on the benzene ring can account for only a relatively minor decrease in both barrier height and reaction energy. The zeolite topology, however, plays a major role in reaction kinetics. For the geminal methylation of hexamethylbenzene the following order of reactivity according to topology is observed: CHA $\gg$ MFI > BEA. The chabazite cages provide the perfect surroundings for a surprisingly stable heptamethylbenzenium cation, while the large beta cages favor neutral species over cations. In the MFI framework, on the other hand, transition-state-shape selectivity takes over for the bulkier methylbenzenes, and lesser methylated cations are the most likely intermediates. Immediately after submission of this paper, a communication by Svelle et al. was published online, including experimental confirmation of the higher activity of the lower methylbenzenes in H-ZSM5.[31]

Further theoretical insights into the effect of zeolite topology are desperately needed, if only to guide development of novel materials with a fine-tuned local spatial environment that optimizes catalytic activity, improves product selectivity, and simultaneously reduces coke formation. Additional insights might even be obtained from enzyme or homogeneous catalysis rather than from traditional zeolite chemistry.[32] To achieve these common goals, strong interaction between experimental work and computational modeling is indispensable.

Experimental Section

All geometry optimizations were performed with the Gaussian03 package.[33] The 5T cluster, treated at the B3LYP/6-31g(d) level of theory,[34] was left unconstrained to verify the true nature of all stationary points. Zero-point-energy (ZPE) corrections were included. Starting from transition-state geometries, the quasi-IRC approach allowed the reactant and product geometries to be acquired. The calculations on the BEA, CHA, and MFI topologies were performed on 44T or 46T clusters at the ONIOM(B3LYP/6-31+g(d):HF/6-31+g(d))//ONIOM(B3LYP/6-31+g(d):MNDO) level of theory,[23,24] where the 5T zeolite active site as well as all organic species were considered at the high QM level. Only the saturating hydrogen atoms were fixed to prevent collapse of the cage. All other low-level framework atoms were allowed to fully adjust themselves to the large incorporated species. As elementary reaction steps were considered separately from adsorption/desorption requirements, only intrinsic energy barriers are shown in kJ mol^{-1}.

Received: October 20, 2006
Published online: January 4, 2007

Keywords: ab initio calculations · arenes · heterogeneous catalysis · methanol-to-olefin process · zeolites

---

[1] M. Stocker, *Microporous Mesoporous Mater.* **1999**, *29*, 3 – 48.
[2] J. F. Haw, W. G. Song, D. M. Marcus, J. B. Nicholas, *Acc. Chem. Res.* **2003**, *36*, 317 – 326.
[3] W. G. Song, D. M. Marcus, H. Fu, J. O. Ehresmann, J. F. Haw, *J. Am. Chem. Soc.* **2002**, *124*, 3844 – 3845.
[4] D. M. Marcus, K. A. McLachlan, M. A. Wildman, J. O. Ehresmann, P. W. Kletnieks, J. F. Haw, *Angew. Chem.* **2006**, *118*, 3205 – 3208; *Angew. Chem. Int. Ed.* **2006**, *45*, 3133 – 3136.
[5] D. Lesthaeghe, V. Van Speybroeck, G. B. Marin, M. Waroquier, *Angew. Chem.* **2006**, *118*, 1746 – 1751; *Angew. Chem. Int. Ed.* **2006**, *45*, 1714 – 1719.
[6] P. W. Goguen, T. Xu, D. H. Barich, T. W. Skloss, W. G. Song, Z. K. Wang, J. B. Nicholas, J. F. Haw, *J. Am. Chem. Soc.* **1998**, *120*, 2650 – 2651.
[7] R. M. Dessau, *J. Catal.* **1986**, *99*, 111 – 116.
[8] I. M. Dahl, S. Kolboe, *J. Catal.* **1994**, *149*, 458 – 464.
[9] W. G. Song, J. F. Haw, J. B. Nicholas, C. S. Heneghan, *J. Am. Chem. Soc.* **2000**, *122*, 10726 – 10727.
[10] B. Arstad, S. Kolboe, *J. Am. Chem. Soc.* **2001**, *123*, 8137 – 8138.
[11] U. Olsbye, M. Bjorgen, S. Svelle, K.-P. Lillerud, S. Kolboe, *Catal. Today* **2005**, *106*, 108 – 111.
[12] T. Xu, D. H. Barich, P. W. Goguen, W. G. Song, Z. K. Wang, J. B. Nicholas, J. F. Haw, *J. Am. Chem. Soc.* **1998**, *120*, 4025 – 4026.
[13] J. F. Haw, J. B. Nicholas, W. G. Song, F. Deng, Z. K. Wang, T. Xu, C. S. Heneghan, *J. Am. Chem. Soc.* **2000**, *122*, 4763 – 4775.
[14] M. Bjorgen, F. Bonino, S. Kolboe, K.-P. Lillerud, A. Zecchina, S. Bordiga, *J. Am. Chem. Soc.* **2003**, *125*, 15863 – 15868.
[15] W. G. Song, J. B. Nicholas, A. Sassi, J. F. Haw, *Catal. Lett.* **2002**, *81*, 49 – 53.
[16] B. Arstad, J. B. Nicholas, J. F. Haw, *J. Am. Chem. Soc.* **2004**, *126*, 2991 – 3001.
[17] W. Song, H. Fu, J. F. Haw, *J. Am. Chem. Soc.* **2001**, *123*, 4749 – 4754.
[18] Z. M. Cui, Q. Liu, W. G. Song, L. J. Wan, *Angew. Chem.* **2006**, *118*, 6662 – 6665; *Angew. Chem. Int. Ed.* **2006**, *45*, 6512 – 6515.
[19] J. A. Martens, J. Perez-Pariente, E. Sastre, A. Corma, P. A. Jacobs, *Appl. Catal.* **1988**, *45*, 85 – 101.
[20] L. A. Clark, M. Sierka, J. Sauer, *J. Am. Chem. Soc.* **2004**, *126*, 936 – 947.
[21] A. M. Vos, X. Rozanska, R. A. Schoonheydt, R. A. van Santen, F. Hutschka, J. Hafner, *J. Am. Chem. Soc.* **2001**, *123*, 2799 – 2809.
[22] B. Arstad, S. Kolboe, O. Swang, *J. Phys. Chem. B* **2002**, *106*, 12722 – 12726.
[23] D. Lesthaeghe, V. Van Speybroeck, G. B. Marin, M. Waroquier, *Chem. Phys. Lett.* **2006**, *417*, 309 – 315.
[24] D. Lesthaeghe, G. Delcour, V. Van Speybroeck, G. B. Marin, M. Waroquier, *Microporous Mesoporous Mater.* **2006**, *96*, 350 – 356.
[25] D. S. Santilli, T. V. Harris, S. I. Zones, *Microporous Mater.* **1993**, *1*, 329 – 341.
[26] M. Schenk, S. Calero, T. L. M. Maesen, L. L. van Benthem, M. G. Verbeek, B. Smit, *Angew. Chem.* **2002**, *114*, 2609 – 2612; *Angew. Chem. Int. Ed.* **2002**, *41*, 2500 – 2502.
[27] A. Sassi, M. A. Wildman, H. J. Ahn, P. Prasad, J. B. Nicholas, J. F. Haw, *J. Phys. Chem. B* **2002**, *106*, 2294 – 2303.
[28] D. Lesthaeghe, V. Van Speybroeck, G. B. Marin, M. Waroquier, *J. Phys. Chem. B* **2005**, *109*, 7952 – 7960.
[29] H. Schulz, M. Wei, *Microporous Mesoporous Mater.* **1999**, *29*, 205 – 218.
[30] S. Svelle, B. Arstad, S. Kolboe, O. Swang, *J. Phys. Chem. B* **2003**, *107*, 9281 – 9289.
[31] S. Svelle, F. Joensen, J. Nerlov, U. Olsbye, K.-P. Lillerud, S. Kolboe, M. Bjorgen, *J. Am. Chem. Soc.* **2006**, *128*, 14770 – 14771
[32] J. F. Haw, D. M. Marcus, *Top. Catal.* **2005**, *34*, 41 – 48.
[33] Gaussian03 (Revision B.03): M. J. Frisch et al., see the Supporting Information
[34] A. D. Becke, *J. Chem. Phys.* **1993**, *98*, 5648 – 5652.

Paper VI

Influence of protein environment on the EPR properties of flavoprotein radicals: a QM/MM study

Pauwels E., Declerck R., Verstraelen T.,
De Sterck B., Kay C.W.M.,
Van Speybroeck V., and Waroquier M.

J. Phys. Chem. B, in preparation

Influence of protein environment on the EPR properties of flavoprotein radicals: a QM/MM study

Ewald Pauwels[1*], **Reinout Declerck**[1+], **Toon Verstraelen**[1], **Bart De Sterck**[1], **Christopher W. M. Kay**[2], **Veronique Van Speybroeck**[1], **Michel Waroquier**[1]
[1]*Center for Molecular Modeling, Ghent University, Technologiepark 903, B-9052 Zwijnaarde, Belgium*
QCMM - alliance Ghent-Brussels, Belgium
[2]*Institute of Structural and Molecular Biology and London Centre for Nanotechnology, University College London, Gower Street, London WC1E 6BT, United Kingdom*

March 18, 2010

Abstract

The neutral and anionic semiquinone radicals of the flavin adenine dinucleotide (FAD) cofactor non-covalently-bound in glucose oxidase from *A. niger* are examined with the aid of QM/MM molecular modeling methods, enabling complete inclusion of the protein environment. Recently, the electron paramagnetic resonance (EPR) characteristics – the anisotropic g tensor and all the significant hyperfine couplings – of these flavoprotein radicals were determined at high resolution (*J. Phys. Chem. B* **2008**, *112*, 3568). The most significant difference between the neutral and anionic radical forms was found to be a shift in the g_y principal value. Within the QM/MM framework, geometry optimization and molecular dynamics simulations are combined with EPR property calculations, employing a new implementation by some of the authors in the CP2K software package. In this way, highly accurate spectroscopic characteristics are computed *on the fly* during the MD simulations of the solvated protein structure. These computational parameters mimic as best as possible the experimental conditions, enabling cross-validation with measured EPR data. The general agreement between calculated and experimental values is found to be excellent. Furthermore, the shift in the g_y principal values between the neutral and anionic radicals is well reproduced by the QM/MM simulations. Incorporation of at least the nearest protein environment of the cofactor radicals proves to be vital for a correct reproduction, indicating that this shift is a *global feature* of the protein rather than a *local* one. In addition, QM/MM techniques are used to make a *prediction* of relative angles between important spectroscopic principal directions, which are not readily determined by conventional EPR experiments. Remarkably, the directions of the g_x and the g_y components of the g-tensor that lie in the plane of the isoalloxazine moiety are rotated by approximately 60° between the neutral and the anionic radicals.

---

[*] To whom correspondence should be addressed. Fax : 32 9 264 66 97 E-mail: ewald.pauwels@UGent.be
[+] Present address: The Boston Consulting Group, Keizerinlaan 13, 1000 Brussels, Belgium

Running Title

QM/MM of flavoprotein EPR properties

Keywords

CP2K, EPR, molecular dynamics, butterfly bend, FAD, QM/MM

1. Introduction

Flavoproteins are ubiquitous electron transfer proteins that catalyze a wide variety of biological processes [1]. The remarkable catalytic versatility of these enzymes is due to the redox-active flavin cofactor, which can assume different oxidation states: fully oxidized, fully reduced but also the one-electron reduced semiquinone radical. The latter can further occur in a neutral or anionic form (Scheme 1), depending on the pH and particular protein environment. Insight into the (electronic) structure of these various cofactor forms in interaction with the protein is vital for a better understanding of their role in catalysis.

The semiquinone radical forms of flavins can be examined with magnetic resonance experiments based on Electron Paramagnetic Resonance (EPR) spectroscopy. The main spectroscopic properties – the hyperfine coupling tensors and the *g* tensor - yield valuable information on the structural and physical properties of the radicals, as they directly probe the unpaired electronic spin density. In recent years, these properties have been determined often with remarkable accuracy for various flavoproteins, including photolyases from *Escherichia coli* [2, 3] and *Xenopus laevis* [4, 5], human monoamine oxidase, D-amino acid oxidase from *Rhodotorula gracilis* [6], oxidoreductase from *Vibrio cholerae* [7] and glucose oxidase from *Aspergillus niger* [8]. The very small *g*-tensor anisotropy of flavin radicals can only be resolved using spectrometers that operate at high magnetic fields / microwave frequencies, rather than with the standard 9 GHz (X-band) set-up and in these studies, it was established that the *g* tensor is unique for each flavoprotein. The principal values are a reliable probe of local changes in the electronic/chemical structure of the flavin cofactor [7, 8, 9], whereas the principal directions are most sensitive to global changes in the cofactor environment and can differ significantly between proteins [2, 3, 4, 5].

In general, calculations based on ab initio methods, such as density functional theory (DFT) [10], can be used to complement the experiment to gain a better understanding of the origin of all spectroscopic properties. A variety of algorithms have been developed to calculate EPR quantities from first principles, but they have mostly been applied to relatively small systems [11]. Their application to molecular systems as extended as proteins is still limited, because these are challenging from the computational point of view [12]. Only very recently, some of the authors have made significant progress in this area by introducing a new, computationally attractive method for the all-electron calculation of NMR and EPR properties in extended molecular systems under periodic boundary conditions [13, 14]. These new features were implemented in the freely available CP2K software [15] and have been applied successfully on smaller systems [16, 17]. Furthermore, the range of state-of-the-art simulation techniques available in CP2K is ideally suited for the examination of large molecular systems, such as proteins. In particular, QM/MM methods are available, enabling the hybrid use of quantum mechanics and molecular mechanics [14, 18]. Finally, molecular dynamics (MD) simulations can be performed [16], a prerequisite to adequately sample the conformational flexibility of a protein.

In the work presented here, all of these computational procedures are combined to examine the structural and electronic properties of the two flavin radicals in glucose oxidase of *A. niger*, that are formed under different pH conditions. The Flavin Adenosine Dinucleotide (FAD) cofactor in this enzyme in both the neutral and anionic radical states thus provides twin spectroscopic landscapes that were recently extensively characterized by Okafuji et al. [8]. The FAD structure is depicted in Scheme 1 with the appropriate atom-numbering scheme. For both forms, the full anisotropy of the significant hyperfine couplings and the *g* tensor were determined. Notably the g_y component was found to shift between the neutral (**FADH•**) and anionic (**FAD•-**) radicals. The authors tentatively attributed this to differences in the local spin density. Here, QM/MM ab initio methods are applied to reproduce this shift in the *g* tensor and trace its origin. In addition, a prediction is made of the principal directions of the hyperfine and *g* tensors. Even though (an)isotropic values were accurately determined in the experiment for these tensors, information on their orientation with respect to the molecular frame is still lacking.

Flavins have been the subject of several DFT studies [e.g. 19], but few have examined flavin semiquinone radicals [20, 21, 22] and even fewer have applied DFT to determine the EPR properties of these radicals [2, 23, 24]. To the best of our knowledge, this is the first study in which the QM/MM methodology is used consistently to study both their structural and magnetic resonance properties.

2. Computational Details

The initial geometries of protein and cofactor were taken from the protein data bank [25] (1CF3 [26]). Missing residues and atoms were added and the complex was then solvated in a cubic box of (98.0 Å)^3 (with 29337 water molecules). Using the GROMACS software [27], a topology was constructed for the GROMOS G96 53a6 [28] united-atom force field - parameters adapted by Feenstra et al. [29] were employed for the FAD cofactor. In the experiments [8], the anionic and neutral flavin forms were measured at different pH values (pH 10 and 5 respectively), implying different protonation states for the titratable residues in the protein. This was taken into account, by fully protonating all histidines (pKa ~ 6) in the neutral flavin simulations. After initial optimization and an MD equilibration at the molecular mechanics level (using GROMACS), the resulting structures were used as input for subsequent QM/MM calculations, which were performed with the CP2K software [15]. The partitioning of the entire molecular system in two regions, treated at the QM and MM level, is illustrated in Figure 1. Included in the (17.0 Å)^3 QM region are the 7,8-dimethyl isoalloxazine part of FAD, along with the C1' and C2' carbons of the ribityl linker with their substituents (see Scheme 1 for atom numbering). A link atom approach was used to saturate with hydrogen the broken C2'-C3' bond crossing the QM/MM boundary. The interaction between the MM and QM layers was calculated at the QM level, using the Gaussian expansion of the electrostatic potential method (GEEP) as developed by Laino et al. [30].

The PBE density functional [31] was used in all calculations but different basis set schemes were adopted. In the geometry optimization and molecular dynamics simulations, the Gaussian and plane waves (GPW) dual basis set method was applied, which employs Gaussian-type atom-centered basis functions to describe the wave functions and an auxiliary plane wave basis to describe the density [32]. A triple-ζ Gaussian basis set augmented with two sets of polarization functions (TZV2P [33]) was used and plane waves were expanded up to a density cutoff of 280 Ry, with GTH pseudopotentials [34, 35] describing the core electrons. For the subsequent electronic and magnetic response properties calculations, an all-electron method is required and therefore the Gaussian and augmented plane wave (GAPW) method was applied [36]. In this approach, the total density is described by a smooth, extended part that is represented by plane waves and parts localized close to the nuclei that are expanded in periodic Gaussian functions. The density cutoff for the auxiliary plane wave basis set was set to 250 Ry and after careful assessment, the all-electron TZVP basis [37] was found to be of sufficient quality. For some structures, *g*-tensor calculations were additionally performed with the Gaussian 03 software suite [38]. Here also, the PBE functional was used with a comparable, triple-zeta quality 6-311G(d,p) basis set [39]. Point charges, replacing all or some (see further) of the MM atoms, were added to account for the polarizing effect of the protein.

Using CP2K, complete QM/MM optimizations were performed of the **FADH•** and **FAD•-** radicals within their solvated protein environment. Only the cell volume was constrained. In the following, these structures are referred to with the *QMMMopt* shorthand.

Subsequently, all EPR properties were consistently calculated in the QM/MM scheme for both structures (referred to as *QMMMepr*). In order to account for the conformational flexibility in the cofactor-protein complex, molecular dynamics were initiated for the **FADH•** and **FAD•-** systems in the NVT ensemble, employing a timestep of 1.0 fs. Nosé-Hoover thermostat chains [40] were activated separately on the MM and QM regions, both with a characteristic frequency of 100 cm^{-1}. After equilibration, a 10 ps MD simulation of production quality was run. The resulting trajectories are referred to as *QMMMmd* and for every 20th structure in them, EPR properties were calculated (again in the *QMMMepr* scheme).

3. Results and discussion

Structural Analysis

Before shifting to an in depth discussion of the magnetic response properties, it is useful to compare the protein structures, as obtained from the simulations, with the crystal structure [26]. In Figure 2, the *QMMMopt* structures are superimposed on the crystal structure. Only part of the protein is shown, but it is clear that its structure is largely retained in the simulations, despite the fact that these actually describe a solution phase. This is confirmed by the root-mean-square-deviation (RMSD) between the protein in the crystal and in the *QMMMopt* structures. After least-square fitting, the RMSD for the backbone atoms of the protein only (excluding all coordinates of the FAD cofactor) amounts to 0.8 Å in the **FADH•** system and 1.2 Å in the **FAD•-** system. During the molecular dynamics these distances are similar, fluctuating between 1.1 - 1.3 Å in both systems. This is also apparent from Figure 2, where the thin blue and red lines – sample snapshots from the MD runs – stay close to the *QMMMopt* structures (blue and red tubes). Analysis of the average RMSD values on a per-residue basis also does not indicate significant changes of the protein structure in the immediate vicinity of either of both FAD radical forms. Although the QM region in the calculations is probably not large enough for an accurate assessment, this nevertheless suggests that the presence of an FAD radical does not alter the geometry of the protein environment significantly.

The neutral and anionic flavin moieties, however, behave in remarkably different ways. Concentrating on the 7,8-dimethyl isoalloxazine ring system of the cofactor, which is the primary locus of the unpaired electron, the neutral **FADH•** radical stays close to the position of the FAD cofactor in the crystal structure. In Figure 2, both ring systems are well aligned. The RMSD for the isoalloxazine ring system amounts to 0.4 Å only in the *QMMMopt* structure and it fluctuates between 0.5 - 1.4 Å in the MD trajectory. The anionic **FAD•-** radical, on the other hand, has dramatically reoriented inside the protein cavity with respect to the crystal structure. Not surprisingly, the RMSD is much larger and amounts to 2.0 Å in the *QMMMopt* structure, fluctuating between 1.7 - 2.7 Å in the dynamics.

A structural feature that is of particular interest in flavins is the (non)planarity of their isoalloxazine ring system, often termed the 'butterfly bend' [41]. It is usually indexed by the angle between the LSQ-fitted planes through either of the aromatic rings flanking the central ring. In crystallographic data, oxidized flavins are often found to be planar, whereas butterfly bend angles of 20° to 30° are not uncommon for reduced flavin proteins. But the oxidation state is not the sole determinant of the flavin planarity, since enzymes have been found that are butterfly-bent in both the reduced and oxidized states [42]. Other works have suggested that the presence and nature of ligands [43], or particular protein residues in the vicinity of the cofactor [44] may affect the butterfly bend. Clearly the modulating effect of (non)planarity on the redox properties of the flavoenzyme is still a part of ongoing debate. In the crystal structure of (fully oxidized) *A. niger* glucose oxidase, the isoalloxazine ring system shows a slight butterfly bend of 10°. This does not change much when an **FADH•** or **FAD•-** radical is considered in the calculations: respectively 17° and 12° for *QMMMopt* structures, 13° and 12° on average in the MD, both fluctuating between 0° and 30°. The slightly enhanced non-planarity of the optimized structures is just visible in Figure 2. In other DFT studies of (one-electron-reduced semiquinone) flavins, comparable angles were reported [21].

Summarizing, all QM/MM calculations indicate that the **FADH•** and **FAD•-** flavin radicals have similar intrinsic structures, with comparable butterfly bend angles as the non-paramagnetic cofactor of the crystal structure. However, the anionic **FAD•-** radical is reoriented inside the protein, whereas the neutral **FADH•** radical largely retains the original orientation from the crystal structure.

Analysis of magnetic resonance properties: hyperfine couplings

A summary of the measured (an)isotropic hyperfine values in the experiments by Okafuji et al. [8] is presented in Table 1. Full anisotropic values are available for the H(N5) hyperfine coupling of **FADH•** (see Scheme 1 for atom numbering), whereas for tensors with an axially symmetric shape only the "parallel" (//) and "perpendicular" (⊥) components are given.

Considering the (an)isotropic hyperfine couplings first, it is clear that the *QMMMopt/QMMMepr* calculations (also taken up in Table 1) completely succeed in reproducing from a qualitative perspective the pattern as observed in the experiments. The proton spectrum of **FADH•** is dominated by the anisotropic H(N5) coupling and the axial proton coupling of the methyl group at C8, which is a free rotor and hence gives rise to one averaged tensor H(C8a). In **FAD•-** the former is not present. Two additional proton couplings have been identified in **FADH•** – a small one (H(C6)) and a larger one (H(C1')). The latter coupling was not formally identified in the **FAD•-** measurements, yet our calculations predict a non-zero coupling for the H(C1') proton. Okafuji et al. pointed out that spectral overlap with other signals might have prevented clear resolution of this signal [8]. In further accordance with the experiments, the calculated ^{14}N coupling of N5 is larger than that of N10 in both anionic and neutral forms of the flavin radical. From a quantitative perspective, the overall performance of the *QMMMopt/QMMMepr* calculations is also convincing, but minor absolute deviations persist. Notably the isotropic hyperfine coupling values are particularly difficult to simulate, with differences of up to 10 MHz, which is within the typical error margin [45, 46]. The errors in the isotropic hyperfine coupling can be attributed to the dependency on the electronic spin density at the location of the nucleus, and are therefore very sensitive to basis set dependencies, the failure to predict nitrogen isotropic couplings being a notorious example [13, 46]. Conversely, the anisotropic shapes of all hyperfine couplings are always well reproduced. The slight overestimation of the H(C8a) isotropic coupling in **FADH•** is not due to this effect. Apparently, in the *QMMMopt* minimum this methyl group assumes a particular conformation with respect to the isoalloxazine ring system which gives rise to a bigger isotropic coupling. This specific conformation is readily abandoned when the potential energy surface is sampled more representatively in the molecular dynamics.

Also reported in Table 1 are the calculated expectation values for the hyperfine values, evaluated over 500 structural snapshots regularly sampled along the MD trajectories. These *QMMMmd/QMMMepr* values were obtained by first computing the average tensor:

$$\langle \mathbf{A} \rangle = \frac{1}{N} \sum_{i}^{N=500} \mathbf{A}_i \tag{1}$$

where the summation runs over all snapshots. Subsequently, this average tensor was diagonalized:

$$(\mathbf{V}_1 \quad \mathbf{V}_2 \quad \mathbf{V}_3)^{\mathrm{T}} \langle \mathbf{A} \rangle (\mathbf{V}_1 \quad \mathbf{V}_2 \quad \mathbf{V}_3) = \begin{bmatrix} A_1 & & \\ & A_2 & \\ & & A_3 \end{bmatrix} \tag{2}$$

This yields three *average* eigenvalues A_1 to A_3 (expectation values) and their corresponding principal directions $\mathbf{V}_1$ to $\mathbf{V}_3$ represented by 3x1 column matrices. The validity of the time-averages was checked by determining the error on the eigenvalues with the block average method [47]. It was found to be sufficiently small, indicating that enough MD samples were taken into account to meet our purposes. Free rotation of the methyl groups at C7 and C8 was observed during the dynamics and accounted for by additionally averaging all individual methyl proton hyperfine coupling tensors. From Table 1 it is clear that dynamic properties are similar to the static ones, illustrating that essentially the same conformational space is described by the *QMMMopt* and *QMMMmd* simulations.

To illustrate the variation throughout the dynamics of a certain hyperfine coupling tensor $\mathbf{A}_i$, its projection can be calculated along an averaged eigenvector direction $\mathbf{V}_\alpha$ (α = 1-3):

$$A_i^{\text{proj}-\alpha} = \left\| \mathbf{A}_i \mathbf{V}_\alpha \right\| \tag{3}$$

The distribution of the resulting 500 projected (absolute) values is shown in Figure 3 for several hyperfine tensors. It is immediately obvious that three individual anisotropic values (A_x, A_y, A_z) can only be extracted for the H(N5) hyperfine coupling tensor of **FADH•** (see also Table 1). In the case of the ^{14}N hyperfine coupling tensors, the projected minor and intermediate hyperfine values can no longer be independently resolved and coalesce into one $A_\perp$ value. These tensors can now be described by a perpendicular component close to zero and an $A_{//}$ component close to 20 MHz (for N10) and 40 MHz (for N5) respectively. The same applies for H(C8a), although the smaller difference between the $A_\perp$ and $A_{//}$ values impedes a clear visual distinction in Figure 3.

Reviewing all the hyperfine values in Table 1, it is clear that the differences between the measurements of **FADH•** and **FAD•-** are only subtle – the obvious absence of H(N5) in the latter notwithstanding. There is a slight change in the isotropic coupling of H(C8a). The anion has a bigger coupling than the neutral flavin radical, reflecting a redistribution of spin in the isoalloxazine ring system towards the methyl group. This shift – a mere 3 MHz and so close to the limit of computational accuracy – is only qualitatively reproduced by the *QMMMmd/QMMMepr* calculations, validating the requirement of adequate conformational sampling. Other hyperfine couplings also shift in magnitude between the **FADH•** and **FAD•-** forms of the cofactor, in line with the minute changes of the spin density distribution: the (absolute) size of H(C6) increases whereas N10 decreases in the anion. These small trends are correctly reproduced in all our calculations.

Analysis of magnetic resonance properties: principal *g* values

The absolute *g* values from the measurements [8] are taken up in Table 1, along with the results of the calculations. Relative Δg values (with respect to the free electron value) are also presented in Table 2 for the experiment and for the *QMMMopt/QMMMepr* results. Both *QMMMopt/QMMMepr* and *QMMMmd/QMMMepr* schemes succeed quite well in reproducing the characteristic values of the experiment, with absolute errors of 500-600 ppm at most. This is of the same order of magnitude as the typical error margin for this property [48]. The experiment also shows that the *g* values of the **FAD•-** radical are quite similar to those of **FADH•**, apart from a 290 ppm rise of the g_y principal value. The QM/MM calculations are apparently more reliable in reproducing this relative difference than in reproducing the absolute *g* values. g_y rises by 434 ppm between **FADH•** and **FAD•-** in the

QMMMopt/QMMMepr calculation and by 384 ppm in *QMMMmd/QMMMepr*, whereas g_x and g_z are practically the same in both radicals. This is made more transparent by considering the changes of the principal *g* values when switching from **FADH•** to **FAD•-**. These relative differences, denoted $\Delta\Delta g_i$ (with i=x,y,z) in Table 2, are given by:

$$\Delta\Delta g_i = g_i(\mathbf{FAD\bullet-}) - g_i(\mathbf{FADH\bullet}) \quad (4)$$

The apparently better performance of the QM/MM DFT methods for the relative ΔΔg differences, might find its origin in the computational algorithms for the calculation of the *g* tensor. These generally include contributions that are the result of the difference between a spin-up and a spin-down term [11]. Since the individual terms are usually much bigger than the final contribution, the accuracy of the *g*-value calculation will depend largely on error cancellation between these terms. Especially when the *g* values are close to the free electron value, minute changes in the spin-up and spin-down terms can give rise to considerable absolute errors. By considering the relative difference between two calculated *g* values, systematic errors are eliminated. Obviously, this is only valid when the molecular systems in each of these calculations are comparable. The **FADH•** and **FAD•-** molecular systems meet this requirement: they differ in one proton only and even the overall conformations of the protein and cofactor are comparable (see above). Additional *g*-tensor calculations on the *QMMMopt* geometry using the Gaussian 03 software [38] (labeled *QMCepr*) further illustrate that relative ΔΔg differences are more easily reproduced, irrespective of the computational algorithm. Table 2 shows that Δg values can easily differ by 500 ppm between the CP2K and Gaussian implementations. The relative ΔΔg differences are far more robust: the difference between the *QMMMepr* and *QMCepr* schemes amounts to 89 ppm at most. Both schemes reproduce the relative pattern of the experiment: $\Delta\Delta g_y$ is much bigger than $\Delta\Delta g_x$ and $\Delta\Delta g_z$, amounting to several hundred ppm.

The computational methods furthermore offer the unique possibility of tracing the origin of the g_y shift. Using both the Gaussian and CP2K implementations, another set of *g*-tensor calculations was performed on the *QMMMopt* optimized structures of **FADH•** and **FAD•-**. But this time the spectroscopic properties were only determined for the molecular system comprised by the QM layer – i.e. the isoalloxazine radical only, without the (protein) atoms in the MM layer (see Figure 1). The results of these *QMepr* calculations are presented in Table 2. Clearly, the protein environment of the radical has an influence on the Δg value and the experimental g_y shift is not reproduced at all. Instead, other shifts emerge which do not fit the experiment. Hence, because the different spin densities of the *isolated* radicals do not give rise to the g_y shift between the neutral and anionic flavin radicals, it is *not* merely an intrinsic or local feature, as Okafuji et al. [8] tentatively concluded.

The influence of the protein on the *g* tensor of the cofactor is intriguing and demands a closer analysis of the amino acids constituting the primary sequence. For instance, it might be possible that the different protonation states of some of the residues in the **FADH•** and **FAD•-** molecular systems are responsible for the characteristic ΔΔg pattern. Alternatively, it could be conceivable that only charged residues (collectively) bring about this pattern. To investigate these possibilities, the *QMCepr* scheme was applied various times on the *QMMMopt* structures of the **FADH•** and **FAD•-** systems. All protein residues were ordered on the basis of the proximity of their Cα atom to the N5 atom of the isoalloxazine ring in **FADH•**. The same sequence was used for the **FAD•-** system. Subsequently, *QMCepr* calculations were performed on a molecular system comprising the entire cofactor (with the isoalloxazine part treated at the QM level), in which gradually every amino acid of the sequence was added to the MM layer. The results of these 583x2 calculations are presented in Figure 4. The *QMepr* data of Table 2 are consistent with the left-hand side of the plot, where only one residue and the MM part of the cofactor are additionally accounted for.

Progressively considering more amino acids in the molecular system, the ΔΔg relative differences vary in size and sign, and from about 10 Å (16-17 residues) they start converging towards the complete *QMCepr* data of Table 2. The residual, minor differences with the values at the right-hand side of Figure 4 are due to the absence of water in these calculations. Some of the residues within the first 10 Å are clearly involved in a hydrogen bond with the cofactor (e.g. Gly108, Met561) or are charged (e.g. His559). Yet, the plot does not show any clear variations of the ΔΔg values due to one specific residue. Inclusion of all the charged or hydrogen-bound residues in the *g*-tensor calculation did not result in the desired *g*-value pattern either, nor did a simulation on a system comprising only the residues with a different protonation state between **FADH•** and **FAD•-**. Instead, the first 10-20 residues seem to have a cumulative effect. The majority of these first few amino acids cannot be easily classified in terms of a hydrogen bonding or electrostatic interaction, but they clearly polarize the spin density of the cofactor radicals such that an essentially correct characteristic pattern of the relative ΔΔg values emerges. It seems to be sufficient to include in the simulations only the amino acids within a 10 Å radius of the cofactor.

Concluding, the QM/MM calculations point out that also the immediate protein environment of the cofactor – and so a *global feature* rather than a *local* one – is responsible for the g_y shift between the **FADH•** and **FAD•-** flavoprotein radicals. This nuances the common conception that the g_y shift directly reflects the changes in the local electronic/chemical structure of the flavin cofactor radical, as resulting from the deprotonation [7, 8, 9]. Although this influences the *g*-tensor values, it is not sufficient alone – the polarizing effect of the immediate protein environment of the cofactor is an equally important contributing factor.

Analysis of magnetic resonance properties: *g*- and hyperfine tensor directions

In EPR measurements on single crystals, the principal directions of e.g. a hyperfine tensor can be determined in an *absolute* fashion with respect to the crystal axes. This makes it possible to directly link this directional information with the structure from the X-ray diffraction, if indeed this structure is representative for the paramagnetic species trapped inside the crystal. The latter is not trivial – e.g. in the case of radiation-induced sugar radicals, the radical will likely assume a different conformation than the undamaged sugar molecule of the crystal [49, 50]. Single crystal measurements on protein radicals are possible [e.g. 51, 52], but to date no such measurements have been performed on flavoproteins.

In EPR experiments on disordered protein samples – (frozen) solutions or powders – the direct link between the X-ray molecular structure and the principal directions is completely lost, since the molecule will be able to assume all possible orientations. Here, correlating the orientation of principal directions with respect to the molecular frame can only proceed in a *relative* fashion. In this way, some anisotropic directional information has become available for several flavoproteins [2, 3, 4, 5]. Spectral simulations allow the determination of the angles between well-defined principal directions, e.g. g_x and $H(C8a)_{//}$. If it is now assumed that $H(C8a)_{//}$ and the C8a-C8 bond direction are collinear, the orientation of g_x with respect to the molecular frame can be inferred. This precise procedure was followed by the Berlin group to characterize the neutral flavin radicals in photolyases [3, 4, 5]. Another approach is to assume that g_z is perpendicular to the plane of the isoalloxazine ring system and that g_x follows the N5-H(N5) bond direction [7]. The validity of these methods, of course, hinges on the correct determination of relative angles and of the assumption linking the molecular frame to one or more principal directions. Not surprisingly, ab initio methods are being used to assist in this process and eliminate some of the approximations [2].

So far, a complete description of the *g*- and hyperfine tensor directions is lacking for the FAD radicals of glucose oxidase in *A. niger*. The QM/MM calculations described in this work enable a *prediction* of these properties. In Figure 5, the principal directions for several computational schemes are plotted with respect to the molecular frame of the *QMMMopt* structures of **FADH•** and **FAD•-**. The hyperfine tensors of the *QMMMopt/QMMMepr* scheme are represented by green vectors, superimposed on the relevant atoms. The corresponding *g*-tensor directions are drawn separately, indicated by the number **1**. The procedure outlined in equations (1) and (2) also extracts average principal directions from the molecular dynamics simulations. These are plotted as red vectors in Figure 5 – the *g* tensor here is labelled **5**. With the outlook of possible future orientation-selective ENDOR experiments that allow determination of the relative directions of the *g*- and hyperfine tensor, the angles between several calculated directions are also determined. In Table 3, these are reported for the neutral and anionic flavin radicals in the *QMMMopt/QMMMepr* and *QMMMmd/QMMMepr* schemes.

Reviewing Figure 5 and Table 3, no substantial differences are obvious between the principal directions of the optimized structure and the molecular dynamics simulations. The mean MD values do not deviate more than 8° from the static optimized structure. In every calculation, the $H(C8a)_{//}$ principal direction virtually coincides with the C8a-C8 bond, validating this approach for the relative determination of the *g*-tensor orientation [4, 5]. The other approach by Barquera et al. [7] would be equally valid for this flavoprotein, since the angle between the g_x and $H(N5)_x$ directions is always small. However, this method is less generally applicable as it only allows the determination of the *g*-tensor orientation in the neutral **FADH•** radical. The various computational schemes for the calculation of the *g* tensor seem to be mostly consistent with each other with respect to the principal directions. This is clearly observed in Figure 5. The *QMCepr* scheme (**2**) gives almost identical results as the *QMMMepr* scheme (**1**). Smaller deviations are apparent for the *QMepr* schemes (**3** and **4**). Apparently, the *g*-tensor principal directions are less influenced by the nearest protein environment than the principal values (see above).

Considering the difference between **FADH•** and **FAD•-**, Figure 5 shows that the g_z, $N5_{//}$ and $N10_{//}$ interactions have similar directions in both radical forms, roughly perpendicular to the plane of the fused ring system. The corresponding angles with the g_z direction in Table 3 are all quite small, attesting their collinearity. On the other hand, the g_x and g_y principal directions considerably differ in orientation with respect to the molecular frame. This is readily seen in Figure 5, where the x and y directions are almost reversed between the neutral and anionic radical. In **FADH•**, the *g*-tensor orientation closely follows that of the H(N5) hyperfine interaction. The angle between g_x and $H(N5)_x$ is 5° (considering the *QMMMopt/QMMMepr* data in Table 3), resulting in a 60° deviation from the $H(C8a)_{//}$ direction. This is bigger than that observed in other flavoproteins: in *X. laevis* (6-4) photolyase the angle between $H(C8a)_{//}$ and g_x was estimated to be 30° [4], in *E. coli* DNA photolyase a value of 46° was determined [3]. To date, no experiments are available that determine the *g*-tensor orientation for an anionic flavoprotein radical. However, *in silico*, the loss of the H(N5) proton in **FAD•-** has a marked effect on the *g*-tensor orientation. The g_x principal direction is almost parallel to $H(C8a)_{//}$ – the angle between these directions amounts to 9° only.

4. Conclusions

QM/MM molecular modeling methods were applied to examine the neutral and anionic semiquinone FAD radicals in glucose oxidase of *A. niger*. Structural analysis after geometry optimization and molecular dynamics simulations indicates that the presence of such a radical does not significantly alter the geometry of the protein environment. The intrinsic structure of the cofactor, as observed in the crystal structure, is essentially retained in the neutral and anionic radical forms, although the latter undergoes an overall reorientation inside the protein cavity.

Magnetic resonance properties of the radicals were consistently evaluated in the QM/MM methodology throughout all simulations, using recently developed routines [13, 14] in the CP2K software package. These calculations reproduce the (an)isotropic hyperfine and *g*-tensor values from the experiment [8] to a satisfactory level of agreement. In addition, computational methods were applied to make a *prediction* of the principal directions for these spectroscopic properties – information that is not (yet) generally obtained by experiment.

The differences between the hyperfine tensors of **FADH•** and **FAD•-** are only subtle. Nevertheless, the QM/MM calculations satisfactorily show the correct trends. The variation of the *g* tensor between both radical forms is more pronounced. Most notably, the experiment indicates a 290 ppm rise of the g_y principal value in the anion as compared to the neutral variant. This shift is well reproduced by the QM/MM methods. Inclusion of the immediate protein environment in the simulations proves to be vital. At least the amino acids within a 10 Å radius of the cofactor need to be taken into account to obtain a correct reproduction of the g_y shift. Therefore, the difference in the g_y principal value between the **FADH•** and **FAD•-** flavoprotein radicals only in part reflects the *local* chemical and electronic changes due to the deprotonation. The *global* polarizing effect of the protein environment should not be neglected.

Our calculations corroborate the evidence that the anisotropic information of the *g* tensor is a sensitive probe of both *local* and *global* changes in flavoproteins, affirming its usefulness as a fingerprint spectroscopic feature. The principal directions of the *g* tensor also differ significantly between both radical forms. Our QM/MM calculations predict that the g_x and g_y directions assume different orientations. In **FADH•**, the orientation of the *g* tensor is dominated by the H(N5) hyperfine interaction: g_x is virtually parallel to $\mathrm{H(N5)}_x$. As a result, the relative angle between the g_x and $\mathrm{H(C8a)}_{//}$ principal directions is calculated to be about 60°, which is larger than in other neutral flavoprotein radicals. Remarkably, the loss of the H(N5) proton in **FAD•-** causes a 60° reorientation, as g_x now aligns with the $\mathrm{H(C8a)}_{//}$ hyperfine interaction. We expect that this prediction will inspire the experimental determination of the principal directions of the *g* tensor in protein-bound anionic flavin radicals.

Acknowledgement

This work is supported by the Fund for Scientific Research – Flanders (FWO), the Research Board of the Ghent University and BELSPO in the frame of IAP 6/27. Part of the computational resources and services used in this work were provided by Ghent University. The authors kindly acknowledge A. Feenstra for providing adapted force field parameters for the FAD cofactor, M. Baer for allowing the use of the GMX2GROMOS program and R. Glaves for her help in setting up the QM/MM simulations in CP2K.

Schemes

Scheme 1

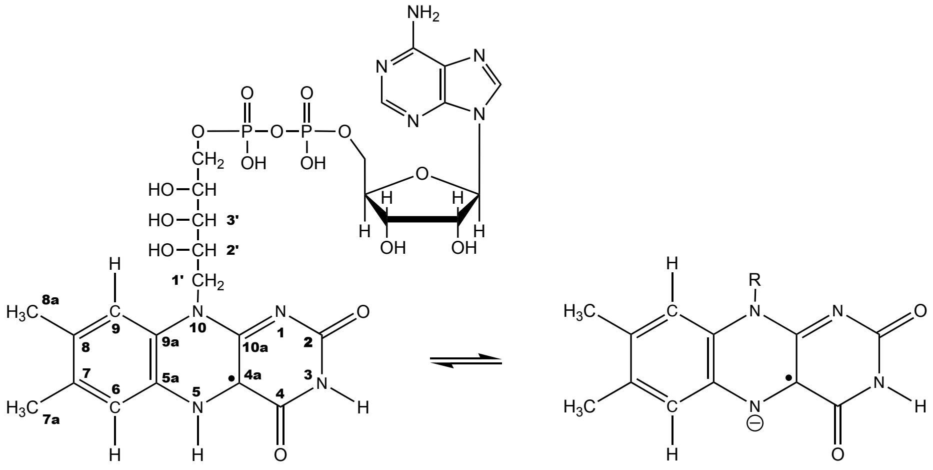

FADH• **FAD•−**

Tables

		Experiment				*QMMMopt* *QMMMepr*		*QMMMmd* *QMMMepr*	
		FADH•		**FAD•-**		**FADH•**	**FAD•-**	**FADH•**	**FAD•-**
g	g_x	2.0043	(1)	2.00429	(3)	2.00489	2.00493	2.00487	2.00493
	g_y	2.0036	(1)	2.00389	(3)	2.00403	2.00446	2.00408	2.00446
	g_z	2.0021	(1)	2.00216	(3)	2.00217	2.00210	2.00235	2.00219
	g_{iso}	2.0035	(1)	2.00345	(3)	2.00370	2.00383	2.00376	2.00386
H (C8a)	$A_{//}$	8.45	(5)	11.45	(5)	11.59	11.82	10.43	11.85
	$A_\perp$	6.85	(5)	9.95	(5)	9.91	9.82	8.78	9.88
	A_{iso}	7.40		10.45		10.47	10.49	9.33	10.54
H (N5)	A_x	-10	(5)			1.77		5.33	
	A_y	-33.9	(1)			-32.61		-27.55	
	A_z	-24.1	(1)			-22.76		-18.10	
	A_{iso}	-22.7				-17.87		-13.44	
N5	$A_{//}$	53	(5)	53	(3)	40.05	42.31	38.66	40.51
	$A_\perp$	0	(5)	0	(3)	-3.78	-5.81	-2.64	-4.96
N10	$A_{//}$	30	(5)	25	(3)	21.44	18.28	22.09	17.27
	$A_\perp$	0	(5)	0	(3)	-1.81	-1.95	-0.99	-1.10
H (C6)	A_{iso}	5.2		8.2		-3.12	-6.85	-3.14	-6.91
H (C1')	A_{iso}	11.3				12.74	7.05	12.33	8.53

Table 1
Hyperfine couplings (in MHz) and *g*-tensor values of the neutral and anionic flavin radicals in glucose oxidase. The experimental values refer to the measurements by Okafuji et al. [8]; the number between brackets indicates the error margin. EPR properties were calculated, in a static approach for the *QMMMopt* structures and by averaging over the MD snapshots (*QMMMmd*). Each time, the QM/MM scheme was consistently applied for the magnetic resonance properties (*QMMMepr*). Calculated H(C8a) values were determined by averaging the three individual methyl proton hyperfine tensors.

			Structure	***QMMMopt***			
		Experiment	EPR scheme	***QMepr***		***QMMMepr***	***QMCepr***
			Program	**CP2K**	**Gaussian**	**CP2K**	**Gaussian**
FADH•	Δg_x	1981		3171	2763	2573	2102
	Δg_y	1281		2399	2067	1710	1463
	Δg_z	-219		-134	-275	-148	-323
FAD•-	Δg_x	1971		2902	2401	2613	2147
	Δg_y	1571		2313	1962	2144	1808
	Δg_z	-159		-229	-446	-218	-447
(FAD•-) - (FADH•)	$\Delta\Delta g_x$	-10		-269	-362	40	45
	$\Delta\Delta g_y$	290		-86	-105	434	345
	$\Delta\Delta g_z$	60		-95	-171	-70	-124

Table 2
Summary of relative *g* values for the experiment and for several computational schemes. The Δg_i values (in ppm, with i=x,y,z) are given relative to the free electron value. The $\Delta\Delta g_i$ values are the corresponding differences between the **FADH•** and **FAD•-** Δg_i values. All calculated *g* values in this table are determined for the *QMMMopt* optimized geometry. In the *QMCepr* scheme (see computational details), all atoms of the MM layer are replaced by point charges. In the *QMepr* scheme, these atoms are just not taken into account, and only the atoms of the QM layer are considered in the calculations.

Angle between:		g_z H(N5)$_z$	g_z N5$_{//}$	g_z N10$_{//}$	C8-C8a H(C8a)$_{//}$	g_x H(C8a)$_{//}$	g_x H(N5)$_x$
QMMMopt/QMMMepr							
FADH•		5	8	2	3	60	5
FAD•-			6	14	1	9	
QMMMmd/QMMMepr							
FADH•	Mean	13	15	9	3	58	13
	Minimum	1	1	0	0	37	1
	Maximum	36	44	30	10	86	37
FAD•-	Mean		9	17	2	13	
	Minimum		0	3	0	1	
	Maximum		32	41	6	39	

Table 3

Angles (in degrees) between structural and/or tensor directions. For the 500 snapshots of the molecular dynamics, mean values are reported as well as the minimum and maximum values throughout the trajectory.

Figure captions

Figure 1
Illustration of the QM/MM partitioning scheme. Protein (gray cartoon), water (red dots) and part of the FAD cofactor (colored green) are taken up in the MM layer. Atoms of the QM layer are shown in orange. An enlarged view of the flavin cofactor (here in its neutral form) is shown at the top. Figure generated with VMD [53].

Figure 2
Structural similarity of calculated and measured data. The crystallographic structure of the FAD isoalloxazine ring system is shown along with the backbone of the nearest protein residues (gray tube). The *QMMMopt* structures are shown superimposed on the crystal structure for **FADH•** and **FAD•-** (respectively blue and red). Thin blue and red lines illustrate the flexibility of the protein chain during the QM/MM molecular dynamics. The protein backbone was used to obtain the shown least-square-fit alignment. Figure generated with VMD [53].

Figure 3
Histograms of projected tensor values. Blue, red and green boxes respectively indicate the occurrence of a *g* value or hyperfine coupling as resulting from projection along the averaged direction corresponding to the minor, intermediate or major averaged eigenvalue. Average values of each distribution are shown at the top of the plots; dashed lines indicate the experimental values.

Figure 4
$\Delta\Delta g$ (**FAD•- - FADH•**) values as a function of the distance between the N5 atom of the neutral radical and the Cα atom of the residue additionally taken up in the *QMCepr* *g*-tensor calculation. The N5-Cα distance is a measure of the number of amino acids taken up in the calculation.

Figure 5
Graphical representation of the principal directions of the *g*- and hyperfine tensors with respect to the isoalloxazine molecular frame. The *QMMMopt* geometries are shown and hyperfine principal directions are superimposed on the atom involved as green arrows – red arrows indicate the average results of the *QMMMmd/QMMMepr* calculations. The *g*-tensor directions are plotted separately for several computational schemes. **1**: *QMMMopt/QMMMepr*, **2**: *QMMMopt/QMCepr*, **3**: *QMMMopt/QMepr* (CP2K), **4**: *QMMMopt/QMepr* (Gaussian), **5**: *QMMMmd/QMMMepr*. Figure generated with VMD [53].

References

---

[1] Massey, V. *Biochem. Soc. Trans.* **2000**, *28*, 283.

[2] Fuchs, M. R.; Schleicher, E.; Schnegg, A.; Kay, C. W. M.; Torring, J. T.; Bittl, R.; Bacher, A.; Richter, G.; Mobius, K.; Weber, S. *J. Phys. Chem. B* **2002**, *106*, 8885.

[3] Kay, C. W. M.; Bittl, R.; Bacher, A.; Richter, G. *J. Am. Chem. Soc.* **2005**, *127*, 10780.

[4] Kay, C. W. M.; Schleicher, E.; Hitomi, K.; Todo, T.; Bittl, R.; Weber, S. *Magn. Reson. Chem.* **2005**, *43*, S96.

[5] Schnegg, A.; Kay, C. W. M.; Schleicher, E.; Hitomi, K.; Todo, T.; Mobius, K.; Weber, S. *Mol. Phys.* **2006**, *104*, 1627.

[6] Kay, C. W. M.; Mkami, H. E.; Molla, G.; Pollegioni, L.; Ramsay, R. R. *J. Am. Chem. Soc.* **2007**, *129*, 16091.

[7] Barquera, B.; Morgan, J. E.; Lukoyanov, D.; Scholes, C. P.; Gennis, R. B.; Nilges, M. J. *J. Am. Chem. Soc.* **2003**, *125*, 265.

[8] Okafuji, A.; Schnegg, A.; Schleicher, E.; Mobius, K.; Weber, S. *J. Phys. Chem. B* **2008**, *112*, 3568.

[9] Schnegg, A.; Okafuji, A.; Bacher, A.; Bittl, R.; Fischer, M.; Fuchs, M. R.; Hegemann, P.; Joshi, M.; Kay, C. W. M.; Richter, G.; Schleicher, E.; Weber, S. *Appl. Magn. Reson.* **2006**, *30*, 345.

[10] For an example of a reference work, see:
Parr, R. G., and W. Yang 1989. Density-Functional Theory of Atoms and Molecules. Oxford University Press, New York.

[11] Kaupp, M.; Bühl, M.; Malkin, V. G. 2004. Calculation of NMR and EPR Parameters: Theory and Applications. Wiley-VCH, Weinheim.

[12] Colombo, M. C.; VandeVondele, J.; Van Doorslaer, S.; Laio, A.; Guidoni, L.; Rothlisberger, U. *Proteins* **2008**, *70*, 1084.

[13] Declerck, R.; Pauwels, E.; Van Speybroeck, V.; Waroquier, M. *Phys. Rev. B* **2006**, *74*, 245103.

[14] Weber, V.; Iannuzzi, M.; Giani, S.; Hutter, J.; Declerck, R.; Waroquier, M. *J. Chem. Phys.* **2009**, *131*, 014106.

[15] http://cp2k.berlios.de

[16] Declerck, R.; Pauwels, E.; Van Speybroeck, V.; Waroquier, M. *J. Phys. Chem. B* **2008**, *112*, 1508.

[17] Tarpan, M.; Sagstuen, E.; Pauwels, E.; Vrielinck, H.; Waroquier, M.; Callens, F. *J. Phys. Chem. A* **2008**, *112*, 3898.

[18] Senn, H. M.; Thiel, W. *Angew. Chem. Int. Ed.* **2009**, *48*, 1198.

[19] Salzmann, S.; Silva, M. R.; Thiel, W.; Marian, C. M. *J. Phys. Chem. B* **2009**, *113*, 15610.

[20] Durbeej, B.; Eriksson, L. A. *J. Am. Chem. Soc.* **2000**, *122*, 10126.

[21] Zheng, X. H.; Garcia, J.; Stuchebrukhov, A. A. *J. Phys. Chem. B* **2008**, *112*, 8724.

[22] Eisenberg, A. S.; Schelvis, J. P. M. *J. Phys. Chem. A* **2008**, *112*, 6179.

[23] Garcia, J. I.; Medina, M.; Sancho, J.; Alonso, P. J.; Gomez-Moreno, C.; Mayoral, J. A.; Martinez, J. I. *J. Phys. Chem. A* **2002**, *106*, 4729.

[24] Weber, S.; Mobius, K.; Richter, G.; Kay, C. W. M. *J. Am. Chem. Soc.* **2001**, *123*, 3790.

[25] http://www.rcsb.org

---

[26] Wohlfahrt, G.; Witt, S.; Hendle, J.; Schomburg, D.; Kalisz, H. M.; Hecht, H. *Acta Cryst. D* **1999**, *55*, 969.

[27] van der Spoel, D.; Lindahl, E.; Hess, B.; Groenhof, G.; Mark, A. E.; Berendsen, H. J. C. *J. Comp. Chem.* **2005**, *26*, 1701.

[28] Oostenbrink, C.; Villa, A.; Mark, A. E.; Van Gunsteren, W. F. *J. Comput. Chem.* **2004**, *25*, 1656.

[29] van den Berg, P. A. W.; Feenstra, K. A.; Mark, A. E.; Berendsen, H. J. C.; Visser, A. J. W. G. *J. Phys. Chem. B* **2002**, *106*, 8858.

[30] Laino, T.; Mohamed, F.; Laio, A.; Parrinello, M. *J. Chem. Theory Comput.* **2005**, *1*, 1176.

[31] Perdew, J. P.; Burke, K.; Ernzerhof, M. *Phys. Rev. Lett.* 1996, 77, 3865.

[32] Lippert, G.; Hutter, J.; Parrinello, M. *Mol. Phys.* **1997**, *92*, 477.

[33] Schaefer, A.; Huber, C.; Ahlrichs, R. *J. Chem. Phys.* **1994**, *100*, 5829.

[34] Goedecker, S.; Teter, M.; Hutter, J. *Phys. Rev. B* **1996**, *54*, 1703.

[35] Hartwigsen, C.; Goedecker, S.; Hutter, J. *Phys. Rev. B* **1998**, *58*, 3641.

[36] Krack, M.; Parrinello, M. *Phys. Chem. Chem. Phys.* **2000**, *2*, 2105.

[37] Godbout, N.; Salahub, D. R.; Andzelm, J.; Wimmer, E. *Can. J. Chem.* **1992**, *70*, 560.

[38] Gaussian 03, Revision B.03, M.J. Frisch, G.W. Trucks, H.B. Schlegel, G.E. Scuseria, M.A. Robb, J.R. Cheeseman, J.A. Montgomery, Jr., T. Vreven, K.N. Kudin, … and J.A. Pople, Gaussian, Inc., Wallingford CT, 2004.

[39] Krishnan, R.; Binkley, J. S.; Seeger, R.; Pople, J. A. *J. Chem. Phys.* **1980**, *72*, 650.
McLean, A. D.; Chandler, G. S. *J. Chem. Phys.* **1980**, *72*, 5639.

[40] Nosé, S. *J. Chem. Phys.* **1984**, *81*, 511.

[41] Zheng, Y. J.; Ornstein, R. L. *J. Am. Chem. Soc.* **1996**, *118*, 9402.

[42] Kitzing, K.; Fitzpatrick, T. B.; Wilken, C.; Sawa, J.; Bourenkov, G. P.; Macheroux, P.; Clausen, T. *J. Biol. Chem.* **2005**, *280*, 27904.

[43] Lyubimov, A.Y.; Heard, K.; Tang, H.; Sampson, N. S.; Vrielink, A. *Protein Sci.* **2007**, *16*, 2647.

[44] van den Hemel, D.; Brigé, A.; Savvides, S. N.; Van Beeumen, J. *J. Biol. Chem.* **2006**, *281*, 28152.

[45] Pauwels, E.; Van Speybroeck, V.; Waroquier, M. *J. Phys. Chem. A* **2004**, *108*, 11321.

[46] Hermosilla, L.; Calle, P.; Garcia de la Vega, J. M.; Sieiro, C. *J. Phys. Chem. A* **2006**, *110*, 13600.

[47] Frenkel, D.; Smit, B. 2001. Understanding Molecular Simulation: From Algorithms to Applications, second edition. Academic Press.

[48] Neese, F. *J. Chem. Phys.* **2001**, *115*, 11080.

[49] De Cooman, H.; Vanhaelewyn, G.; Pauwels, E.; Sagstuen, E.; Waroquier, M.; Callens, F. *J. Phys. Chem. B* **2008**, *112*, 15045.

[50] Pauwels, E.; De Cooman, H.; Vanhaelewyn, G.; Sagstuen, E.; Callens, F.; Waroquier, M. *J. Phys. Chem. B* **2008**, *112*, 15054.

[51] Fittipaldi, M.; Steiner, R. A.; Matsushita, M.; Dijkstra, B. W.; Groenen, E. J. J.; Huber, M. *Biophys. J.* **2003**, *85*, 4047.

[52] Sottini, S.; Gast, P.; Blok, A.; Canters, G. W.; Cavazzini, D.; Rossi, G. L.; Groenen, E. J. J. *Appl. Magn. Reson.* **2010**, *37*, 219.

[53] Humphrey, W.; Dalke, A.; Schulten, K. *J. Mol. Graphics* **1996**, *14*, 33.

Bibliography

[1] W. Koch and M.C. Holthausen, *A Chemist's Guide to Density Functional Theory* volume 2, Wiley-VCH Verlag (2001).

[2] R. G. Parr and W. T. Yang, *Density Functional Theory of Atoms and Molecules*, Oxford Science Publications (1988).

[3] C. D. Christ, A. E. Mark, and W. F. van Gunsteren, *J. Comput. Chem.* **31**(8), pp. 1569–1582 (2010).

[4] M. Orozco and F. J. Luque, *Chem. Rev.* **100**(11), pp. 4187–4225 (2000).

[5] J. Tomasi and M. Persico, *Chem. Rev.* **94**(7), pp. 2027–2094 (1994).

[6] C. J. Cramer and D. G. Truhlar, *Chem. Rev.* **99**(8), pp. 2161–2200 (1999).

[7] J. Tomasi, B. Mennucci, and R. Cammi, *Chem. Rev.* **105**(8), pp. 2999–3093 (2005).

[8] A. Bennaim and Y. Marcus, *J. Chem. Phys.* **81**(4), pp. 2016–2027 (1984).

[9] M. W. Wong, M. J. Frisch, and K. B. Wiberg, *J. Am. Chem. Soc.* **113**(13), pp. 4776–4782 (1991).

[10] F. J. Luque, C. Curutchet, J. Munoz-Muriedas, A. Bidon-Chanal, I. Soteras, A. Morreale, J. L. Gelpi, and M. Orozco, *Phys. Chem. Chem. Phys.* **5**(18), pp. 3827–3836 (2003).

[11] S. Yomosa, *J. Phys. Soc. Jpn.* **35**(6), pp. 1738–1746 (1973).

[12] M. J. Frisch, G. W. Trucks, H. B. Schlegel, G. E. Scuseria, M. A. Robb, J. R. Cheeseman, G. Scalmani, V. Barone, B. Mennucci, G. A. Petersson, H. Nakatsuji, M. Caricato, X. Li, H. P. Hratchian, A. F. Izmaylov, J. Bloino, G. Zheng, J. L. Sonnenberg, M. Hada, M. Ehara, K. Toyota, R. Fukuda, J. Hasegawa, M. Ishida, T. Nakajima, Y. Honda, O. Kitao, H. Nakai, T. Vreven, J. A. Montgomery, Jr., J. E. Peralta, F. Ogliaro, M. Bearpark, J. J. Heyd, E. Brothers, K. N. Kudin, V. N. Staroverov, R. Kobayashi, J. Normand, K. Raghavachari, A. Rendell, J. C. Burant, S. S. Iyengar, J. Tomasi, M. Cossi, N. Rega, J. M. Millam,

M. Klene, J. E. Knox, J. B. Cross, V. Bakken, C. Adamo, J. Jaramillo, R. Gomperts, R. E. Stratmann, O. Yazyev, A. J. Austin, R. Cammi, C. Pomelli, J. W. Ochterski, R. L. Martin, K. Morokuma, V. G. Zakrzewski, G. A. Voth, P. Salvador, J. J. Dannenberg, S. Dapprich, A. D. Daniels, . Farkas, J. B. Foresman, J. V. Ortiz, J. Cioslowski, and D. J. Fox, "Gaussian 09 Revision A.1", Gaussian Inc. Wallingford CT 2009.

[13] H. H. Uhlig, *J. Phys. Chem.* **41**, pp. 1215 (1937).

[14] B. Susskind and I. Kasarnowski, *Z. Anorg. Allg. Chem.* **214**, pp. 385 (1933).

[15] D. D. Eley, *Transactions of the Faraday Society* **35**, pp. 1281 (1939).

[16] O. Sinanoglu, *J. Chem. Phys.* **75**(1), pp. 463–468 (1981).

[17] V. Gogonea and E. Osawa, *J. Mol. Struct.-Theochem* **117**, pp. 305–324 (1994).

[18] R. A. Pierotti, *Chem. Rev.* **76**(6), pp. 717–726 (1976).

[19] P. Claverie, *Intermolecular Interactions: from Diatomics to Biomolecules*, J. Wiley Chichester (1978).

[20] F. Floris and J. Tomasi, *J. Comput. Chem.* **10**(5), pp. 616–627 (1989).

[21] F. M. Floris, J. Tomasi, and J. L. P. Ahuir, *J. Comput. Chem.* **12**(7), pp. 784–791 (1991).

[22] M. Cossi and V. Barone, *J. Chem. Phys.* **109**(15), pp. 6246–6254 (1998).

[23] M. Cossi, N. Rega, G. Scalmani, and V. Barone, *J. Comput. Chem.* **24**(6), pp. 669–681 (2003).

[24] V. Barone and M. Cossi, *J. Phys. Chem. A* **102**(11), pp. 1995–2001 (1998).

[25] M. J. Frisch, G. W. Trucks, H. B. Schlegel, G. E. Scuseria, M. A. Robb, J. R. Cheeseman, J. A. Montgomery, T. Vreven Jr., K. N. Kudin, J. C. Burant, J. M. Millam, S. S. Iyengar, J. Tomasi, V. Barone, B. Mennucci, M. Cossi, G. Scalmani, N. Rega, G. A. Petersson, H. Nakatsuji, M. Hada, M. Ehara, K. Toyota, R. Fukuda, J. Hasegawa, M. Ishida, T. Nakajima, Y. Honda, O. Kitao, H. Nakai, M. Klene, X. Li, J. E. Knox, H. P. Hratchian, J. B. Cross, V. Bakken, C. Adamo,

J. Jaramillo, R. Gomperts, R. E. Stratmann, O. Yazyev, A. J. Austin, R. Cammi, C. Pomelli, J. W. Ochterski, P. Y. Ayala, K. Morokuma, G. A. Voth, P. Salvador, J. J. Dannenberg, V. G. Zakrzewski, S. Dapprich, A. D. Daniels, M. C. Strain, O. Farkas, D. K. Malick, A. D. Rabuck, K. Raghavachari, J. B. Foresman, J. V. Ortiz, Q. Cui, A. G. Baboul, S. Clifford, J. Cioslowski, B. B. Stefanov, G. Liu, A. Liashenko, P. Piskorz, I. Komaromi, R. L. Martin, D. J. Fox, T. Keith, M. A. Al-Laham, C. Y. Peng, A. Nanayakkara, M. Challacombe, P. M. W. Gill, B. Johnson, W. Chen, M. W. Wong, C. Gonzalez, and J. A. Pople, "Gaussian 03, revision c.02".

[26] D. M. Chipman, *Theor. Chem. Acc.* **107**(2), pp. 80–89 (2002).

[27] E. Cances, B. Mennucci, and J. Tomasi, *J. Chem. Phys.* **107**(8), pp. 3032–3041 (1997).

[28] E. Cances and B. Mennucci, *J. Math. Chem.* **23**(3-4), pp. 309–326 (1998).

[29] B. Mennucci, E. Cances, and J. Tomasi, *J. Phys. Chem. B* **101**(49), pp. 10506–10517 (1997).

[30] G. Scalmani and M. J. Frisch, *J. Chem. Phys.* **132**(11).

[31] I. Değirmençi, D. Avci, V. Aviyente, K. Van Cauter, V. Van Speybroeck, and M. Waroquier, *Macromolecules* **40**(26), pp. 9590–9602 (2007).

[32] C. P. Kelly, C. J. Cramer, and D. G. Truhlar, *J. Phys. Chem. A* **110**(7), pp. 2493–2499 (2006).

[33] J. R. Pliego and J. M. Riveros, *J. Phys. Chem. A* **105**(30), pp. 7241–7247 (2001).

[34] V. S. Bryantsev, M. S. Diallo, and W. A. Goddard, *J. Phys. Chem. B* **112**(32), pp. 9709–9719 (2008).

[35] B. De Sterck, V. Van Speybroeck, S. Mangelinckx, G. Verniest, N. De Kimpe, and M. Waroquier, *J. Phys. Chem. A* **113**(22), pp. 6375–6380 (2009).

[36] V. Van Speybroeck, K. Moonen, K. Hemelsoet, C.V. Stevens, and M. Waroquier, *J. Am. Chem. Soc.* **128**, pp. 8468–8478 (2006).

[37] A. K. Manukyan and J. L. Radkiewicz-Poutsma, *J. Mol. Struct.-Theochem* **766**(2-3), pp. 105–112 (2006).

[38] C. P. Kelly, C. J. Cramer, and D. G. Truhlar, *J. Chem. Theory Comput.* **1**(6), pp. 1133–1152 (2005).

[39] N. Sadlej-Sosnowska, *Theor. Chem. Acc.* **118**(2), pp. 281–293 (2007).

[40] E. F. da Silva, H. F. Svendsen, and K. M. Merz, *J. Phys. Chem. A* **113**(22), pp. 6404–6409 (2009).

[41] S. C. L. Kamerlin, M. Haranczyk, and A. Warshel, *ChemPhysChem* **10**(7), pp. 1125–1134 (2009).

[42] D. Frenkel and B. Smit, *Understanding Molecular Simulation*, Computational Science Series. Academic Press 2 edition (2002).

[43] R.W. Hockney and Eastwood J.W., *Computer simulations using particles.*, McGraw-Hill New York (1981).

[44] L. Martinez, R. Andrade, E. G. Birgin, and J. M. Martinez, *J. Comput. Chem.* **30**(13), pp. 2157–2164 (2009).

[45] T. Verstraelen, V. Van Speybroeck, and M. Waroquier, *J. Chem. Inf. Model.* **48**(7), pp. 1530–1541 (2008).

[46] T. Verstraelen, M. Van Houteghem, V. Van Speybroeck, and M. Waroquier, *J. Chem. Inf. Model.* **48**(12), pp. 2414–2424 (2008).

[47] A. Laio, A. Rodriguez-Fortea, F. L. Gervasio, M. Ceccarelli, and M. Parrinello, *J. Phys. Chem. B* **109**(14), pp. 6714–6721 (2005).

[48] G. Bussi, A. Laio, and M. Parrinello, *Phys. Rev. Lett.* **96**, pp. 090601 (2006).

[49] Y. Crespo, F. Marinelli, F. Pietrucci, and A. Laio, *Physical Review E* **81**(5), pp. 055701 (2010).

[50] R. Martonak, A. Laio, and M. Parrinello, *Phys. Rev. Lett.* **90**(7), pp. 075503 (2003).

[51] A. Laio and F. L. Gervasio, *Rep. Prog. Phys.* **71**(12), pp. 126601 (2008).

[52] V. Leone, F. Marinelli, P. Carloni, and M. Parrinello, *Curr. Opin. Struct. Biol.* **20**(2), pp. 148–154 (2010).

[53] D. Branduardi, F. L. Gervasio, and M. Parrinello, *J. Chem. Phys.* **126**(5), pp. 054103 (2007).

[54] B. Ensing, A. Laio, M. Parrinello, and M. L. Klein, *J. Phys. Chem. B* **109**(14), pp. 6676–6687 (2005).

[55] P. Raiteri, A. Laio, F. L. Gervasio, C. Micheletti, and M. Parrinello, *J. Phys. Chem. B* **110**(8), pp. 3533–3539 (2006).

[56] R. E. Bulo, H. Van Schoot, D. Rohr, and C. Michel, *Int. J. Quantum Chem.* **110**, pp. 2299–2307 (2010).

[57] A. Krief, *Tetrahedron* **36**, pp. 2531–2640 (1980).

[58] N. Giubellina, W. Aelterman, and N. De Kimpe, *Pure Appl. Chem.* **75**(10), pp. 1433–1442 (2003).

[59] S. Mangelinckx, N. Giubellina, and N. De Kimpe, *Chem. Rev.* **104**(5), pp. 2353–2399 (2004).

[60] A. Job, C. F. Janeck, W. Bettray, R. Peters, and D. Enders, *Tetrahedron* **58**(12), pp. 2253–2329 (2002).

[61] R. Knorr and P. Low, *J. Am. Chem. Soc.* **102**(9), pp. 3241–3242 (1980).

[62] G. Stork and S.R. Dowd, *J. Am. Chem. Soc.* **85**, pp. 2178–2180 (1963).

[63] R. R. Fraser, J. Banville, and K.L. Dhawan, *J. Am. Chem. Soc.* **100**(25), pp. 7999–8001 (1978).

[64] J. T. Welch and K. W. Seper, *J. Org. Chem.* **53**(13), pp. 2991–2999 (1988).

[65] N. De Kimpe, P. Sulmon, and N. Schamp, *Angew. Chem.* **97**, pp. 878–879 (1985).

[66] N. De Kimpe, W. Coppens, J. T. Welch, and B. De Corte, *Synthesis* **8**, pp. 675–677 (1990).

[67] P. Sulmon, N. De Kimpe, and N. Schamp, *Synthesis* **1**, pp. 8–12 (1989).

[68] N. Giubellina and N. De Kimpe, *Synlett* **6**, pp. 976–980 (2005).

[69] N. Giubellina, S. Mangelinckx, K. W. Tornroos, and N. De Kimpe, *J. Org. Chem.* **71**(16), pp. 5881–5887 (2006).

[70] W. Aelterman, N. De Kimpe, V. Tyvorskii, and O. Kulinkovich, *J. Org. Chem.* **66**(1), pp. 53–58 (2001).

[71] W. Aelterman, N. De Kimpe, and J. P. Declercq, *J. Org. Chem.* **63**(1), pp. 6–11 (1998).

[72] E. Van Hende, G. Verniest, R. Surmont, and N. De Kimpe, *Org. Lett.* **9**(15), pp. 2935–2938 (2007).

[73] W. Aelterman, N. De Kimpe, and O. Kulinkovich, *Bull. Soc. Chim. Belg.* **106**(11), pp. 703–708 (1997).

[74] G. Verniest, R. Surmont, E. Van Hende, A. Deweweire, F. Deroose, J. W. Thuring, and N. De Kimpe, *J. Org. Chem.* **73**(14), pp. 5458–5461 (2008).

[75] N. De Kimpe, P. Brunet, R. Verhe, and N. Schamp, *J. Chem. Soc,, Chem. Commun.* **12**, pp. 825–827 (1988).

[76] W. Aelterman, K. A. Tehrani, W. Coppens, T. Huybrechts, N. De Kimpe, D. Tourwe, and J. P. Declercq, *Eur. J. Org. Chem.* **1**, pp. 239–250 (1999).

[77] V. Capriati, S. Florio, R. Luisi, and M. T. Rocchetti, *J. Org. Chem.* **67**(3), pp. 759–763 (2002).

[78] S. Florio, F. M. Perna, R. Luisi, J. Barluenga, F. Rodriguez, and F. J. Fahanas, *J. Org. Chem.* **69**(16), pp. 5480–5482 (2004).

[79] N. De Kimpe, E. Stanoeva, and N. Schamp, *Tetrahedron Lett.* **29**(5), pp. 589–592 (1988).

[80] N. De Kimpe, W. Aelterman, K. DeGeyter, and J. P. Declercq, *J. Org. Chem.* **62**(15), pp. 5138–5143 (1997).

[81] W. Aelterman, N. Giubellina, E. Stanoeva, K. De Geyter, and N. De Kimpe, *Tetrahedron Lett.* **45**(2), pp. 441–444 (2004).

[82] P. Sulmon, N. De Kimpe, N. Schamp, J. P. Declercq, and B. Tinant, *J. Org. Chem.* **53**(19), pp. 4457–4462 (1988).

[83] V. Capriati, L. Degennaro, S. Florio, R. Luisi, C. Tralli, and L. Troisi, *Synthesis* **15**, pp. 2299–2306 (2001).

[84] F. M. Perna, V. Capriati, S. Florio, and R. Luisi, *J. Org. Chem.* **67**(24), pp. 8351–8359 (2002).

[85] F. Bona, L. De Vitis, S. Florio, L. Ronzini, and L. Troisi, *Tetrahedron* **59**(9), pp. 1381–1387 (2003).

[86] L. Troisi, L. De Vitis, C. Granito, P. Metrangolo, T. Pilati, and L. Ronzini, *Arkivoc* **xiv**, pp. 61–73 (2004).

[87] R. Luisi, V. Capriati, S. Florio, and R. Ranaldo, *Tetrahedron Lett.* **44**(13), pp. 2677–2681 (2003).

[88] L. De Vitis, S. Florio, C. Granito, L. Ronzini, L. Troisi, V. Capriati, R. Luisi, and T. Pilati, *Tetrahedron* **60**(5), pp. 1175–1182 (2004).

[89] R. Luisi, V. Capriati, S. Florio, P. Di Cunto, and B. Musio, *Tetrahedron* **61**(13), pp. 3251–3260 (2005).

[90] L. Troisi, C. Granito, C. Carlucci, F. Bona, and S. Florio, *Eur. J. Org. Chem.* (3), pp. 775–781 (2006).

[91] L. Troisi, S. Florio, and C. Granito, *Steroids* **67**(8), pp. 687–693 (2002).

[92] V.K. Aggarwal, D.M. Badine, and V.A. Moorthie, *Aziridines and Epoxides in Organic Synthesis*, Wiley-VCH Weinheim (2006).

[93] D. T. Bowron, J. L. Finney, and A. K. Soper, *J. Am. Chem. Soc.* **128**(15), pp. 5119–5126 (2006).

[94] C. Adamo and V. Barone, *J. Chem. Phys.* **108**(2), pp. 664–675 (1998).

[95] N.E. Schultz, Y. Zhao, and D.G. Truhlar, *J. Phys. Chem. A* **109**, pp. 11127–11143 (2005).

[96] L.M. Pratt, B. Ramachandran, J. Xidos, C.J. Cramer, and D.G. Truhlar, *J. Org. Chem.* **67**, pp. 7607–7612 (2002).

[97] T. Fujisawa, R. Hayakawa, and M. Shimizu, *Tetrahedron Lett.* **33**, pp. 7903–7906 (1992).

[98] J. Barluenga, C. del Pozo Losada, and B. Olano, *Tetrahedron Lett.* **34**, pp. 5497–5498 (1993).

[99] M. Nakamura, T. Hatakeyama, K. Hara, and E. Nakamura, *J. Am. Chem. Soc.* **125**(21), pp. 6362–6363 (2003).

[100] H. O. House, D. S. Crumrine, A. Y. Teranishi, and H. D. Olmstead, *J. Am. Chem. Soc.* **95**(10), pp. 3310–3324 (1973).

[101] R. Glaser and A. Streitwieser, *J. Org. Chem.* **56**(23), pp. 6612–6624 (1991).

[102] S. Florio, V. Capriati, R. Luisi, A. Abbotto, and D. J. Pippel, *Tetrahedron* **57**(31), pp. 6775–6786 (2001).

[103] V. M. Rayon and J. A. Sordo, *J. Chem. Phys.* **122**(20), pp. 204303 (2005).

[104] M. Strajbl and J. Florian, *Theor. Chem. Acc.* **99**(3), pp. 166–170 (1998).

[105] B. Cadioli, E. Gallinella, C. Coulombeau, H. Jobic, and G. Berthier, *J. Phys. Chem.* **97**(30), pp. 7844–7856 (1993).

[106] M. J. Bedard-Hearn, R. E. Larsen, and B. J. Schwartz, *J. Phys. Chem. B* **107**(51), pp. 14464–14475 (2003).

[107] J. Chandrasekhar and W. L. Jorgensen, *J. Chem. Phys.* **77**(10), pp. 5073–5079 (1982).

[108] J. VandeVondele, M. Krack, F. Mohamed, M. Parrinello, T. Chassaing, and J. Hutter, *Comput. Phys. Commun.* **167**(2), pp. 103–128 (2005).

[109] A. D. Becke, *Phys. Rev. A* **38**(6), pp. 3098–3100 (1988).

[110] C. T. Lee, W. T. Yang, and R. G. Parr, *Phys. Rev. B.* **37**(2), pp. 785–789 (1988).

[111] G. Lippert, J. Hutter, P. Ballone, and M. Parrinello, *J. Phys. Chem.* **100**(15), pp. 6231–6235 (1996).

[112] S. Goedecker, M. Teter, and J. Hutter, *Phys. Rev. B.* **54**(3), pp. 1703–10 (1996).

[113] C. Hartwigsen, S. Goedecker, and J. Hutter, *Phys. Rev. B.* **58**(7), pp. 3641–3662 (1998).

[114] D. R. Lide, *CRC Handbook of Chemistry and Physics*, Chichester, Wiley 84 edition (2003).

[115] C. Carvajal, K. J. Tölle, J. Smid, and M. Szwarc, *J. Am. Chem. Soc.* **87**(24), pp. 5548–5553 (1965).

[116] H. Li and J. H. Jensen, *J. Comput. Chem.* **25**(12), pp. 1449–1462 (2004).

[117] J. Y. Lee, T. J. Lynch, D. T. Mao, D. E. Bergbreiter, and M. Newcomb, *J. Am. Chem. Soc.* **103**(20), pp. 6215–6217 (1981).

[118] J. K. Smith, D. E. Bergbreiter, and M. Newcomb, *J. Org. Chem.* **46**(15), pp. 3157–3158 (1981).

[119] L. M. Pratt, N. Van Nguyen, and B. Ramachandran, *J. Org. Chem.* **70**(11), pp. 4279–4283 (2005).

[120] P. L. Fast, M. L. Sanchez, and D. G. Truhlar, *Chem. Phys. Lett.* **306**(5-6), pp. 407–410 (1999).

[121] J. A. Pople, M. Headgordon, and K. Raghavachari, *J. Chem. Phys.* **87**(10), pp. 5968–5975 (1987).

[122] L. M. Pratt and A. Streitwieser, *J. Org. Chem.* **68**(7), pp. 2830–2838 (2003).

[123] Y. Takano and K. N. Houk, *J. Chem. Theory Comput.* **1**(1), pp. 70–77 (2005).

[124] A. Laio and M. Parrinello, *Proc. Natl. Acad. Sci. U.S.A.* **99**(20), pp. 12562–12566 (2002).

[125] O. F. Olaj, I. Bitai, and F. Hinkelmann, *Makromol. Chem.* **188**(7), pp. 1689–1702 (1987).

[126] O. F. Olaj and I. Schnollbitai, *Eur. Polym. J.* **25**(7-8), pp. 635–641 (1989).

[127] A. M. Van Herk, *Macromol. Theory Simul.* **9**(8), pp. 433–441 (2000).

[128] S. Beuermann and M. Buback, *Prog. Polym. Sci.* **27**(2), pp. 191–254 (2002).

[129] C. Barner-Kowollik, M. Buback, M. Egorov, T. Fukuda, A. Goto, O. F. Olaj, G. T. Russell, P. Vana, B. Yamada, and P. B. Zetterlund, *Prog. Polym. Sci.* **30**(6), pp. 605–643 (2005).

[130] K. Van Cauter, V. Van Speybroeck, P. Vansteenkiste, M.-F. Reyniers, and M. Waroquier, *ChemPhysChem* **7**(1), pp. 131–140 (2006).

[131] K. Van Cauter, K. Hemelsoet, V. Van Speybroeck, M.-F. Reyniers, and M. Waroquier, *Int. J. Quantum Chem.* **102**(4), pp. 454–460 (2005).

[132] I. Değirmençi, V. Aviyente, V. Van Speybroeck, and M. Waroquier, *Macromolecules* **42**(8), pp. 3033–3041 (2009).

[133] X. R. Yu, J. Pfaendtner, and L. J. Broadbelt, *J. Phys. Chem. A* **112**(29), pp. 6772–6782 (2008).

[134] S. C. Thickett and R. G. Gilbert, *Macromolecules* **41**(12), pp. 4528–4530 (2008).

[135] D. M. Huang, M. J. Monteiro, and R. G. Gilbert, *Macromolecules* **31**(16), pp. 5175–5187 (1998).

[136] K. Van Cauter, V. Van Speybroeck, and M. Waroquier, *ChemPhysChem* **8**(4), pp. 541–552 (2007).

[137] O. F. Olaj and I. Schnoll-Bitai, *Monatsh. Chem.* **130**(6), pp. 731–740 (1999).

[138] S. Beuermann, *Macromol. Rapid Commun.* **30**(13), pp. 1066–1088 (2009).

[139] S. Beuermann and N. Garcia, *Macromolecules* **37**(8), pp. 3018–3025 (2004).

[140] H. R. Lin, *Eur. Polym. J.* **37**(7), pp. 1507–1510 (2001).

[141] S. A. Seabrook, M. P. Tonge, and R. G. Gilbert, *J. Polym. Sci. Pol. Chem.* **43**(7), pp. 1357–1368 (2005).

[142] Y. Jiang, M. Garland, K. J. Carpenter, P. S. Suresh, and E. Widjaja, *J. Polym. Sci. Pol. Chem.* **45**(23), pp. 5697–5704 (2007).

[143] F. Ganachaud, R. Balic, M. J. Monteiro, and R. G. Gilbert, *Macromolecules* **33**(23), pp. 8589–8596 (2000).

[144] I. Değirmençi, Ş. Eren, V. Aviyente, B. De Sterck, K. Hemelsoet, V. Van Speybroeck, and M. Waroquier, *Macromolecules* **43**(13), pp. 5602–5610 (2010).

[145] B. De Sterck, R. Vaneerdeweg, F. Du Prez, M. Waroquier, and V. Van Speybroeck, *Macromolecules* **43**(2), pp. 827–836.

[146] Y. Zhao and D. G. Truhlar, *J. Phys. Chem. A* **108**(33), pp. 6908–6918 (2004).

[147] A. D. Boese and J. M. L. Martin, In *229th National Meeting of the American-Chemical-Society* , p. 274 San Diego, CA (2005).

[148] K. Hemelsoet, V. Van Speybroeck, and M. Waroquier, *J. Phys. Chem. A* **112**(51), pp. 13566–13573 (2008).

[149] C. Y. Lin, E. I. Izgorodina, and M. L. Coote, *Macromolecules* **43**(1), pp. 553–560 (2010).

[150] P. Pascal, D. H. Napper, R. G. Gilbert, M. C. Piton, and M. A. Winnik, *Macromolecules* **23**(24), pp. 5161–5163 (1990).

[151] A. Klamt, *From Quantum Chemistry to Fluid Phase Thermodynamics and Drug Design*, Elsevier Amsterdam (2005).

[152] D. Kahne and W. C. Still, *J. Am. Chem. Soc.* **110**(22), pp. 7529–7534 (1988).

[153] R. M. Smith and D. E. Hansen, *J. Am. Chem. Soc.* **120**(35), pp. 8910–8913 (1998).

[154] Arthur B. Robinson, James W. Scotchler, and James H. McKerrow, *J. Am. Chem. Soc.* **95**(24), pp. 8156–8159 (1973).

[155] B. A. Robinson and J. W. Tester, *Int. J. Chem. Kinet.* **22**(5), pp. 431–448 (1990).

[156] H. Slebocka-Tilk, F. Sauriol, M. Monette, and R. S. Brown, *Can. J. Chem.-Rev. Can. Chim.* **80**(10), pp. 1343–1350 (2002).

[157] M. N. Khan, *Int. J. Chem. Kinet.* **41**(9), pp. 599–611 (2009).

[158] L. Gorb, A. Asensio, I. Tunon, and M. F. Ruiz-Lopez, *Chem.-Eur. J.* **11**(22), pp. 6743–6753 (2005).

[159] S. Chalmet, W. Harb, and M. F. Ruiz-Lopez, *J. Phys. Chem. A* **105**(51), pp. 11574–11581 (2001).

[160] M. Cascella, S. Raugei, and P. Carloni, *J. Phys. Chem. B* **108**(1), pp. 369–375 (2004).

[161] D. Zahn, *Eur. J. Org. Chem.* **19**, pp. 4020–4023 (2004).

[162] D. M. Du, A. P. Fu, and Z. Y. Zhou, *Int. J. Quantum Chem.* **99**(1), pp. 1–10 (2004).

[163] W. C. Liang, H. R. Li, X. B. Hu, and S. J. Han, *J. Phys. Chem. A* **108**(46), pp. 10219–10224 (2004).

[164] Q. G. Li, Y. Xue, and G. S. Yan, *J. Mol. Struct.-Theochem* **868**(1-3), pp. 55–64 (2008).

[165] J. Florian and J. Leszczynski, *J. Am. Chem. Soc.* **118**(12), pp. 3010–3017 (1996).

[166] S. Catak, G. Monard, V. Aviyente, and M. F. Ruiz-Lopez, *J. Phys. Chem. A* **113**(6), pp. 1111–1120 (2009).

[167] Y. A. Mantz, D. Branduardi, G. Bussi, and M. Parrinello, *J. Phys. Chem. B* **113**(37), pp. 12521–12529 (2009).

A

List of Symbols

A	Preexponential Factor in the Arrhenius Equation
A_k	Tessera Surface Area in ASC Methods
β	Temperature Inversed
D	Diffusion Coefficient
E_A	The Activation Energy in the Arrhenius Equation
ϵ	Dielectric Constant
ϵ_i	Dielectric Constant of region i
ε	The Error on the FES obtained from a MTD Simulation
F_j	Force on Atom j
$F(s)$	Free Energy as a function of CVs in the MTD Method
G_{cav}	Cavitation Contribution to ΔG_{sol}
G_{dis}	Dispersion Contribution to ΔG_{sol}
G_{rep}	Repulsive Contribution to ΔG_{sol}
G^S	Gibbs Free Energy in Solution
ΔG_{el}	Electrostatic Contribution to ΔG_{sol}
ΔG_{sol}	Gibbs Free Energy of Solvation
ΔG_{sol}^{pcm}	Gibbs Free Energy of Solvation using a Polarizable Continuum Method
ΔG_{sol}^{vacuo}	Gibbs Free Energy of Solvation Using Explicit Solvent *in vacuo*
Γ	Cavity Surface
$\hat{H}_M^0$	The Hamiltonian of a Solute in Vacuo
k_p	Propagation Rate Coefficient
m_j	Mass of Atom j
$\vec{n}_{ij}$	Normal Vector on a Surface Pointing from Region i to j
n_S	Numerical Solvent Density
P	Pressure
$P_i(\vec{r})$	Polarization Vector, Pointing Towards Region i

	on a Surface
q_k	Point charge Associated with Tessera k
R	Ideal Gas Constant (8.314 $\mathrm{JK}^{-1}\mathrm{mol}^{-1}$)
r_0	Cutoff Distance for a Coordination Number
r_{AS}	Distance between Atoms A and S
$R_{eff,M}$	Effective Solute Radius
R_M	Solute Radius
R_{MS}	Sum of Solvent Radius and Solute Radius
R_S	Solvent Radius
$\rho_M(\vec{r})$	Charge Density of a Solute Molecule
S_i	Solvent Exposed Surface
$s(x)$	Set of CVs as a Function of Internal Coordinates
δs	Gaussian Width of a CV in the MTD Method
$\sigma^*(s)$	The Ideal Screened Charge Density in the C-PCM Method
$\sigma(\vec{s})$	Surface Charge Distribution
t	Time
T	Temperature in Kelvin
τ_G	Deposition Time in the MTD Method
$\hat{V}$	The Total Electrostatic Potential in a Continuum Model
$V_G(s(x),t)$	Time-Dependent Biasing Potential as a Function of the CVs in the MTD Method
V_M	Solute Volume
$\hat{V}_M$	The Electrostatic Potential of a Solute
$\hat{V}_{int}$	The Reaction Field
w	Gaussian Height in the MTD Method
Ψ	The Molecular Wavefunction

B

List of Abbreviations

AA	Acrylamide
ACE	Acetic Acid
AMD	Acetamide
ASC	Apparent Surface Charge
BEM	Bias-Exchange Metadynamics
C-PCM	Conductor-like Polarizable Continuum Model
CSE	Coordination Solvation Energy
CN	Coordination Number
CV	Collective Variable
D-PCM	Dielectric Polarizable Continuum Model
DSE	Dielectric Solvation Energy
DFT	Density Functional Theory
EHMA	Ethyl-2-(hydroxymethyl)acrylate
EPSR	Empirical Potential Structure Refinement
FES	Free Energy Surface
GEM	*Gem*-diol
GB	Generalized Born Model
HF	Hartree-Fock
IEF-PCM	Integral Equation Formalism of the Polarizable Continuum Model
IRC	Internal Reaction Coordinate
MAA	Methacrylamide
MAMD	N-methylacetamide
MM	Molecular Mechanics
MMA	Methyl Metacrylate
MC	Mont Carlo
MD	Molecular Dynamics
MPE	Multipole Expansions

MTD	Metadynamics
NIPAM	N-Isopropyl Acrylamide
NPE	Non-homogeneous Poisson Equation
NPT	Isothermal-Isobaric Ensemble
NVE	Microcanonical Ensemble
NVT	Canonical Ensemble
PBC	Periodic Boundary Condition
PCM	Polarizable Continuum Model
PLP	Pulsed Laser Polymerization
QM/MM	Combined Quantum Mechanical and Molecular Mechanics Methodology
SAS	Solvent Accessible Surface
SCRF	Self-Consistent Reaction Field
SES	Solvent Excluding Surface
TAUT	Tautomeric Form
THF	Tetrahydrofuran
TST	Transition State Theory

C

List of Publications

Publications In International Peer-reviewed Journals

1. *Theoretical Study on the Structural Properties of Various Solvated Metalated 3-Halo-1-azaallylic Anions*
   De Sterck B., Van Speybroeck V., Mangelinckx S., Verniest G., De Kimpe N., and Waroquier M.
   J. Phys. Chem. A, **2009**, *113*, 6375-6380
2. *Insight into the Solvation and Isomerization of 3-Halo-1-azaallylic Anions from Ab Initio Metadynamics Calculations and NMR Experiments*
   Declerck R,. De Sterck B., Verstraelen T., Verniest G., Mangelinckx S., Jacobs J., De Kimpe N., Waroquier M., and Van Speybroeck V.
   Chem.-Eur. J., **2009**, *15*, 580-5840
3. *Solvent Effects on Free Radical Polymerization Reactions: The Influence of Water on the Propagation rate of Acrylamide and Methacrylamide*
   De Sterck B., Vaneerdeweg R., Du Prez F., Waroquier M., and Van Speybroeck V.
   Macromolecules, **2010**, *43*, 827-836
4. *Modeling the Solvent Effect on the Tacticity in the Free Radical Polymerization of Methyl Methacrylate*
   Değirmençi İ., Eren Ş., Aviyente V., De Sterck B., Hemelsoet K., Van Speybroeck V., and Waroquier M.
   Macromolecules, **2010**, *43*, 5602-5610
5. *Zeolite Shape-Selectivity in the gem-Methylation of Aromatic Hydrocarbons*
   Lesthaeghe D., De Sterck, B., Van Speybroeck V., Marin G.B., and Waroquier M.
   Angew. Chem. Int. Ed., **2007**, *46*, 1311-1314
6. *Influence of protein environment on the EPR properties of flavoprotein radicals: a QM/MM study*

Pauwels E., Declerck R., Verstraelen T., De Sterck B., Kay C.W.M., Van Speybroeck V., and Waroquier M.
in preparation

Oral Contributions to International Conferences

1. *Ab initio evaluation of 3-halo-1-azaallylic anions as synthetic building blocks.*
   De Sterck B., Van Speybroeck V., and Waroquier M.
   ACS Fall 2007 National Meeting & Exposition, Boston, MA, 19 - 23 August, **2007**
2. *Elucidation of the acetamide hydrolysis mechanism using QM metadynamics simulations as a model for amide hydrolysis in proteins.*
   De Sterck B., Catak S., Waroquier M., and Van Speybroeck V.
   ACS Spring 2010 National Meeting & Exposition , San Francisco, CA, 17 - 25 March, **2010**

Poster Contributions

This research was presented via poster presentations on a number of international conferences and workshops.